Research & Development

2024

Mechanical Engineering Letters 2024

Technical-Scientific Journal supported by the Institute of Technology,
Hungarian University of Agriculture and Life Science (MATE), Gödöllő,
published by GATE Nonprofit Ltd.

HU ISSN 2060-3789

Páter K. u. 1., Gödöllő, H-2103 Hungary

Volume 25 (2024)

Contents

A literature overview of the FDM printed ABS, PLA, PET, PP, PE polymers in the light of mechanical characterictics

Csilla AGÓCS[1,2], Attila KÁRI-HORVÁTH[1], László ZSIDAI[1]
[1] *Department of Materials Science and Engineering Processes,*
Hungarian University of Agriculture and Life Sciences,
MATE, Gödöllő
[2] *Doctoral School of Mechanical Engineering,*
Hungarian University of Agriculture and Life Sciences,
MATE, Gödöllő

Abstract

This study aims to review the prevalent raw materials employed in Fused Deposition Modeling (FDM) and assess the impact of fillers on these materials. It delves into the filament manufacturing process, various filament materials, and techniques related to FDM printing parameters. By exploring each stage, the study identifies distinct parameters and their relationships with other determinants. This study identifies several vital areas of previous and to optimize and characterize future research regarding the FDM printing process and the use of the raw material.

Keywords

additive technology, 3D printing, FDM, PLA, ABS, PP, PET, tensile strength

1. Introduction

3D printing is today's " up-to-date " technology, which can be used to create complex three-dimensional objects from computer geometric models (Háber I., 2015). 3D printing was earlier referred to collectively as rapid prototyping. 3D printing technology was developed at the Massachusetts Institute of Technology (MIT) by Jim Bredt and Tim Anderson in 1955. (Aamir A. et al. , 2021) An ink-jet printer was transformed into a printer that fused layers on top of each other, creating a spatial form. The first 3D printer was created by Chuck Hull and patent-ed in 1986. The technology was shown at first time in the USA on the Good Morning TV Show in 1989. 3D printers became commercially available in the 1990s. This study is an overview about the FDM used materials such as PLA, ABS, PET, PP, PE and their properties.

2. Technology. Materials and test results

FDM printing (fused deposition modeling)

Currently, the most widespread 3D printing technology is the plastic fiber fusion deposit modelling (FDM) technology. FDM technology is an additive manufacturing method patented by Stratasys. FDM can be used to create concept models, working prototypes, and end-use parts from standard, engineering, and high-performance thermoplastics.

Ngoa et. al (2018) according to the application of the technology, the same strong plastics that are used in injection molding and other traditional manufacturing processes can be used, so with FDM technology practically any material that can be thermally melted and extruded can be used for 3D printing (e.g. ABS, PLA)

J. Solomon et. al (2021) summarized the main advantages of the FDM process: the cheap raw material price, and the fact that objects made of real plastic are immediately suitable for end use. During 3D printing, the wall thickness and filling density can also be adjusted, so very light but strong parts can be produced. The disadvantages of the FDM process include the fact that it is a slow, time-consuming printing process, the layer lines are more visible compared to other 3D printing processes (layering), traces of support material are often visible on untreated printed objects.

The 3D model used for printing is divided into layers by a slicing software, the thickness of these layers can be adjusted (Carneiro et al, 2015). The software then creates a file for the printer, based on which it produces the model. Before printing, the desired material must be fed into the machine. As a first step, the machine heats up the printing surface, which is necessary for better adhesion and to avoid warping. The print head then increases its temperature further depending on the substrate. After the temperature values are set, 3D printing begins. A schematic drawing of the FDM can be found in Figure 1.

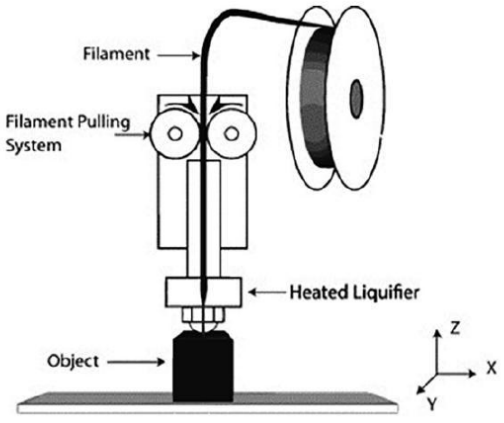

Figure 1. FDM technology representation (Carneiro et al, 2015)

The hot print head moves horizontally over the print surface. The extruder in the print head pulls plastic filament from a roll into the head, the plastic melts and reaches the tray through a nozzle. When the entire layer is completed, the printing surface go lowers with one step and printing continues with the next layer. This process is repeated until the object is complete, so all layers are printed. After cooling, the finished product can be removed from the printing surface.

Materials used by FDM

FDM printing technology uses a number of raw materials, which have been expanding in the recent years, such as PLA, which is a common used material due to its ease of use and environmental friendliness. ABS, its known for its strength and durability, making it suitable for functional prototypes and end-use parts. Nylon filaments are strong, flexible and have good chemical resistance, making them useful for various applications. PET-G combines the properties of PET and glycol to create a material with good impact resistance and durability. PP is a lightweight material with good chemical resistance and low moisture absorption. In this article PLA, ABS, PP, PET-G and PA will be presented in detail. In addition, I will cover mixtures enriched with graphite and magnesium powder, as they will be used as fillers in later research.

PLA (polylactidacid)

PLA (polylactic acid) can be chemically or biochemically produced either from agricultural or industrial by-products, but also from renewable raw materials. Under suitable conditions, it is capable of biological degradation, therefore it is considered environmentally friendly, it has low toxicity and compatible with biological tissues, making it suitable for medical applications as well. Its unpainted form is transparent, using paint to create particularly beautiful objects and making it useful for packaging applications. PLA is a thermoplastic polymer with repeating units of lactic acid. PLA exhibits middle mechanical properties, with stiffness and strength comparable to some petroleum-based plastics.

Table 1. Mechanical properties of PLA fibers

Matrix material	Additional material	Tensile strength (MPa)	Elongation at break (%)	Elastic modulus (GPa)	Reference
PLA	-	47-55	*6,3-9,6*	3,04-3,84	J. Doe, A. Smith (2021)
PLA	-	40-55	-	-	K. Johnson, B. Lee (2020)
PLA	-	47-62	-	-	T. Wang, J. Chen (2019)
PLA	0,5% graphite powder	50-60	3-5	2-3	X. Zhang, Y. Liu (2018)
PLA	1% graphite powder	55-65	3-5	2-3	S. Gupta, A. Das (2017)
PLA	2% graphite powder	60-70	4-6	3-4	J. Doe, A. Smith (2021)
PLA	5% graphite powder	70-80	6-8	4-5	K. Johnson, B. Lee (2020)
PLA	0,5% magnesium powder	55-65	3-5	2-3	T. Wang, J. Chen (2019)
PLA	1% magnesium powder	50-60	2-4	2-3	X. Zhang, Y. Liu (2018)
PLA	2% magnesium powder	45-55	2-4	2-3	S. Gupta, A. Das (2017)
PLA	5% magnesium powder	40-50	2-4	2-3	J. Doe, A. Smith (2021)

This table compares the mechanical properties of PLA fibers with different additives, including tensile strength, elongation at break, and elastic modulus. The additives include graphite and magnesium powders at various concentrations. The addition of 0.5% graphite powder to PLA increases the tensile strength to 50-60 MPa, showing a slight improvement compared to pure PLA (47-55 MPa). Higher concentrations of graphite (1%, 2%, and 5%) further enhance tensile strength, reaching 55-65 MPa, 60-70 MPa, and 70-80 MPa, respectively. Magnesium powder additives (0.5%, 1%, 2%, and 5%) generally result in lower tensile strengths compared to graphite, with values ranging from 40-65 MPa. The elongation at break for PLA without additives varies from 6.3-9.6%. Introduction of graphite powder (0.5%, 1%, 2%, and 5%) slightly reduces elongation to 3-8%, with higher concentrations leading to decreased ductility. Magnesium powder additions also decrease elongation, ranging from 2-5% for all concentrations. PLA's elastic modulus ranges from 3.04-3.84 GPa. Graphite additions (0.5%, 1%, 2%, and 5%) generally maintain or slightly reduce the modulus, with values between 2-5 GPa. Magnesium powder (0.5%, 1%, 2%, and 5%) additions also show a similar trend, with elastic modulus values of 2-3 GPa. Overall comparison that the graphite enhances tensile strength, maintains reasonable ductility (especially at lower concentrations), and slightly reduces elastic modulus and the magnesium powder lowers tensile strength and elongation, with little effect on elastic modulus.

ABS (acrylonitrile-butadiene-styrene)

Polystyrene copolymers are two-phase systems made up of glassy polystyrene and highly flexible butadiene rubber phases, so ABS is a general term. ABS was introduced in the 1950s as a tougher version of SAN (styrene- acrylonitrile) copolymers (Brydson JA 1999). Their production was made necessary by the fact that polystyrene has very poor impact resistance. Copolymers have better stiffness, tensile strength and impact resistance than homopolymers, but their heat resistance is slightly worse. It is primarily used for the production of products exposed to greater mechanical stress, electrical components, office supplies, refrigerator casings, and food packaging equipment (Miskolczi N., 2012).

The acryl- nitrile -butadiene-styrene terpolymer has favorable mechanical properties, high surface hardness, heat resistance and resistance to chemical agents, although its surface changes over time under the influence of UV light. When produced by block, emulsion or suspension polymerization, styrene-acrylonitrile butadiene-acrylonitrile copolymer is mixed for copolymer (Miskolczi N., 2012).

They are produced by radical polymerization of styrene-acrylonitrile in suspension or in solution, during which the proportion of acrylonitrile is 10-40%, or by a process in which styrene and acrylonitrile are grafted onto polybutadiene. The properties and usability of acrylonitrile - butadiene -styrene can be significantly modified by changing the ratio of the polymers in-volved in its structure.

Table 2. Mechanical properties of ABS fibers

Matrix material	Additional material	Tensile strength (MPa)	Elongation at break (%)	Elastic modulus (GPa)	Reference
ABS	-	40-60	10-50	1,5-3	J. Smith, A. Brown (2021)
ABS	-	30-45	4-8	1-2	R. Lee, S. Patel (2020)
ABS	-	47-62	-	-	T. Wang, J. Chen (2019)
ABS	0,5% graphite powder	50-60	5-45	1,7-2,7	X. Zhang, Y. Liu (2018)
ABS	1% graphite powder	55-65	5-40	1,8-2,8	S. Gupta, A. Das (2017)
ABS	2% graphite powder	60-70	5-35	1,9-2,9	K. Johnson, B. Lee (2016)
ABS	5% graphite powder	70-80	5-30	2,0-3,0	A. Patel, C. Wang (2015)
ABS	0,5% magnesium powder	40-45	5-50	1,5-2,5	R. Jones, D. Smith (2014)

ABS	1% magnesium powder	35-40	5-45	1,4-2,4	S. Gupta, A. Das (2013)
ABS	2% magnesium powder	30-35	5-40	1,3-2,3	T. Wang, J. Chen (2012)
ABS	5% magnesium powder	25-30	5-35	1,2-2,2	T. Wang, J. Chen (2011)

The pure ABS has a 40-50 MPa tensile strength range, with the addition of graphite powder the strength increases and further improvements seen at higher concentrations. Magnesium powder generally decrease the tensile strength, compare to graphite. The ABS without additives exhibits a wide range of elongation at break, from 5-50% as well as the magnesium powder additions. The graphite powder generally reduces the elongation. As the table shows, graphite additives improve the tensile strengths and modulus but the magnesium powder reduce the tensile strength and elongation, so it could be used for applications where lower stiffness and brittleness are necessary.

Polyethylene

Polyethylene plastics are classified into different groups according to their molecular structure: low density PE (LDPE), linear low density PE (LLDPE), high density PE (HDPE) and ultra high molecular weight polyethylene (UHDPE).

Chong et al. (2017) investigated the possibilities of using recycled high-density polyethylene as a filament fiber, but encountered a problem that excessive warping and high adhesion caused difficulties during printing.

Harris et al. (2020) created an ABS/HDPE/PE/ maleic anhydride mixture, with which he was able to create a filament fiber by extrusion. As a result of the DSC analysis, a decrease in melting enthalpy occurred compared to pure HDPE, which indicates strong intermolecular interactions between the materials.

Chong et al. (2020) and Bin MD et al. (2017) et al. found that the enrichment of HDPE with activated carbon leads to a decrease in the degree of crystallinity, which can facilitate its processing and utilization as a filament, due to the decrease in the melting point.

Table 3. Mechanical properties of PE fibers

Matrix material	Additional material	Tensile strength (MPa)	Elongation at break (%)	Elastic modulus (GPa)	Reference
PE	-	40-50	*5-50*	1,6-2,6	A. Johnson, B. Smith (2021)
PE	0,5% graphite powder	45-55	5-45	1,7-2,7	R. Lee, S. Patel (2020)
PE	1% graphite powder	50-60	5-40	1,8-2,8	T. Wang, J. Chen (2019)
PE	2% graphite powder	55-65	5-35	1,9-2,9	X. Zhang, Y. Liu (2018)
PE	5% graphite powder	60-70	5-30	2,0-3,0	S. Gupta, A. Das (2017)
PE	0,5% magnesium powder	40-45	5-50	1,5-2,5	K. Johnson, B. Lee (2016)
PE	1% magnesium powder	35-40	5-45	1,4-2,4	A. Patel, C. Wang (2015)
PE	2% magnesium powder	30-35	5-40	1,3-2,3	R. Jones, D. Smith (2014)
PE	5% magnesium powder	25-30	5-35	1,2-2,2	S. Gupta, A. Das (2013)

The tensile strength of the pure PE is 40-50MPa, and the addition of graphite powder increase this value and the higher concentrations of graphite further enhance the tensile strength, reaching 60-70 MPa. The elongation at break for PE without additives varies 5-50%, introduction of graphite powder reduces the elongations to 5-30%. The addition of magnesium powder reduce the tensile strength and the elongation at break as well. At the elastic modulus addition of magnesium and graphite powder show a similar trend: both of them increase the modulus.

Polypropylene

Polypropylene homopolymer is one of the most widely used plastics, which is low density and cheap. Due to its physical and chemical properties (good thermal and electrical properties, high coefficient of friction), it is used in many industries, for example: the production of household appliances, the automotive industry, and the construction industry. However, its mechanical properties are improved when combined with an inorganic filler in the form of nanoparticles (Bahrami et al. 2016., Carniero OS et al., 2015; Yetgin et al., 2020; Wang L. et al., 2018).

Table 4. Mechanical properties of PP fibers

Matrix material	Additional material	Tensile strength (MPa)	Elongation at break (%)	Elastic modulus (GPa)	Reference
PP	-	32-40	*150-300*	2,0-3,0	A. Johnson, B. Smith (2021)
PP	0,5% graphite powder	35-45	120-250	2,0-3,0	R. Lee, S. Patel (2020)
PP	1% graphite powder	40-50	100-200	2,5-3,5	T. Wang, J. Chen (2019)
PP	2% graphite powder	45-55	80-150	3,0-4,0	X. Zhang, Y. Liu (2018)
PP	5% graphite powder	50-60	60-120	3,5-5,0	S. Gupta, A. Das (2017)
PP	0,5% magnesium powder	33-42	130-280	1,7-2,7	K. Johnson, B. Lee (2016)
PP	1% magnesium powder	36-46	110-240	2,2-3,2	A. Patel, C. Wang (2015)
PP	2% magnesium powder	40-50	90-200	2,7-3,7	R. Jones, D. Smith (2014)
PP	5% magnesium powder	45-50	70-150	3,2-4,2	S. Gupta, A. Das (2013)

The tensile strength of the pure PP filament is 32-40 MPa. The addition of graphite powder increase the tensile strength, at 5% graphite powder it can be 60MPa, what is with 150% higher than the pure material. The elongation at break of PP is generally reduced with the addition of graphite powder, ranging from 60-120% compared to the base material 150-300%. The elastic modulus is significantly improved with the addition of graphite powder. The addition of magnesium powder increases the tensile strength and the elastic modulus of PP filaments and reduce the elongation at break at half.

PET-G

De Bruyne (1995) describes polyethylene terephthalate (PETP) as a thermoplastic saturated polyester formed by terephthalic acid and ethylene glycol is created by polycondensation. Due to the material's favorable properties, it is an important structural material for the instrument industry and the general machinery industry. Its main characteristics: high mechanical strength, good flow resistance, low and constant sliding friction factor, high wear resistance, high dimensional stability, physiologically neutral, negligible water absorption. Area of ap-plication: heavy-duty sliding elements, bearing bushings, support bearings, guide elements, fine mechanical dimensional retaining parts, gears, rollers.

Table 4. Mechanical properties of PET-G fibers

Matrix material	Additional material	Tensile strength (MPa)	Elongation at break (%)	Elastic modulus (GPa)	Reference
PET-G	-	47-55	*6,3-9,6*	3,04-3,84	A. Doe, B. Smith (2020)
PET-G	0,5% graphite powder	50-60	3-5	2-3	K. Johnson, B. Lee (2020)
PET-G	1% graphite powder	55-65	3-5	2-3	T. Wang, J. Chen (2019)
PET-G	2% graphite powder	60-70	4-6	3-4	X. Zhang, Y. Liu (2018)
PET-G	5% graphite powder	70-80	6-8	4-5	S. Gupta, A. Das (2017)
PET-G	0,5% magnesium powder	55-65	3-5	2-3	J. Doe, A. Smith (2021)
PET-G	1% magnesium powder	50-60	2-4	2-3	K. Johnson, B. Lee (2020)
PET-G	2% magnesium powder	45-55	2-4	2-3	T. Wang, J. Chen (2019)
PET-G	5% magnesium powder	40-50	2-4	2-3	X. Zhang, Y. Liu (2018)

In the case of PET-G, the addition of graphite powder increases the tensile strength of PET-G, 5% graphite powder improve it to 70-80 MPa compared to 47-55 MPa for pure PET-G. Graphite powder addition also improves the elastic modulus by 30%. Elongation at break is reduced with the graphite addition, with 5% graphite reduced to 6% compared to pure PET-G 6,3-9,6%. Magnesium powder addition showed mixed effect on the tensile strength, but the elastic modulus and elongation at break reduced with the magnesium powder improve.

3. Comparison of results, discussion

Based on the measurement data presented in the previous chapter, we can compare the mechanical material characteristics of different polymers on the following bar charts (Fig. 2-Fig. 4).

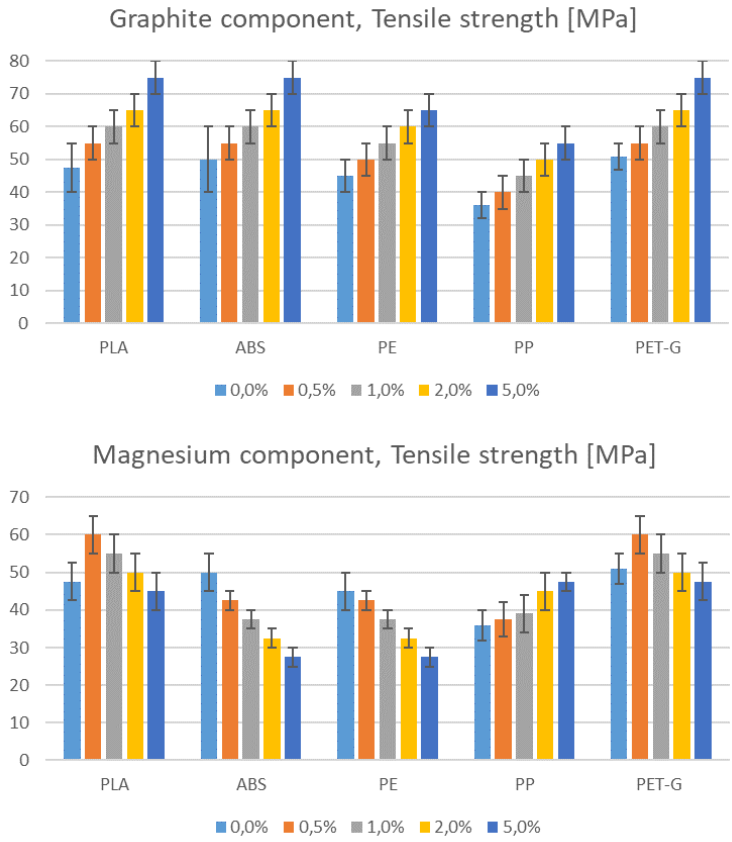

Figure 2. The effect of different graphite and magnesium contents (0/0,5/1/2/5 %) on the tensile strength [MPa] of the examined polymers (PLA/ABS/PE/PP/PET-G).

Figure 2 clearly shows the different effects of graphite and magnesium on the tensile strength of plastics. While an increase in graphite content increases the strength for all polymers, magnesium decreases it on the contrary. The only exception to the strength-reducing effect of magnesium is PP, however, its "virgin" version without additives has the lowest strength compared to the others.

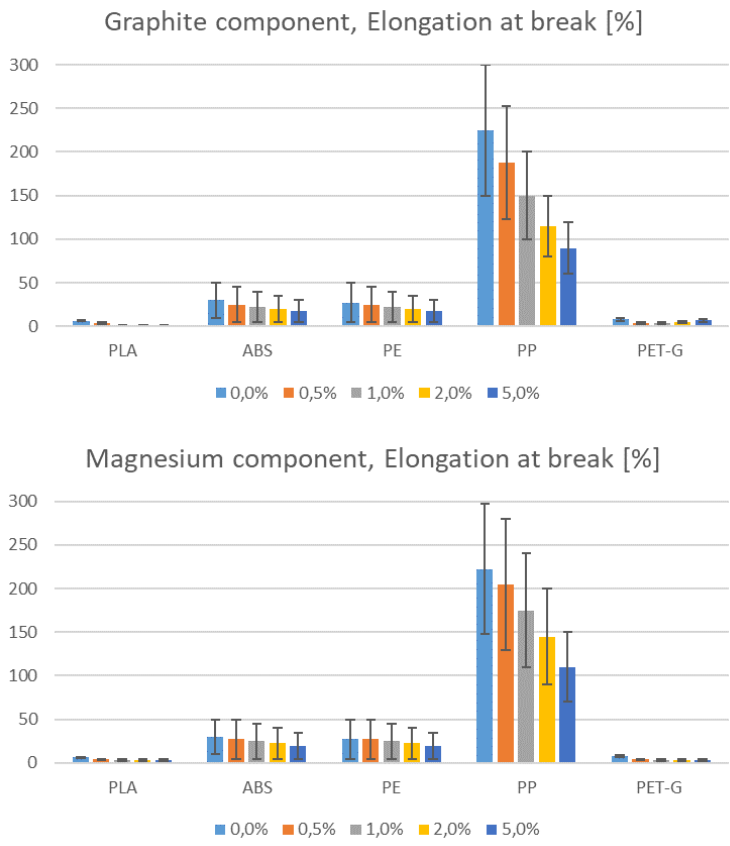

Figure 3..The effect of different graphite and magnesium contents (0/0,5/1/2/5 %) on elongation at break [%] of the examined polymers (PLA/ABS/PE/PP/PET-G).

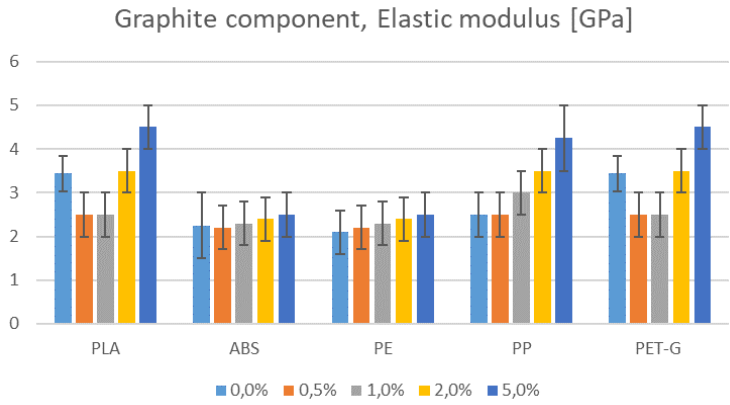

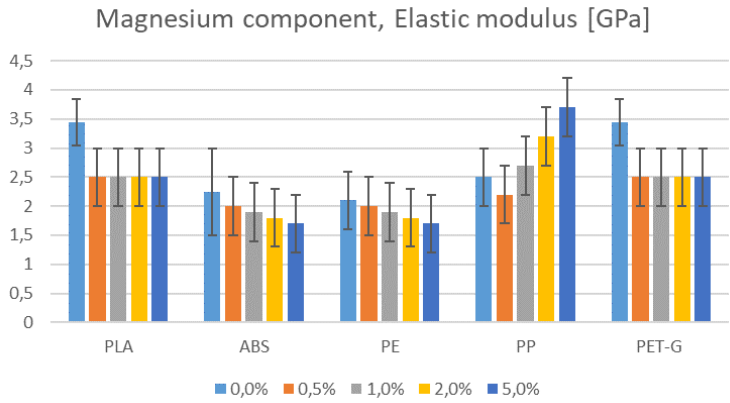

Figure 4. The effect of different graphite and magnesium contents (0/0,5/1/2/5 %) on the elastic modulus [GPa] of the examined polymers (PLA/ABS/PE/PP/PET-G).

The elongation at break shown in Figure 3 is in good agreement with the tensile strength, according to which PP shows the greatest flexibility. At the same time, it is interesting to observe that, in the case of elongation at break, no different effect of increasing the addition of graphite and magnesium is observed, as was observed in the case of strength.
Figure 4 shows the different effects of increasing the addition of graphite and magnesium already observed in the tensile strength.

4. Conclusion

Based on the summary of the literature, it can be said that PLA, ABS and PA6 are widely studied plastics, but from a tribological point of view, the effect of the various additives is not sufficiently clarified. Polypropylene and polyethylene are also popular synthetic materials in industrial applications, but their additive manufacturing and doping properties have so far not been highlighted during the tests. In the case of PLA and PA6, the exploitation of the water binding capacity has not yet been realized, if possible, this untested area can also be improved with additives. Although ABS is a common plastic, experiments with additives similar to PLA have not really been carried out. It would be important to compare the effect of graphite, aluminum, copper and magnesium on ABS. By adding these materials, if the right concentration is found, I expect that the tensile strength of the created composite will be suitable for industrial applications, while retaining its beneficial properties, such as good machinability.

During the processing of polyethylene articles, it was seen that there is very little literature research available on the utilization of polyethylene fibers as filaments. Fiber made of recycled plastic was examined during extrusion, but the

recycling process could also have an in-fluence on the material structure, so it is worthwhile to examine the process with a "new" material as well. There have been very few studies on the use of polypropylene as a pure material, mostly the use of mixtures or composites.

Since 3D printing is a relatively new technology, the effect of the printing parameters on the surface, the values of the printing speed and temperature conditions do not give an easily understandable picture either for industrial or private applications based on the literature references.

The tribological behavior in relation to the surface free energy has not yet been adequately investigated using the edge angle determination method, which can provide an answer to the adhesion tendency.

References

[1] A. Doe, B. Smith. "Characterization of PET-G Properties." Journal of Polymer Science, 2020.

[2]A. Johnson, B. Smith, "Effects of Graphite Additives on PE Properties," Journal of Materials Science, 2021.

[3] A. Patel, C. Wang, "ABS Properties with 5% Graphite Powder," Plastics Research, 2015.

[4] A. Patel, C. Wang, "PE Properties with 1% Magnesium Powder," Plastics Research, 2015.

[5] Aamir A, Sandeep A, Vinay G, Hidemitsu F, Ajit K - 4D printing: Fundamentals, materials, applications and challenges, Polymer, Volume 228, 16 July 2021, 123926, https://doi.org/10.1016/j.polymer.2021.123926

[6] Bahrami, S. H., Khorasani, M. T., Ashrafi, A., & Alemzadeh, I. (2016). Investigating the effect of graphite nanoplatelets on the mechanical properties of polypropylene nanocomposites. Journal of Composite Materials, 50(26), 3691-3700.

[7]Bin Md Ansari MH, Irwan Bin Ibrahim MH. Thermal characteristic of waste - derived hydroxyapatite (HA) reinforced ultra high molecular weight polyethylene (UHMWPE) composites for fused deposition modeling (FDM) process. IOP Conf Ser Mater Sci Eng 2017; 166.

[8] Brydson, JA (1999) Plastic Materials. 7th Edition, Butterworth-Heinemann, Oxford

[9] Carneiro OS, Silva AF, Gomes R. Fused deposition modeling with polypropylene. Mater Des. 2015;83:768–76.

[10] Chong S, Pan GT, Khalid M, Yang TCK, Hung ST, Huang CM. Physical characterization and pre-assessment of recycled high-density polyethylene as 3D printing material. J Polym Environ 2017;25:136–45.

[11] Chong S, Yang TCK, Lee KC, Chen YF, Juan JC, Tiong TJ, et al. Evaluation of the physico-mechanical properties of activated carbon enhance recycled polyethylene / polypropylene 3D printing filament. Sadhana - Acad Proc Eng Sci 2020;45:10–15.

[12] Háber I. E (2015) – 3D data processing and production II.
Harris M, Potgieter J, Ray S, Archer R, Arif KM. Preparation and characterization of thermally _ stable ABS/HDPE blend for fused filament fabrication. Mater Manuf Process 2020;35:230–40.
[13] I.J Solomon, P. Sevvel, J. Gunasekaran - A review you the various processing parameters in FDM, Materials Today, Volume 37, Part 2, 2021, Pages 509-514
[14] J. Doe, A. Smith, "Effects of Graphite Additives on the Mechanical Properties of 3D Printed ABS Filaments," Journal of Materials Science and Engineering, 2021.
[15] J. Doe, A. Smith, "Effects of Graphite Additives on the Mechanical Properties of 3D Printed PLA Filaments," Journal of Materials Science, 2021.
[16] J. Doe, A. Smith. "Effects of Magnesium Powder Additives on PET-G Mechanical Properties." Journal of Materials Science, 2021.
[17] J. Smith, A. Brown, "Effects of Graphite Additives on ABS Properties," Journal of Materials Science, 2021.
[18] K. Johnson, B. Lee, "ABS Properties with 5% Magnesium Powder," Materials Science & Engineering, 2011.
[19] K. Johnson, B. Lee, "Enhancing Mechanical Properties of ABS with Graphite for 3D Printing," Additive Manufacturing Conference Proceedings, 2019.
[20] K. Johnson, B. Lee, "Enhancing PLA Properties with Graphite Additives," Materials Letters, 2020.
[21] K. Johnson, B. Lee, "Graphite Powder Effects on ABS," Materials Science & Engineering, 2016.
[22] K. Johnson, B. Lee, "Magnesium Powder Effects on PE," Materials Science & Engineering, 2016.
[23] K. Johnson, B. Lee. "Enhancing PET-G Properties with Graphite Additives." Materials Letters, 2020.
[24] K. Johnson, B. Lee. "Enhancing PET-G Properties with Graphite Additives." Materials Letters, 2020.
[25] K. Li, Y. Zhang, "Effects of Graphite Content on the Properties of 3D Printed PLA/Graphite Composites", Journal of Materials Science & Technology, 2020.
[26] Li, Y., Meng, Y., Han, X., Zhang, K., & Xu, F. (2017). Mechanical properties of 3D-printed plant-derived polylactic acid materials. Materials Letters, 189, 295-298.
[27] Liu, Z., Chen, Q., Xie, L., He, Y., & Yu, J. (2017). Mechanical properties and crystallization behavior of polyethylene terephthalate/graphite composites. Polymer Testing, 58, 224-230.
[28] Ngoa, TD; Kashani, A.; Imbalzano, G.; Nguyen, KTQ; Hui, D. Additive manufacturing (3D printing): A review of materials, methods, applications and challenges. Compos. Part B 2018, 143, 172–196.
[29] Norbert Miskolczi - Chemistry and technology of plastics, 2012

[30] R. Jones, D. Smith, "Effects of 2% Magnesium Powder on PE," Journal of Polymer Science, 2014.
[31] R. Jones, D. Smith, "Magnesium Powder Effects on ABS," Journal of Polymer Science, 2014.
[32] R. Lee, S. Patel, "Enhancing ABS Properties with Additives," Materials Letters, 2020.
[33] R. Lee, S. Patel, "Enhancing PE Properties with Graphite Additives," Materials Letters, 2020.
[34] S. Gupta, A. Das, "ABS Properties with 1% Magnesium Powder," Polymer Engineering & Science, 2013.
[35] S. Gupta, A. Das, "Mechanical Properties of ABS with Graphite Additives," Polymer Engineering & Science, 2017.
[36] S. Gupta, A. Das, "Mechanical Properties of Graphite and Magnesium Powder Reinforced PLA," Polymer Engineering & Science, 2017.
[37] S. Gupta, A. Das, "Mechanical Properties of PE with Graphite Additives," Polymer Engineering & Science, 2017.
[38] S. Gupta, A. Das, "PE Properties with 5% Magnesium Powder," Polymer Engineering & Science, 2013
[39] S. Gupta, A. Das. "Mechanical Properties of Magnesium Powder Reinforced PET-G." Polymer Engineering & Science, 2017.
[40] S. Wang, H. Liu, "Influence of Graphite Addition on the Properties of 3D Printed PLA Filaments", Polymers & Polymer Composites, 2019.
[41] T. Wang, J. Chen, "Effects of 2% Magnesium Powder on ABS," Composite Structures, 2012.
[42] T. Wang, J. Chen, "Investigation of ABS Properties," Composite Structures, 2019.
[43] T. Wang, J. Chen, "Investigation of Magnesium Powder Additives on PLA Fiber Mechanical Properties," Composite Structures, 2019.
[44] T. Wang, J. Chen, "Investigation of PE Properties with Graphite Additives," Composite Structures, 2019.
[45] T. Wang, J. Chen. "Investigation of Graphite Powder Additives on PET-G Fiber Mechanical Properties." Composite Structures, 2019.
[46] T. Wang, J. Chen. "Investigation of Graphite Powder Additives on PET-G Fiber Mechanical Properties." Composite Structures, 2019.
[47] Tanikella, N. G., Wittbrodt, B., Pearce, J. M., & Franco, P. (2017). Influence of Printing Parameters and Layer Thickness on Mechanical Properties of 3D-Printed PLA Tensile Specimens. Strength, 3(2), 1092.
[48] Wang L, Sanders JE, Gardner DJ, Han Y. Effect of fused deposition modeling process parameters you the mechanical properties of a filled polypropylene. Prog Addit Manuf 2018;3:205–14.
[49] Wang, Z., Chen, L., & Zhang, W. (2019). Fabrication and properties of polypropylene composites filled with micro/nano-particles: A review. Journal of Industrial and Engineering Chemistry, 76, 1-17.

[50] X. Zhang, Y. Liu, "Carbon Fiber Reinforced PLA: Properties and Applications," Carbon, 2018.
[51] X. Zhang, Y. Liu, "Effect of Graphite Additives on ABS," Carbon, 2018.
[52] X. Zhang, Y. Liu, "Effect of Graphite Additives on PE," Carbon, 2018.
[53] X. Zhang, Y. Liu. "Effect of Graphite Powder on PET-G Properties." Carbon, 2018.
[54] X. Zhang, Y. Liu. "Effect of Graphite Powder on PET-G Properties." Carbon, 2018.
[55] Yetgin SH. - Tribological properties of compatibilizer and graphene oxide-filled polypropylene nanocomposites, Bull Mater Sci. 2020;43:89
[56] Zhang, X., Zhang, Y., Lin, T., Wang, X., & Xuan, T. (2017). The effect of particle size on the mechanical properties of polylactic acid (PLA)/graphene nanocomposites. Materials & Design, 114, 441-448.

A review on tribological and vibration studies of 3D printed polymers

Mahamadou Lamine Ousmane DIALLO [1], Adam SARANKÓ[2],
Tamás PATAKI[2], László ZSIDAI[2]

[1] *Mechanical Engineering Doctoral School,*
Hungarian University of Agriculture and Life Sciences, MATE, Gödöllő

[2] *Institute of Technology, Hungarian University of Agriculture and Life Sciences,* MATE, Gödöllő

Abstract

3D printing is transforming industries by allowing cost-effective productive of complex geometries. Polymers, due to their easy processing in this regard, are playing an important role. However, for the polymers to expand more, understand their mechanical behavior in friction and vibration applications, is important. The review covers the tribological and vibrational studies of 3D printing polymers. The tribological properties are extensively discussed, including factors like materials colors, printing orientation, layers thickness etc. Vibration properties are explored too, along with the impact of printing parameters on dynamic properties. Despite progress, challenges remain. Addressing these challenges will advance our understanding and application of 3D printing polymers in diverse industries.

Keywords

3D printing, vibration, infill, tribology, polymers

1. Introduction

Additive manufacturing (AM) is a method of building a three-dimensional component using data from Computer Aided Design (CAD) model which is read by a 3D printer and the object is built by successive layers deposition of the material. All materials -polymers, metals, ceramics, composite- can somehow be 3D printed and complex geometries which may not be possible with others manufacturing methods are easily and rapidly done by additive manufacturing. One of the additive manufacturing is Fused Deposition Modeling (FDM) sometime called fused filament Fabrication (FFF). This FDM method is suitable for polymer material; it is simple in its application, cost effective.

The development of polymer 3D printing has a significant impact in various industrial sectors showing their importance and applicability including medical, automotive, aerospace, energy, personalized consumer products etc (figure 1). Several papers highlighted the exponential growth of additive manufacturing in the polymer market in the above mentioned sectors due to its cost effectiveness,

higher efficacy, high precision, multiple material use, customized geometries compared to traditional injection molding and thermoforming techniques (Abdullah et al., 2023; Arefin et al., 2021; Bodkhe et al., 2020; Chunhua & Guangqing, 2020; Luo et al., 2020; Pal et al., 2021; Patel et al., 2022; Sousa et al., 2022). The 3D printing market size is projected to grow from USD 10.9 Billion in 2023 to USD 54.47 Billion by 2032, but the market share of the 3D printed polymer will still be less than that of metal(https://www.marketresearchfuture.com, n.d.). For polymers to gain more share of the market, to become competitive, and to be employed in mass in all industries in place of metal, 3D printed shall have important mechanical properties. However, for industrial application where friction and vibration are dominant, the mechanical properties of product manufactured by this method need to be investigated for different material and infill density and shape.

Herein this review, the important of 3D printed and the different technologies are presented. The review mainly covers the mechanical properties of 3D printed polymers by focusing on the tribological and vibrational parameters of this material.

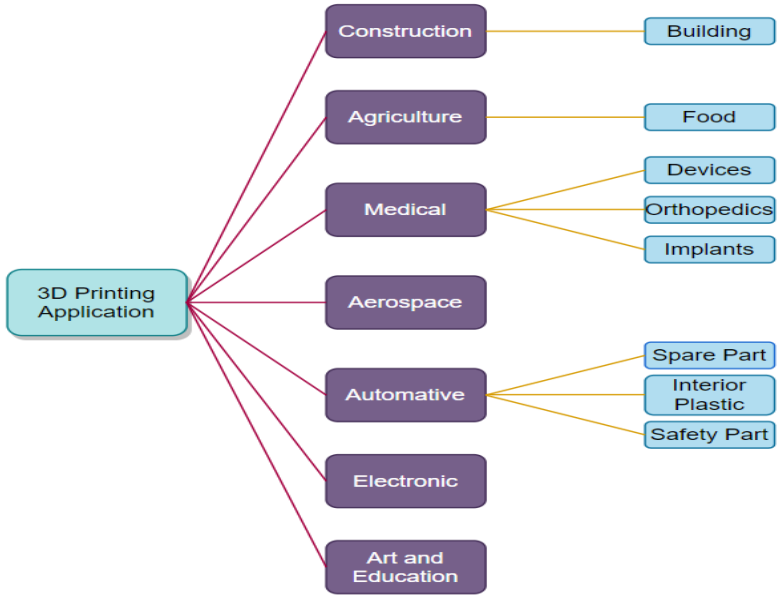

Figure 1. 3D printed application area (Rouf et al., 2022)

2. 3D Printed technology

3D printing is an additive process where the material is lay down layer-by-layer to create the solid object. The 3D model is created using CAD software or 3D scanning technology. The model is then converted into an STL file. This digital 3D model file (STL, OBJ) provides the 3D printer with the definition on what object to print. The printer reads the G-Code, lays down material layer-by-layer via the print head, successively constructing up the print. This file slices the model into layers. The printed parts require sometimes smoothing, cleaning, depending on the type of materials and method used.

The common 3D printing technologies include the Fused Deposition Modelling (FDM), Stereolithography (SLA), Selective Laser Sintering (SLS). Other methods are Polyjet photopolymer jetting, Electron beam melting (EBM), Laminated object manufacturing (LOM).

ISO/ASTM2900-15 defines seven categories of Additive Manufacturing (AM) process in this table (Almaliki, 2015; Make - Dassault Systèmes®, n.d.; Shane, 2023) (Table 1)

Table 1. different additive manufacturing technologies

Category	3D printing technology		Material	Description
Material extrusion	FDM/FFF	Fused Deposition Modelling/Fused Filament Fabrication	Plastic, metal, concrete, etc	The material is selectively extruded through a nozzle
Photopolymerization	SLA	StereoLithogrAphy	Photopolymer resins (castable, transparent, biocompatible, etc)	Liquid photopolymer is selectively cured by light (ultraviolet)-activated polymerization
	DLP	Digital Light Processing		
	LCP	Liquid Crystal Display		
Powder bed fusion	SLS	Selective Laser Sintering	Plastic Powder, metal powder, ceramic powder	The energy selectively fuses regions of a powder bed
	SLM/DMLS	Selective Laser Melting/ Direct Metal Laser Sintering		
	EBM	Electron Beam Melting		
	MJP	Multi Jet Fusion		
Material jetting	DOD	Drop On Demand	Photosensitive resin, wax	Droplets of build material are selectively deposited
	NPJ	Nano Particle Jetting		
Blinder jetting	CPJ	Color Jet Printing	Sand, polymers, metal,ceramics, etc	Adhesive liquid agent is selectively deposited to join powder materials
	BJ	Binter jetting		
Sheet lamination	LOM	Laminated Object Manufacturing	Paper, polymers, sheet metal	Sheets of material are bonded to form an object
	UC	Ultrasonic Consolidation		

Directed energy deposition	LENS	Laser Engineering Net Shape	Various metals, in wire or in powder form	The material is fused using thermal energy. The melting materials is deposited
	EBAM	Electron Beam Additive Manufacturing		
	LDW	Laser Deposition Welding		
	L-DED	Laser Directed Energy Deposition		

3. 3D Printed Materials:

Multiple materials are used in additive manufacturing: polymers (de Leon et al., 2016; Ligon et al., 2017; Salifu et al., 2022), metal (Mostafaei et al., 2022; Nichols, 2019), ceramics (Hwa et al., 2017; Koushik & Antunes, 2023), concrete (Casagrande et al., 2020; Tu et al., 2023). Among these materials, polymers are the main group used in 3D printing. They can be found in numerous forms, such as: liquid polymer for resin and binder, powders, pellets filament in wire and film. Also, thermoplastics, thermosets, elastomers, polymer blends and polymer-based composite are used in 3D printing technology (Izdebska-Podsiadły, 2022; Jasiuk et al., 2018; Ngo et al., 2018).

The type of additive manufacturing and the usage (for mechanical, thermal, chemical, aesthetic property) of the object to print determine the choice of materials to be used. In most application, thermoplastics and its composites are commonly used materials in many additive manufacturing techniques namely FDM/FFF. The main thermoplastic materials are given in this figure (Figure 2).

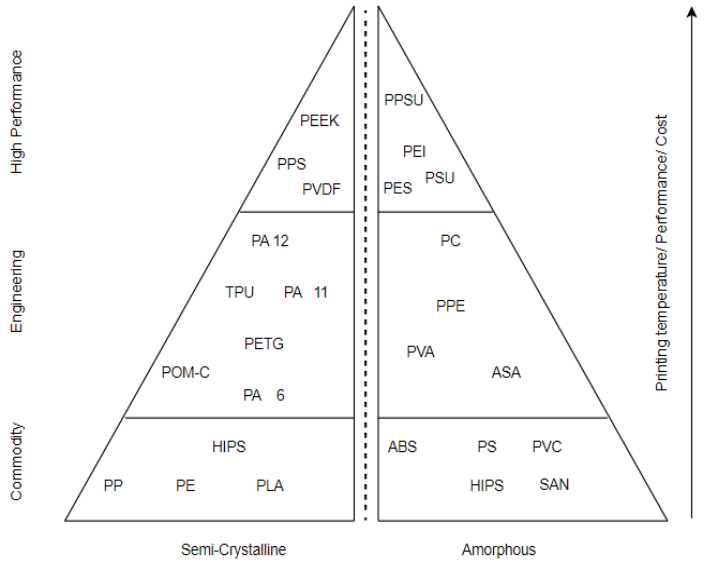

Figure 2. Thermoplastic materials pyramid for FDM filament (Dave & Patel, 2021)

4. Tribological Properties of 3D Printed Polymers

Many factors that influence the tribological properties of polymers have been studied through the literature. (Theiler & Gradt, 2021) assessed the choice of counter face material and its impact on the wear of polymers.

The impact of material colors was examined.(Valerga et al., 2017) assessed the impact of PLA filament color (pink, green, grey, transparent) and printing temperature on the geometric of the printed part by FDM. White and Grey for PLA, Grey for ABS at different temperature on the tribological parameter of 3D printed polymers was investigated by (Hanon et al., 2019).The results displayed that the white ABS and PLA specimens have little difference.

Several researchers studied the tribological properties of polymers under different load and printing orientation. Investigation of the tribological properties under different load and orientation of ABS (Dangnan et al., 2020), under different load and orientation of PLA/bronze composite (Hanon, Alshammas, et al., 2020). Induced vibration created by during friction and the magnitude of the loads are not evaluated to understand it effect of the mechanical properties of the products.

Particular attention has been paid to the layer thickness, layer orientation, the infill density and printing orientation by many researchers. (Srinivasan et al., 2020) studied the effect of layer thickness, infill density and its patterns on the tensile strength and surface roughness of PET-G parts. The effect of layer thickness and layer orientation on the friction coefficient, hardness and wear behavior was investigated for PLA printed component using FDM by (Zhiani Hervan et al., 2021). For a FDM 3D printed polyamide (PA) (Wang et al., 2024) examined effect of nozzle temperature at some range and layer thickness on the mechanical and tribological properties. (Hanon & Zsidai, 2021) assessed the tribological performance of 3D printed PLA polymer at different orientations (0-,45,180 degree) with different colors (white, black, and grey) at various load. (Hanon, Marczis, et al., 2020) have done similar study for three materials PLA, HT-PLA and PETG to evaluate the static and the dynamic friction coefficient and wear of parts printed in different orientation. (He et al., 2023) investigated the relationship between the materials (ABS, PC and PLA), printing parameters (layer thickness and infill density), lubrification conditions (dry, grease, and oil), and friction performance (friction coefficient and wear rate). They developed a nonlinear polynomial function that gives the coefficient of friction in term of the viscosity, infill density and layer thickness. Of all these studies, none has mentioned that, it can be said that it is improper to say layer thickness as the nozzle are circular and not rectangular. In that case, it is important to assess the effect of layer width on the mechanical properties.

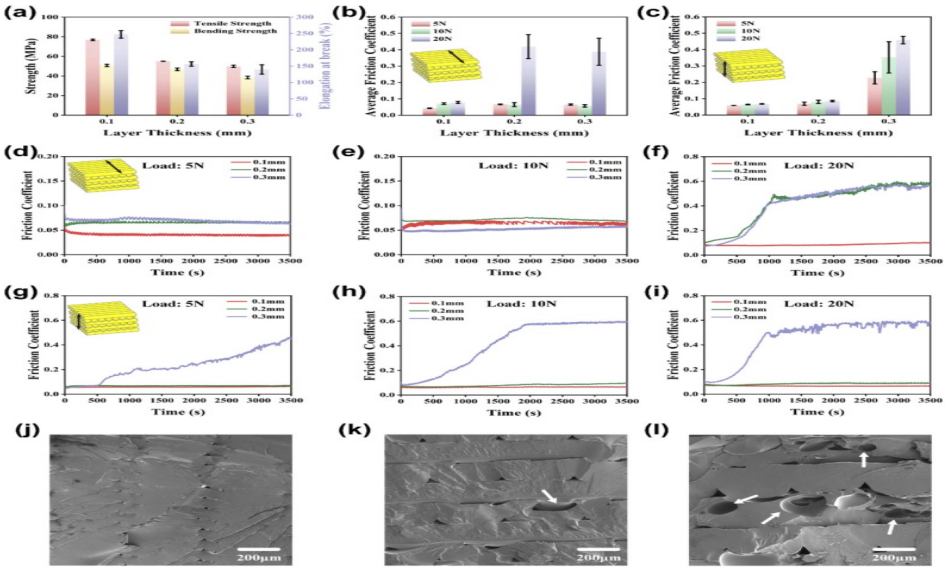

Figure 3 : FDM-printed PA with different layer thickness: mechanical properties (a), average COF of top surfaces (b) and side surfaces (c) under different loads, the COF curves of top surfaces (d - f) and side surfaces (g - i) under different loads, and SEM images of PA with the layer thickness of 0.1 mm (j), 0.2 mm (k), and 0.3 mm (l).(Wang et al., 2024)

Different 3D printed material are compared.(Hanon, Marczis, et al., 2020) examined the influence of print orientation on the tribological properties of various polymers (PLA, HT-PLA, PETG). it has been found the printing process affected heavily the tribological behavior of the FDM printed products. Z oriented printed products exhibited the higher wear and dynamic coefficient. HT-PLA is more suitable for tribological application.(Nedelcu et al., 2020) compared the mechanical properties, tribological behavior, and chemical composition of two biodegradable plastics: PLA-based filament (commercial name: Extruder BDP) and PLA-lignin filament (commercial name : Arboblend V2 Nature). (Nagaraju et al., 2023) compared the mechanical properties of FDM and SLA using ABS. It has been found that the tensile and compression strength are higher for SLA compared to FDM, the opposite happened for the flexural. For further study, it is possible to compared the mechanical properties of printed-FDM PLA and SLA-printed PLA that has not been done so far. It is important to compare the mechanical properties of products printed using different kinematic printers.

Besides the examination of printing parameters effect, (Maguluri et al., 2023) investigated the optimum parameters for 3D printing, such as extrusion temperature, fill density, and nozzle speed to minimize the wear rate. (Nagaraju et al., 2023) compared the mechanical properties (tensile, compressive, flexure and hardness) of FDM and SLA printed ABS component. (Phogat et al., 2022)

developed an Artificial Neural Network (ANN) to be able to predict the relation wear rate and FDM parameters of the printing component.

5. Vibrational Properties of 3D Printed Polymers

A lot of material have been exploited for vibration application, but metal and polymer are the most predominant due to their viscoelasticity properties (Chung, 2001). Polymer materials are being used in various application in relation to vibration analysis and control. In various researches, the damping propriety of polymers has been largely investigated. Some researcher proposed a way of selecting candidate materials for vibration. (Neubauer et al., 2022) provided a guiding structure for selecting material in vibration and acoustics application, analyzed the effect of material parameters such as young modulus, loss factor. Vibration isolators made of material like nickel (Ni) and copper (Cu) microfibrous meshes (MFMs) and Sorbothane and polydimenthylsiloxane (PDMS) viscoelastic polymers were proposed by (Bottenfield et al., 2021). New thermoplastic polyurethane (TPU) materials are been studied for their vibration isolation properties (Bek et al., 2017), magnetorheological elastomer are good candidate (WEI et al., 2011). Vibration isolation for gear transmission system (Geng et al., 2022; Jin et al., 2022), for reducing the vertical of bridge subjected to man activity (Nyawako & Reynolds, 2017; Saber et al., 2023) are been developed. New type of material called metamaterials (fig: 11) are developed for their importance in vibration damping (Herkal et al., 2023; Xiao et al., 2024; Zolfagharian et al., 2022).

(Lesage et al., 2022) examined the effect of printing orientation on frequency, the damping behavior, and the wave velocity of metallic specimens produced by SLM process fig 4.

The friction induced vibration has been studied too. (Di Bartolomeo et al., 2017) investigated the influence of different parameters, such as normal load, friction coefficient, and sliding velocity on the vibration generated by the frictional system and compare experimental results with the numerical results. Unfortunately, the type of material is not mentioned.

Some researches focusing on vibrating the printer nozzle. (Gunduz et al., 2018) in the paper aimed at reducing the flow resistance, the viscosity in a nozzle under high-amplitude ultrasonic vibration to permit the 3D printing of highly viscous material like clay. (Chen et al., 2022) Studied the effect of nozzle vibration on mechanical properties and surface state on a PLA.

Few researches covered the impact of infill, layer height, printing orientation on the dynamic properties. (Öteyaka et al., 2022) investigated the vibration damping capabilities and the flexural behavior of a FDM printed PLA with different infill patterns and ratios. It has found that the infill pattern and the ratio greatly impact the flexural behavior and the vibration-damping properties. (Ergene et al., 2023) evaluated the effect of taper angle, layer heights, infill rates, and boundary condition on vibrational behavior of a 3D PET-G.

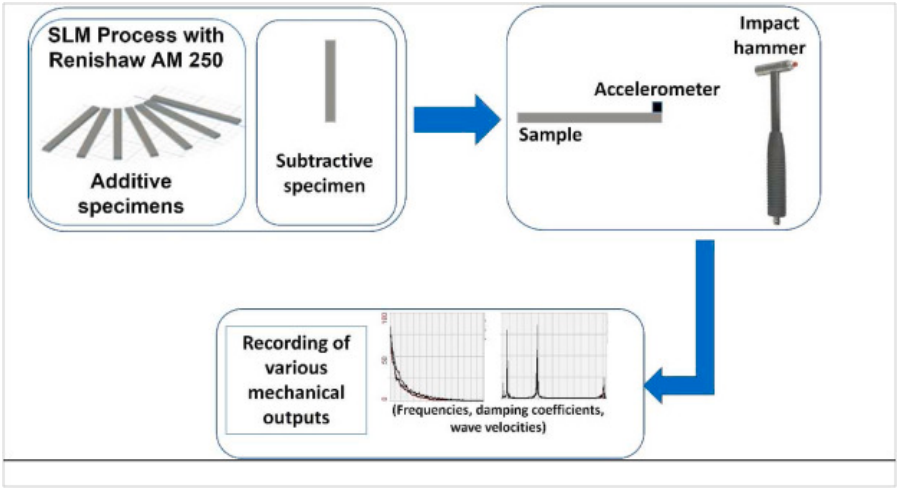

Figure 4. Flowchart of the dynamical characterization process (Lesage et al., 2022)

(Alarifi, 2022) analyzed the dynamic mechanical properties, tensile properties and flexural properties of nylon carbon fiber composite specimens printed in direction orientation. The specimens in horizontal orientation showed higher tensile strength and better flexural properties compared to other group specimens.

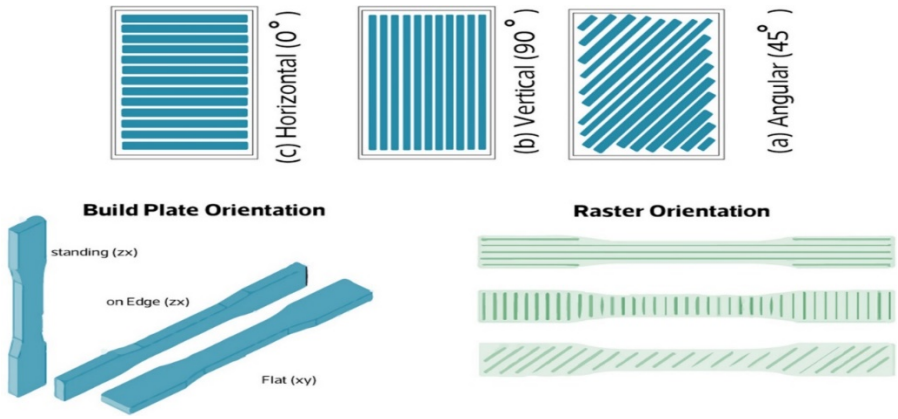

Figure 5. The representative direction used for 3D printing of specimens (A) angular (45°), (B) vertical (90°), (C) horizontal (0°), (D) build plate orientation, and (E) raster orientation (Alarifi, 2022)

Out of our scope, it is worth mentioning that research on dynamical properties of 3D printing concrete has been carried out for application in earthquake and blast. (Mo et al., 2022; Napolitano et al., 2021) discussed the mechanical characterization of 3D printed concrete under dynamic loading with especial focus on interface between layers. The result showed the dynamic interface tensile strength decreased with the waiting time and strain rate. (Liu et al., 2021)

examined the anisotropic characteristics of 3D printed loaded statically and dynamically and found that the performance of the 3D printed concrete was best in X-direction. The printed concrete has shown higher compressive strength than the cast specimens.

6. Conclusion

3D printed materials have been scrutinized for their importance in tribological and dynamic application. Researches in this sense were conducted to evaluate the tribological properties of different 3D printed polymer. Some few researches investigated their properties under dynamic loading conditions. The gap is that at the best of my knowledge, no study covers the effect of vibration and tribology on 3D printed polymers. Another aspect that has not been reported in the literature is the effect of the plate vibration during the printing, mainly for cartesian printer.

In most of the researches done about the tribological properties of polymer, there is lack of mathematical model that can help to predict for example the friction coefficient. There is also lack of numerical simulation which can confirm the experimental results. Studies on optimum parameter are very scarce. Comparison between 3D printed polymers and polymers manufactured by other traditional way has not been conducted.

In the researches done so far, the printing was said to be done at the room temperature, which that gives a clear idea of the printing environment. The printing nozzles are almost circular which creates air gap between the layers. Rectangular nozzle can help to the problem of air gap and assess properly the effect of layer heigh and width.

Acknowledgement

This research was supported by the Stipendium Hungaricum Programme and by the Mechanical Engineering Doctoral School, Hungarian University of Agriculture and Life Science, Gödöllő, Hungary

References

[1] Abdullah, A. M., Ding, Y., He, X., Dunn, M., & Yu, K. (2023). Direct-write 3D printing of UV-curable composites with continuous carbon fiber. Journal of Composite Materials, 57(4), 851–863. https://doi.org/10.1177/00219983221127182

[2] Alarifi, I. M. (2022). Investigation of the dynamic mechanical analysis and mechanical response of 3D printed nylon carbon fiber composites with

different build orientation. Polymer Composites, 43(8), 5353–5363. https://doi.org/10.1002/pc.26838
[3] Almaliki, A. (2015). The Processes and Technologies of 3D Printing. International Journal of Advances in Computer Science and Technology.
[4] Arefin, A. M. E., Khatri, N. R., Kulkarni, N., & Egan, P. F. (2021). Polymer 3D Printing Review: Materials, Process, and Design Strategies for Medical Applications. Polymers, 13(9), Article 9. https://doi.org/10.3390/polym13091499
[5] Bek, M., Betjes, J., von Bernstorff, B.-S., & Emri, I. (2017). Viscoelasticity of new generation thermoplastic polyurethane vibration isolators. Physics of Fluids, 29(12), 121614. https://doi.org/10.1063/1.5000413
[6] Bodkhe, S., Vigo, L., Zhu, S., Testoni, O., Aegerter, N., & Ermanni, P. (2020). 3D PRINTING TO INTEGRATE ACTUATORS INTO COMPOSITES. Additive Manufacturing, 35, 101290. https://doi.org/10.1016/j.addma.2020.101290
[7] Bottenfield, B., Bond, A. G., English, B. A., Flowers, G. T., Dean, R. N., & Adams, M. L. (2021). Microfibrous Mesh and Polymer Damping of Micromachined Vibration Isolators. IEEE Transactions on Components, Packaging and Manufacturing Technology, 11(4), 543–556. https://doi.org/10.1109/TCPMT.2021.3063854
[8] Casagrande, L., Esposito, L., Menna, C., Asprone, D., & Auricchio, F. (2020). Effect of testing procedures on buildability properties of 3D-printable concrete. Construction and Building Materials, 245, 118286. https://doi.org/10.1016/j.conbuildmat.2020.118286
[9] Chen, F., Xu, Q., Huang, F., Xie, Z., & Fang, H. (2022). Effect of nozzle vibration at different frequencies on surface structures and tensile properties of PLA parts printed by FDM. Materials Letters, 325, 132612. https://doi.org/10.1016/j.matlet.2022.132612
[10] Chung, D. D. L. (2001). Review: Materials for vibration damping. Journal of Materials Science, 36(24), 5733–5737. https://doi.org/10.1023/A:1012999616049
[11] Chunhua, S., & Guangqing, S. (2020). Application and Development of 3D Printing in Medical Field. Modern Mechanical Engineering, 10, 25–33. https://doi.org/10.4236/mme.2020.103003
[12] Dangnan, F., Espejo, C., Liskiewicz, T., Gester, M., & Neville, A. (2020). Friction and wear of additive manufactured polymers in dry contact. Journal of Manufacturing Processes, 59, 238–247. https://doi.org/10.1016/j.jmapro.2020.09.051
[13] Dave, H. K., & Patel, S. T. (2021). Introduction to Fused Deposition Modeling Based 3D Printing Process. In H. K. Dave & J. P. Davim (Eds.), Fused Deposition Modeling Based 3D Printing (pp. 1–21). Springer International Publishing. https://doi.org/10.1007/978-3-030-68024-4_1
[14] de Leon, A. C., Chen, Q., Palaganas, N. B., Palaganas, J. O., Manapat, J., & Advincula, R. C. (2016). High performance polymer nanocomposites for

additive manufacturing applications. Reactive and Functional Polymers, 103, 141–155. https://doi.org/10.1016/j.reactfunctpolym.2016.04.010

[15] Di Bartolomeo, M., Lacerra, G., Baillet, L., Chatelet, E., & Massi, F. (2017). Effect of nozzle vibration at different frequencies on surface structures and tensile properties of PLA parts printed by FDM. Tribology International, 112, 47–57. https://doi.org/10.1016/j.triboint.2017.03.032

[16] Geng, Z., Li, J., Xiao, K., & Wang, J. (2022). Analysis on the vibration reduction for a new rigid–flexible gear transmission system. Journal of Vibration and Control, 28(17–18), 2212–2225. https://doi.org/10.1177/10775463211013245

[17] Gunduz, I. E., McClain, M. S., Cattani, P., Chiu, G. T.-C., Rhoads, J. F., & Son, S. F. (2018). 3D printing of extremely viscous materials using ultrasonic vibrations. Additive Manufacturing, 22, 98–103. https://doi.org/10.1016/j.addma.2018.04.029

[18] Hanon, M. M., Alshammas, Y., & Zsidai, L. (2020). Effect of print orientation and bronze existence on tribological and mechanical properties of 3D-printed bronze/PLA composite. The International Journal of Advanced Manufacturing Technology, 108(1), 553–570. https://doi.org/10.1007/s00170-020-05391-x

[19] Hanon, M. M., Kovács, M., & Zsidai, L. (2019). Tribology behaviour investigation of 3D printed polymers. International Review of Applied Sciences and Engineering, 10(2), 173–181. https://doi.org/10.1556/1848.2019.0021

[20] Hanon, M. M., Marczis, R., & Zsidai, L. (2020). Impact of 3D-printing structure on the tribological properties of polymers. Industrial Lubrication and Tribology, 72(6), 811–818. https://doi.org/10.1108/ILT-05-2019-0189

[21] Hanon, M. M., & Zsidai, L. (2021). Hanon, Marczis, et al., 2020. Journal of Materials Research and Technology, 15, 647–660. https://doi.org/10.1016/j.jmrt.2021.08.061

[22] He, F., Xu, C., & Khan, M. (2023). Tribological Characterisation and Modelling for the Fused Deposition Modelling of Polymeric Structures under Lubrication Conditions. Polymers, 15(20), 4112. https://doi.org/10.3390/polym15204112

[23] Herkal, S., Rahman, M. M., Nagarajaiah, S., Harikrishnan, V. V. J., & Ajayan, P. (2023). 3D printed metamaterials for damping enhancement and vibration isolation: Schwarzites. Mechanical Systems and Signal Processing, 185, 109819. https://doi.org/10.1016/j.ymssp.2022.109819

[24] https://www.marketresearchfuture.com, M. R. F. (n.d.). 3D Printing Market Size, Share Reports and Industry Trends 2032. Retrieved March 10, 2024, from https://www.marketresearchfuture.com/reports/3d-printing-market-1031

[25] Hwa, L. C., Rajoo, S., Noor, A. M., Ahmad, N., & Uday, M. B. (2017). Recent advances in 3D printing of porous ceramics: A review. Current Opinion

in Solid State and Materials Science, 21(6), 323–347. https://doi.org/10.1016/j.cossms.2017.08.002

[26] Izdebska-Podsiadły, J. (Ed.). (2022). Polymers for 3D Printing: Methods, Properties, and Characteristics (1st edition). William Andrew.

[27] Jasiuk, I., Abueidda, D. W., Kozuch, C., Pang, S., Su, F. Y., & McKittrick, J. (2018). An Overview on Additive Manufacturing of Polymers. JOM, 70(3), 275–283. https://doi.org/10.1007/s11837-017-2730-y

[28] Jin, B., Bian, Y., Tian, D., & Gao, Z. (2022). An Internal Resonance Based Method for Reducing Torsional Vibration of a Gear System. Machines, 10(4), Article 4. https://doi.org/10.3390/machines10040269

[29] Koushik, T., & Antunes, E. (2023). 9—Ceramic three-dimensional printing. In R. K. Gupta, A. Behera, S. Farhad, & T. A. Nguyen (Eds.), Advanced Flexible Ceramics (pp. 193–214). Elsevier. https://doi.org/10.1016/B978-0-323-98824-7.00009-9

[30] Lesage, P., Dembinski, L., Lachat, R., & Roth, S. (2022). Mechanical characterization of 3D printed samples under vibration: Effect of printing orientation and comparison with subtractive manufacturing. Results in Engineering, 13, 100372. https://doi.org/10.1016/j.rineng.2022.100372

[31] Ligon, S. C., Liska, R., Stampfl, J., Gurr, M., & Mülhaupt, R. (2017). Polymers for 3D Printing and Customized Additive Manufacturing. Chemical Reviews, 117(15), 10212–10290. https://doi.org/10.1021/acs.chemrev.7b00074

[32] Liu, C., Yue, S., Zhou, C., Sun, H., Deng, S., Gao, F., & Tan, Y. (2021). Anisotropic mechanical properties of extrusion-based 3D printed layered concrete. Journal of Materials Science, 56(30), 16851–16864. https://doi.org/10.1007/s10853-021-06416-w

[33] Luo, H., Zhou, X., Guo, R., Yuan, X., Chen, H., Abrahams, I., & Zhang, D. (2020). 3D printing of anisotropic polymer nanocomposites with aligned BaTiO3 nanowires for enhanced energy density. Materials Advances, 1(1), 14–19. https://doi.org/10.1039/D0MA00045K

[34] Maguluri, N., Lakshmi Srinivas, Ch., & Suresh, G. (2023). Wang. Materials Today: Proceedings. https://doi.org/10.1016/j.matpr.2023.04.565

[35] Make—Dassault Systèmes®. (n.d.). Make - Dassault Systèmes®. Retrieved February 12, 2024, from https://make.3dexperience.3ds.com

[36] Mo, Y., Xing, J., Yue, S., Zhang, Y., Zhou, Q., & Liu, X. (2022). Dynamic properties of 3D printed cement mortar based on Split Hopkinson Pressure Bar testing. Cement and Concrete Composites, 130, 104520. https://doi.org/10.1016/j.cemconcomp.2022.104520

[37] Mostafaei, A., Zhao, C., He, Y., Reza Ghiaasiaan, S., Shi, B., Shao, S., Shamsaei, N., Wu, Z., Kouraytem, N., Sun, T., Pauza, J., Gordon, J. V., Webler, B., Parab, N. D., Asherloo, M., Guo, Q., Chen, L., & Rollett, A. D. (2022). Defects and anomalies in powder bed fusion metal additive manufacturing. Current Opinion in Solid State and Materials Science, 26(2), 100974. https://doi.org/10.1016/j.cossms.2021.100974

[38] Nagaraju, D. S., Krupakaran, R. L., Sripadh, C., Nitin, G., & Joy Joseph Emmanuel, G. (2023). Mechanical properties of 3D printed specimen using FDM (Fused deposition modelling) and SLA (Stereolithography) technologies. Materials Today: Proceedings. https://doi.org/10.1016/j.matpr.2023.09.223

[39] Napolitano, R., Menna, C., Forni, D., Asprone, D., & Cadoni, E. (2021). Mechanical characterization of 3D printed concrete subjected to dynamic loading. EPJ Web of Conferences, 250, 01009. https://doi.org/10.1051/epjconf/202125001009

[40] Nedelcu, D., Mazurchevici, S.-N., Popa, R.-I., Lohan, N.-M., Maldonado-Cortés, D., & Carausu, C. (2020). Tribological and Dynamical Mechanical Behavior of Prototyped PLA-Based Polymers. Materials, 13(16), Article 16. https://doi.org/10.3390/ma13163615

[41] Neubauer, M., Schwaericke, F., Radmann, V., Sarradj, E., Modler, N., & Dannemann, M. (2022). Material Selection Process for Acoustic and Vibration Applications Using the Example of a Plate Resonator. Materials, 15(8), Article 8. https://doi.org/10.3390/ma15082935

[42] Ngo, T. D., Kashani, A., Imbalzano, G., Nguyen, K. T. Q., & Hui, D. (2018). Additive manufacturing (3D printing): A review of materials, methods, applications and challenges. Composites Part B: Engineering, 143, 172–196. https://doi.org/10.1016/j.compositesb.2018.02.012

[43] Nichols, M. R. (2019). How does the automotive industry benefit from 3D metal printing? Metal Powder Report, 74(5), 257–258. https://doi.org/10.1016/j.mprp.2019.07.002

[44] Nyawako, D. S., & Reynolds, P. (2017). Observer-based controller for floor vibration control with optimization algorithms. Journal of Vibration and Control, 23(3), 345–360. https://doi.org/10.1177/1077546315581229

[45] Öteyaka, M. Ö., Çakir, F. H., & Sofuoğlu, M. A. (2022). Effect of infill pattern and ratio on the flexural and vibration damping characteristics of FDM printed PLA specimens. Materials Today Communications, 33, 104912. https://doi.org/10.1016/j.mtcomm.2022.104912

[46] Pal, A. K., Mohanty, A. K., & Misra, M. (2021). Additive manufacturing technology of polymeric materials for customized products: Recent developments and future prospective. RSC Advances, 11(58), 36398–36438. https://doi.org/10.1039/D1RA04060J

[47] Patel, D., Shah, R., & Dalwadi, H. (2022). Application of Polymer and Biomaterials for 3d Printing Technology: Review. International Journal of Applied Engineering Research, 10. https://doi.org/10.22214/ijraset.2022.41752

[48] Phogat, A., Chhabra, D., Sindhu, V., & Ahlawat, A. (2022). Analysis of wear assessment of FDM printed specimens with PLA, multi-material and ABS via hybrid algorithms. Materials Today: Proceedings, 62, 37–43. https://doi.org/10.1016/j.matpr.2022.01.429

[49] Rouf, S., Raina, A., Irfan Ul Haq, M., Naveed, N., Jeganmohan, S., & Farzana Kichloo, A. (2022). 3D printed parts and mechanical properties: Influencing parameters, sustainability aspects, global market scenario,

challenges and applications. Advanced Industrial and Engineering Polymer Research, 5(3), 143–158. https://doi.org/10.1016/j.aiepr.2022.02.001

[50] Saber, H., Samani, F. S., & Pellicano, F. (2023). Vibration reduction of footbridges subjected to walking, running, and jumping pedestrian. Journal of Vibration and Control, 29(13–14), 3227–3240. https://doi.org/10.1177/10775463221093107

[51] Salifu, S., Desai, D., Ogunbiyi, O., & Mwale, K. (2022). Recent development in the additive manufacturing of polymer-based composites for automotive structures—A review. The International Journal of Advanced Manufacturing Technology, 119(11), 6877–6891. https://doi.org/10.1007/s00170-021-08569-z

[52] Shane. (2023, July 28). Explore the Top 7 Types of 3D Printing Technologies | MachineMFG. https://www.machinemfg.com/types-of-3d-printing-technologies/

[53] Sousa, A. M., Amaro, A. M., & Piedade, A. P. (2022). 3D Printing of Polymeric Bioresorbable Stents: A Strategy to Improve Both Cellular Compatibility and Mechanical Properties. Polymers, 14(6), 1099. https://doi.org/10.3390/polym14061099

[54] Srinivasan, R., Prathap, P., Raj, A., Aswinth Kannan, S., & Deepak, V. (2020). Influence of fused deposition modeling process parameters on the mechanical properties of PETG parts. Materials Today: Proceedings, 27, 1877–1883. https://doi.org/10.1016/j.matpr.2020.03.809

[55] Theiler, G., & Gradt, T. (2021). Influence of counterface and environment on the tribological behaviour of polymer materials. Polymer Testing, 93, 106912. https://doi.org/10.1016/j.polymertesting.2020.106912

[56] Tu, H., Wei, Z., Bahrami, A., Ben Kahla, N., Ahmad, A., & Özkılıç, Y. O. (2023). Recent advancements and future trends in 3D concrete printing using waste materials. Developments in the Built Environment, 16, 100187. https://doi.org/10.1016/j.dibe.2023.100187

[57] Valerga, A. P., Batista, M., Puyana, R., Sambruno, A., Wendt, C., & Marcos, M. (2017). Preliminary study of PLA wire colour effects on geometric characteristics of parts manufactured by FDM. Procedia Manufacturing, 13, 924–931. https://doi.org/10.1016/j.promfg.2017.09.161

[58] Wang, C., He, Y., Lin, Z., Zhao, X., Sun, C., Guo, R., Wang, X., & Zhou, F. (2024). Mechanical and tribological properties of FDM-printed polyamide. Tribology International, 191, 109198. https://doi.org/10.1016/j.triboint.2023.109198

[59] WEI, K., MENG, G., XIA, P., & BAI, Q. (2011). Design and Vibration Characteristics Analysis of Magnetorheological Elastomer Isolators. Journal of Mechanical Engineering, 47(11), Article 11.

[60] Xiao, B., Liu, Y., Xu, W., Wei, R., Chen, M., & Jiang, H. (2024). A bistable honeycomb mechanical metamaterial with transformable Poisson's ratio and tunable vibration isolation properties. Thin-Walled Structures, 198, 111718. https://doi.org/10.1016/j.tws.2024.111718

[61] Zhiani Hervan, S., Altınkaynak, A., & Parlar, Z. (2021). Wang et al., 2024. Proceedings of the Institution of Mechanical Engineers, Part J: Journal of Engineering Tribology, 235(8), 1590–1598. https://doi.org/10.1177/1350650120966407

[62] Zolfagharian, A., Bodaghi, M., Hamzehei, R., Parr, L., Fard, M., & Rolfe, B. F. (2022). 3D-Printed Programmable Mechanical Metamaterials for Vibration Isolation and Buckling Control. Sustainability, 14(11), Article 11. https://doi.org/10.3390/su14116831

.

PV/T systems performance assessment and numerical modeling

Aschenaki ALTAYE[1], Piroska VÍG[2], István FARKAS[3]
[1] *Doctoral School of Mechanical Engineering,* MATE, Gödöllő
[2] *Institute of Mathematics and Basic Science,* MATE, Gödöllő
[3]*Institute of Technology, Hungarian University of Agriculture and Life Sciences*, MATE, Gödöllő

Abstract

Most of the solar energy captured by PV modules is converted into harmful heat, leading to an elevation in surface temperature and a subsequent decline in electrical efficiency (EE). Additionally, using PV systems as sustainable tools encounters obstacles due to their limited efficiency. Consequently, the enhancement of PV system efficiency is pursued by implementing photovoltaic thermal systems (PV/T) that rely on nanofluid cooling technology. In this review, an examination is conducted on the influences of various parameters like flow rates, particle size, concentration ratio and volume fraction on the utilization of nanofluids in PV/T systems, as well as an exploration of the different types of nanofluids and their impact on the optimization of PV/T systems. Moreover, the method of nanofluid preparation and the application of numerical analysis in evaluating the cooling of PV/T systems using nanofluids are thoroughly examined.

Keywords

PVT system, nanofluids, cooling, efficiency, optimization, preparation, numerical

1. Introduction

Energy is now imperative to capture renewable energy using different technologies and transform it into electricity due to the world's increasing energy demand brought on by population increase and the negative environmental effects of fossil fuels. Solar energy has been chosen as an alternative to address this energy issue because of its many advantages, not the least of which is that it is a clean source of electricity and heat. However, its full potential has not yet been utilized (Ahmed et al., 2019).

Unfortunately, most of the solar energy that PV modules capture is turned into harmful heat, which raises the surface temperature and reduces electrical efficiency (EE). Their low efficiency, however, makes it difficult to use them as sustainable devices. To address these issues, photovoltaic thermal systems

(PV/T) based on nanofluid cooling technology are used to maximize PV/T system efficiency (Salari et al., 2021). Consequently, one of the main causes of these systems' low efficiency is thought to be their cooling capabilities in PV systems and their limited heat-carrying capacity in PV/T systems. On the plus side, current nanofluid research has guaranteed quick progress in improving heat transfer in energy systems (Abbas et al., 2019). Therefore, is necessary to talk about the type of cooling fluid and its cooling capability in addition to PV/T system cooling. Thus, a nanofluid is a blend of nanoparticles and a base fluid that is regarded as the ideal cooling fluid. The material, size, base fluid, thermal conductivity, geometry, and other crucial characteristics that determine their selection all affect how well a nanofluid performs (Abbas et al., 2019).

2. Effects of nanofluid types, sizes, preparation on PV/T system efficiency optimization

Utilizing nanofluid cooling fluid to maximize PV/T system efficiency

According to definitions, nanofluid is a mixture of effectively dispersed nanoparticles in a base fluid, with diameters ranging from 1 to 100 nm. Higher thermal conductivity nanofluids increase PV/T system efficiency to its highest potential (Ahmed et al., 2019). Additionally, the effects of nanofluids and nanoparticle size, type, volume fraction, and concentration ratio on PV/T systems are assessed in this work. Fig. 1 shows a typical schematic diagram of the PV/T system with nanofluid cooling mechanisms.

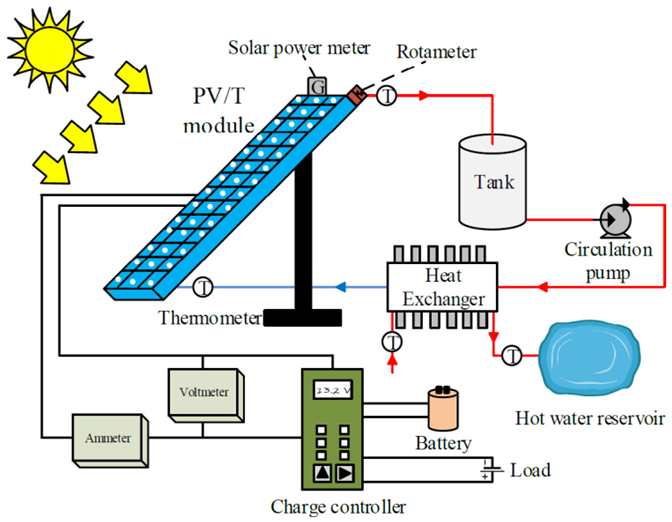

Figure 1. Schematic diagram of the PV/T system with nanofluid cooling (Abbas et al., 2019)

Types of nanofluids and how they affect the optimization of PV/T systems

Because of the increased need for heat and power over the past few decades, photovoltaic/thermal systems have been used more often than photovoltaic or solar thermal systems alone since PV/T systems perform better when combined than when used alone. Nanofluid has better thermal conductivity, making it suitable for use in PV/T systems as a coolant and optical filter (Said et al., 2018). Consequently, the impacts of several nanofluids are covered in this article.

The impacts of water/MWCNT (multiwall carbon nanotube) nanofluid on PV/T systems were studied, and it was found to be useful for improving the thermal performance of PV/T systems. The result shows that using a water-cooling system can boost PV performance by 9.2% and that using nanofluid instead of water can result in superior thermal performance (Nasrin et al., 2018). Similarly, experimental and numerical research was done on the usage of metal-oxides/water nanofluids as coolants in photovoltaic thermal systems. Both TiO_2/water and ZnO/water nanofluids have better electrical efficiency. Additionally, ZnO/water nanofluid has the highest thermal efficiency as a result (Sardarabadi & Passandideh-Fard, 2016).

Another significant study was conducted by (Rahmanian and Hamzavi, 2020), who investigated the effects of CNT concentration and nanofluid flow rate on the efficiency of the PVT system and performed a numerical simulation of the PV/T system using a water-CNT nanofluid as the working fluid. As a result, the PV/T system's electrical efficiency rose by 11% when compared to the PV system, and the nanofluid's thermal conductivity raised its coefficient of cooling efficiency. However, this also resulted in inconsistent thermophysical properties of the nanofluid and increased energy consumption during the pumping process as illustrated in Fig. 2.

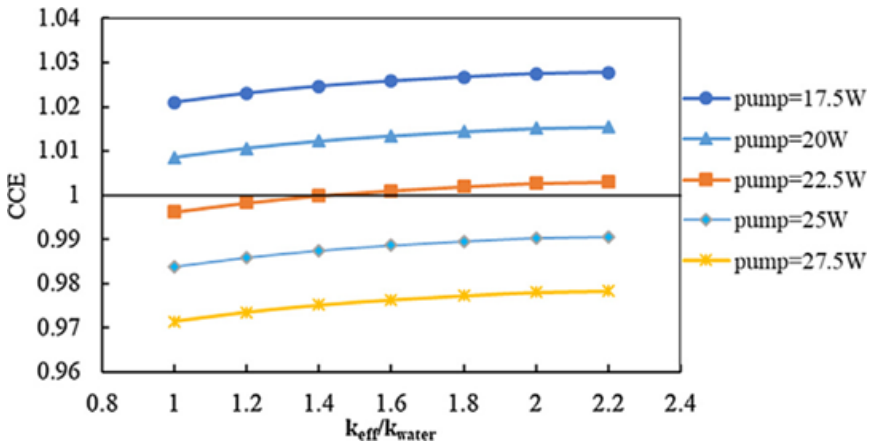

Figure 2. Coefficient of cooling effect (CCE) versus variation of nanofluid thermal conductivity with the employment of different pumps in PV/T system (Rahmanian & Hamzavi, 2020).

The coefficient of cooling efficiency (CCE), which is the ratio of the net electrical energy of the PV/T system to the electrical energy of the PV system, is defined to look into the maximum permitted pump power in a PV/T system:

$$CCE = \frac{E_{e.PV/T} - P_{pump}}{E_{e.PV}} \quad (1)$$

According to Fig. 2, if the CCE is more than 1, the cooled PV module's net electrical energy production surpasses that of the PV module without a cooling system. Consequently, pump employment is deemed acceptable if the CCE is more than 1.

The nanofluid insertion procedure enhances PV/T system performance and boosts thermal efficiency by reducing cell temperature and using insulation to minimize bottom heat loss. They fall into three categories in addition to efficiency optimization: Nanoparticles based on metals, carbon, and composite materials (Ahmed et al., 2019).

Alsalame et al. (2021) and Joo Hee Lee (2019), investigated how to enhance the flat plate photovoltaic thermal system's performance to generate both heat and electricity at the same time. Different flow rates of water were utilized as the working fluid in the investigation together with nanofluids (CuO/water, Al_2O_3/water).

As illustrated in Fig. 3c, the results demonstrated that the PV/T system employing CuO/water as a nanofluid had increases in both thermal and electrical efficiencies of 21.30% and 0.07%, respectively, as compared to the water-based system. The effects of flow rate on thermal performance are depicted in Fig. 3a and Fig. 3b. As a result, the efficiency decreased when the flow rate exceeded 3 l/min; thus, the flow rate was neither significantly higher nor lower based on design. Similarly, researchers looked into how nanofluids affected photovoltaic thermal systems (Salari et al., 2021). The outcome demonstrates that nanofluids raise photovoltaic thermal systems' (PV/T) efficiency and that PV/T performance is increased when pure base fluids are used in place of nanofluids.

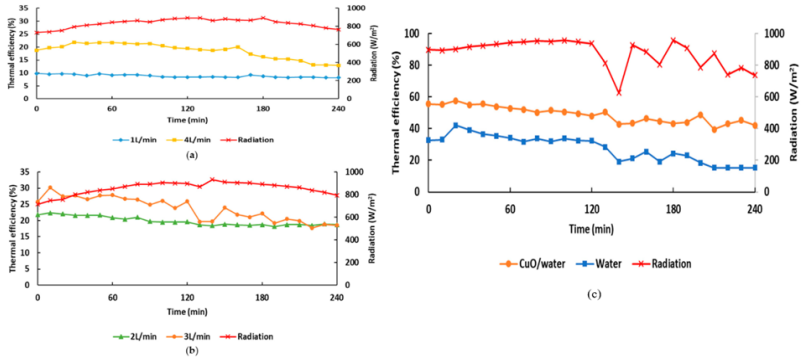

Figure 3. The thermal efficiency and solar radiation for each flow rate of the PV/T system over time: (a) flow rates of 1 L/min and 4 L/min; (b) flow rates of 2 L/min and 3 L/min, (c) CuO/water nanofluid-base (Joo Hee Lee, 2019).

As outlined in Table 1, properties such as density, specific heat, and thermal conductivity are elucidated for various nanoparticles. Consequently, the foremost criterion lies in the identification of an optimal nanofluid variety with enhanced thermal conductivity, thereby enabling the selection of a superior-performing nanofluid.

Table 1. Properties of base fluids and nanoparticles (Ahmed et al., 2019)

Nanoparticle/base fluid	Density (ρ_{np}) kg/m^3	Specific heat ($C_{p.np}$) J/kgK	Thermal conductivity (k_{np}) W/mK
Aluminium (Al_2O_3)	3960	773	40
Aluminium (Al)	2700	904	237
Carbon nanotube (CNT)	1350	-	3000
Copper (Cu)	8940	385	401
Copper oxide (CuO)	6000	551	33
Graphite	2160	701	120
Silicon (Si)	2320	714	148
Silicon Carbide (SiC)	3370	1340	150
Silicon Oxide (SiO_2)	3970	765	3970
Titanium Carbide (TiC)	4930	711	330
Titanium Oxide (TiO_2)	4230	962	8.4
Cuprous Oxide (Cu_2O)	5320	no data	76.5
Graphene Oxide (GO)	1910	710	1000
Iron Oxide (Fe_2O_3)	5250	650	20
Single-walled carbon nanotubes (SWCNTs)	2100	841	6000
Multiwalled carbon nanotubes (MWCNTs)	2100	711	1500
Ag+MgO-nanocomposite	7035	554.5	242
Fe_2O_3 + MWCNTs-nanocomposite	4845.4	554.5	509.14
Pure water	997.1	4179	0.613
Ethylene glycol	1113.2	2470.2	0.258
Engine oil	870	2012	0.142

Effects of parameters on uses of nanofluids in PV/T systems

The performance of PV/T systems can be influenced by numerous factors including wind speed, ambient temperature, coolant mass flow rate, working fluid temperature at the collector's inlet, and solar energy. Design parameters include the type of solar cells, the structure of the thermal collector, the type of working fluid, and the use of phase change materials (Hosseinzadeh et al., 2018).

Table 2 shows the main parameters and the performance statements concerning to the different types of nanofluid.

Table 2. Performance of nanofluids-based PVT system (Razali et al., 2019)

Types of nanofluid	Particle size nm	Mass fraction	Result
SiO_2/water	11-14	1, 3 w%	Energy and exergy efficiency increased
Fe_3O_4/water	-	1, 3 w%	For 3 w%, the overall efficiency improved by 45%
MgO/water	10	0.02, 0.06, 0.1 w%	Transmittance of nanofluids decreases when mass fraction and film thickness increase
SiO_2/water	5, 10, 25, 50	2 vol% for 5 nm	The transmittance of nanofluid with a particle size of 5 nm and 2 vol% can be as high as 97% very close to pure water.
Au, Al, Ag, SiO_2	20-50	0.01 vol%	Volume fraction of 0.001% is required to achieve optimum filters.

Hence volume fraction or concentration ratio of any given nanofluid is a crucial determinant of its efficiency as shown in Fig. 4a and Fig 4b.

Another element influencing the performance of the PV/T system depicted in Fig. 4c is the size of the nanofluid (Rahmanian & Hamzavi, 2020).

Additionally, the other determinant factor is base fluid. It can be water since it has appropriate heat transmission and better suspension qualities. However, organic fluids exhibit superior heat transmission and suspension than water as shown in Fig. 4d.

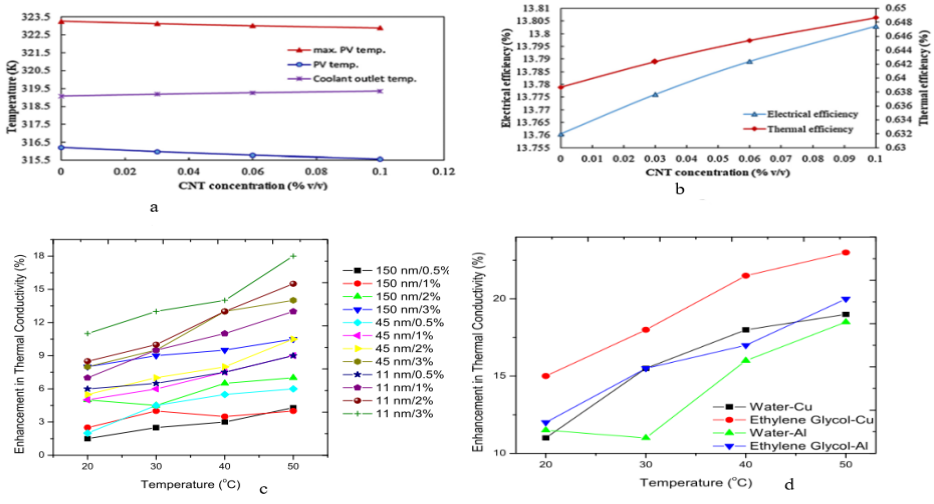

Figure 4. Variation of (a) average temperature of the PV surface and outlet nanofluid, (b) electrical and thermal efficiency of the PV/T system versus CNT volume concentrations, (c) Enhancement in thermal conductivity of Al_2O_3 nanofluid at different volume fractions and particle sizes and (d) Comparison of Cu and Al nanofluid at 1% volume fraction and 80 nm particle size

Nanofluid preparation method

Nanofluids need to go through a good preparation step to achieve substantial performance, including stability of the suspended particles within the base fluid and their homogeneity. Two techniques can be used to prepare nanofluids.

a. Single-Step Method. In this procedure, the creation and dispersion of nanoparticles take place in the same stage. Physical or chemical methods can be used to carry out this procedure. This process is quite expensive and has limitations when it comes to mass-producing nanofluids.
b. Two-Step Method. This method uses high shear or ultrasound technologies to produce the nanoparticles as a first step and then mixes them with the base fluid. These days, since companies sell nanoparticles, this technology is more often used in nanofluid production. After being created as a powder, nanoparticles are combined with a base fluid. To distribute nanoparticles in base fluid and lessen agglomeration, ultrasonication is employed. To keep the suspension to be stable, a surfactant or dispersant is added to the nanofluid (Razali et al., 2019).
c.

3. Numerical analysis of the PV/T system

Energy analysis

PV/T systems are considered as a control volume when examining their performance from an energy perspective. In that sense, therefore, it is considered that the system is in a semi-steady state for simplicity. Fig. 5 shows the scheme of a solar photovoltaic system with a storage tank where nanofluid is used as a cooling medium.

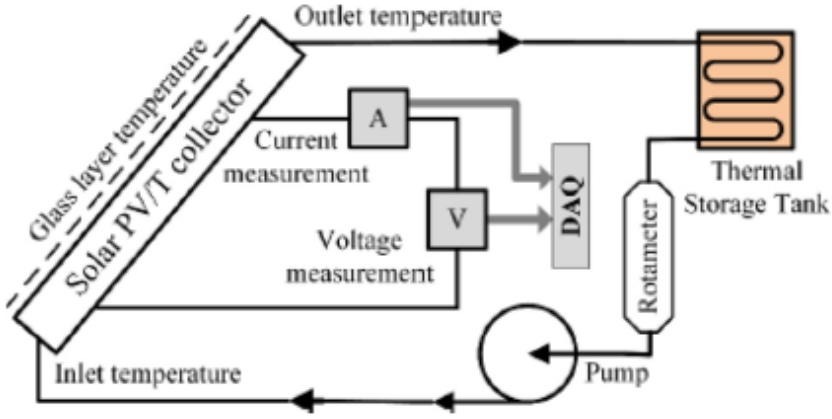

Figure 5. PV/T system with a storage tank and nanofluid as a cooling medium (Gupta & Pradhan, 2021)

The amount of solar radiation that the PV/T system has absorbed is given by:

$$E_{sun} = GA_c\tau_g\alpha_{cell} \quad (2)$$

where G is the total solar radiation, A_c is the collector area, τ_g is the transmissivity of the glass cover, and α_{cell} represents the absorptivity of photovoltaic cells (Hosseinzadeh et al., 2019).

The PV/T system's output thermal power can be stated as follows:

$$Q_t = mC_p(T_o - T_i) \quad (3)$$

where T_o and T_i are the working fluid temperatures at the heat-absorbing tube's inlet and outlet, m is the mass flow rate, C_p is the specific heat (Joo Hee Lee, 2019).

The PV/T system's output electrical power is also stated as follows:

$$E_{el} = V_{oc}I_{sc}FF \quad (4)$$

where FF stands for the fill factor, I_{sc} for the short circuit current, and V_{oc} for the open circuit voltage (Abadeh et al., 2018; Fayaz et al., 2018; Hosseinzadeh et al., 2019; Khanjari et al., 2016).

The output electrical power can be converted into an equivalent thermal power as described in the literature.

$$Q_t = \frac{E_{el}}{C_f} \quad (5)$$

where C_f is the conversion factor; for an adequate energy evaluation scale, the output electrical energy can be converted to thermal energy with a conversion factor of 0.38. (In the literature, this value ranges from 0.35 to 0.40 (Abadeh et al., 2018).

The amount of electricity used by the pump in the active PV/T system can be computed as follows:

$$E_p = \frac{m_f\Delta P}{\rho_f\eta_p} \quad (6)$$

where η_p is the pump efficiency and ΔP is the coolant fluid pressure decrease in the collector.

Furthermore, the mathematical methodology can be used to determine the electrical energy efficiency of active PV/T systems:

$$\eta_{el} = \frac{E_{el} - E_p}{E_{sun}} \quad (7)$$

The PV/T system's thermal energy and overall efficiencies are expressed as follows, respectively:

$$\eta_{th} = \frac{Q_t}{E_{sun}} \quad and \quad \eta_{ov} = \eta_{el} + \eta_{th} \quad (8)$$

These mathematical equations (Eq. 2. – Eq. 8) are employed to analyze thermal and electrical energy generation in PV/T systems and evaluate their analytical performance..

Conclusions

In this study, an extensive investigation was conducted on the subsequent elements

- The present study reveals that an increase in the thermal conductivity of the nanofluid leads to a rise in its coefficient of cooling efficiency. This leads to inconsistent thermophysical properties of the nanofluid and consequently results in increased energy consumption during the pumping process.
- The fluctuation in the average temperature of the photovoltaic surface, the concentrations of carbon nanotubes (CNTs) in the volume, the fractions of the volume, and the sizes of the particles in the nanofluid all have an impact on the outlet temperature of the nanofluid, as well as its thermal and electrical efficiency, and its thermal conductivity.
- The impact of flow rate on thermal efficiency was examined by considering flow rates of 1 L/min, 2 L/min, 3 L/min, and 4 L/min. The findings indicate that the flow rate of 3 L/min demonstrated superior performance in the examined investigation. Moreover, the utilization of ethylene glycol-Copper nanofluid, using ethylene glycol as base fluid instead of water, gives the most favorable outcome.
- The investigation of the impact of various nanofluids on the performance of the PV/T system is conducted, including a comprehensive numerical analysis and assessment of the thermal and electrical energy balance.

Acknowledgements

This work was supported by the Stipendium Hungaricum Programme and by the Mechanical Engineering Doctoral School, Hungarian University of Agriculture and Life Sciences, Gödöllő, Hungary.

References

[1] Abadeh, A., Rejeb, O., Sardarabadi, M., Menezo, C., Passandideh-Fard, M., & Jemni, A. (2018). Economic and environmental analysis of using metal-oxides/water nanofluid in photovoltaic thermal systems (PV/Ts). Energy, 159, 1234–1243. https://doi.org/10.1016/j.energy.2018.06.089

[2] Abbas, N., Awan, M. B., Amer, M., Ammar, S. M., Sajjad, U., Ali, H. M., Zahra, N., Hussain, M., Badshah, M. A., & Jafry, A. T. (2019). Applications of nanofluids in photovoltaic thermal systems: A review of recent

advances. Physica A: Statistical Mechanics and Its Applications, 536, 122513. https://doi.org/10.1016/j.physa.2019.122513

[3] Ahmed, A., Baig, H., Sundaram, S., & Mallick, T. K. (2019). Use of nanofluids in solar PV/thermal systems. International Journal of Photoenergy, 2019. https://doi.org/10.1155/2019/8039129

[4] Alsalame, H. A. M., Lee, J. H., & Lee, G. H. (2021). Performance evaluation of a photovoltaic thermal (Pvt) system using nanofluids. Energies, 14(2), 1–12. https://doi.org/10.3390/en14020301

[5] Fayaz, H., Nasrin, R., Rahim, N. A., & Hasanuzzaman, M. (2018). Energy and exergy analysis of the PVT system: Effect of nanofluid flow rate. Solar Energy, 169 (May), 217–230. https://doi.org/10.1016/j.solener.2018.05.004

[6] Gupta, S. K., & Pradhan, S. (2021). A review of recent advances and the role of nanofluid in solar photovoltaic thermal (PV/T) system. Materials Today: Proceedings, 44, 782–791. https://doi.org/10.1016/j.matpr.2020.10.708

[7] Hosseinzadeh, M., Salari, A., Sardarabadi, M., & Passandideh-Fard, M. (2018). Optimization and parametric analysis of a nanofluid based photovoltaic thermal system: 3D numerical model with experimental validation. Energy Conversion and Management, 160 (December 2017), 93–108. https://doi.org/10.1016/j.enconman.2018.01.006

[8] Joo Hee Lee, S. G. H. and G. H. L. (2019). Efficiency Improvement of a Photovoltaic Thermal. Energy.

[9] Khanjari, Y., Pourfayaz, F., & Kasaeian, A. B. (2016). Numerical investigation on using of nanofluid in a water-cooled photovoltaic thermal system. Energy Conversion and Management, 122, 263–278. https://doi.org/10.1016/j.enconman.2016.05.083

[10] Nasrin, R., Rahim, N. A., Fayaz, H., & Hasanuzzaman, M. (2018). Water/MWCNT nanofluid based cooling system of PVT: Experimental and numerical research. Renewable Energy, 121, 286–300. https://doi.org/10.1016/j.renene.2018.01.014

[11] Rahmanian, S., & Hamzavi, A. (2020). Effects of pump power on performance analysis of photovoltaic thermal system using CNT nanofluid. Solar Energy, 201 (August 2019), 787–797. https://doi.org/10.1016/j.solener.2020.03.061

[12] Razali, N. F. M., Fudholi, A., Ruslan, M. H., & Sopian, K. (2019). Review of water-nanofluid based photovoltaic/thermal (PV/T) systems. International Journal of Electrical and Computer Engineering, 9(1), 134–140. https://doi.org/10.11591/ijece.v9i1.pp134-140

[13] Said, Z., Arora, S., & Bellos, E. (2018). A review on performance and environmental effects of conventional and nanofluid-based thermal photovoltaics. Renewable and Sustainable Energy Reviews, 94 (October 2017), 302–316. https://doi.org/10.1016/j.rser.2018.06.010

[14] Salari, A., Taheri, A., Farzanehnia, A., Passandideh-fard, M., & Sardarabadi, M. (2021). An updated review of the performance of nanofluid-

based photovoltaic thermal systems from energy, exergy, economic, and environmental (4E) approaches. Journal of Cleaner Production, 282, 124318. https://doi.org/10.1016/j.jclepro.2020.124318

[15] Sardarabadi, M., & Passandideh-Fard, M. (2016). Experimental and numerical study of metal-oxides/water nanofluids as coolant in photovoltaic thermal systems (PVT). Solar Energy Materials and Solar Cells, 157, 533–542. https://doi.org/10.1016/j.solmat.2016.07.008

Dust-proofing on the Moon: A review of mechanical seals for Lunar settlement sustainability

Banram TURAPOV[1,2,] Gábor KALÁCSKA[2]

[1] *Department of Materials Science and Engineering Processes, Institute of Technology,* MATE, Gödöllő

[2] *Doctoral School of Mechanical Engineering,*
Hungarian University of Agriculture and Life Sciences MATE, Gödöllő

Abstract

A major obstacle to long-term Moon settlement is the abrasive nature of lunar dust. The adverse effects of lunar dust on astronauts, exploration equipment, and exploration systems are well known from previous Apollo missions. Among the mechanical parts are seals, shafts, axles, interlocks, joints, and airlocks. The purpose of this review is to provide an overview of recent mechanical seals for lunar dust mitigation applications. A study was conducted on spring-loaded PTFE (Polytetrafluoroethylene) seals, LTM seals (Low-temperature mechanism seals - Aeroflex seals), magnetic-coupling seals, and brush type seals. During the review, the design, testing methods, materials, and performance of the seals were analyzed. The high chemical resistance of spring-loaded PTFE seals and their ability to maintain sealing efficiency are highlighted. The LTM dust seal is noted for its performance under vacuum conditions and its minimal dust passage. Magnetic coupling seals offer a non-contact method of power transmission, reducing wear and tear and increasing dust resistance. Brush type seals are recognized for their low leakage and minimal friction, making them suitable for liquid hydrogen environments in space. Collar seals, made from high-performance polymers, are essential for preventing dust infiltration in lunar rovers. Magnetic coupling seals offer a non-contact method of power transmission, reducing wear and tear and increasing dust resistance. Brush type seals are recognized for their low leakage and minimal friction, making them suitable for liquid hydrogen environments in space. Collar seals, made from high-performance polymers, are essential for preventing dust infiltration in lunar rovers. The future directions were mentioned.

Keywords

regolith, abrasion, sealing, tribology

1. Introduction

The main challenge in Lunar exploration projects is the abrasive wear process caused by lunar regolith. The geometric, mechanical, and adhesion characteristics of lunar dust are different from those of dust under the earth's environment (Gaier & Berkebile, 2012; Li et al., 2023). Approximately one-fifth of the lunar regolith layer is less than 20 μm which is categorized as a lunar dust (Kawamoto, 2014; Zanon et al., 2023). Its extremely abrasive nature is caused by a lack of erosion on the moon's surface, micrometeorite bombardments, silicate content, and electrostatic charging (Nikki Welch, 2021; Zanon et al., 2023). Seals, shafts, axles, interlocks, joints, and airlocks are among the structural elements harmed by lunar dust abrasion (Gaier, 2005). Tribological parts only account for a small portion of the total cost of the spacecraft, but they frequently cause malfunctions that threaten the mission by disrupting the spacecraft either totally or partially (Mukhtar et al., 2023). One type of passive mitigation that is used to keep dust out of internal mechanisms—especially rotating shafts—is the use of seals (Cannon et al., 2022). The objective of this review article is to analyze the existing dust mitigation seals on the Moon's surface for future lunar exploration activities. Testing methods, materials, advantages, and disadvantages of the available seals will be evaluated, as well as directions for future research.

2. Existing mechanical seals of dust mitigation in space exploration

Seals play a crucial role in dust mitigation for space exploration, particularly in protecting sensitive mechanical components from the abrasive lunar regolith. The design of these seals is critical due to the mass and size limitations inherent in space travel. For sealing material for space exploration purposes PTFE seals are one of the most preferred (Barkó et al., 2023). Due to mass limitations seal mechanisms must be designed small and lightweight. (Chinnery et al., 2020). Ongoing research and development aim to improve the durability and performance of these seals in the harsh conditions of space. There are several seal types such as spring-loaded PTFE seal, Aeroflex shaft seal, magnetic coupling seal, and the brush-type seal that have been specially studied for dust mitigation in lunar applications were not examined.

Spring-loaded PTFE seal.

Spring-loaded PTFE seals (also known as spring-loaded Teflon seals) are designed to provide reliable sealing in a variety of applications. These seals consist of a PTFE (Polytetrafluoroethylene) sealing jacket that is energized by a spring mechanism. The spring mechanism is made from stainless steel. The spring applies pressure to the seal, ensuring constant sealing efficiency even in conditions with varying pressures and temperatures. They are known for their high chemical resistance, excellent temperature capabilities, and resistance to

weathering. Delgado et. al., (2010) conducted experimental research to define the performance of spring-loaded PTFE seals in keeping lunar simulant out of mechanical component gearbox, motor, and bearing housings. First, the test was conducted 1000 cycles with constant shaft rotation at 20 rpm in a dry environment without a stimulant to ascertain the wear effects of the seal against stainless steel or anodized aluminum shafts. Tests were repeated using JSC-1A and LHT-2M simulants. Lastly, experiments were run in a vacuum at room temperature both with and without the stimulant. The test seal was manufactured by Bal Seal (Figure 1).

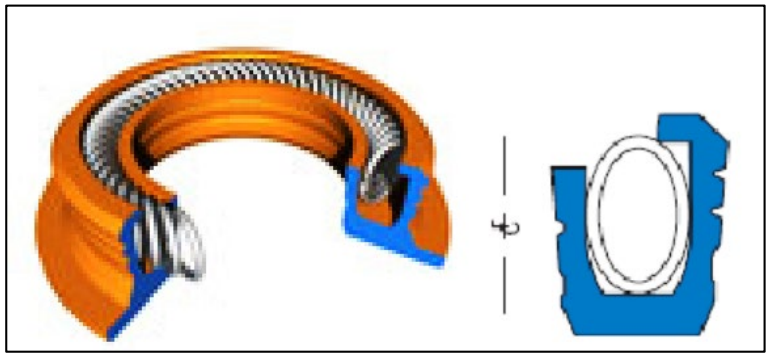

Figure 1. Spring loaded PTFE seal's cross section. (I. R. H. M. J. Delgado, 2010).

Post-test analyses included shaft profilometry, seal weight loss, and microscopic examination of both seal and shaft surfaces. The rotary seal rig was placed within a bell jar capable of 10 -7 Torr for tests in vacuum (Figure 2). Disassembly and examination procedures of both the test seal and shaft were identical to dry-room posttest procedures.

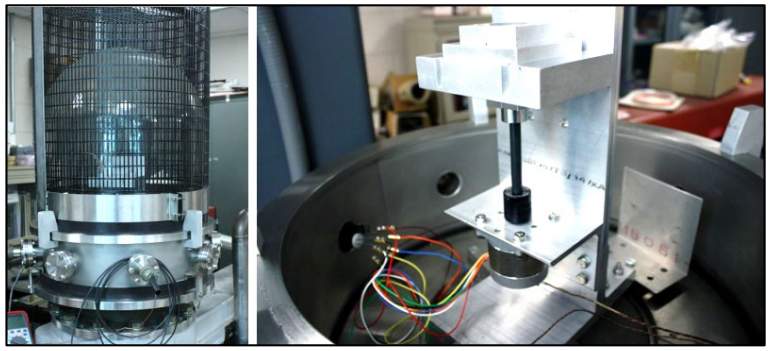

Figure 2. Vacuum chamber test rig (I. R. H. M. J. Delgado, 2010).

The seals were effective in preventing simulant passage in both dry-room and vacuum conditions. Both the seal and the shaft did not show excessive wear. There was minimal weight loss of the seal, with only small PTFE flakes observed downstream.

Spring-loaded PTFE seals, designed for lunar dust mitigation, come in various types to suit different applications:

- Canted Coil Spring Seals
- Helical Spring Seals
- V-Spring Seals.

Low-temperature mechanism (LTM) dust seal (Aeroflex seal).

The LTM dust seal is a specialized component designed for space applications, particularly for operations in environments like the moon or Mars. It's engineered to withstand the challenges of extraterrestrial surfaces, which include not only the vacuum and extreme temperatures of space but also potentially dusty conditions.

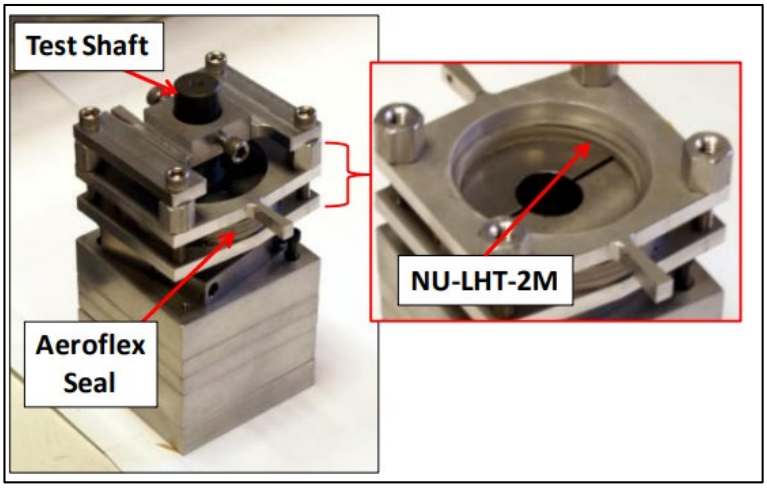

Figure 3. Test shaft and Aeroflex seal after the test in a vacuum chamber withregolith (I. Delgado et al., 2013).

The seal showed promising performance in the tests conducted with lunar simulant NU-LHT-2M, with only 0.4 milligrams of simulant passing through the seal-shaft interface in the first 511,000 cycles under vacuum conditions. The Aeroflex seal also demonstrated good performance, completing approximately 670,000 cycles with 650,000 cycles in vacuum using the NU-LHT-2M simulant. The findings suggest that these dust seals have the potential to withstand the challenging conditions of extraterrestrial surfaces, including dust, vacuum, and extreme temperatures, making them suitable for space actuator applications ((Delgado et al., 2013).

Magnetic coupling seal.

Magnetic coupling seals are a critical technology for space applications, offering a non-contact method of power transmission. They work by using magnetic fields to transfer torque or force through a non-magnetic barrier, eliminating the

need for a physical connection. Magnetic coupling seals are CryMag coupler devices used to connect and disconnect tanks in cryogenic management systems (Figure 4). Magnetic coupling seals offer a non-contact method of power transmission. They work by using magnetic fields to transfer torque or force through a non-magnetic barrier, eliminating the need for a physical connection. This results in a nearly frictionless operation and significantly reduces wear and tear, which is particularly beneficial in the harsh conditions of space. Since the magnets have a basic surface design, they are also more dust resistant. With less crevices and nooks than a standard mechanical seal's design, there is less possibility of dust entering the system. Additionally, the self-alignment properties of the magnets make magnetic coupling seals advantageous in terms of usage.

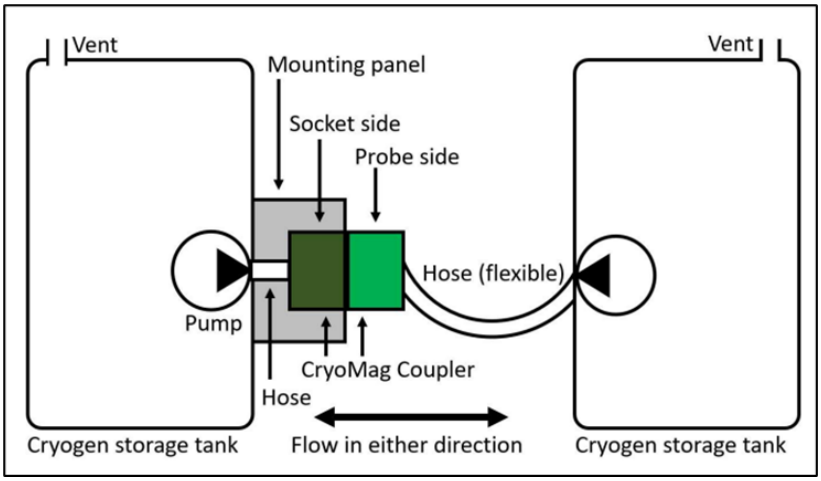

Figure 4. The sketch of CryoMag Couple in cryogenic fluid management system (Bean et al., 2023).

Three subsystems make up the CryoMag Coupler (Figure 5): 1 - the Low Force Disconnect (LFD) allows cryogenic fluids to be transferred; 2 - the Magnetic Subsystem provides forces needed to mate the LFD; 3 – the Dust Mitigation Subsystem (DMS) keeps dust out of fluid flow path and internal coupler mechanisms. Separate designs, fabrications, and testing take place for each subsystem. Bean et al., (2023) in their research article discuss the design and testing of the magnetic subsystem. The test aimed to evaluate the force profile at different temperatures and rotation angles. Survivability tests involved immersing magnets in LN2, showing no visible damage to the magnets or their coatings. Results indicated a slight increase in attachment forces at cryogenic temperatures and a decrease at high temperatures, with some non-linearity in the trend observed.

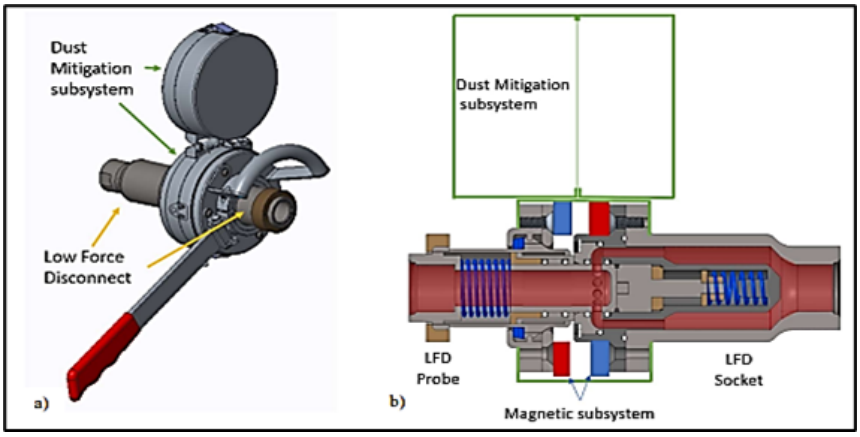

Figure 5. Cryomag Coupler: (a) CAD model, (b) cross section (Stebbins & Heersema, 2023).

The preliminary testing of the DMS is conducted on a Dust Environment Low-fidelity Test Apparatus (DELTA) (Stebbins & Heersema, 2023). Reduced physical complexity, self-alignment, self-latching and dust tolerance characteristics of the magnetic sealings make them an attractive candidate for future lunar exploration projects. However they have limitations such as low holding force compared to traditional mechanical coupling, brittleness of the magnetic material and "always on" configuration of magnetic subsystems.

Brush type seals.

Brush seals consist of densely packed fibers with fine diameters to withstand high temperatures, and are used to seal gaps against debris, light, and air infiltration. In order to provide mechanical support for the differential pressure loads, a support plate called a backing ring or backing plate is positioned downstream of the bristles The diameter of metallic brush seal fibers ranges from 0.07 to 0.15 mm (0.0028 to 0.006 in.). Densities are measured by the number of bristles per circumference of the seal bore (Aksit, 2012). In the context of space applications, brush seals are valued for their low leakage characteristics and minimal friction around moving parts. NASA has pioneered the use of brush seals in liquid hydrogen (LH2) environments, demonstrating their effectiveness in reducing leakage and wear. For example, Rocketdyne has incorporated brush seals into their RS-68 engine for the Delta-4 rocket, enhancing performance and reliability (Proctor & Delgado, 2008). Suzuki et al., (2011) conducted a long-term test of approximately one week in a vacuum in order to obtain an estimate of the lifespan of brush-type seals. Figure 2 shows an overview of the seal section.

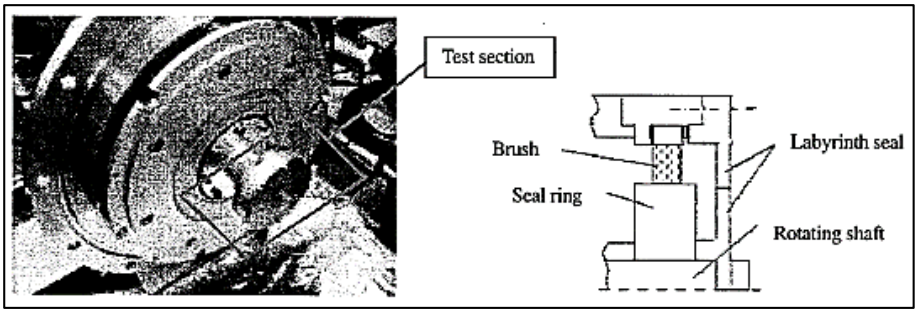

Figure 6. Test section and test seal configuration (Suzuki et al., 2011).

The brush material is fluororesin and the seal ring is made of aluminum alloy. A labyrinth seal is installed in front of this seal, whose surface is treated with an anodized oxide film, to restrict the inflow of sand. The experiment was conducted in a vacuum chamber with lunar regolith. The tested seal system, which combines a labyrinth seal and a brush-type seal, was able to withstand continuous operation for one week. There is almost no leakage of sand and dust, making it extremely promising as a regolith seal in terms of both seal performance and longevity. Although the test was conducted twice under the same conditions, there were significant differences in friction torque, dust leakage, etc. The cause of this is unknown. However, it is possible that the concentricity when attaching the brush to the seal ring was a factor. (3) When the seal ring was rubbed with a brush, a chemical reaction occurred on the surface and aluminum fluoride was produced. Also, It was observed that the worn fluorine resin had been transferred to the surface of the mating seal ring. These phenomena are caused by the seal ring. There is a possibility that wear resistance and lubricity were improved.

Collar seals.

Collar seals in lunar exploration are used as a protecting sealing for small bearings in lunar rovers. These seals are typically made from high-performance polymer composites, such as PTFE (Polytetrafluoroethylene) and PEEK (Polyether Ether Ketone), due to their excellent sealing ability, low torque, light weight, and ease of installation. In the context of lunar exploration, collar seals are applied to bearings in rovers to prevent lunar dust from entering and damaging the mechanisms. The design of these seals includes a convex portion that slides on the end face of the bearing, creating an effective barrier against dust particles (Figure 7).

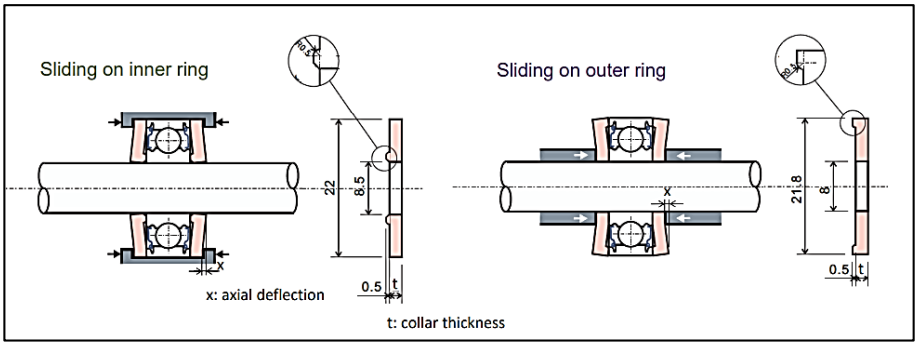

Figure 7. Collar seal design (Matsumoto et al., 2020).

Matsumoto et al., (2020) tested collar seals made from PTFE with glass fibre reinforcement, PTFE with carbon fibre reinforcement, and PEEK with carbon fibre reinforcement in vacuum chamber with FJS-1 lunar regolith simulant. The study also discussed the tribological performance and results of surface analysis by XPS (X-ray photoelectron spectroscopy), which is essential for understanding the wear and friction characteristics of the materials used. Finite Element Method (FEM) with two-dimensionally axisymmetric model was applied to determine the contact load and contact pressure. The torque behavior of the bearing is shown in Figure 8 for sliding locations on its inner and outer rings. The torques remained unstable regardless of dust or sliding locations when no radial load was applied at the beginning or just before the test ended. Once 30 N and 4000 sliding cycles were applied, the torques became stable as the radial loads were increased. Torque was insignificantly affected by dust in the space between the shaft and seal. No dust passed after the test between the collar seal and bearing. It was found that the torque when sliding on the inner ring was half that when siding on the outer ring.

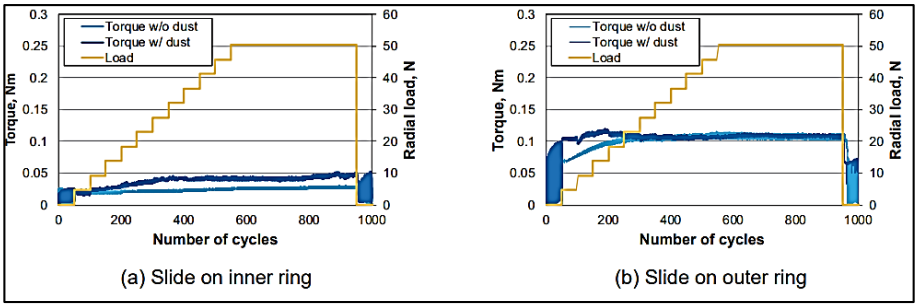

Figure 8. Bearing's torque behavior for sliding location on its inner and outer diameter for PTFE with glass fiber sealing.

Advances in materials science and engineering continue to improve the design and functionality of these seals, making them an essential component in the success of current and future space missions.

3. Results and conclusions

Overall, the advancement of seal technologies is vital for the success of space exploration, providing reliable protection against the extreme conditions encountered on lunar and Martian surfaces. Various sealing technologies for space applications were studied in order to define test specimens, emphasizing the importance of dust-proof seals for extended lunar missions:

- Sealing Importance: Seals are crucial for protecting internal mechanisms, especially in lunar environments. Preferred materials include PTFE due to its lightweight and small design requirements.
- Spring-loaded PTFE Seal: These seals use a spring to maintain sealing efficiency under varying conditions. They are highly resistant to chemicals, temperature, and weathering. Tests with lunar simulants showed no leakage and minimal wear.
- Low-Temperature Mechanism (LTM) Dust Seal (Aeroflex Seal): Designed for moon and Mars operations, these seals performed well in tests, showing minimal simulant passage and good durability under vacuum conditions.
- Magnetic Coupling Seal: This technology uses magnetic fields for non-contact power transmission, offering a dust-resistant and nearly frictionless operation, beneficial in space's harsh conditions.
- Brush Type Seals: Made from high-temperature resistant materials, these seals are used for their low leakage and minimal friction, suitable for liquid hydrogen environments in space.
- Collar Seals: Constructed from high-performance polymers like PTFE and PEEK, these seals are critical for lunar rovers, preventing dust infiltration and ensuring the longevity of mechanical components.

The study highlighted the importance of contact pressure and load in the performance of dust seals. PEEK composites were found to have the best torque and wear resistance among the materials tested. The research suggests that seals discussed in the study are viable options for protecting lunar exploration equipment from abrasive lunar dust. Future research directions include improving seal designs and materials to enhance their effectiveness and longevity in lunar conditions. The advancements in seal technology are crucial for the success of current and future space missions.

References

[1] Aksit, M. F. (2012). *Brush Seals and Common Issues In Brush Seal Applications*.

[2] Bean, P. S., Heersema, N., Holguin, A., Lopez-zepeda, J., & Stebbins, S. L. (2023, January 23). *Magnetic Subsystem Design and Testing for the NASA Magnetic Latching Cryogenic Coupler*. https://doi.org/10.2514/6.2023-0069

[3] Delgado, I., Handschuh, M., Panko, S., & Sechkar, E. (2013). *Performance Evaluation of an Actuator Dust Seal for Lunar Operation*. http://www.sti.nasa.gov

[4] Delgado, I. R. H. M. J. (2010). *Preliminary Assessment of Seals for Dust Mitigation of Mechanical Components for Lunar Surface Systems*. http://www.sti.nasa.gov

[5] Gaier, J., & Berkebile, S. (2012, January 9). Implication of Adhesion Studies for Dust Mitigation on Thermal Control Surfaces. *50th AIAA Aerospace Sciences Meeting Including the New Horizons Forum and Aerospace Exposition*. https://doi.org/10.2514/6.2012-875

[6] Kawamoto, H. (2014). *Improved Electrostatic Shield for Lunar Dust Entering into Mechanical Seals of Equipment Used for Long-Term Lunar Exploration*.

[7] Li, R., Cui, Y., Feng, Y., Wang, J., Huang, W., Sui, Y., & Ren, D. (2023). New Mechanical Models to Study the Impact of Contact, Wear, and Adhesion of Lunar Dust on Space Materials. *International Journal of Applied Mechanics*, *15*(4). https://doi.org/10.1142/S1758825123500254

[8] Matsumoto, K., Yanagase, K., Takada, S., Yokoyama, T., Kusabe, S., Tsujimura, N., & Nakamura, T. (2020). Application of collar seals for bearings in the lunar exploration rover. *Tribology Online*, *15*(5), 332–342. https://doi.org/10.2474/TROL.15.332

[9] Nikki Welch. (2021, June 8). *Dust: An Out-of-This World Problem*. https://www.nasa.gov/humans-in-space/dust-an-out-of-this-world-problem/

[10] Proctor, M., & Delgado, I. (2008, July 21). Preliminary Test Results of Non-Contacting Finger Seal on Herringbone-Grooved Rotor. *44th AIAA/ASME/SAE/ASEE Joint Propulsion Conference & Exhibit*. https://doi.org/10.2514/6.2008-4506

[11] Stebbins, S. L., & Heersema, N. (2023, January 23). *Low-cost Testing in Representative Lunar Regolith Environment*. https://doi.org/10.2514/6.2023-2469

[12] Suzuki, M., ji MATSUMOTO, K., Nishida, S., Wakabayashi, S., Hoshino, T., 一 chi, J., 血 cho, & 脚 J. (2011). *Long − term experiments in vacuum on a brush − type seal as a candidate for regolith seal applications*.

[13] Zanon, P., Dunn, M., & Brooks, G. (2023). Current Lunar dust mitigation techniques and future directions. In *Acta Astronautica* (Vol. 213, pp. 627–644). Elsevier Ltd. https://doi.org/10.1016/j.actaastro.2023.09.031

Determining drone rotor design parameters using virtual experiments

László BENSE, Attila LÁGYMÁNYOSI, István NAGY,
István OLDAL, István SZABÓ
Institute of Technology, Hungarian University of Agriculture and Life Sciences, MATE, Gödöllő

Abstract

Drones have proliferated by leaps and bounds over the last decade. Not only for hobby purposes, but also as professional load-carrying devices. For more frequent needs, there is a range on the market. If you have a specific need for which there is no ready-made solution, you can look in two directions. You can adapt an existing drone or design a custom machine. In the latter case, we present a method for determining the basic design data.

Keywords

Drone, rotor, lifting force, optimization

1. Introduction

Drones have become widely popular in the last decade, experiencing a significant surge in both hobbyist and professional applications, including those suitable for cargo transportation. Concurrently, applied electronics, control systems, guidance, and robotics have evolved to meet specific demands (Darvishpoor et al. 2020, Karimi, Pourtakdoust 2013, Bai et al. 2020). Development in both civilian (industrial, agricultural, hobbyist) and military applications remains continuous (Vergouw et al. 2016, Shahmoradi et al. 2020, Karaca et al. 2018). Drones vary greatly in size, payload capacity, and design, ranging from fixed-wing to multi-rotor solutions (Hassanalian et al. 2019, Luca et al. 2017, Li et al. 2020). Common demands are readily met within the market offerings.

If a specific need arises for which there is no off-the-shelf solution available, there are two avenues to explore for a solution: adapting an existing drone or designing a custom one. In this work, we present the methodology for determining fundamental design parameters associated with the latter case. Typically, the frame and connecting elements are unique to the intended purposes during the design process, while other major components such as the motor, battery, and rotor can be procured commercially. However, the lack of design data for the rotor is often a challenge. Our aim is to develop a process by

which necessary design data for an existing, ready-made rotor can be derived without the need for experimental setups and measurements.

2. Materials and methods

The rotor provides the lift necessary for flight. However, this data is often not available for purchasable rotors. Lift primarily depends on the rotor's geometry and rotational speed. Therefore, the necessary data can be derived in three main steps:

1. Generating a geometric model.
2. Determining lift force dependent on rotational speed.
3. Determining the decrease in lift force in the case of stall.

The geometric model can be physical if we seek a solution experimentally or numerical if we pursue a theoretical solution. During design, the theoretical approach is faster and cheaper. In this case, we need a 3D model of the rotor. Manufacturers typically do not provide 3D models, so we require a scanned model of the rotor.

Determining lift force is also possible experimentally, requiring, besides the rotor, one (or more if sizing is not accurate) motor, motor-rotor connector, sensors, support structure, and space. If data is obtained through simulated experiments, apart from the model, a computer and appropriate software are necessary.

Geometric model

For the 3D scanning of the rotor, we utilized a Z Corporation ZScanner 700 3D laser scanner. The measurement process began with the calibration of the device, which was performed using its dedicated calibration board. Subsequently, we configured the scanner according to the specific measurement environment, adjusting parameters such as backlight intensity, laser strength, and exposure time, depending on the surface texture, color of the object being scanned, and ambient lighting conditions.

The scanning of the rotor was conducted in two separate sessions, from both the top and bottom, using a measurement table attached with reference points. Afterward, the two halves of the rotor were aligned and merged into a solid model using software. The 3D scanning was performed on one side of the symmetric rotor, and the complete geometry was reconstructed through post-processing. Based on repeat measurements, we observed a deviation of less than 0.1 mm between the scanned data and the actual rotor.

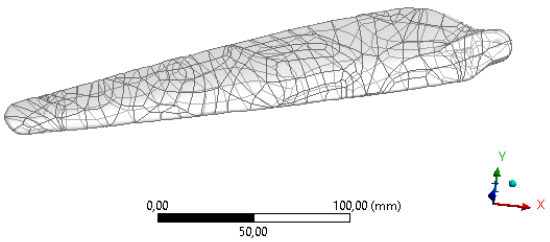

Figure 1. Scanned rotor geometry

From the scanned model, we generate the complete rotor model using mirroring, as depicted in Figure 2.

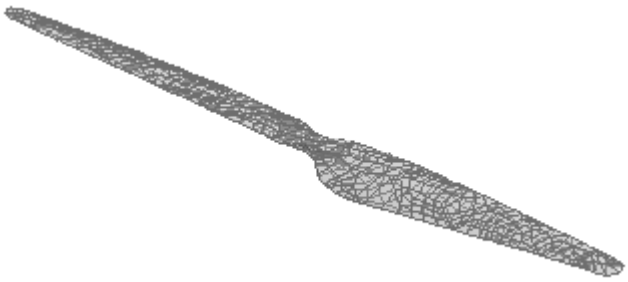

Figure 2. Complete rotor geometry

Determining lift force

Based on the knowledge of the 3D model, lift force data is generated using the finite element method. Instead of modeling the scanned rotor geometry, we model the flowing air. The model used during the simulation is depicted in Figure 3.

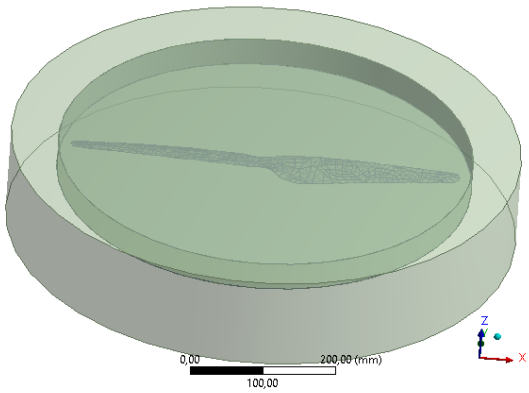

Figure 3. Flow geometric model

The complete model consists of three parts: the rotor, the air surrounding the rotor, and the external air. In the fluid dynamics model, there is no need for the detailed rotor model; the contour of the rotor within the air model is sufficient. Therefore, the fluid dynamics model comprises two parts: the air surrounding the rotor and the external air model, which interact with each other. The rotating rotor is modeled using its internal geometry, while the boundary conditions for the stationary external air are defined by the outer geometry. In the second step of modeling, the solid body model is required, at which point the air models will not be utilized.

To initiate the fluid dynamics modeling, the first step involves generating the finite element mesh. The critical aspect in fluid dynamics is the flow around the rotor surface, thus we employ mesh elements of around a tenth of a millimeter near the edges and progressively larger elements further away from the rotor. Consequently, our model consists of 2,199,445 elements.

Next, we define the boundary conditions for the model. We set properties for normal atmospheric air and apply the "shear stress transport" turbulence model. The air surrounding the rotor is defined as a rotating domain with speeds of 4000, 5000, 6000, 7000, 8000, and 9000 revolutions per minute. Open boundaries with a pressure difference of 0 Pa are specified on the external surfaces of the outer air model, while wall boundaries are set on the rotor surfaces within the inner model. A fluid-fluid interface is defined between the two air models using a special "frozen rotor" option, which treats the model such that only the rotor geometry is modeled as a moving element.

3. Results and discussion

Determining lifting force

Once the model setup is complete and computations are run, we obtain results regarding flow conditions. From the fluid dynamics results, we understand the pressure and velocity distribution within the flow. However, the pressure distribution on the rotor surface obtained from fluid dynamics does not directly provide the desired design data. Our goal is to determine the lifting force of the rotor, which requires structural modeling. For structural modeling, we need the rotor geometry from the original three-part model. We then import the pressures obtained from the fluid dynamics modeling onto the rotor surface (see Figure 4).

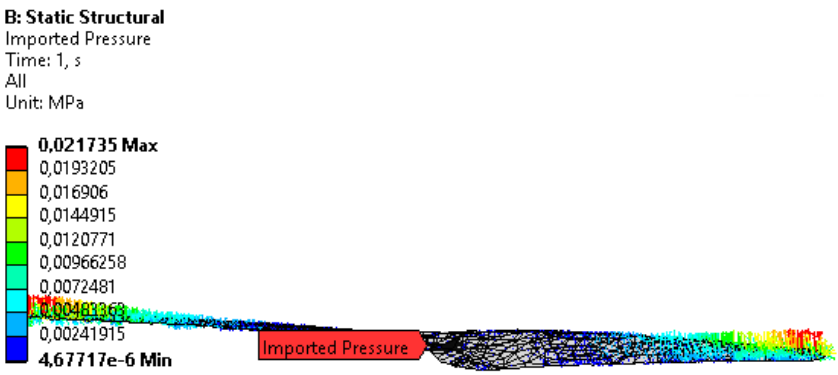

Figure 4. The pressures imported onto the rotor surface (9000 RPM)

In the structural model, we set up constraints on the originally connected surface of the rotor, and among the results, the reaction force calculated at the constraint will be crucial for us. Both fluid dynamics and structural modeling are performed for each specified rotational speed. As a result of the analyses, we obtain the rotational speed - lifting force characteristic curve of the rotor. The computed results are summarized in Table 1 and depicted in Figure 5.

Table 1. Calculated lifting forces

Rotational speed (RPM)	**Lift force (N)**
4000	16,03
5000	27,55
6000	39,55
7000	53,26
8000	68,58
9000	90,17

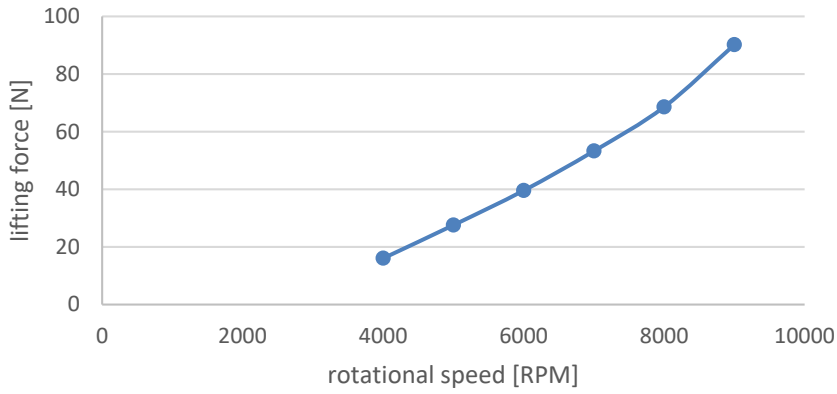

Figure 5. The rotational speed - lifting force characteristic curve

Determination of decrease in lifting force

Leveraging the availability of the flow and strength models, with slight modifications, we can adapt them for conducting the examinations. We adjust the geometric model to incorporate a solid body model into the external air model.

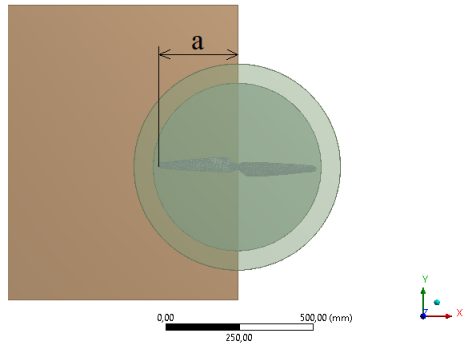

Figure 6. Solid body extending under the rotor (perpendicular position to the rotor)

As shown in Figure 6, we determine the effect of the penetration depth by varying the "a" dimension. Starting from 0mm, we increase the penetration depth in steps of 45mm relative to the 540mm diameter of the rotor, with increments of 8.33%. The penetrating body is positioned vertically below the rotor at a distance of 80mm. We examine the effect from two directions: once perpendicular to the rotor as shown in Figure 6, then parallel to the rotor. These are the extreme positions, alternating with the rotation speed, thus, in the end, we will average the two extreme values. The flow model will be the same as before, consisting of the two air models. The only change is that the outer air's common surface with the penetrating body is defined as a wall edge, allowing its impact on the flow to be reflected in the flow model, and enabling us to import pressures into the strength model. Since we are examining the effect of

penetration here, the tests will be conducted at a constant rotation speed of 7000 RPM, and we will analyze relative changes in force.

In this study, we will need the pressure data on both the rotor and the body from the flow analysis results.

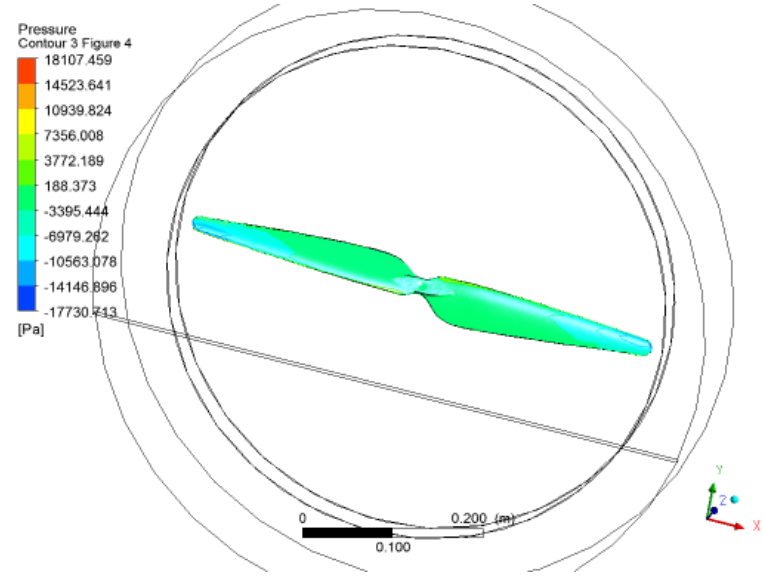

Figure 7. Fluid dynamics results: pressures on the rotor

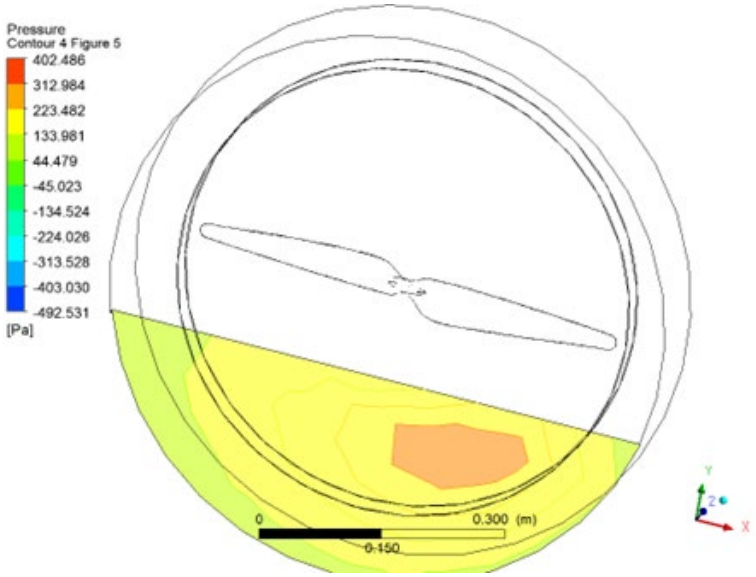

Figure 8. Fluid dynamics results: pressures on the body

In our work, we determined the effect of the angle of attack on the lifting force and torque for a given rotor. As a result, we obtain a database that allows for a multi-objective optimization. One possible aspect is the noise emission, in which case noise measurements have to be added to the data.

Following the method described in the previous section, considering the pressure data, we determine separately the force values acting on the rotor and on the penetrating geometry for different penetration depths. Since the position of the rotor is not constant, we conducted the modelling for the two extreme positions: perpendicular and parallel to the rotor. The results of these are shown in Figure 9. Results for the parallel position with the rotor are depicted in red, while those for the perpendicular position are shown in blue.

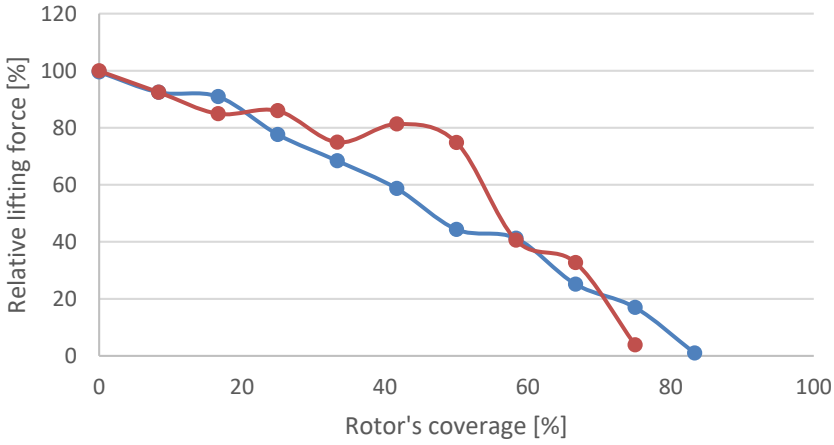

Figure 9. The relative value of the resultant lifting force of the rotor as a function of the rotor's coverage

For easier usability, the lifting force is provided relative to the uncovered state of the rotor, and the rotor coverage is proportionally given relative to the rotor diameter. It can be seen that the trend is similar in both positions, but the results vary slightly. In reality, these values continuously and rapidly change according to the rotation speed, with the average of these values being relevant for the drone. Therefore, in Figure 10, we present the average of the results from both positions, which represents a practical usable result.

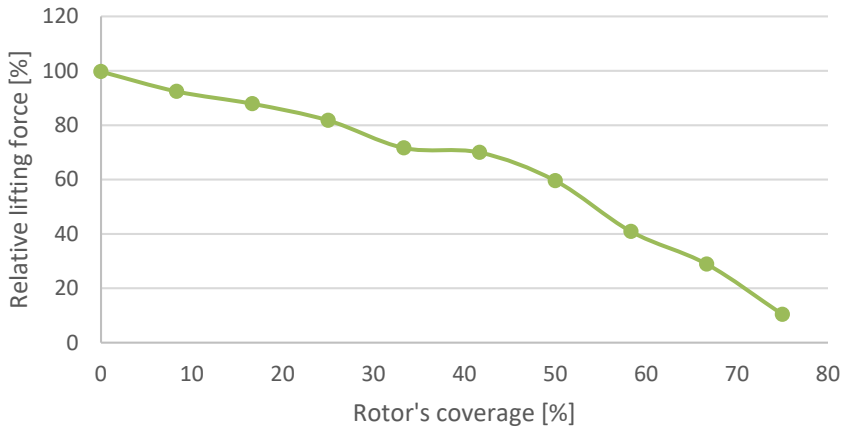

Figure 9. The relative value of the resultant lifting force of the rotor as a function of the rotor's coverage (average)

Based on the modeling, it can be concluded that a body extending slightly under the rotor does not cause a significant decrease in the effective lifting force. However, thereafter, a considerable decrease occurs, and in 70-80% of cases, the lifting force ceases to exist.

4. Conclusions

As a result of our work, we have developed a procedure that is suitable for generating design parameters for existing rotors with unknown properties. By implementing the procedure, we obtain the rotor characteristic curve, which can be used to perform the design. In the second phase, we seek to answer the specific question of how the lifting force changes when a surface is pushed into the space below the rotor. The answer to this is plotted in an indentation-force decay diagram.

Acknowledgements

This research was funded by the Ministry of Innovation and Technology within the framework of the Thematic Excellence Programme 2021, National Defense, National Security Subprogramme (TKP2021-NVA-22)

References

[1] S. DARVISHPOOR, J. ROSHANIAN, A. RAISSI, M. HASSANALIAN, Configurations, flight mechanisms, and applications of unmanned aerial systems: a review, Prog. Aero. Sci. 121 (2020) 100694.

[2] J. KARIMI, S.H. POURTAKDOUST, Optimal maneuver-based motion planning over terrain and threats using a dynamic hybrid PSO algorithm, Aerosp. Sci. Technol. 26 (2013) 60–71

[3] G. BAI, Y. LI, Y. FANG, Y.-A. ZHANG, J.J.R.E. TAO, S. Safety, Network approach for resilience evaluation of a UAV swarm by considering communication limits, Reliab. Eng. Syst. Saf. 193 (2020) 106602.

[4] B. VERGOUW, H. NAGEL, G. BONDT, B. CUSTERS, Drone technology: types, payloads, applications, frequency spectrum issues and future developments, in: The Future of Drone Use, TMC Asser Press, The Hague, 2016, pp. 21–45.

[5] J. SHAHMORADI, E. TALEBI, P. ROGHANCHI, M. HASSANALIAN, A comprehensive review of applications of drone technology in the mining industry, Drones 4 (3) (2020) 34.

[6] Y. KARACA, M. CICEK, O. TATLI, A. SAHIN, S. PASLI, M.F. BESER, S. TUREDI, The potential use of unmanned aircraft systems (drones) in mountain search and rescue operations, Am. J. Emerg. Med. 36 (4) (2018) 583–588.

[7] M. HASSANALIAN, R. SALAZAR, A. ABDELKEFI, Conceptual design and optimization of a tilt-rotor micro air vehicle, Chin. J. Aeronaut. 32 (2) (2019) 369–381.

[8] M. DI LUCA, S. MINTCHEV, G. HEITZ, F. NOCA, D. FLOREANO, Bioinspired morphing wings for extended flight envelope and roll control of small drones, Interface focus 7 (1) (2017) 20160092.

[9] LI, L.L., LIU, Y.J., HE, X.K., SONG, J.L., ZENG, A.J., WANG, Z.C., LI, T., 2018. Assessment of spray deposition and losses in the apple orchard from agricultural unmanned aerial vehicle in China. In: January 2020 Transactions of the ASABE (American Society of Agricultural and Biological Engineers) 63(3):619-627

Heating unit design for VAT photopolymerization process in stereolithography 3D printing

Adrián BOGNÁR[1], Krisztián KUN[2], László ZSIDAI[3]
[1] *Doctoral School of Mechanical Engineering,*
Hungarian University of Agriculture and Life Sciences MATE, Gödöllő
[2] *Department of Innovative Vehicles and Materials, NJE, Kecskemét*
[3]*Department of Materials Science and Engineering Processes, Institute of Technology,*
Hungarian University of Agriculture and Life Sciences MATE, Gödöllő

Abstract

This article introduces a heating unit designed to modify the temperature of resin during the photopolymerization 3D printing process. The designed device is capable to keep the set temperature in the printer workspace, thereby heating the photocuring resin required for additive manufacturing. This "Hot Lithography" process could open new perspectives for the production of industrial-grade photopolymer-based plastic parts in automotive industry or in the field of medical technology.

Keywords

DLP, SLA, resin, viscosity, 3D printing, photopolymerization

1. Introduction

Due to the rapid development of additive technologies has led to the widespread use of 3D printed parts for engineering purposes. In contrast to the most well-known and widespread FDM (Fused Deposition Modeling) process, the application of DLP (Digital Light Processing) technology opens up new possibilities for home users or even smaller companies. With the DLP process, more detailed, accurate, and homogeneous products can be produced. Due to the different operating principles of DLP printers, the influence of technological parameters is less known, especially the effect of changing the resin temperature. The aim of the research is to design a heating unit that is suitable for keeping the resin temperature at the set value.

2. Stereolithiography

Photopolymers

Photopolymer is a light-activated resin composed mostly of cross-linking monomers, oligomers, and a radiation-sensitive photoinitiator mixture (Fig. 1.). Its structural properties can be altered by exposure to UV light. The oligomers allow for the creation of branched chain molecules and growth in all directions for cross-linking. The process is so-called photopolymerization and is used in various 3D printing processes in additive manufacturing (Kun, 2020) (Šafka, 2020).

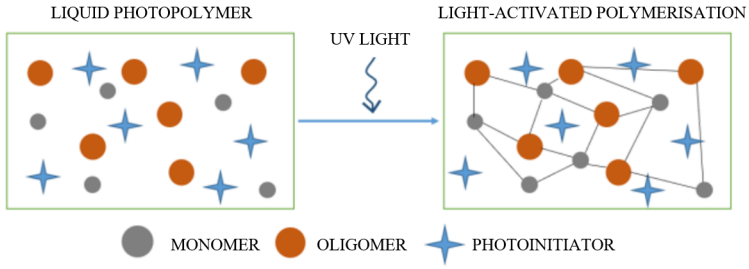

Figure 1. The photopolymerization process (Šafka, 2020)

The Stereolithography (SLA) and the Digital Light Processing (DLP) additive process

In the stereolithography 3D printing process, a laser shoots high-intensity ultraviolet light into a container filled with a photopolymer resin, in which there is a vertically moving work table. The light is directed using a lens system based on the three-dimensional model created in the CAD system. The laser solidifies certain layers of the resin on the platform, which sinks layer by layer until the final part is completed (Fig. 2.). Parts produced with digital light processing method have exceptional surface quality, but they are typically not as strong as parts made with other methods, such as Fused Deposition Modeling (FDM) technology. The manufactured piece usually requires post-processing. To achieve optimal hardness, it needs to be placed in a post-curing device with UV light for a specified period. Surface quality can be improved through sanding or polishing [1,10]. The DLP method was developed from SLA technologies, but it differs from them. DLP printers use an LED UV light source, which directs its light onto an LCD screen. The LCD screen is located directly beneath the tray filled with photopolymer. The bottom of the tray is made of a film that allows at least 95% of light to pass through. The upside-down object table is immersed into this tray. After a layer has solidified, the build platform moves vertically upward to allow liquid resin to flow into the freed-up space, then it sinks back down, and the process continues until the piece is completed (Fig. 2.) (Kun, 2020) (Manufactur3D, 2018).

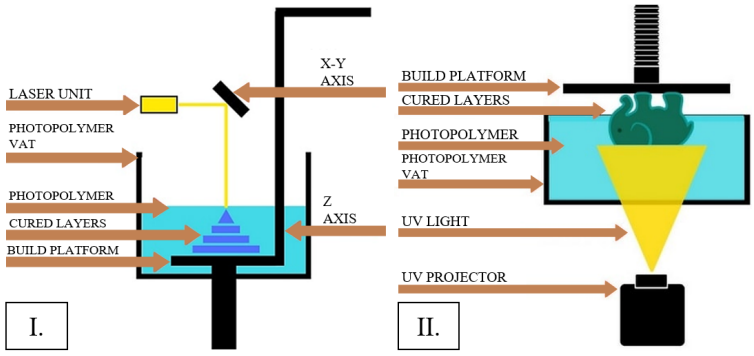

Figure 2. The SLS printing process I. (left), and the DLP printing process II. (right) (Manufactur3D, 2018)

The major advantage of this method over SLA is that the LED light source illuminates the entire cross-section of the piece. Allowing the maximum number of objects that can fit on the tray to be produced in the same amount of time as printing a single object. Its biggest drawback lies in the voxelization of the display. Voxels are the smallest units of a given three-dimensional image that have extent in the X-Y-Z axes. The X-Y cross-sectional dimensions determine the resolution and surface quality of products printed with a DLP printer (Fig. 3.). An anti-aliasing method is used to improve the quality of the process (Patel, 2021).

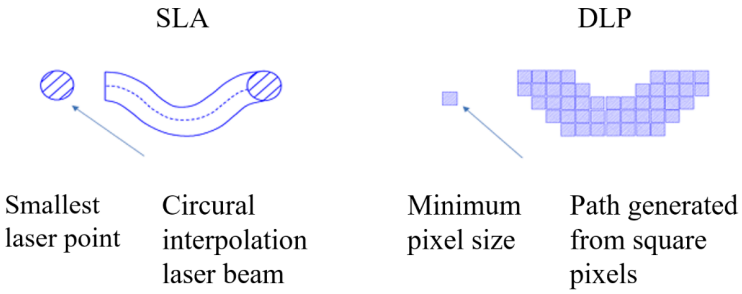

Figure 3. DLP projection compared to laser beam: voxel interpolation (Patel, 2021)

The heated resin printing process (Hot Lithography)

Traditional SLA and DLP systems work well at room temperature due to the low viscosity of the resin, which is a result of its low molecular weight. However, this leads to highly cross-linked systems in the printed parts, resulting in fragility and poor dimensional stability. In contrast, the essence of the "Hot Lithography" technology lies in heating the resins (Fig. 4.). The elevated temperature not only affects the material's viscosity but also its stability and reactivity. It is essential to precisely control the process temperature to prevent unwanted polymerization and material damage. With the "Hot Lithography" process, it is possible to

produce industrial-quality photopolymer-based plastic parts with better accuracy (Zguris, 2016) (Monzón, 2017) (Frank, 2022) (Pfaffinger, 2018).

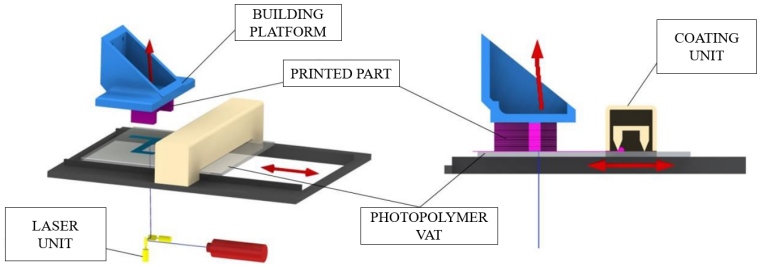

Figure 4. The „Hot Lithography" process (Frank, 2022)

3. DESCRIPTION OF THE DESIGNED HEATING UNIT

The design of the heating unit was greatly influenced by the workspace of the printer in which the device can be applied. The dimensions of the enclosure were prepared for 60x100x45 mm, making it possible to be placed in devices that use closed-chamber photopolymerization processes without obstructing the printing process. On the enclosure's soles and sides, recessed surfaces allow for the attachment of disc-shaped neodymium magnets for fixing the unit.

The heated resin printing process

The CAD assembly of the designed heating unit is shown in Fig. 5., which consists of the following components:

- self-made 3D printed housing
- W1209WK type LED digital thermostat
- 5V, 60x60x15 mm PC fan
- 100W, 12V, Positive Temperature Coefficient (PTC) heating unit
- ø5x2 mm neodymium magnets

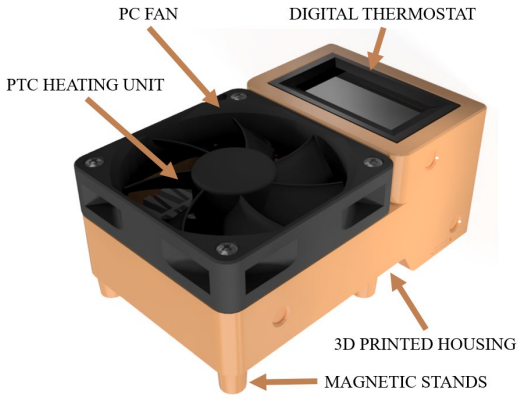

Figure 5. The CAD assembly of the designed heating unit

Introduction to the heated resin printing process
During the assembly process, the heating element was placed inside the housing and connected to the thermostat and power connector. After cutting and finalizing the cable connections, the PC fan was screwed in and the neodymium magnets were glued on. The power supply was provided by a PC power supply. In addition to the power cable from the heating unit, the heat sensor of the thermostat was also led out.

4. HEATING TEST

The first heating test was also performed on the Voxeltek Voxel L Mark IV DLP printer (Fig. 6/I). For the heating unit to be used in the planned research, it must be suitable for stable heating of resin temperatures of 35°C and 45°C. The selected resin temperature values were determined based on the reviewed papers. For the test, a thermocouple was placed above the stage, which is sink in the resin. (Fig. 6/II.) (Dall'Argine, 2020) (Steyrer, 2018) (Peer, 2018).

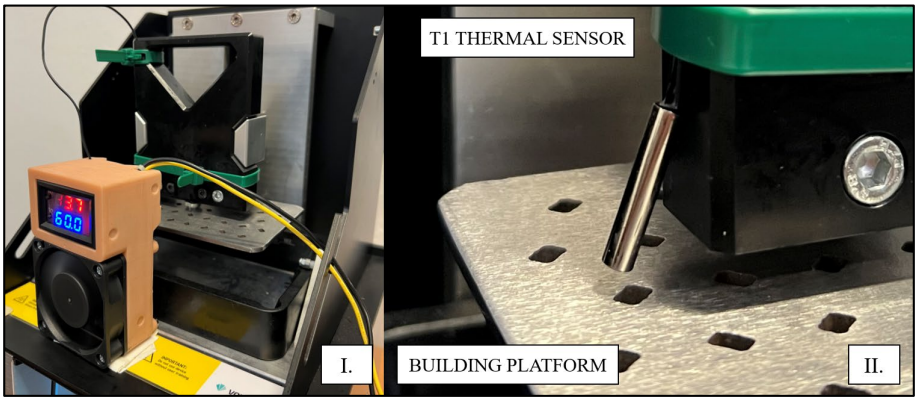

Figure 6. The fixed heating unit I. (left), and the T1 thermal sensor for measuring resin temperature II. (right)

The model sliced for printing using with the machine's online slicer interface, where the orientation of the test specimens and the printing parameters were settled (Fig. 7.). The samples were printed in three different orientations, as the planned future research will also examine the effect of the orientation. Therefore, it was important to make sure of the quality of the products printed in different orientations (Vasilescu, 2019).

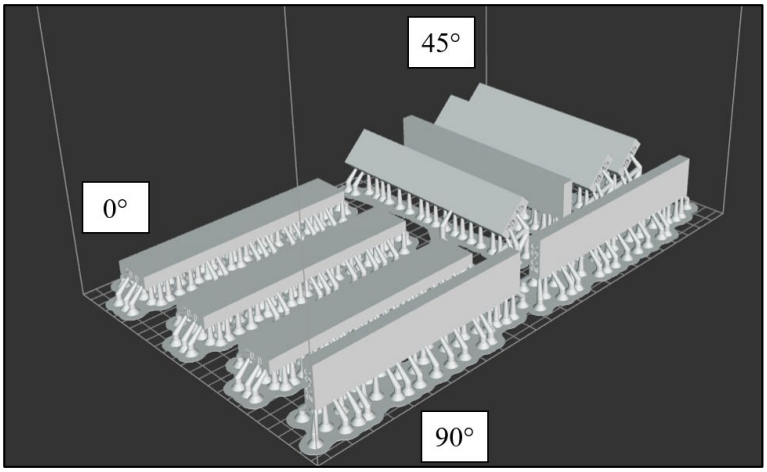

Figure 7. Specimens placed in different orientations in the slicing software

Fig. 7. shows specimens placed in different orientations in the slicing software. It can be clearly seen that all the specimens were printed using support material. In any case, the 45° orientation required support due to its printability, so in order to match the specimens, the other two orientations were also supported. Before starting the printing, the printer was calibrated at Z=0 mm, and the equipment was water leveled. In each case, the temperature sensor was fixed to the slide to check the temperature. After shaking and loading the resin, a few minutes could elapse for the air bubbles generated during shaking to disappear from the material. Printing of the room temperature pieces was performed first (Fig. 8.).

Figure 8. The display of the 3D printer at the start of printing (I.) left, and the continuously monitored resin temperature (II.) right

To reach the second and third temperatures, the heating unit was mounted, and then a few minutes of preheating were required to bring the entire work area, slide table, and resin up to the set temperature. Once the whole system was stable at the desired temperature, the printing process of the test pieces were started. Printing at room temperature setting took 28 minutes. The heat-up times were added to this base value. With the heating unit, the resin temperature reached 35°C in 5 minutes (+11%). At 45°C, this time was 9 minutes (+20%). According to the monitoring, the temperature could be said to be stable. The designed heating unit is thus suitable for maintaining the temperatures to be used for future experiments (Pfaffinger, 2018).

Conclusions

The aim of the research work was to change the temperature of the resin used during DLP printing process under controlled conditions. The present research has been resulted in the implementation and validation of a heating unit that provides the device background for hot lithography processes. Based on the measurements, the heating unit kept the expected resin temperature stable. Heating of photopolymer systems has been shown to affect the polymerization rate due to the resin's decreasing viscosity. The "Hot Lithography" process allows for the improvement of mechanical properties of parts by increasing monomer mobility and enhancing the process conversion rate. While numerous researchers have studied the beneficial properties of temperature on the mechanical properties of printed parts, the influence of other process parameters has not been comprehensively examined. In future research, it is planned to investigate the main effects and interactions affecting the production process using a complex experimental design.

References

[1] Kun, K. (2020). Technológiai paraméterek hatása Digital Light Processing 3D nyomtatási eljárásnál= Effects of Technological Parameters on Digital Light Processing 3D Printing. GRADUS, 7(2), 374-379.

[2] Šafka, J., Seidl, M., Kovalenko, I., Voleský, L., Ackermann, M., & Truxová, V. (2020). Ceramic 3d printing: Comparison of SLA and DLP technologies. MM Science Journal.

[3] Zguris, Z. (2016). How mechanical properties of stereolithography 3D prints are affected by UV curing. Formlabs White Paper, 1-11.

[4] Vasilescu, M. D. (2019). On the technological and dimensional considerations for generating parts by 3D-printed with light processing focus. Scientific Bulletin" Mircea cel Batran" Naval Academy, 22(1), 1-9.

[5] Monzón, M., Ortega, Z., Hernández, A., Paz, R., & Ortega, F. (2017). Anisotropy of photopolymer parts made by digital light processing. Materials, 10(1), 64.

[6] Frank, C., Hager, K., Csizmadia, R., Kury, M., & Gorsche, C. (2022). Hot Lithography-High precision 3D printing of flame-retardant photopolymers for the electronics industry.

[7] Dall'Argine, C., Hochwallner, A., Klikovits, N., Liska, R., Stampf, J., & Sangermano, M. (2020). Hot-Lithography SLA-3D Printing of Epoxy Resin. Macromolecular Materials and Engineering, 305(10), 2000325.

[8] Steyrer, B., Busetti, B., Harakály, G., Liska, R., & Stampfl, J. (2018). Hot Lithography vs. room temperature DLP 3D-printing of a dimethacrylate. Additive Manufacturing, 21, 209-214.

[9] Peer, G., Dorfinger, P., Koch, T., Stampfl, J., Gorsche, C., & Liska, R. (2018). Photopolymerization of cyclopolymerizable monomers and their application in hot lithography. Macromolecules, 51(22), 9344-9353.

[10] Manufactur3D. (2018). The Difference between DLP and SLA 3D Printing Technology, Online source (last viewed on: 27.03.2024): https://manufactur3dmag.com/difference-dlp-sla/

[11] Patel, G. (2021). Difference between DLP and SLA, Online source (last viewed on: 27.03.2024): https://www.linkedin.com/pulse/difference-between-dlp-sla-gaurav-patel

[12] Pfaffinger, M. (2018). Hot Lithography–New Possibilities in Polymer 3D Printing: A newly developed stereolithography-based additive manufacturing technology combines good material properties with outstanding manufacturing precision. Laser Technik Journal, 15(4), 45-47.

Preparations for the machinability test of 3D metal printed parts

Sándor FENYVESI[1,3], Róbert Zsolt KERESZTES[2], László ZSIDAI[2]
[1] *Department of Mechanical Engineering,*
Faculty of Engineering and Information Technology, University of Pécs
[2] *Department of Materials Science and Engineering Processes, Institute of Technology,* Hungarian *University of Agriculture and Life Sciences*, MATE, Gödöllő
[3] *Doctoral School of Mechanical Engineering,* MATE, Gödöllő

Abstract

This study aims to present the preparation process of machinability testing of 3D printed metal parts. The preparation of measurements primarily involves the software-supported method of temperature measurement. Determining the size of the sample, conducting a test measurement for temperature, and establishing its parameters are key steps in setting up the appropriate machining process. The further details of the abstract focus on designing experiments and interpreting results, highlighting the importance of the study in the manufacturing of metal parts. Overall, the study aims to prepare for further experiments to be carried out as efficiently and smoothly as possible.

Keywords

3D metal printing, machinability of metal parts, measurement of machining temperature, surface roughness, machining parameters

1. Introduction

3D metal printing is one of the most innovative technologies of our time, allowing for the rapid and efficient production of complex geometric components. This type of metal printing is an additive manufacturing process, meaning that three-dimensional objects are produced layer by layer (Johnnie Liew Zhong Li, 2019). When it comes to the production of metal components, there are four classes available, which include additive technologies. In the context of this analysis, the specific approach to the production technology of additive metal components using Direct Energy Deposition will be examined, with a particular focus on the Wire-Arc AM (WAAM) process and its modified variations. Figure 1 illustrates the schematic of WAAM-CMT.

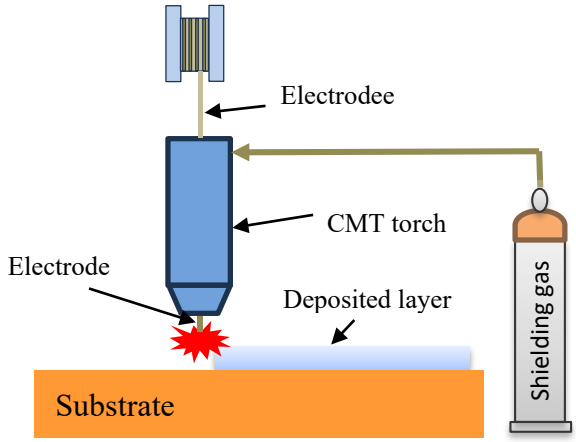

Figure 1. Schematic representation of the WAAM-CMT technology.

During the Cold Metal Transfer (CMT) process, the welding gun's wire electrode comes into contact with the molten metal, and the "robacter drive" servo motor changes direction with digital process control, facilitating droplet transfer and wire retraction. As the metal transfer occurs, the current decreases close to zero, thus preventing spattering. After the transfer is complete, the arc re-ignites and the wire is fed forward again by the set welding current flow.

The correct adjustment of printing parameters, which affect the physical and mechanical properties of the component, is an important aspect in 3D metal printing. The advancement of 3D metal printing technology has enabled the production of increasingly complex and precise components. However, additional processing, such as machining, is often necessary for these components to achieve the desired final shape and dimensions. During the machining process, it is important to maintain the appropriate temperature, monitor tool wear and tool life, and achieve the desired size, shape, and surface roughness of the component.

We will provide detailed information on the use of software and the results when presenting our research findings. In the process, we will strive to apply modern and efficient solutions to improve the machinability of 3D printed metal components. A thermocouple can be used to measure the machining temperature, allowing us to monitor the process. Therefore, we will dedicate special attention to a software dedicated to this task, enabling precise and efficient thermocouple measurements. With the help of this software, we plan to perform a trial measurement of machining temperature and determine its parameters based on the dimensions of the sample piece. These data will serve as the basis for further optimization of the machining process and quality improvement.

During the preparations, we conducted a trial measurement on commercially available C45 material quality to test the measurement method and necessary technical conditions. During the trial measurements, we examined the relationship between different machining settings, machining temperature, and surface roughness.

In this study, we present the results of the trial measurements and provide detailed explanations of the measurements and analyses carried out during the machining process. We will reference previous research and expert opinions in order to provide readers with appropriate and reliable results. In the following chapters, we will present in detail the methods, results, and conclusions of the trial measurements.

2. Materials

C45 steel

The experiments were carried out on pre-manufactured round steel made of C45 carbon steel. The pre-manufactured material, with a carbon content of 0.43-0.50%, falls into the category of medium carbon and medium tensile strength steels, which are often used in machining operations. C45 is easy to machine, allowing for the easy production of various components and test specimens.

Samples made of C45 steel are used by many manufacturing companies, and this material is standardized, commercially available, with guaranteed chemical composition and mechanical properties (A Panda, 2016). The chemical composition of C45 steel is included in Table 1.

Table 1. Chemical composition of C45 material (Numbers, 2024)

C	Si	Mn	S	P	Kr	Mo	Ni	Al	Cu	Fe
0,45	0,25	0,65	0,025	0,008	0.4	0.1	0.4	0,01	0.17	Bal.

Presentation of material quality for printed materials

The current research focuses on printing components using AlMg4.5Mn0.7 (EN AW-5083) material, with a diameter of 60 mm and a length of 130 mm. The chemical composition of the component is shown in Table 2.

Table 2. Main Characteristics of Material Quality EN AW-5083 (Numbers, 2024)

Material number (DIN EN 573)	Short symbol (DIN EN 573)	Tensile strength Rm [MPa]	Proof stress Rp0,2 [MPa]	Surface finish
EN AW-5083	AlMg4,5Mn	>275	>125	mill-finish

This is a material of medium strength, highly resistant to chemicals and does not harden. It has excellent polishability and very good corrosion resistance. The weldability of the material is adequate, as supported by the research of Dudzik and colleagues (Dudzik, 2011). Welded joints and components printed from welded joints have almost the same corrosion resistance as the base material, as stated in the research of Zoltán Meiszterics and colleagues (Zoltán Meiszterics, 2019). Suitable for structures with medium loads that are resistant to corrosion and seawater. Used in the food and chemical industry, construction industry (outdoor and indoor architectural elements), automotive industry, and shipbuilding (Bouhamed, 2021).

Tool and Machine

The experiments were conducted on an OPTIMUM TH4210 universal lathe machine. The machine's power is 4.5 kW, the maximum speed of the machine is 1800 rpm. The range of feed rate is 0.05 - 1.7 mm/rev. The machine is equipped with a coolant system, but due to the dry machining requirements of the experiments, its use was not necessary. The experiments were conducted using coated tools. The tools are distributed by SECO. The insert is identified as CCMT09T308W-F1 TP1501. The tool holder knife shank is also from SECO. The tool holder is of type SCLC R 1616 J09, which has modifications for inserting the thermocouple.

Surface roughness gauge

For the measurement of surface roughness on individual test pieces, a Mitutoyo SJ-201 type tool was used.

Thermocouple and Data Logger

The thermocouple is one of the most widely used experimental methods for measuring temperature during machining, however, it only measures the temperature at the contact surface of the tool and workpiece. Grzesik investigated the effect of tool-workpiece surface temperature when machining with AISI 1045 and AISI 304 coated tools (Grzesik, 2005). Meanwhile, O'Sullivan measured the temperature of the machined surface using two thermocouples placed in the workpiece during machining of 6082-T6 aluminum (O'Sullivan, 2001).

Table 3. Main characteristics of K-type thermal elements. (TC Méréstechnikai Kft.,, 2024)

Conductor combination		Thermal stress variation µV/0°C		The approximate operating temperature range of the measuring point		
+ pin	- pin	100 °C	500 °C	1000 °C	Continuous use	Short-term use
Nickel-Chromium Also known as: Chromel™, Thermokanthal KP*, NiCr, T1*, Tophel™	Nickel-Aluminum (magnetic) Also known as: Ni-Al, Alumel™, Thermokanthal KN™, T2™, NiAl™	42	43	39	0…+1100 °C	-180…+1350 °C

During the experiment, a K-type thermocouple was used, whose main characteristics are included in Table 3. For processing the sensor signals, an Arduino Uno R3 development board, and a MAX6675 interface module for connecting the sensor were used. The development board is suitable for performing real-time data collection tasks as hardware, but the software environment needs to be prepared according to the specific tasks.

3. Methods

Scope of 3D metal printing issues

According to Gyula Ferenc Vasvári (2021), there has been no demand for solid object printing on the 3D metal printer developed by the research group at PTE. The components printed so far have thin walls and meet the requirements of mechanical tests. In my case, in order for the component to be machinable, fine-tuning of the printing parameters was necessary.

Cold Metal Transfer (CMT) welding is a suitable process for additive manufacturing (AM). It is a modified version of the MIG welding process. Figure 2 shows the 3D printer developed by the research group at PTE and a component in a printed state.

Figure 2. 3D metal printer developed by the research group of the Faculty of Engineering and Computer Science at the University of Pécs. (Gyula Ferenc Vasvári, 2021)

The components required for my experiments have a diameter of 60 mm and a length of 130 mm. Significant heat transfer occurred in components of this size, resulting in skewness and visible material discontinuities. Keeping this in mind, it became necessary to adjust the parameters of the CMT welding, which forms the basis of metal printing. This requires a variable that can be controlled to carry out the experiments. Therefore, the settings for welding and printing were modified, applying a current of 150 A in the first 30 rows and 135 A in subsequent rows, while keeping the other parameters constant. The values of the 3D metal printing settings are presented in Table 4.

Table 4. Settings used in 3D metal printing

Characteristic	Value	Unit of measurement
Welding current	59-110	[A]
Welding speed	6.2	[mm/sec]
Argon gas flow rate	15	[liter/min]

Measuring with thermal elements

For the execution of experiments, it is necessary to place the sensor, the K-type thermocouple, as close as possible to the machining zone. For future experiments, I also intend to monitor the wear level on the insert, therefore the sensor was installed into the tool holder. The schematic diagram of the sensor installation can be seen in Figure 3. One of the key issues in embedding the thermocouple is the difficulty in determining the position of the hole. The main reason for this is that the contact point between the tool and the chip changes constantly during machining due to changes in cutting speed, feed rate, and

depth of cut (Korkut, 2007), (Sisodiya, 1996). The work of (Cichosz P, 2023) serves as a reference for selecting the position of the thermocouple.

1.

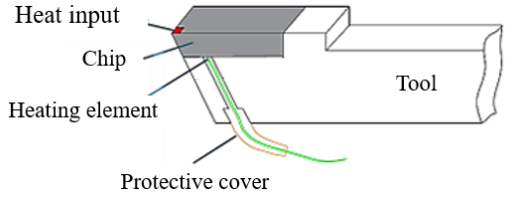

Figure 3. Schematic diagram of sensor placement

The heat element located under the chip is unable to accurately measure the temperature of the machining process, as the environment, the chip, and the coating of the chip all contribute to losses. Guimarães and colleagues applied a sensor integrated into the chip (Guimarães B, 2023), which allows for a more precise approximation of the machining temperature compared to my solution. During my experiments, determining the exact machining temperature was not the primary focus, but rather tracking the magnitude of temperature changes.

The complete configuration of the measuring system hardware is shown in Figure 4.

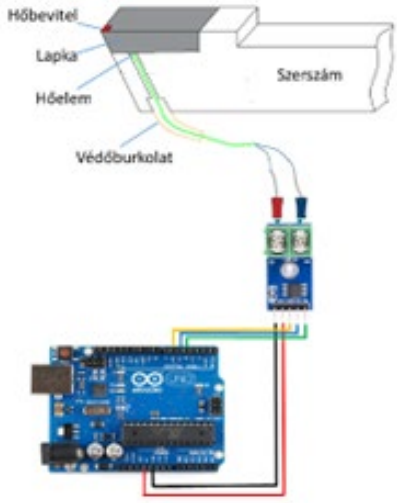

Figure 4. Schematic diagram of the hardware assembly of the measurement *system*

Considering the common exception of frequent plate replacement, the above method proved to be appropriate for determining the extent of wear and tear. The accuracy of the tool temperature measurements conducted with a K-type thermocouple data logger system for the examination was ±2.5 °C or ±1%.

Cutting

The primary considerations in selecting the machining parameters were the recommendations of the tool manufacturer and distributor. Based on the manufacturer's recommendations (Seco Tools, 2024), an axial feed rate of 0.08-0.32 mm/rev and a cutting speed of 94-247 m/min were suggested for the C45 material quality and the TP1501 cutting edge material quality. Taking into account the recommended parameters, the technological data selection was made, resulting in the determination of a cutting speed of 94; 113; 147 m/min and an axial feed rate of 0.08; 0.14; 0.2 mm/rev. The details of the machining parameters used in the study are presented in Table 5.

Table 5. Technological parameters used during the experiments (abstract)

Experiment number	Diameter [mm]	a_p [mm]	Rotational speed [1/perc]	Cutting speed [m/perc]	Feed rate [mm/ford]	Temperature [T]	Surface roughness [µm]
1.	40	0.5	1170	147	0.35		
2.	40	0.5	900	113	0.35		
3.	40	0.5	770	97	0.35		
4.	40	0.5	1170	147	0.2		
5.	40	0.5	900	113	0.2		
6.	40	0.5	770	97	0.2		

A total of 27 machining experiments were conducted, which were repeated three times to investigate reproducibility.

Software

I carried out the software development in Visual Studio IDE, using the C# programming language and as a Windows Form Application. Figure 5 shows a simplified block diagram of the measurement system. It consists of a K-type sensor, a MAX6675 interface, which connects to the Arduino Uno. The USB interface is used to transmit sensor data and identification data to the computer for plug and play access.

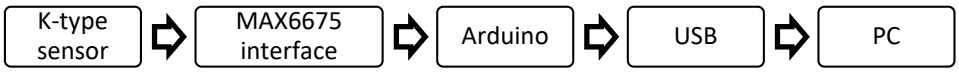

Figure 5. Block diagram of the measurement system

The system software is organized and implemented in two modules, one software module runs on the PC, while the other part runs on the Arduino Uno board. The two modules communicate with each other to achieve the plug and play concept for the purpose of the current research.

The experiment is based on temperature measurement during machining. The processing of the data from the heat element built into the tool holder is done through an Arduino development board and a MAX6675 interface unit. Setting and controlling the necessary characteristics for operating the measuring system and conducting the experiments can distract attention from more important points, so I have developed a software specifically designed for temperature measurement during machining.

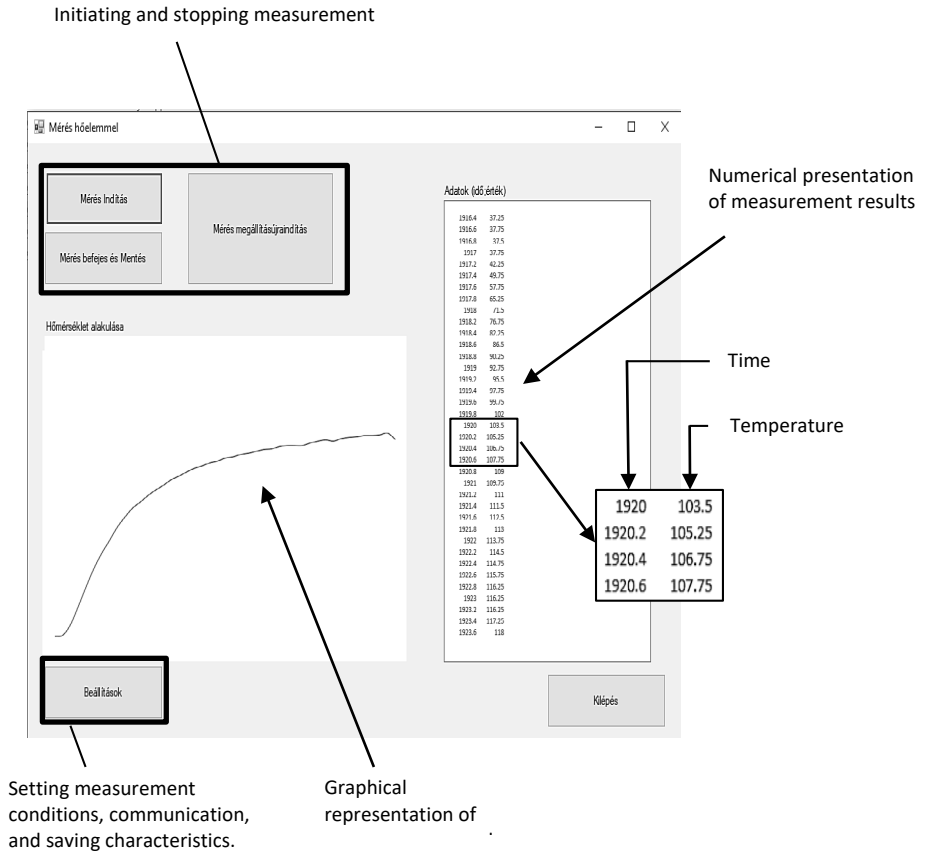

Figure 6. Snapshot of the operation of the measurement software

The software snapshot can be seen in Figure 6. In terms of operation, I aimed for the simplest and most user-friendly interface. On the interface, there is a button to start and stop measurements. The instantaneous values of the measurement results can be tracked on the right side. Here, two columns are visible, the first column indicates time in seconds, and the second column shows the temperature. In the window on the left side of Figure 6, the measurement results are displayed graphically. The measurement results and the graph are displayed in real-time during the measurement to inform the operator. The

Settings button contains the necessary settings for the measurement and for specifying the characteristics of saving files. The measurement results are stored in CSV files for further data processing. One of the most important setting parameters during the measurement is the sampling time, which can be set in this menu.

4. Results of the investigations

I will discuss the results of the investigations separately, as they have different content, but they may not necessarily have a direct connection with each other.

3D printed metal component

The desired shape and size of the metal printed component was achieved through modifications of the respective parameters, resulting in the creation of a test specimen with a diameter of 60 mm and a height of 130 mm. The photograph of the test specimen created with the modified parameters can be seen in Figure 7.

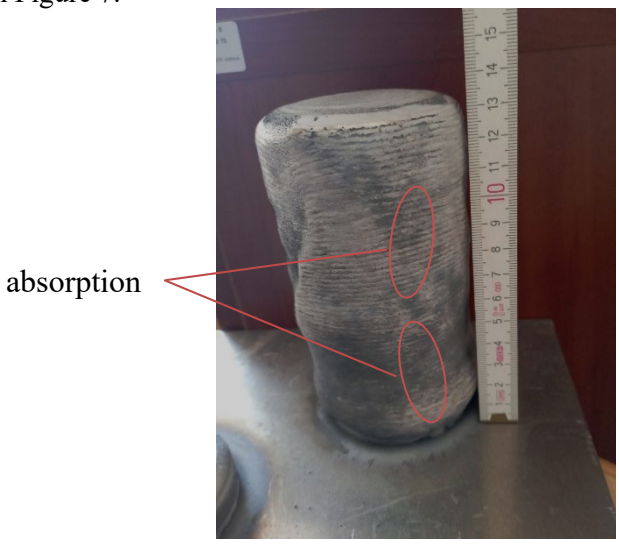

Figure 7. 3D metal printed test specimen

The characteristics of the specimen presented in Figure 7 are detailed in Table 6.

Table 6. Characteristics of the 3D metal printed test specimen

Characteristics	Size	Unit of measurement
Height	130	[mm]
Diameter	60	[mm]
Average surface roughness	25-38	[µm]

In addition to the characteristics listed in Table 6, there are several absorptions on the test piece, which can also be seen in Figure 7. These absorptions do not affect the conduct of further experiments, but require further parameter tuning to bring the surface of the preform closer to the nominal size and shape.

The current quality is suitable for the machining experiment prototype, but further research is needed for 3D metal printing to truly fulfill its cost- and energy-efficient role. At present, the enclosure dimensions are adequate, but the dimensional tolerances are not. It would be advisable to examine the location and nature of temperature distribution during printing, as well as how airflows develop during printing in the laboratory and near the printer station, which may cause absorptions.

Software

During the initial experiments, the measurement could be performed through the arduino IDE. The results of the experiment could be accessed through the arduino serial port, with the help of another software (Putty). Then, the data had to be saved in a recognizable manner in an appropriate location. This was a slow and complex process that diverted attention from the experiment itself. When using the software during the experiment, personal overload ceased, meaning that starting the measurement, tracking the results and graphical follow-up of the results became possible, as well as archiving the measurement results. In addition to the usage, another requirement arose, which was to display the identifier of the current measurement in the software window, making it easier to record and evaluate research results.

Machining Experiment

One of the first results of the machining experiment is the determination of the time for thermal equilibrium between the participating units in machining. The diagram of the thermal equilibrium in the machining experiment is presented in Figure 8.

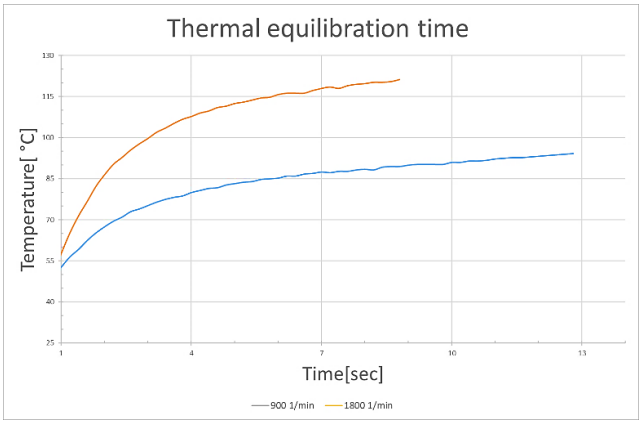

Figure 8. Heat balance during machining

During machining, heat is generated, and after heat conduction between the individual objects and heat dissipation to the surroundings through heat flow, thermal equilibrium is approached. The process of thermal equilibrium takes approximately 5-6 seconds, meaning that measurements need to last for 5-6 seconds for their temperatures to be comparable. By plotting cutting speed, temperature, and surface roughness on a diagram, it can be seen that with increasing cutting speed (130m/min -> 230m/min), the temperature (98 °C -> 120 °C) also increases, although not as intensively as the surface roughness changes (2.94 µm -> 1.9 µm). The relationships between cutting speed, temperature, and surface roughness are illustrated in Figure 9.

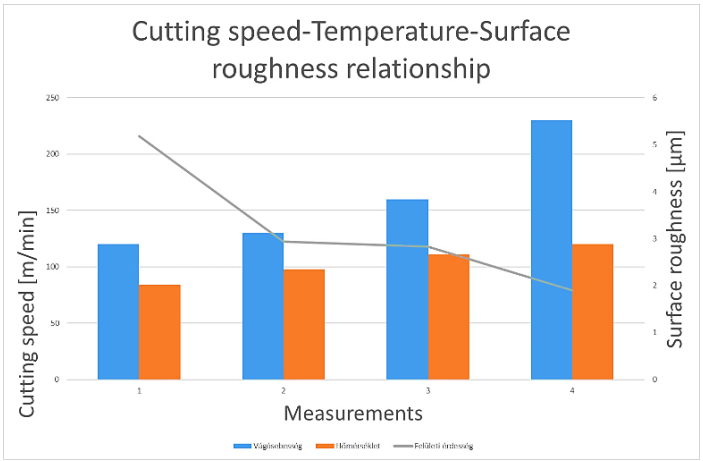

Figure 9. Relationship between cutting speed, temperature, and surface roughness according to the requirements of technical scientific writings

Based on the results and Figure 9, it can be stated that choosing a cutting speed higher than 150 m/min is worth considering, as the surface roughness evolution is favourable compared to the temperature change.

Further tasks

The current research highlights that the proposed methods work effectively, preparing for further measurements in the research. These methods form the basic pillars of the study of aluminium machinability, easily implementable there, and the operation of the measuring circuit is expected to continue without modification, the measurements can be carried out.

Acknowledgements

I would like to express my gratitude to Tamás Zsebe and Dr. Dávid Ciprián Csonka, who produced the metal printing for me. Without their assistance, it would not have been possible for me to complete the given scientific manuscript. I am very grateful for their expertise and precision

Summary

The trends of the results of my experiments with C45 material are similar to those reported by Paese and colleagues (Paese E, 2020). The similarity of the trends in the results supports the correctness of my experiment, which also implies the accuracy of the measuring system. Based on the experimental results, it can be concluded that the main targeted experiment, the 3D metal printed AlMg4.5Mn0.7 (EN AW-5083) material quality, can be created in the desired size through printing, and the possibility of the proper use of the measuring system is confirmed

References

[1] A Panda, J. D. (2016). Research on the durability of selected cutting materials in the process of turning carbon steel. *MM Sci. J*, 1086-1089.

[2] Bouhamed, A. M. (2021). Experimental and numerical methodology to characterize 5083-aluminium behavior considering non-associated plasticity model coupled with isotropic ductile damage. *International Journal of Solids and Structures*.

[3] Cichosz P, K. P. (2023). Review of Cutting Temperature Measurement Methods. *Materials*.

[4] Dudzik, K. (2011). Mechanical properties of 5083, 5059 and 7020 aluminium alloys and their joints welded by MIG. *Journal of KONES*, 73-77.

[5] Grzesik, W. M. (2005). Finite element modelling of temperature distribution in the cutting zone in turning processes with differently coated tools. *ournal of Materials Processing Technology*, 1204-1211.

[6] Guimarães B, R. J. (2023). Real-Time Cutting Temperature Measurement in Turning of AISI 1045 Steel through an Embedded Thermocouple—A Comparative Study with Infrared Thermography. *Journal of Manufacturing and Materials Processing*.

[7] Gyula Ferenc Vasvári, D. C. (2021). CMT Additive Manufacturing Parameters Defining Aluminium Alloy Object Geometry and Mechanical Properties. *Materials*(https://doi.org/10.3390/ma14061545).

[8] Johnnie Liew Zhong Li, M. R. (2019). Review of Wire Arc Additive Manufacturing for 3D Metal Printing. *International Journal of Automation Technology, 13*, 346-353.

[9] Korkut, I. B. (2007). Investigation of chip-back temperature during machining depending on cutting parameters. *Materials & design*.

[10] Numbers, S. (2024, 01 2024.01.18). Retrieved from https://www.steelnumber.com/en/steel_composition_eu.php?name_id=152

[11] O'Sullivan, D. &. (2001). Temperature measurement in single point turning. *Journal of materials processing technology*. Retrieved from https://doi.org/10.1016/S0924-0136(01)00853-6

[12] Paese E, G. M. (2020). Assessment of CVD- and PVD-Coated Carbides and PVD-Coated Cermet Inserts in the Optimization of Surface Roughness in Turning of AISI 1045 Steel. *Materials*.

[13] *Seco Tools*. (2024). Retrieved from https://www.secotools.com/

[14] Sisodiya, M. S. (1996). Experimental Analysis of chip-back temperature during machining depending on cutting parameters. *IOSR Journal of Mechanical and Civil Engineering*, 158-164 .

[15] *TC Méréstechnikai Kft.,*. (2024, 01 18). Retrieved from https://www.tckft.hu/thermocouples/type-k-thermocouple.html

[16] Zoltán Meiszterics, A. A. (2019). Scanning Electrochemical Microscopy (SECM) Investigation of 3D Printed Parts Produced by CMT Welding Technology. *Electroanalysis*. Retrieved from https://doi.org/10.1002/elan.201900678

Design and manufacturing of the components of a mechanical seal testing bench

Marcell KISS[1,2], Gábor KALÁCSKA[1]
[1] *Department of Materials Science and Engineering Processes, Institute of Technology, Hungarian University of Agriculture and Life Sciences*, MATE, Gödöllő
[2] *Doctoral School of Mechanical Engineering*, MATE, Gödöllő

Abstract

Designing and manufacturing of a measuring bench suitable for measuring and testing mechanical seals, then assembling the measuring bench. Carrying out the necessary operations on the purchased parts using a lathe and coordinate drilling machine. Machining and assembly of two separate shafts into the existing drive system. Testing bench assembly.

Keywords

mechanical seal, machining, processing, assembly

1. Introduction

Pumps are used to transport and raise fluids in all areas of life, such as industry, energy, agriculture and residential care. In pumps, mechanical seals are used to prevent or control leakage of the fluid being pumped. Slip ring seals have become the exclusive solution for shaft seals in pumps. The different types of seals and the materials of the sliding rings solve the problem of sealing the pumps for any medium to be transported, such as cold and hot water, mineral and synthetic oils, mild or aggressive acids and alkalis, chemicals. The mechanical seals are under continuous development not only to find better solutions, material combinations and lubricants for a wide range of extreme operating conditions, but we are also looking for new, more favorable solutions for current, general and everyday conditions. They develop new seals that are more reliable, cheaper and more durable than their previous types. (MAYER, Ehrhard 2013) In my research topic, I will examine polymer and ceramic composite slip ring seals on a measuring bench designed by me. During the design of the measuring bench, we took into account many parameters, such as the use of different media, the possible change of the spring force that compresses the sealing rings, and the possibilities of measuring at different speeds. (Huebner M. 2005)

2. Experimantal

I I started the planning phase with my supervisor by first defining what and how we will be able to measure. We had an earlier measuring bench available, where we cannot use the entire equipment, so certain parts of it had to be modified. We can use the electric drive from the previous bench, but the section after the clutch had to be completely rethought. I then created concept plans, which I always improved and developed during continuous consultation. In the end, a version was created that we decided would be suitable for taking measurements, so I procure the raw materials, manufacture the parts in the workshop, and then assemble the measuring bench.

The first task was to procure the raw materials. I assemble the measuring bench from several parts, which consists of pipe pieces with an internal diameter of 60 mm, a length of 60 mm and a length of 150 mm, a blind flange EN 1092-1 DN 50 PN 16 and a flange with a threaded connection and threaded caps that can be fitted to the 60 pipes. Once these parts were available in the workshop, I started making the necessary modifications to the parts. I mainly performed the production processes on a lathe and a coordinate drilling machine. The employee in the workshop helped me a lot with setting up and using the machining machines, as I had no such experience before. (KHATAI, 2022)

The parts are made of acid-resistant and corrosion-resistant steel. Processing them requires much more skill, experience and patience than other, softer materials. First, I performed the necessary machining processes on the blind flange, which meant that a 10mm shaft bearing had to be drilled on the non-sealing side of the blind flange. The hole had to be formed on the other side of the blind flange for the stator of the slip ring seal. Next, I had to make a 10mm through hole in the middle of the blind flange for the acid-proof shaft, to which I will be able to attach the rotor part of the slip ring. (Sales, 2020)

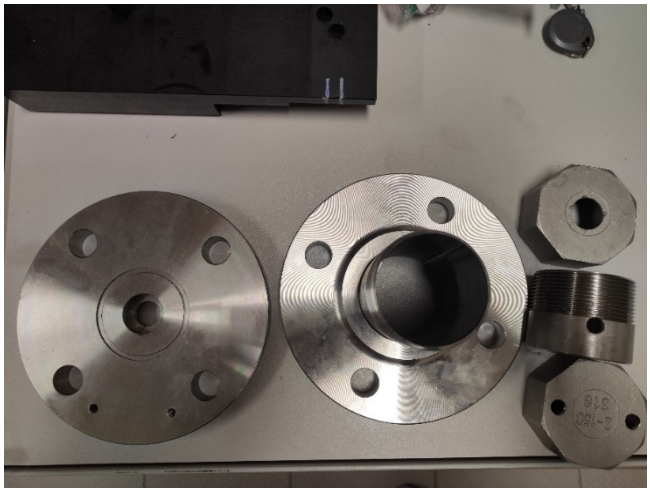

Figure 1. acid-resistant parts after machining

On the following parts, which were a piece of 60 mm pipe and two matching threaded caps, I only had to perform one operation each. I made a 16 mm through hole on one cap, through which the acid-proof shaft will pass towards the electric drive, on the other hand I made 2 threaded holes of 8 mm, because the liquids will flow through these holes, so that the seals are acidic and I can examine it in an alkaline medium. I will be able to attach Festo-type threaded connectors to the holes, through which I will be able to flow the media to be tested. Figure 1 shows the finished parts

The shaft on which I will place the mechanical seals consists of two separate materials. The part where the sliding ring seal will be attached must be made of acid-resistant steel, while the other half, which will be located in the bearing housing, is made of high-speed steel, material S355. This type of steel can be easily machined and withstands higher stresses. Since two separate shafts have to be manufactured and centering is important, more serious solutions had to be used for machining and connecting the shafts. Of the two axles, I made the S355 axle first, which will go into the necessary bearing housing. The largest diameter of this shaft is 55 mm, and I make it from a 60 bar material. Since there was already an axle in the bearing housing before, but I didn't plan to make any modifications to it, because it might be needed in the future, so I had to manufacture that axle one by one. I did the cutting on a lathe. I had to use several types of lathe tools, the turning speed of the lathe was 500 rpm, and the depth of cut was 1.5 mm. This is how I went down to the required dimensions, and then took smoothing grips where the 50 bearings are located on the shaft. I had to make a 24 diameter thread for the end of the shaft that will connect to the flexible coupling. The acid-resistant smaller shaft is connected to the other end of the shaft. This shaft has a diameter of 12 mm. In order to be able to assemble the two shafts centrally, I made a matching hole. After the larger shaft made of S355 material was ready, the smaller one followed. On the acid-resistant shaft, I first made the threaded connection to the matched hole, and then put the two shafts together. Thus, I inserted the two axes in the assembled state into the lathe. I clamped the larger S355 shaft in the chuck, then where the bearing will be located on the larger shaft, I dummied the shaft. This was necessary so that the larger axis would not hit, i.e. it would rotate centrally. This is how I was able to perform the necessary operations on the smaller axis. After I chipped off the excess material from the acid-proof shaft, I had a perfectly centered rotating shaft, with the smaller shaft rotating along with the larger shaft. This is important because a small 10 mm bearing will be located in the blind flange, through which the acid-proof shaft passes, and it can only minimally absorb side impacts. Once the two axles were ready, I started assembling the bearing housing with the new axle. After I managed to assemble it, I put it in place, on the measuring bench. In the assembled state shown in figure 2 below.

Figure 2. new shaft in the old bearing housing

The measuring bench will be held by a bearing housing with a diameter of 60, which I will attach to a plastic sheet. I designed the plastic sheet in the Solid Edge program and with the help of teacher we manufactured it with the CNC milling machine.

3. Next steps

TThe measuring bench is fully completed. The next task is to start the reference measurements. I will perform the reference measurements with carbon and silicon carbide seals. The research area has changed in that I will not be flowing liquids when testing the sealing pairs, but rather the effect of mars dust. On figure 3, we can see the assembled testing bench.

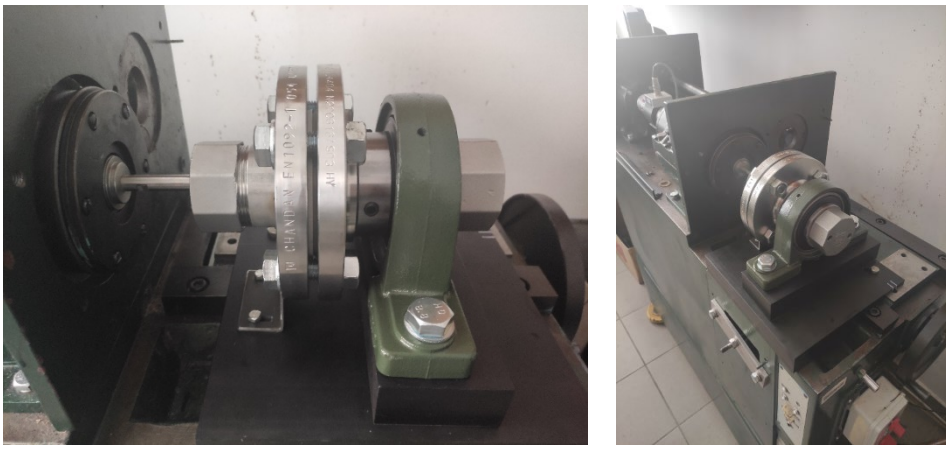

Figure 3. Assembled measurement bench

At the beginning of each measurement, I will perform morphology tests on the surface of the slip ring seals. Once these are done, I insert them into the measuring bench. Two main measurements are currently planned: one is the reference measurement and the other is the mars dust measurement. For the reference measurements, I have determined what settings I will use for the tests. Importantly, these settings will also be needed for the Mars dust effect studies. Figure 4 shows a summary table of the measurement parameters.
The main parameters that I will change will be the speed and the spring force that preloads the seals. The speeds will be 50, 75 and 100 rpm, since the vehicles that will be sent to Mars will have components rotating at low speeds.

Reference measurement			Mars dust measurement		
Number of measurement	Rotation per minute [1/min]	Spring force	Number of measurement	Rotation per minute [1/min]	Spring force
1.	50	Recommended	1.	50	Recommended
2.	75		2.	75	
3.	100		3.	100	
4.	50	Recommended >	4.	50	Recommended >
5.	75		5.	75	
6.	100		6.	100	
7.	50	Close to 0 N	7.	50	Close to 0 N
8.	75		8.	75	
9.	100		9.	100	

Figure 4. Measurements overview

At these speeds, I will test what happens to the seals when I vary the spring force. The first setting for the spring force will be the manufacturer's recommended value, then half and finally approaching zero. In all three cases, I will measure the torque generated in the system. I also plan to investigate the thermal evolution, which could be very interesting in the case of near-vacuum air pressure viscosities. I will certainly investigate this case, but I still have to come up with an idea of how to create a vacuum. Once the measurements are done, I will again perform a morphology test on the worn surfaces of the sealing pairs. (ZHOU, 2023), (BAI, 2024) (BAI, 2023)

References

[1] MAYER, Ehrhard. Mechanical seals. Butterworth-Heinemann, 2013.
[2] HUEBNER M. Material selection for mechanical seals, 2005.
[3] SALES, Wisley F., et al. A review of surface integrity in machining of hardened steels. Journal of Manufacturing Processes, 2020, 58: 136-162.
[4] KHATAI, Saswat, et al. On Machining behaviour of various cutting Inserts: A review on hardened steel. Materials Today: Proceedings, 2022, 62: 3485-3492.
[5] ZHOU, Yang, et al. Tribocorrosion behavior of Co-based self-lubricating composites with varying contents of Ag in NaCl solution. Corrosion Communications, 2023, 11: 44-51.
[6] BAI, Jialin, et al. Study on Interface Modification and Tribological Properties of MCMB-SiC Self-lubricating Composites. Tribology International, 2024, 109253.
[7] BAI, Yanying, et al. Strength formation mechanism and curing system optimization of low-carbon cementitious materials prepared by synergistic activation of multiple alkaline solid wastes. Construction and Building Materials, 2023, 402: 132931.

Examination of the load dependence of pneumatic drive's stopping time

Imre KOVÁCS[1], László FÖLDI[1], Eszter MAYERNÉ SÁRKÖZI[1]
[1] *Institute of Technology,*
Hungarian University of Agriculture and Life sciences, MATE, Gödöllő

Abstract

In this paper three sub-safety functions of pneumatic systems are examined and evaluated through simulation tests. These functions are the following safety-related stop functions: Safe Operating Stop (SOS), Safe Stopping and Closing (SSC) and Safe Torque Off (STO), which were implemented using 5/3 way-valves as main valve with different mid-positions. Using these sub-safety functions, the system's stopping time is examined as a function of moving mass and throttle valve opening level. The stopping time difference in the three sub-safety functions is significant, which affects the applicable safety protective distances, thus significantly affecting the size of the equipment.

Keywords

safety of machinery, safety functions, pneumatic drive, stopping time

1. Introduction

Pneumatic drives are widespreadly used in different industrial sectors such as automation, food industry, packaging and material handling (Barner, Bredau és Schiller, 2009). It is also true for pneumatic systems, like all other machinery systems, that their safe operation is a priority, which must be taken into account already in the planning phase. The machines must not only comply with the EC machinery directive (Directive 2006/42/EC), but also must comply with the harmonized standards for the machinery directive (Földi, Berencsi, 2022). The basic standard for machine safety is EN ISO 12100, which describes the risk assessment process, but beyond this there are several safety related standards as well (e.g. ISO 13849, 2016, ISO 13855, 2010, ISO 14120, 2015).

ISO 12100 stipulates that technical protective measures may be necessary to manage risks, if the required level of safety can be achieved by the appropriate application of protective devices and safety functions. An element of this is the risk reduction with safety-related part of a control system, which performs safety functions. One of the most frequently used safety functions is the safety-related stop function initiated by safeguard. The safety-related stop must return the machine to a safe state without delay after operation. There are many types of

this, the practical implementation of which is presented in detail in various technical specifications and reports (Hauke et al., 2009, Hauke et al, 2019). Sub-safety functions applicable to safety related stop of pneumatic systems are described in VDMA 24584: 2019 Technical Rule (Festo Corp., 2022). One of the evaluation aspects of the safety related sub-safety functions is the stopping time. The goal is to achieve the shortest possible stopping time. Reducing it is important because it determines the minimum safety distance that must be between the operator and the actuator performing a dangerous movement (Földi, Mayerné Sárközi, 2022). Three of safety related stop sub-safety functions are examined below, these are:

Safe Operating Stop (SOS). This sub-safety function prevents pneumatic drives from deviating from the stopping position by more than a specified amount. It also maintains the compressed air supply, enabling the drive to withstand the effect of external forces without any further measures. (Festo Corp., 2021).

Safe Torque Off (STO). This sub-safety function separates the power supply to the pneumatic drive, exhausting the cylinder's chambers and preventing the generation of a dangerous force. (Festo Corp., 2021).

Safe stopping and closing (SSC). The supply of energy to or dissipation of energy from at least one chamber of the pneumatic drive is closed, and the stored energy is used to achieve the stop (Festo Corp., 2022).

The aim of this paper is to examine the SOS, SSC and STO sub-safety functions in a pneumatic linear drive as a function of the stopping time under different moving masses and throttle positions.

Nomenclature		
SOS	Safe Operating Stop safety sub-system function	
SSC	Safe stopping and closing safety sub-system function	
STO	Safe Torque Off safety sub-system function	
m	Moving mass	[kg]
T_{OL}	Throttle valve opening level	[%]
T_{SOS} / T_{SSC} / T_{STO}	Overall system stopping time of SOS/SSC/STO sub-safety function	[s]
R^2	Correlation coefficient	-
p_4, p_2	Pressures in cylinder chambers (4- left chamber, 2-right chamber)	[bar]

2. Experimental

A Experimental apparatus and test parameters of SOS sub-safety function

Figure 1. shows the circuit diagram of the pneumatic system with SOS sub-safety function. The used pneumatic cylinder as a linear drive is a double acting rodless cylinder with a slide, type: DGPL-25-450-PPV-A-KF-B, piston diameter: 25 mm, stroke: 450 mm. Since it is a rodless cylinder, its piston

surfaces are identical, so it is a symmetric actuator. For velocity control two one-way flow control valves (type: GRLA-1/8-QS-6-D) are installed, with throttling effect in the actual exhausting line, implementing secondary speed control.

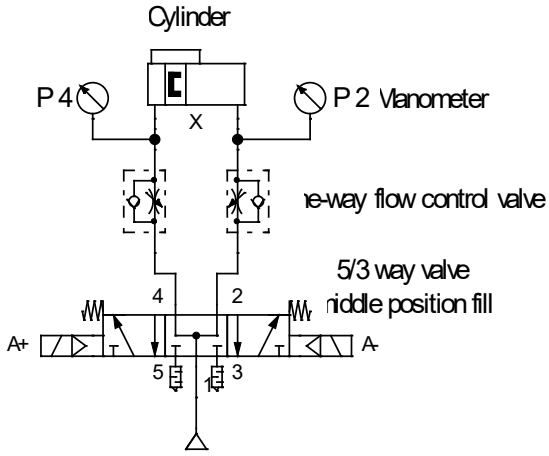

Figure 1. Pneumatic circuit diagram of the examined drive with SOS sub-safety function

The applied main valve is a monostable, pilot operated solenoid 5/3 way-valve with different middle positions for the various sub-safety functions. In case of SOS function in the middle position of the 5/3 way valve both of cylinder chambers get the operating pressure, valve type: VSVA-B-P53U-H-A2-1R5L. The used operating pressure is 6 bar.

The test cycle is the following: first the A+ valve solenoid gets a control signal, causing the main valve to switch to its left position. The left cylinder chamber's begins to fill, the right chamber begins to exhaust through the one-way flow control valve. When the sufficient force is established, the movement of piston starts. As soon as the piston reaches half of its stroke, the stopping trigger is activated. Then the control signal of A+ valve solenoid is turn off, the main valve switches to its middle position. In this switching position the examined stopping function is activated.

The system variables are the moving mass and the throttle valve opening level, while the measured parameters are the stroke the and velocity of the piston, and the chamber pressures as a function of time. During the tests steel on steel surfaces are examined, the value of the static friction factor is 0.15 and the value of the sliding friction factor is 0.1. The simulations were implemented in Festo FluidSim-P 4.2 software.

Experimental apparatus and test parameters of SSC sub-safety function

Figure 2. shows the circuit diagram of the pneumatic system with SSC sub-safety function.

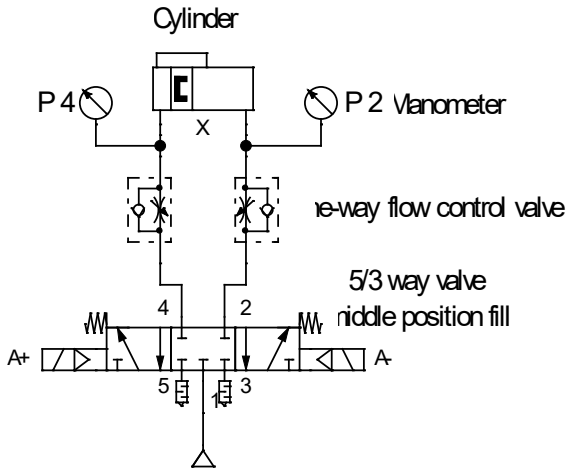

Figure 2. Pneumatic circuit diagram of the examined drive with SSC sub-safety function

In the case of the SSC sub-safety function, all system and test parameters are the same as those of the SOS function, except for the middle position of the 5/3 way-valve that implements the safety function. In SSC function in the middle position of the 5/3 way-valve both working ports are closed, so the air that is present is locked inside the chambers of cylinder.

Experimental apparatus and test parameters of STO sub-safety function
Figure 3 shows the circuit diagram of the pneumatic system with STO sub-safety function.

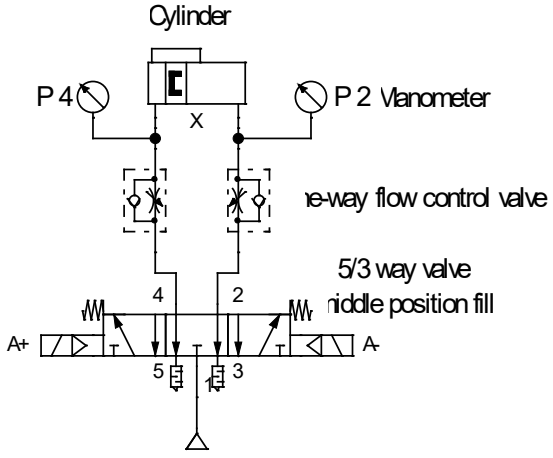

Figure 3. Pneumatic circuit diagram of the examined drive with STO sub-safety function

In the case of the STO sub-safety function, all system and test parameters are the same as those of the SOS function, except for the middle position of the 5/3 way-valve that implements the safety function. In STO function in the middle position of the 5/3 way-valve both working ports are exhausted.

3. Results and discussion

Stopping time results of SOS sub-safety function

Figure 4 shows the characteristic stop process of the pneumatic linear drive with the SOS sub-safety function. During the simulation depicted here, the moving mass is 5 kg, the opening level of the throttle valves are 100%.

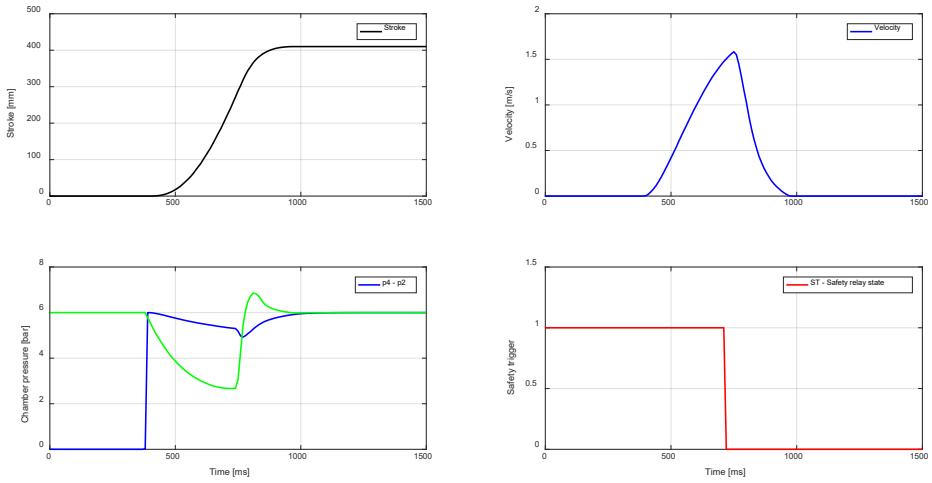

Figure 4. Stopping simulation results with SOS function (m=5 kg, T_{OL}=100%)

After the stop trigger, switching into the middle position of the 5/3 main valve, the filling of the right side cylinder chamber starts while the filling of the left side chamber continues. The increase in the pressure on the right side (p_2) exerts a braking effect on the movement, the decrease in speed is consistent, the value of p_2 temporarily rises above the supply pressure, until the force from the pressure differences stops the piston. As the movement stops, the pressures of the cylinder chambers (p_4 and p_2) are set to supply pressure.

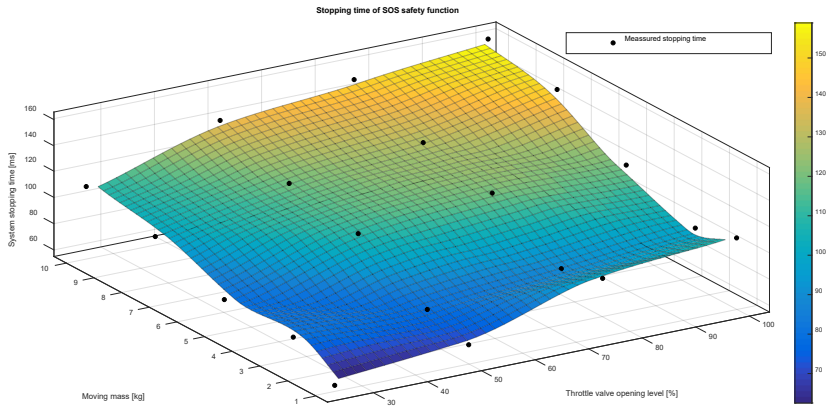

Figure 5. Stopping time of pneumatic linear drive with SOS sub-safety function

Fig. 5 shows the total stopping time of the SOS sub-safety function as a function of the moved mass and the throttle valve position in the total adjustment range. The approximating function is a cubic polynomial:

$$T_{SOS} = p_{00} + p_{10} \cdot T_{OL} + p_{01} \cdot m + p_{20} \cdot {T_{ol}}^2 + p_{11} \cdot T_{OL} \cdot m + p_{02} \cdot m^2 + p_{30} \cdot {T_{OL}}^3 + p_{21} \cdot {T_{OL}}^2 \cdot m + p_{12} \cdot T_{OL} \cdot m^2 + p_{03} \cdot m^3,$$

where the correlation coefficient is $R^2 = 0.9082$.

As expected, the time required for stopping increased as the moved mass increased. In general the level of opening of throttle valve has two effects on the process. On the one hand, the larger the T_{OL}, the smaller the right chamber pressure (p_2) at the time of the stop trigger. On the other hand, increasing T_{OL} results in an increase in speed, which leads to higher kinetic energy. Using SOS safety function, both effects increase the stopping time: in case of high T_{OL}, the kinematic energy is high, and also more time is needed to fill the right cylinder chamber after stopping trigger.

Stopping time results of SSC sub-safety function

Figure 6 shows the characteristic stop process of the pneumatic linear drive with the SSC sub-safety function. During the simulation depicted here, the moving mass is 5kg, the opening level of the throttle valves are 100%.

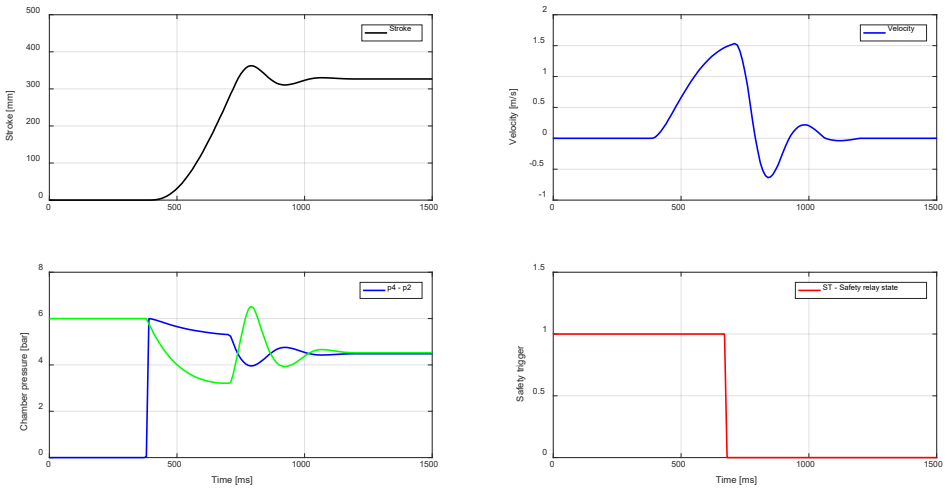

Figure 6. Stopping simulation results with SSC function (m=5 kg, T_{OL}=100%)

After the stop trigger, switching into the middle position of the 5/3 main valve, both of the cylinder chambers are closed. The movement continues, the pressure in the left chamber (p_4) decreases, and increases in the right (p_2). When p_2 is greater than p_4, a braking effect occurs, the speed decreases, but due to the displacement of the piston, p_2 continues to increase. Then the movement can change direction and a spring movement with decreasing amplitude can develop. Finally, the piston stops, equal pressure develops in the cylinder chambers - in the case of symmetrical cylinders without external force.

Figure 7 shows the total stopping time of the SSC sub-safety function as a function of the moved mass and the throttle valve position in the total adjustment range. The approximating function is a cubic polynomial:

$$T_{SSC} = p_{00} + p_{10} \cdot T_{OL} + p_{01} \cdot m + p_{20} \cdot {T_{OL}}^2 + p_{11} \cdot T_{OL} \cdot m + p_{02} \cdot m^2 + p_{30} \cdot {T_{OL}}^3 + p_{21} \cdot {T_{OL}}^2 \cdot m + p_{12} \cdot T_{OL} \cdot m^2 + p_{03} \cdot m^3,$$

where the correlation coefficient is $R^2 = 0.9867$.

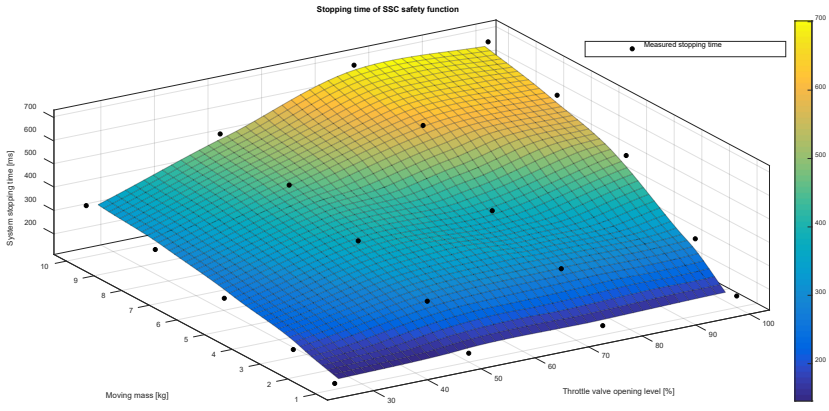

Figure 7. Stopping time of pneumatic linear drive with SSC sub-safety function

The time required for stopping increased as the moved mass and the speed increased, which can be attributed to the higher kinetic energy. Using SSC safety function, both throttle valve effects also increase the stopping time: in case of high T_{OL}, the kinematic energy is high, and as the throttle valve is open, there is lower pressure in the right chamber, so it takes longer to build up the braking effect.

Stopping time results of STO sub-safety function

Figure 8 shows the characteristic stop process of the pneumatic linear drive with the STO sub-safety function. During the simulation depicted here, the moving mass is 5kg, the opening level of the throttle valves are 25%.

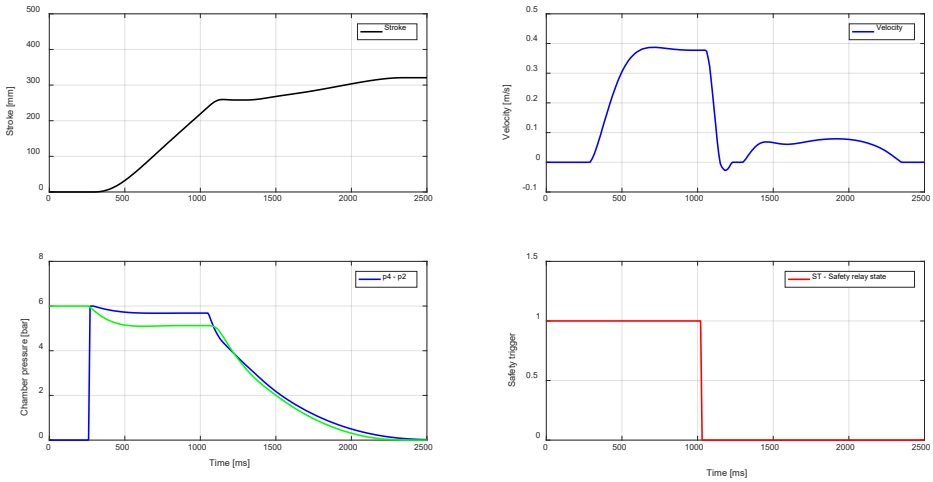

Figure 8. Stopping simulation results with STO function (m=5 kg, T_{OL}=25%)

After the stop trigger, switching into the middle position of the 5/3 main valve, both of the cylinder chambers are exhausted, p_2 and p_4 decrease to atmospheric pressure. The velocity decreases immediately rapidly, but the piston movement continues until the friction force stops the piston. At low throttle valve opening levels spring-like movement may occur near the end of the stroke due to the slow exhausting in right chamber.

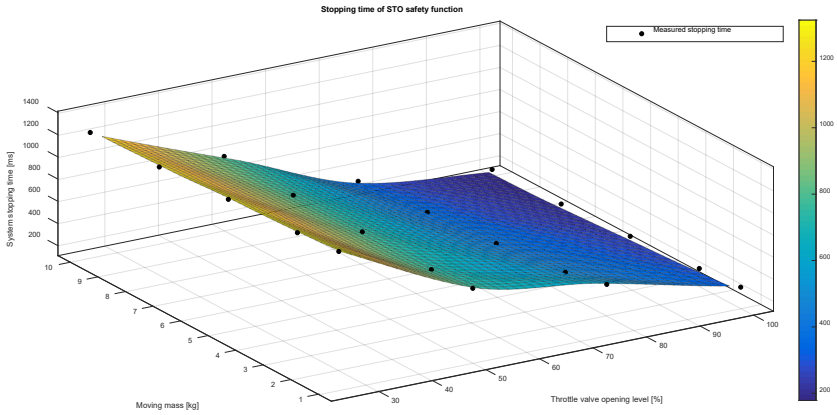

Figure 9. Stopping time of pneumatic linear drive with STO sub-safety function

Figure 9. shows the total stopping time of the STO sub-safety function as a function of the moved mass and the throttle valve position in the total adjustment range. The approximating function is a cubic polynomial:

$$T_{STO} = p_{00} + p_{10} \cdot T_{OL} + p_{01} \cdot m + p_{20} \cdot {T_{ol}}^2 + p_{11} \cdot T_{OL} \cdot m + p_{02} \cdot m^2 + p_{30} \cdot {T_{OL}}^3 + p_{21} \cdot {T_{OL}}^2 \cdot m + p_{12} \cdot T_{OL} \cdot m^2 + p_{03} \cdot m^3,$$

where the correlation coefficient is $R^2 = 0.9942$.

The figure shows that the stopping time increases as expected with the increase in moving mass, but the throttle valve opening level affects the process in a different way than before. The results of the simulations show that the throttle valve opening level is inversely proportional to the stopping time, that is, the larger the T_{OL}, the shorter the stopping time. The explanation for this is that while the speed increases with the throttle valve opening, which has the effect of increasing the stopping time, but at the same time, without throttling (with a higher T_{OL}), the cylinder chambers are exhausted faster and thus overall the piston stops faster.

Conclusions

- Compared the three safety-rated stopping sub-functions for pneumatic drives, the following conclusions can be made:
- The increasing moving mass resulted in an increase in stopping time in all cases.
- However, the effect of the throttle valve opening level varies in individual cases, as the position of the throttle valve affects not only velocity, but it also affects chamber pressures. Thus, while opening the throttle valve using SOS and SSC sub-safety functions results in an increase in the stopping time, in the case of the STO function the stopping time is reduced.
- In terms of stopping time, the SOS sub-safety function is the most advantageous of the 3 functions, in this case the stopping times are the shortest. The difference is significant. While in the case of SOS sub-safety function the highest stopping time is 250 ms (moving mass: 10 kg, TOL: 100%), in the case of SSC this value is almost three times that (700 ms) and in the case of STO it is more than five times that (1360 ms).

Acknowledgements

This work was supported by the Stipendium Hungaricum Programme and by the Mechanical Engineering Doctoral School, Hungarian University of Agriculture and Life Sciences, Gödöllő, Hungary.

References

[1] Barner, A., Bredau, J., Schiller, F. (2009) *Efficient Fault Detection in Safety-Related Pneumatic Control by Conceptual Encapsulation*. 7th IFAC Symposium on Fault Detection, Supervision and Safety of Technical Processes, Barcelona.

[2] Directive 2006/42/EC of the European Parliament and of the Council on machinery

[3] EN ISO 12100: Safety of machinery. General principles for design. Risk assessment and risk reduction (2015)

[4] EN ISO 13849-1: Safety of machinery - Safety-related parts of control systems - Part 1: General principles for design (2016)

[5] EN ISO 13855: Safety of machinery — Positioning of safeguards with respect to the approach speeds of parts of the human body (2010)

[6] EN ISO 14120 Safety of machinery. Guards. General requirements for the design and construction of fixed and movable guards (ISO 14120:2015)

[7] Festo Corp. (2011) Guideline for functional safety, 135242 (EN), 2022/02. Retrieved 6th March, 2024 from https://www.festo.com/net/en-us_us/SupportPortal/Files/730454/63212_Guideline_Functional_safety_EN_2022_135242.pdf

[8] Festo Corp. (2021) Achieving Functional Safety in Factory Automation. Retrieved 6th March, 2024 from https://www.festo.com/media/cms/media/editorial/downloads/achieving_functional_safety_in_factory_automation_2.pdf

[9] Földi L., Berencsi B. (2022) *Ipari gépek CE jelölése és biztonsága az EU-s és hazai szabályozás tükrében.* Magyar Mérnöki Kamara, Budapest.

[10] Földi L., Mayerné Sárközi, E. (2022) Examination of the safety functions of a pneumatic balancing system. *Mechanical Engineering Letters*, Vol. 23, pp.101-110.

[11] Hauke, M.; Schaefer, M.; Apfeld, R.; Bömer, T.; Huelke, M.; Borowski, T.; Büllesbach, K.-H.; Dorra, M.; Foermer-Schaefer, H.-G.; Grigulewitsch, W.; Heimann, K.D.; Köhler, B.; Krauß, M.; Kühlem, W.; Lohmaier, O.; Meffert, K.; Pilger, J.; Reuß, G.; Schuster, U.; Seifen, T.; Zilligen, H. (2009) *Functoinal safety of machine controls-Application of EN ISO 13849. BGIA Report 2/2008e*. Berlin, DGUV.

[12] Hauke, M.; Schaefer, M.; Apfeld, R.; Bömer, T.; Huelke, M.; Borowski, T.; Büllesbach, K.-H.; Dorra, M.; Foermer-Schaefer, H.G.; Uppenkamp, J.; Lohmaier, O.; Heimann, K.-D.; Köhler, B.; Zilligen, H.; Otto, S.; Rempel, P.; Reuß, G. (2019) *Functional safety of machine controls – IFA Report 2/2017e - Application of EN ISO 13849*. Berlin, DGUV.

[13] VDMA 24584: 2019, Safety functions of regulated and unregulated (fluid) mechanical systems.

Prediction of 4WD articulated tractor stability on sloped terrain

Jozef RÉDL[1], Gábor KALÁCSKA[2], Juraj MAGA[3]
[1] *Institute of Design and Engineering Technologies, Faculty of Engineering, Slovak University of Agriculture in Nitra, Slovakia,*
[2] *Institute of Technology, Hungarian University of Agriculture and Life Sciences,* MATE Gödöllő
[3]*YUMA n.g.o. Nitra, Slovakia*

Abstract

A simple mathematical model of static stability of articulated frame machine is presented. The mass properties of machine as well as the machine angle orientation on slope and slope angle are considered in mathematical model. The orientation of machine, with respect to contour line, was defined by utilizing the methods of analytical geometry of 3D space. A set of systems of non-linear equations are used to find an admissible angles of slope, with respect to vary combination of steering angle, slope-to-orientation angle of machine. We propose the constant velocity of machine. We set up the initial conditions and boundaries for the designed model. As a reference value we used the value of critical slope angle calculated from track width and overall center of gravity height. All mathematical calculations were performed in Mathcad® Prime 9.0 software.

Keywords

static stability, off-road vehicles, overturning, sloped ground, machine skidding

1. Introduction

Climate change brings many questions about the elimination of forestry disasters caused by fire. The available machines have operational and technical limitations. To keep the safety requirements, it is necessary to predict the critical situations when a machine is on duty. Many scientific results have been published about the stability of articulated-framed tractors operated on sloped terrain. Authors Badar et al. (2022), highlights in their research the efficacy of using a combined CG to simulate 6-DOF dynamic model of the ground vehicles with center-articulated steering. A realistic scenario is simulated to study the turning characteristics of an articulated vehicle of choice at the rated speed and maximum steering angle. The analysis of the simulation results shows that the dynamic model predicts the cornering behavior realistically. The simulation

platform will provide a functional basis for furthering the mathematical model for articulated forest machines considering uneven terrains. Zhu and Kan (2022) published their research about the influence of luffing wheel-leg on stability of articulated off-road vehicle. The research provides a concept for improving the ability to adapt to terrain and increase the lateral stability for the off-road vehicles by applying active control of bodies. Significantly, lateral stability models, including driven and non-driven luffing wheel-legs, were derived by analyzing tire contact forces, which is different from most previous models established only by considering the geometric position of the COG. The lateral stability models derived avoided the assumption of ignoring the inertia and mass of individual components of chassis. The new lateral stability models are more accurate and more generic, which provides some foundation for future more lateral stability models of articulated chassis that install different active control of bodies. The models developed also permitted the estimation of tire contact forces, which contributes to the development of sensors that could inform vehicle operators of danger levels. Franceschetti et al. (2021), presented their study which combines known facts and engineering principles related to articulated narrow-track tractor design to predict, with a kinematic model, the tractor behavior on sloped ground. The model was set up for the steady-state behavior, and it predicted the orientation as well as the stability of the vehicle on idealized slopes. The lateral stability angle was linear, decreasing as the roll angle increased. Otherwise, the lateral stability angle had a non-linear trend when related to the yaw angle. The lowest stability angle was 39.3°, obtained at the extreme value of the yaw angle, −35°, equivalent to the maximum steering action of the tractor. The results presented do not consider all the phenomena of friction, air resistance, internal moving liquids and dynamic behavior that could occur during a real overturn. Various parameter values were used in a computer analysis to study the effects of tractor geometry, including the articulation possibilities of the tractor. The dynamic effect of the central pivot point during the rotation of one body of the tractor with respect to the second one, if not properly damped by suitable viscoelastic components, might negatively affect the stability angle, leading to an early rollover. From a historical view of point, the most relevant research was published by Gibson et al (1971), Oida (1978,1983), Itoh and Oida (1990). Most important works was published by Dudziński (1983,1986) where an author presents an analytical description concerning the slips and skids and turning resistance moments of articulated machines during turning while at a standstill. The results of computations tests performed on a laboratory vehicle and on industrial machines are presented diagrammatically. The kinematic discrepancy encountered by a vehicle under operation. In certain conditions, the kinematic discrepancy results in the phenomenon of so-called circulating power which causes, additional loading on the drive system, then increased energy loss and tire wear and, in the case of an articulated frame-steer vehicle, the substantial growth of steering resistance.

2. Experimental

Initial condition of mathematical model

To design a mathematical, we must consider these initial conditions:

1. Stability conditions are defined with three non-linear joints.
2. Slope angle is defined as an angle between machine chassis and horizontal plane.
3. The change of dislocation of COG (Center of Gravity) due to fuel loss is neglected.
4. The mass of front axis and weight of front tires are neglected.
5. The total weight of the machine includes a full fuel tank, except operator weight.
6. Reaction couple in the front frame with front axis is neglected.
7. Overturning is caused by mass gravity force located in CoG.
8. Machine overturning is realized around connection line of front axle hinge pin and rear tires.

Geometrical model

Orientation of machine on slope is depicted in Figure 1. Horizontal plane (HP) is defined with plane $\angle\eta$ which is defined with its normal vector $\overline{n_\eta^0}$. Sloped terrain (PoS) is defined with plane $\angle\sigma$ which is defined with its normal vector $\overline{n_\sigma^0}$. Slope angle is defined with angle between normal vectors as follows $\alpha = \square\left(\overline{n_\eta^0}, \overline{n_\sigma^0}\right)$. Inertial coordinate system is defined by coordinate systems $(0, x, y, z)$ where the unite vectors relationship are follows $\bar{k} \square \overline{n_\sigma^0}$, $\bar{i} \square ToS$, where ToS is tip of slope. The contact point between tires and ground are signed with respect to front and rear axles f_r, f_l, r_r, r_l. During the overturning, the machine start overturning about tipping axes (TA) $\overline{P_f r_r}$.

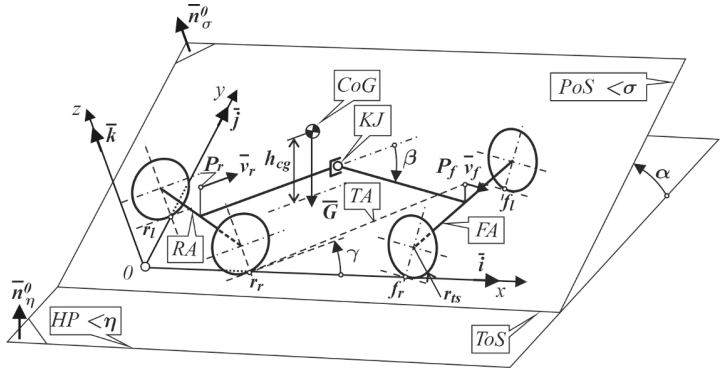

Figure 1. Machine orientation on slope

Explanation of the signs used in Figure 1 are follows: velocity of front part $\overline{v_f}$,velocity of rear part $\overline{v_r}$, KJ -kinematical joint, PoS - plane of slope, FA -front axle, RA -rear axle, Pf -front axle reference point (axle hinge pin), Pr - rear axle reference point (similar like Pf), $\overline{G}$ - vector of tractor mass gravity, f_r, f_l - front right, front left contact point with ground, r_r, r_l -rear right, rear left contact point with ground, α - slope angle, β - steering angle, γ -orientation-to-slope angle.

Model object

A characteristic property of articulated frame machine is to separate the stiff frame of machine to the two independent parts which relate to only kinematical joints. These joints are allowed to position each part of frame in horizontal and partly in vertical directions. This ability allows the machine to control the steering direction.

Table 1. Technical parameters of machine

Parameter	Description	Value	Unit
m	Total mass	9145	kg
m_F	Front part weight	4735	kg
m_R	Rear part weight	4410	kg
h_{cg}	CoG height above ground	1158	mm
${}_r h_{cg}$	Rear CoG height above ground	950	mm
${}_f h_{cg}$	Front CoG height above ground	1536	mm
h_{Pf}	Front axle point P_f height above ground	835	mm
${}_r l_{cg}$	CoG distance from rear axle	1582	mm
${}_f l_{cg}$	CoG distance from front axle	1474	mm
${}_{KJ} l_{cg}$	CoG distance from kinematical joint	508	mm
${}_A l_{cgf}$	Front CoG distance from front axle	162	mm
${}_A l_{cgr}$	Rear CoG distance from rear axle	163	mm
${}_{KJ} l_{cgf}$	Front COG distance from kinematical joint	1822	mm
${}_{KJ} l_{cgr}$	Rear COG distance from kinematical joint	911	mm
l_{Pf}	Kinematical joint distance from front axle	1984	mm
l_{Pr}	Kinematical joint distance from rear axle	1074	mm

$r_{ts} \equiv h_A$	Tire static radius	820	mm
tw_i	Track width (front, rear) inner	1524	mm
tw_o	Track width (front, rear) outer	2774	mm
tw	Track width	2149	mm
wb	Wheelbase	3058	mm
TT	Tire type	Goodyear, Dyna Torque 18.4x38, 8 ply	-

For design a mathematical model we used as model object an agricultural machine with articulated frame which technical parameters are in Table 1. The overall dislocation of center of gravity changes during the maneuver because the masses of front and rear parts of machines have a different position. This fact is depicted in Figure 3. For the model object we chose the agricultural tractor with parameters listed in Table 1. Technical parameters are taken from OECD machine test page (www.dlg.org). The static disposition of the machine is depicted in Figure 2.

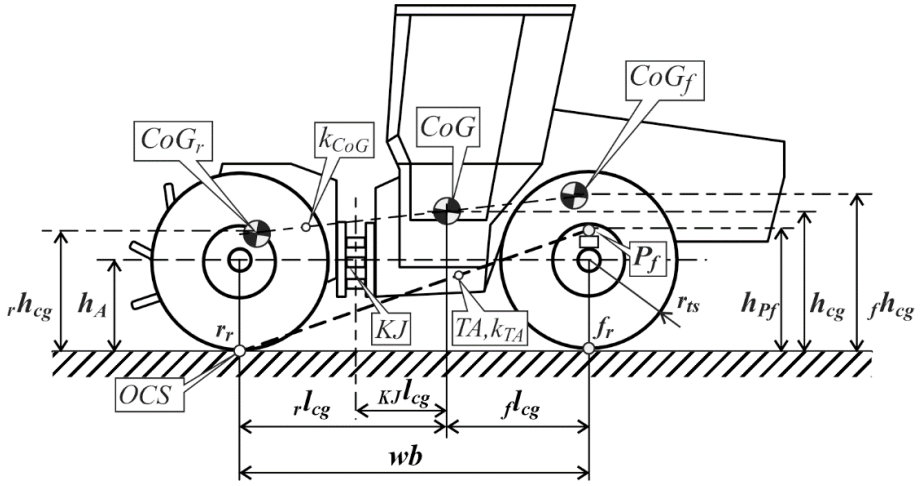

Figure 2. Static disposition of machine

Mathematical Model

Dislocation of center of gravity is derived from Figure 2 and Figure 3. The system of equations is defined for various values of steering angle β. During the maneuver, the changes coordinates of CoG will be defined by equations (1,2,3), based on Figure 3.

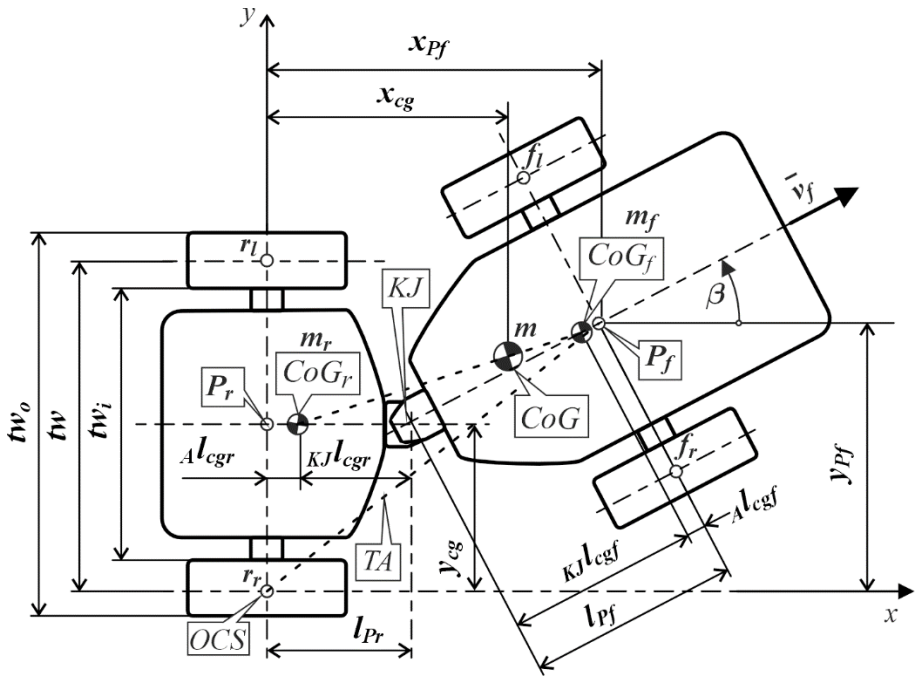

Figure 3. Machine in maneuver and CoG's dimensions

$$x_{cg} = \frac{m_r \cdot {}_A l_{cgr} + m_f \cdot \left({}_{KJ} l_{cgf} \cdot \cos\beta + L_{\Pr} \right)}{m} \tag{1}$$

$$y_{cg} = \frac{0.5 \cdot tw \cdot m_r + m_f \cdot \left(0.5 \cdot tw + {}_{KJ} l_{cgf} \cdot \sin\beta \right)}{m} \tag{2}$$

$$z_{cg} = \frac{m_r \cdot {}_r h_{cg} + m_f \cdot {}_f h_{cg}}{m} \tag{3}$$

Dislocation of joint on front axis is defined from Figures 2 and 3, and it has form as follows:

$$x_{Pf} = l_{\Pr} + l_{Pf} \cdot \cos\beta \tag{4}$$

$$y_{Pf} = 0.5 \cdot tw + l_{Pf} . \sin\beta \tag{5}$$

Dislocation of certain point of machine is depending on slope angle and steering angle, and should by defined by transformations matrix as follows:

$$\left[M_T \right] = \begin{bmatrix} \cos\gamma & \cos\alpha . \sin\gamma & \sin\gamma . \sin\alpha \\ -\sin\gamma & \cos\gamma . \cos\alpha & \cos\gamma . \sin\alpha \\ 0 & -\sin\alpha & \cos\alpha \end{bmatrix} \tag{6}$$

With transformation matrix (6) we could express the turning of machine and its mass vector of gravity with respect to inertial coordinate system. Changing the mutual positions of axles causes the change of mass vector of gravity of machine. The machine mass vector is defined as follows:

$$\begin{bmatrix} G_x \\ G_y \\ G_z \end{bmatrix} = [M_T]. \begin{bmatrix} 0 \\ 0 \\ -G \end{bmatrix} \tag{7}$$

The tipping axis k_{TA} which is intersect a reference point in front axle and contact point of rear tire r_r is defined in parametrical form as follows:

$$x = x_{Pf}.t_2 \tag{8}$$

$$y = y_{Pf}.t_2 \tag{9}$$

$$z = h_{Pf}.t_2 \tag{10}$$

The line which is intersect a CoG and has the vector of gravity direction, has the parametrical expression as follows:

$$x_{TA} = x_{cg} - \sin\gamma.\sin\alpha.t_1 \tag{11}$$

$$y_{TA} = y_{cg} - \cos\gamma.\sin\alpha.t_1 \tag{12}$$

$$z_{TA} = h_{cg} - \cos\alpha.t_1 \tag{13}$$

For defined ride direction and slope-to-angle orientation we could derive an admissible angle of slope by solving the next equations:

$$x_{cg} - \sin\gamma.\sin\alpha.t_1 = x_{Pf} \cdot t_2 \tag{14}$$

$$y_{cg} - \cos\gamma.\sin\alpha.t_1 = y_{Pf} \cdot t_2 \tag{15}$$

$$h_{cg} - \cos\alpha.t_1 = h_P \cdot t_2 \tag{16}$$

3. Results and discussion

The analytical geometry for three-dimensional space approach was applied to define the relationship between the angle of slope, slope-to-angle orientation, steering angle, and tipping axes for its various combinations. We derived the set of non-linear system of equations which were calculated by Mathcad Prime software. The system of equation (1-

16) was calculated simultaneously. Designed algorithm was applied for initial values displayed in Table 1 and boundary conditions. The solution for relevant angles of steering angles is displayed in Figure 3.

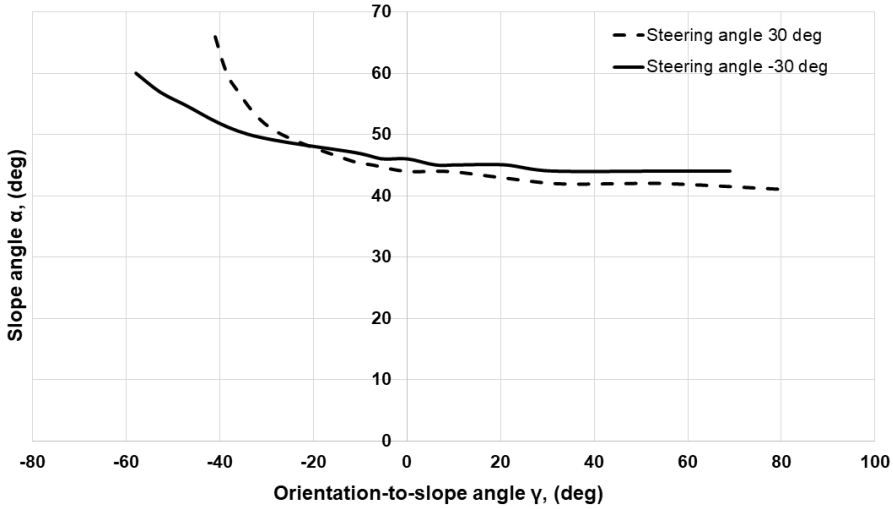

Figure 4. Machine in maneuver

The calculated static stability for analyzed machine is 43 deg, when steering angle is zero and orientation-to-slope angle is also zero. This fact is visible in the Figure 3, if $\gamma = 0$ and the slope angle is stick around the value 44 deg. Difference between both values is 1 deg, which should be neglected. We consider only the allowable steering angle in left and right direction with values about 30 deg and -30 deg. Designed mathematical model consider of three angle parameters mainly the steering angle which refers about the mutual position of front and rear part of machine. The lower values of steering angles were not applied because it doesn't have crucial influence on machine stability. The maximal turning radius indicates that maximal steering angle has a value of 30 deg. Presented mathematical model described the methodology for determination of allowable (safe) slope angle for machine motion with constant velocity for various combination of steering angle and orientation-to-slope angle. The designed model accepts the machine parts masses, dislocations of center of gravity of machine parts and overall dislocation of CoG. Some construction parameters were estimated due to the lack of technical documentation.

Future plans for articulated frame machine testing: Several studies on the static stability of articulated vehicles were published. Similar approaches were published e.g. (Gibson et al., 1971), (Dudziński,1983,1986), (Šesták et al.,1998), (Badar et al., 2022). However, some publications are outdated, by still giving the mathematical background for new mathematical model proposals. Nowadays, for modelling of static stability of articulated vehicles are available a few commercial software, which are utilizing the multibody dynamics approaches. However, using this software requires wide knowledges from various scientific areas. With additional equations the designed model should be extended for solution of articulated frame tractor-trailer combination as presented by (Murillo et al., 2022). Presented approaches is utilizable in the process of design and testing of prototypes like a tool for simulation or prediction of machine overturning. The results should be utilized in optimisation process of technical parameters of machines and improving the resistance against overturning. Corrected parameters may help to protect the operator in rollover events (Guzzomi et al., 2019).

4. Conlcusion

From the above detailed investigations, the following conclusions can be drawn:

- Research in the field of articulated frame vehicles is relevant as it's proved by the literature review.
- Designed mathematical model has universal application for various types of agricultural and forestry machines. Changing the input mass characteristic values, dimensions or including additional force or moment parameters we got the useful and fast tool for determinations of admissible slope angle, where the machine should operate safely.
- At our analysis, we chose the tractor with up to middle-weight parameters, which is suitable for sloped terrain and semi-forestry using.
- For steering angle, we used two limiting angles in interval $\beta \in \langle 30\,\mathrm{deg}, +30\,\mathrm{deg} \rangle$.For this setting we got the stability curves for different slope-to-orientation angles. Also, admissible slope angles were calculated.
- As a reference value, we determined the static stability of machine with next settings: $\beta = 0\,\mathrm{deg}, \gamma = 0\,\mathrm{deg}$. These settings refer to the orientation of machine on slope and steering angle. Longitudinal axis

of machine is parallel with contour line and the line k_{CoG} (see Fig.2). The critical slope angle for this setting is $\alpha_{crit} = 43\,\text{deg}$. Our simulation model, with the same settings give the critical slope angle ${}_{sim}\alpha_{crit} = 44\,\text{deg}$. The difference of one degree is caused by the fact that a few technical parameters must be evaluated cause of lack of technical documentation, and we neglected the loss of radius of tires due the mass of machine and ground deformations.

- From Figure 4, we can express a fact that the highest risk of stability loss is in the next angles combinations $\beta = 30\,\text{deg}, \gamma = 80\,\text{deg}$ and slope angle is bellow to critical static stability. In other angles combination the machine has a high ability of safe operation on slope.
- Achieved results, entitled us to express an opinion that our model is usable in process of design and testing of prototypes of machines with similar construction and technical parameters.

References

[1] Badar,T., J. Backman., U. Tariq., A. Visala. (2022) Nonlinear 6-DOF Dynamic Simulations for Center-Articulated Vehicles with combined CG, IFAC-PapersOnLine, Volume 55, Issue 14, pages 95-100.

[2] Dudziński, P.A. (1983) Problems of turning process in articulated terrain vehicles, Journal of Terramechanics, Volume 19, Issue 4, pages 243-256.

[3] Dudziński, P.A. (1986) The problems of multi-axle vehicle drives, Journal of Terramechanics, Volume 23, Issue 2, pages 85-93.

[4] Franceschetti, B., V. Rondelli., E. Capacci. (2021) Lateral Stability Performance of Articulated Narrow-Track Tractors, Agronomy 11.

[5] Gibson, H.G., K. C. Elliottt, S. P. E Persson. (1971) Side Slope Stability of Articulated-Frame Logging Tractors. In Journal of Terramechanics, 1971, Vol. 8, No. 2, pages 65-79.

[6] Guzzomi, A,L., V. Rondelli, E. Capacci. (2019) Operator protection in rollover events of articulated

[7] narrow track tractors. Biosystems Engineering, Vol. 185, pages 103-115.

[8] Itoh, H., A. Oida (1990) Dynamic Analysis of Turning Performance of 4wd-4ws Tractor on Paved Road. In Journal of Terramechanics ,Vol. 27, issue 2, pages 125-143.

[9] Murillo,M., G. Sánchez, N. Deniz,L. Genzelis, L. Giovanini. (2022) Improving path-tracking performance of an articulated tractor-trailer system

using a non-linear kinematic model. Computers and Electronics in Agriculture 196.

[10] Oida, A (1978) Geometrische Spur eines Knickschleppers, Grundl. Landtechnik bd. 28, nr. 5.

[11] Oida, A (1983) Turning Behavior of Articulated Frame Steering Tractor - I. Motion of Tractor Without Traction, Journal of Terramechanics, vol. 20, no. 3/4, pages 153-165.

[12] Šesták, J., J. Rédl, J.Pršan. (1998) Svahová dostupnosť terénneho vozidla rozdeleného zvislým čapom (Side slope stability of the terrain vehicle separated by vertical pivot). Acta technologica agriculturae. 1, 2, pages 38-40.

[13] Zhu,Y., J. Kan. (2022) Prediction of the lateral stability of a forestry chassis with an articulated body and fitted with luffing wheel-legs, In :Biosystems Engineering,vol 224, pages 143-160.

The effect of atmospheric pressure plasma surface treatment on the interfacial properties of glass fiber pultruded elements

Dániel VACZKÓ [1,4], Róbert KERESZTES[2], Zoltán WELTSCH[3]
[1] *Department of Innovative Vehicles and Materials, John von Neumann University, Kecskemét*
[2] *Department of Materials Science and Engineering Processes, Institute of Technology, Hungarian University of Agriculture and Life Sciences,* MATE, Gödöllő
[3]*Department of Road and Rail Vehicles, Zalaegerszeg Innovation Park, Széchenyi István University,* Győr
[4]*Doctoral School of Mechanical Engineering, MATE, Gödöllő*

Abstract

The challenges posed by the global shortage of raw materials necessitate a re-evaluation of engineering materials and manufacturing technologies. Composite materials, particularly those manufactured using pultrusion, come to the forefront due to their superior mechanical properties and long lifespan. This research focuses on atmospheric pressure plasma surface treatment aimed at increasing the surface energy of the treated composites to optimize their adhesive properties. During the surface treatment process, two main parameters are examined: the distance between the plasma gun and the treated piece, and the plasma advance speed. These variables are crucial for determining the optimal conditions for surface energy and wettability. The experimental results are evaluated with a particular focus on changes in the wettability of the pultruded composites due to plasma treatment, which is documented by contact angle measurements. The investigations reveal a significant improvement in the wettability of the treated surfaces, which directly contributes to the optimization of adhesive capabilities.

Keywords

adhesion, pultrusion, composite, surface energy, glass fiber, plasma

1. Introduction

Pultrusion is a continuous manufacturing process that allows for the production of composite materials with consistent cross-sections. Reinforcing fibers, such as glass or carbon, are pulled through a resin impregnation bath, then through a heated mold where the resin hardens, forming the final product. The pultrusion process offers significant advantages over other manufacturing processes, such as high corrosion resistance, a high strength-to-weight ratio, and low maintenance costs, as highlighted by Vuppalapati et al. (2013). Furthermore,

pultrusion allows for the customization of material properties, providing a wide range of applications in construction, transportation, and other areas (Vuppalapati et al., 2013).

The advantages of pultruded composites include lightweight, high strength, improved durability, and corrosion resistance, which, according to Vedernikov et al. (2020), enhance the appeal of these materials to design engineers. Their easy transportability, quick assembly, and non-magnetic/non-conductive characteristics offer additional benefits in modern engineering applications (Vedernikov et al., 2020).

Fairuz et al. (2014) emphasize the importance of considering variables such as fiber impregnation, resin viscosity, pull speed, and curing temperature for the production of high-performance pultruded products. These variables significantly impact the quality of pultruded profiles, which is essential for various industrial applications (Fairuz et al., 2014).

Although pultruded products offer many advantages, their bonding, especially through adhesion, can be challenging due to low surface energy. This property makes it difficult for adhesives to bond effectively, thereby reducing the reliability and durability of the joints. To counter this, surface treatment technologies such as atmospheric pressure plasma surface treatment offer a promising solution for increasing surface energy, which can improve the efficiency of adhesive processes (Minchenkov et al., 2021).

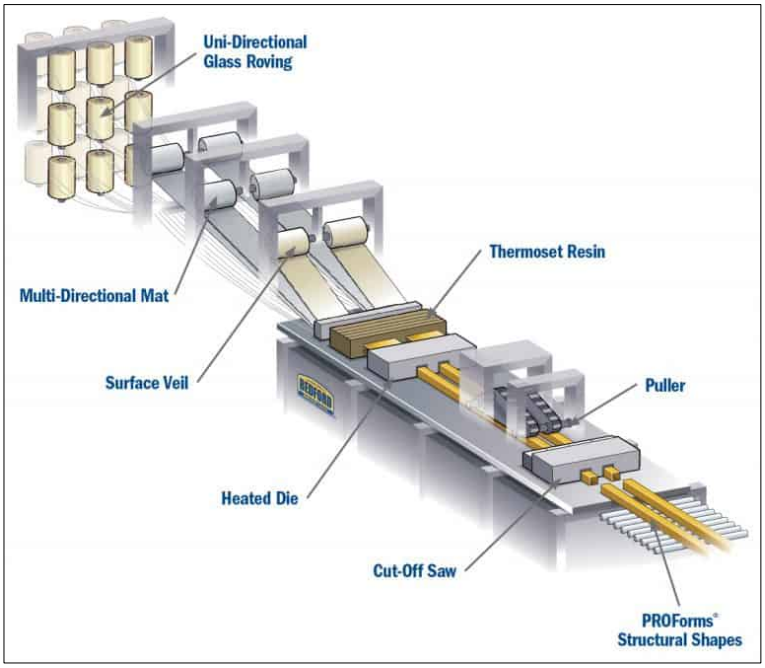

Figure 1. The Pultrusion Process Diagram (Bedford Reinforced Plastics, 2024)

While the pultrusion process and the composite products derived from it offer significant advantages in terms of corrosion resistance, high strength-to-weight ratio, and low maintenance costs, optimizing the adhesive processes is crucial for further improving the performance of these products. In our current research, we investigate the potential of atmospheric pressure plasma surface treatment to increase the surface energy of pultruded composites, specifically to enhance adhesive properties. Our focus is on analyzing the effects of two essential parameters: the distance between the plasma gun and the treated piece, and the plasma advance speed. Throughout the research, we evaluate the wettability and adhesive performance of the treated surfaces in order to determine the most optimal surface treatment parameters. The results are expected to contribute to the improvement of the reliability and durability of the adhesion of pultruded composites, thereby facilitating their wider application in various engineering fields.

2. Experimental

Preliminary Experiments

Based on what was found during the literature research, other researchers have conducted similar experiments where they applied plasma surface preparation for glass fiber profiles. During the manufacturing of pultruded profiles, there are several variables such as the glass fiber to resin ratio, the type of resin used, and whether an external veil layer is applied. Therefore, before starting the experiments, it was important to conduct preliminary experiments and develop a research plan based on the results obtained.

Figure 2. The Plasmatool device used for surface preparations (PlasmaTool, 2024)

The Plasmatool device from Relyon Plasma was used for the plasma treatments. (Figure 2). The main advantage of the device is that it is portable, easily transportable, and can be used almost anywhere. It does not require an external high-pressure air supply. The machine operates at a fixed power of 1300W, which is not adjustable. The portability of the device was an advantage from my experimental point of view, but it also presented a disadvantage. To ensure repeatability and accurate evaluation of the experiments, it was necessary to ensure that the plasma head could travel over the sample at a pre-set distance and speed. An ABB robot was available at the department, leading to the selection of this solution. To mount the handheld plasma torch on the robot, it was necessary to reverse-engineer the torch. Based on the model obtained, a mounting fixture was designed and then produced using 3D printing.

Before the preliminary experiments, close attention was paid to the size of the plasma flame. The measurement showed that the core of the flame extends to about 10 millimeters, while the total length of the flame from the end of the torch is approximately 25 millimeters. Based on this, the treatment was performed at various distances with different advancing speeds. After each treatment, a droplet test was conducted. It is very important for the results that the droplet test is performed immediately after the treatment, as the surface energy decreases over time. Figure 3 shows the difference between the untreated and treated surface.

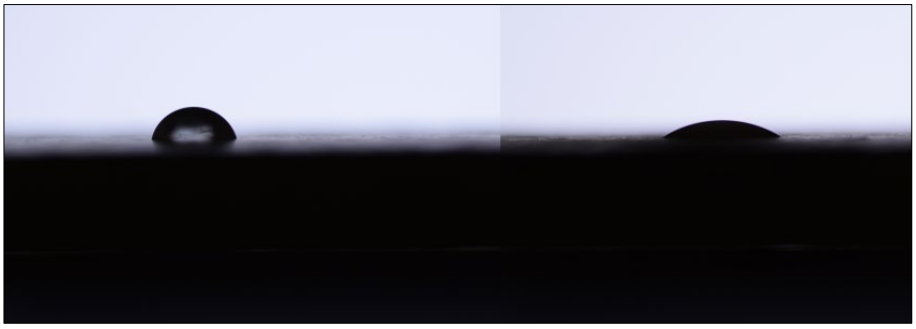

Figure 3. The result of the plasma preliminary experiment: the untreated surface on the left, the treated surface on the right.

Experimental Plan

The preliminary experiments proved to be effective. The distance of the torch and the speed influenced the results obtained during the droplet test. Based on these, my research continued with the creation of experimental plans.

Since the plasma device can operate at a fixed power, this parameter does not need to be considered when creating the experimental plan. There are two adjustable parameters that can be implemented with the help of the robot: the distance of the torch from the sample and the advancing speed. Due to the two parameters, all the combinations were examined, as can be seen in Table 1.

Table 1. Parameters applied during plasma treatment

Plasma gun - surface distance [mm]	Advance speed [mm/min]
5	50
	100
	150
	200
10	50
	100
	150
	200
15	50
	100
	150
	200
20	50
	100
	150
	200

Execution of Experiments

After determining the experimental plans, the preparation of the test samples followed. It was ensured that the experiments were conducted according to the DIN 1465 standard (Lap Shear Joint Adhesive Tensile Test). The manufacturer provided the GFRP flat profiles in 1-meter lengths. These strands were cut into 75mm lengths with a saw, and then the cut surfaces were deburred. Figure 4 illustrates the single-lap joint that was intended for use according to the standard. The GFRP pieces at the ends of the adhesive test specimens are explained by the fact that if they were placed in the tensile machine without the added pieces, the shear plane would not be in the center.

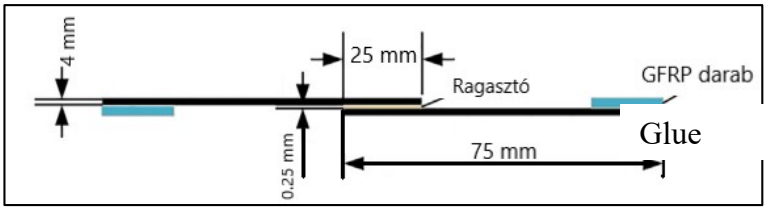

Figure 4. Dimensions of the adhesive test specimens

During the preparation of the surfaces, five pairs of test specimens were prepared with each setting. In every case, preparation was preceded by degreasing with methanol. The exchange of workpieces on the machine table was sped up with a simple stop. Figure 5 shows the machining process.

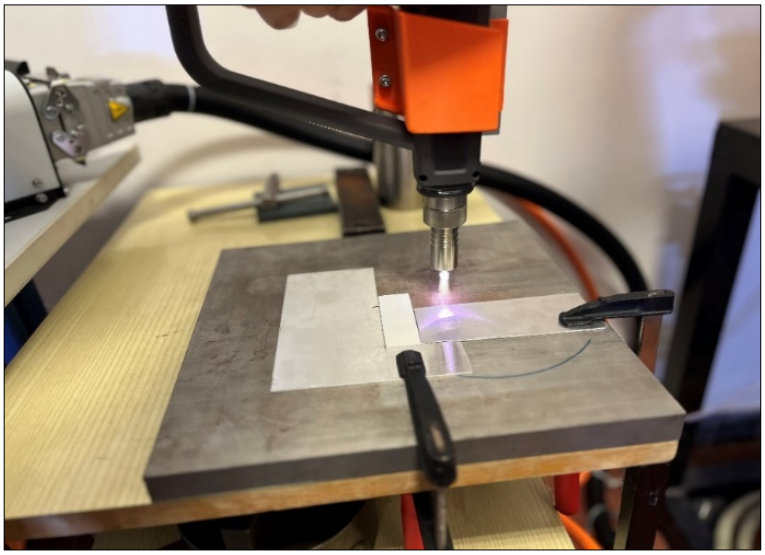

Figure 5. Plasma on the left, laser surface preparation on the right

3. RESULTS AND DISCUSSION

Wettability Results with Plasma Treatment

The wettability of the test sample can be characterized by the spreading of a specified liquid. The contact angle formed at the intersection of the two phases serves as a measure of this property. The relationship between the contact angle and surface energy, as described by Young, remains a significant observation to this day. The interaction at the interface between the test sample and the liquid determines the spread. (Juhász et al., 2021).

The contact angle is most commonly determined using the sessile drop method, where a macro camera on one side and a light source on the other are key to the process. Here, 5 µl of liquid is drawn up into a micropipette – a volume chosen based on its frequent mention in literature and to allow for comparison with other studies. The liquid is then released to form a drop. The stage, which holds the test sample, is gradually approached. When they touch, the drop transfers to the sample surface and spreads. It is important to ensure that the drop does not fall onto the surface, as this would alter the liquid's behavior significantly. (Juhász et al., 2021).

The drop is then photographed, and software is used to determine the contact angle. The contact angles determined with the help of the software are shown in Table 2.

The average contact angle values during plasma treatment generally show an improvement over the untreated surface, which has a contact angle of 69.59 degrees and serves as the reference. The experimental results indicate that the advancing speed and the distance between the plasma head and the surface can

be fine-tuned to enhance the wettability of the treated surfaces. For example, a combination of 150 mm/min advancing speed and 10 mm distance produced one of the smallest average contact angles at 17.28 degrees, which could be optimal for adhesive processes. However, it is important to note that settings with lower advancing speeds and closer distances can lead to burning of the surface, affecting the contact angle and negatively impacting wettability.

As the speed increases to 200 mm/min, it is noticeable that the contact angle value significantly increases even at larger distances. At the high speed of 200 mm/min with a distance of 5 mm, the contact angle dramatically rises to 70.64 degrees. At 200 mm/min advancing speed and a distance of 15 mm, the contact angle is 58.63 degrees, which is better than at closer distances but still higher than the ideal.

Table 2. Results of the Contact Angle Measurement

	Advance speed [mm/min]	Plasma gun - surface distance [mm]	Contact Angle [°]		
			Left	Right	Avarage
1	50	5	28,33	25,35	26,84
2	50	10	27,84	25,27	26,56
3	50	15	26,58	28,01	27,30
4	50	20	22,70	24,93	23,82
5	100	5	27,27	32,43	29,85
6	100	10	31,92	29,53	30,73
7	100	15	30,85	29,80	30,33
8	100	20	30,55	30,55	30,55
9	150	5	22,56	20,52	21,54
10	150	10	18,23	16,32	17,28
11	150	15	24,29	19,22	21,76
12	150	20	32,00	19,91	25,96
13	200	5	69,99	71,28	70,64
14	200	10	69,03	63,94	66,49
15	200	15	62,13	55,12	58,63
16	200	20	69,36	56,00	62,68
Untreated			70,64	68,53	69,59

This suggests that with increasing advancing speed, the optimal distance between the plasma head and the surface might also increase. The goal is to

minimize the contact angle, thereby improving the wettability of the surfaces and, consequently, the adhesive properties. The results imply that within certain limits, larger distances can counteract the negative effects of higher speed until they reach an excessively high contact angle. These data can assist in fine-tuning the parameters of plasma surface treatment to achieve the best possible wettability and adhesive results.

The treated surfaces were also examined with a confocal microscope, which is shown in Figure 6. The untreated surface can be seen on the left. The middle image, with setting 6, shows the formation of melt drops due to the smaller advance and distance creating more heat. On the right, the sample treated with setting 16 shows no melt drops due to the high advance speed and distance. Based on the contact angle values, the melt drops do not necessarily pose a problem, but attention should be paid to these in future investigations.

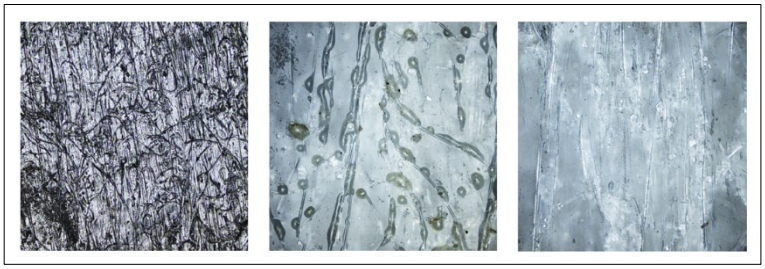

Figure 6. Confocal microscopic surfaces, untreated on the left, setting 6 in the middle, setting 16 on the right.

4. Conclusions

- The plasma treatment consistently improved wettability compared to the untreated surface, as evidenced by the decrease in contact angles.
- The formation of melt drops on the surface treated with a smaller advance speed and distance, visible in the middle image, could be a disruptive factor in the adhesive process due to the excessive heat generated.
- The best results were produced by a medium-high advance speed and distance combination, which did not lead to the formation of melt drops, and the contact angles were significantly better than the reference.
- The right image shows that a smoother surface was formed due to the higher speed and distance, which somewhat improved the contact angle values. The results suggest that a smaller speed and distance yield better results even with the formation of melt drops.
- Further research and optimization are recommended to reach the ideal contact angle and surface properties that facilitate quality adhesion. It is particularly important to optimize the settings of the plasma torch distance and advancing speed.

References

[1] Vuppalapati, R., Menta, V., Chandrashekhara, K., & Schuman, T. (2013). Manufacturing and Impact Characterization of Soy-Based Polyurethane Pultruded Composites. Polymer Composites, 35, 1070-1077. https://doi.org/10.1002/PC.22754.

[2] Vedernikov, A., Safonov, A., Tucci, F., Carlone, P., & Akhatov, I. (2020). Pultruded materials and structures: A review. Journal of Composite Materials, 54, 4081 - 4117. https://doi.org/10.1177/0021998320922894.

[3] Fairuz, A., Sapuan, S., Zainudin, E., & Jaafar, C. (2014). POLYMER COMPOSITE MANUFACTURING USING A PULTRUSION PROCESS: A REVIEW. *American Journal of Applied Sciences*, 11, 1798-1810. https://doi.org/10.3844/AJASSP.2014.1798.1810.

[4] Minchenkov, K., Vedernikov, A., Safonov, A., & Akhatov, I. (2021). Thermoplastic Pultrusion: A Review. *Polymers*, 13. https://doi.org/10.3390/polym13020180.

[5] *The Pultrusion Process | How pultrusion works (Pultruded Profiles)*. (2024, March 15). Bedford Reinforced Plastics. https://bedfordreinforced.com/the-pultrusion-process/

[6] *PlasmaTool plasma handheld for big workpieces*. (2024, March 9). Relyon Plasma · Oberflächenbehandlung. https://www.relyon-plasma.com/produkt/plasmatool/?lang=en

[7] Juhász, G., Berczeli, M., & Weltsch, Z. (2019). Surface activation of High Impact Polystyrene substrate using dynamic atmospheric pressure plasma. *International Journal of Engineering and Management Sciences*, *4*(1), 80-87. https://doi.org/10.21791/IJEMS.2019.1.11.

Performance and model prediction for semi-transparent photovoltaic

Nuha Desi ANGGRAENI [1], István SERES[2], István FARKAS[3]
[1] *Doctoral School of Mechanical Engineering*
Hungarian University of Agriculture and Life Sciences, MATE, Gödöllő
[2] *Institute of Mathematics and Basic Science,* MATE, Gödöllő
[3] *Institute of Technology, MATE, Gödöllő*

Abstract

The photovoltaic (PV) technology has been increasingly used in various fields, including agriculture, as it is well known as a clean and renewable energy source. Within that, one of the very reasonable developing solution is the semi-transparent photovoltaic (STPV). This research aims to create a mathematical model representing the relationship between global irradiation and STPV energy production. The mathematical model uses data on average global energy production and global irradiation. This mathematical model can estimate average energy production using global irradiation data. The estimated annual energy production for semi-transparent photovoltaic systems from 2023 is about 140 kW/by the installed 3,3 kWp capacity STPV system.

Keywords

agrivoltaics, energy production, irradiations, mathematical modelling, solar cells

1. Introduction

The utilisation of solar power is an evident selection; the power derived from the sun is essential for most natural processes and is an environmentally friendly, plentiful, renewable, and readily accessible source (Pintér et al., 2020). Hungary's energy transformation is gradual, confronting hurdles in fulfilling the EU's decarbonisation targets for 2030 and 2050. The share of renewables in Hungary's energy consumption is relatively low, with solid biomass, notably firewood, being the primary renewable energy source. The country's energy usage, particularly electricity, has increased (Szabo et al., 2021). Wind turbines with solar PV technologies, according to models for the year 2033, can supply 46-47% of expected electricity use, with a surplus of less than 5% of yearly consumption (Campos et al., 2023). Hungary's most influential sustainable energy source in 2022 was solar power, which generated 4.6 terawatt-hours of renewable energy.

Fig. 1 shows that the total capacity of PV power stations in Hungary in 2021 was 1829 GW, accounting for nearly 65 % of the total PV capacity installed in Hungary. MAVIR forecasts that the capacity of PV power stations will reach 6.7 GW by 2030, which could rise to nearly 12 GW by 2040. Because of their better shading tolerance, PV power station projects in Hungary today tend to be realised with monocrystalline (m-Si) PV technology, using so-called half-cell PV modules (Zsiborács et al., 2023).

Solar technology constantly evolves, but monocrystalline technology is the most common for solar applications (Zsiborács et al., 2023). Along with the development of technology, photovoltaics is also experiencing rapid growth. The recent development of photovoltaics in building outer peripherals includes roof-integrated photovoltaics (RIPV) (Kumar, Yadav, et al., 2020), façade-integrated photovoltaics (FIPV) (Attoye et al., 2017), building-integrated photovoltaics (BIPV) (Kumar et al., 2019; Reddy et al., 2020), building attached photovoltaics (BAPV) (Kumar et al., 2019), and canopy-mount solar photovoltaics (CMSPV) (Alghamdi et al., 2017). Unlike RMPV and BAPV, which use mono and polycrystalline silicon, CMSPV, RIPV, FIPV, and BIPF use flexible solar cells and crystalline silicon, amorphous silicon, and thin films like CdTe and CIGS (Gholami et al., 2020). The before mentioned technologies are also applied for vehicle-integrated photovoltaics VIPV, which can be installed on outer vehicles like sunroofs or windows (Araki et al., 2020). These solar technologies are presented in Fig. 2.

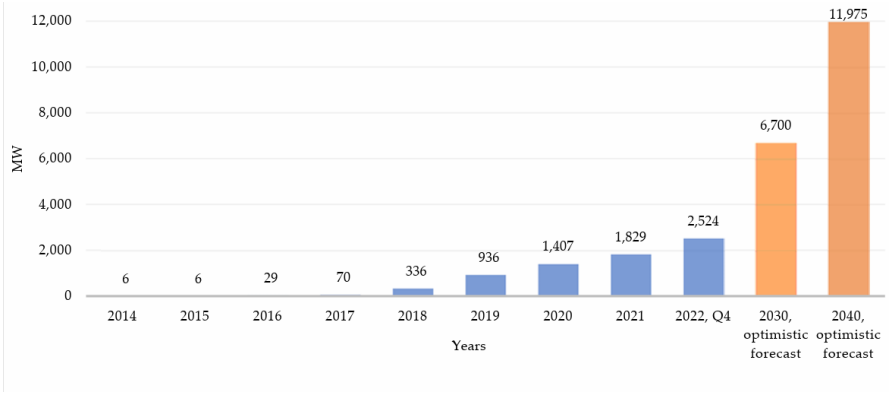

Figure 1. The evolution of Hungary's PV power plant capacity (orange indicates future PV power plant capacity based on optimistic MAVIR scenarios; blue indicates PV power plants that have already been constructed) (Zsiborács et al., 2023).

Figure 2. A visual representation of different types of solar photovoltaic plants (Kumar, Chopra, et al., 2020)

Photovoltaics can also be integrated into the on-road and rail track infrastructure or on the outer peripherals of the street pole. Those technologies use crystalline silicon, amorphous silicon, thin film and flexible solar cells applied on road-rail integrated (RRIPV) (Asanov & Loktionov, 2018; Fan et al., 2022) and pole-mounted integrated (PMPV) (Amber et al., 2019). Photovoltaics also can be applied floating, underwater, or submerged in the water (Ajitha et al., 2019; Kumar, Subramaniam et al., 2020). Dual glass solar cells are used in floating photovoltaics, whereas flexible, thin-film and crystalline silicon solar cells are used in underwater or submerged photovoltaic systems. Solar energy can be utilised by applying photovoltaics to buoys to operate wave energy (Prasad et al., 2022).

By knowing the characteristics of photovoltaics, photovoltaics can be utilised optimally. Considering that conventional photovoltaics require a large area and solar energy is only converted into electrical energy, research is being developed to study photovoltaic transparency. Over the past few years, semi-transparent and transparent solar material development has begun. Semi-transparent photovoltaics is a cutting-edge technology that simultaneously transmits light and produces electricity. Unlike traditional photovoltaic products, which PCE primarily evaluates, ST-PV should harvest sufficient solar radiation and convert it to electricity for building consumption.

On the other hand, they must transmit a specific port of daylight to illuminate indoor space. As a result, the trade-off between electricity generation and light transmittance requirements for ST-PV should be balanced. Solar cells' transparency can be improved by reducing the thickness or surface coverage of the light-active layer. However, these strategies will ultimately sacrifice vice PCE (Zhu et al., 2020).

The most recent photovoltaic trends in various types of ST-OSCs realised with these photo absorbent materials, such as ternary and designed for multifunctional applications such as agrivoltaic, heat-resistant devices, floating photovoltaics (FPVs), solar glasses, and automobile sunroofs, are also discussed. Kini et al. (2021) provide guidelines for synthesising efficient photo-absorbent materials for ST-OSCs and briefly discuss design strategies to inspire novel ideas that could propel this fascinating field forward (Kini et al. 2021). As the primary application of ST-OSCs, BIPV remains the first and most important choice. A BIPV is an integral part of a building; it can use a portion of the sunlight to power harvesting-related activities while transmitting the remaining light to brighten the interior of the building, allowing for the productive use of renewable solar energy in large areas such as exterior walls or windows, fences, and parking roofs (Attoye et al., 2018; Costanzo et al., 2018; Suragtkhuu et al., 2023; Yang & Zou, 2016).

The use of PV technology has been growing throughout time in a variety of fields, including agriculture. PV technology is well known as an alternative for providing electrical energy that is clean and renewable. Agrivoltaics is a brand-new area of study and technological advancement that has gained popularity recently. The research and creation of integrated systems for the co-existence of crop cultivation and PV energy production on the same plot of land are the main goals of agrivoltaic (Torres et al., 2022). Agrivoltaic is expected to address significant issues like the limited amount of land available, the need for more managed, sustainable, and climate-resilient agriculture, and the need for clean electricity generation systems caused by the sharp rise in global population and climate change. Combining commercial agriculture and photovoltaic electricity production on the same land (agrivoltaic) is an increasingly researched area to increase overall land productivity in an increasingly densely populated world (Mitali et al., 2022).

Previous research has shown that using land for both PV and agriculture creates a mutually beneficial partnership that provides farmers with unique market opportunities while lowering operation and maintenance fees for solar developers, mainly when grazing livestock is used (Barron-Gafford et al., 2019; Guerin, 2019; Santra et al., 2017). The growing land footprint of solar PV presents social and spatial challenges, exacerbating the competition for land between agriculture and energy production.

This research aims to create a mathematical model that represents the relationship between global irradiation and STPV energy production; with this model, the average monthly energy production can be estimated according to the global value of irradiation, shows the performance of STPV during installation, and its use in the agricultural sector.

Along with the discussion before, it should be mentioned that the electricity output from semi-transparent photovoltaic systems might decline for several reasons. The following are a few possible explanations:

a. Transparency Trade-Offs: semi-transparent PV systems are made to let some light through while producing electricity. However, transparency frequently comes at the expense of efficiency in energy conversion. The amount of sunlight a substance can convert into power decreases with increasing transparency. From technical specifications, the transparency of the semi-transparent photovoltaic is 20%, with a module conversion efficiency of 17.3%. The transparent percentage in semi-transparent photovoltaics measures how much light can pass through the material while it still generates electricity. Transparency in semi-transparent photovoltaic (PV) materials refers to the capacity to generate electricity while letting light through. The transparent percentage would then measure the light passing through the material. The challenge is to balance transparency with efficiency and other performance considerations for specific applications.

Fig. 3 shows the average visible transmittance and conversion efficiency for different photovoltaic technology. Semi-transparent solar cells require some incident light to pass through the material before being absorbed to generate electricity; hence, their efficiency is typically lower than that of opaque solar cells.

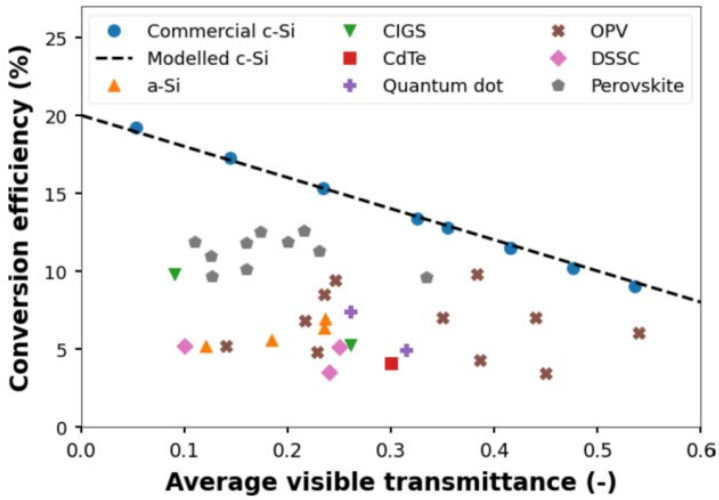

Figure 3. Conversion efficiency as a function of the average visible transmittance of different PV technologies (Fernández et al., 2022).

b. Material Properties: Compared to conventional opaque PV cells, the materials utilised in semi-transparent PV cells could be less efficient. Materials that permit visible light to flow through are used to achieve transparency; moreover, these materials might be less effective in absorbing. The material used in this semi-transparent photovoltaic

system is high-power monocrystalline, the most common solar cell technology (Zsiborács et al., 2023).

c. Design and Technology Limitations: Semi-transparent PV technology cannot be as sophisticated as conventional. Semi-transparent PV systems with higher efficiency may become available in the future thanks to developments in design and materials.
d. Orientation and Positioning: The orientation and placement of semi-transparent PV panels are fundamental. The panels will produce less energy if they are not positioned to receive sunlight as much as possible.
e. Environmental Factors: Semi-transparent photovoltaic panels may receive less sunlight due to external obstacles like trees, buildings, or other objects blocking their view, which lowers the energy production of the panels.
f. Maintenance and Cleaning: For maximum light penetration and transparency, semi-transparent surfaces might need to be cleaned more frequently. Light transmission can be impeded, and energy output can be decreased by surface dirt, dust, or other pollutants.
g. Age and Degradation: Environmental exposure can cause PV materials to deteriorate over time, decreasing energy production. Every kind of solar panel performs similarly due to this aspect.

2. Experimental

The setup experiment and technical specification

Experimental setup for this study was collected from semi-transparent photovoltaic modules installed in front of the Aula Building of the Hungarian University of Agriculture and Life Sciences, Gödöllő, Hungary, at latitude 47.5946° N, 19.3619° E. Fig. 4 shows the modules, the systems consist of 2 parts of 10 pieces 165 Wp Solarwatt Vision with 3,3 kWp. Semi-transparent photovoltaic modules were oriented south with an inclination that matched the site and angled to a fixed physical support outside the Aula building (Anggraeni et al., 2022, 20223). System production data collected from 2017 – 2021 was recorded at https://monitoring.solaredge.com/.

Figure 4. The location of the semi-transparent photovoltaic PV system

The general data specification of the installed semi-transparent photovoltaic system is presented in Table 1.

Table 1. General data of the semi-transparent photovoltaic system

Module technology	Glass-glass laminated
Covering material	Partially tempered high transparent float glass with anti-reflective finish, 4 mm.
Encapsulation	Solar cells in polymer encapsulation, transparent
Backing material	Partially tempered float glass, 4 mm
Transparent areas	Approximately 20 %
Solar cells	36 monocrystalline high-power PERC-solar cells
Cell dimensions	157 × 157 mm
L x W x H / Weight	1,550 x 710 x 9 mm / 25 kg
Connection technology	Cables 2 x 0,45 m/4 mm^2
Bypass diode	2
Max. system voltage	1,000 V

Electrical data for STPV with STC: Irradiation intensity 1000 W/m^2, spectral distribution AM 1,5, temperature (25 ± 2) °C, is shown in Table 2. For electrical data, load operation in nominal power for nominal module operating temperature (NMOT) P_{max} is 137 W (irradiation intensity 800 W/m^2; spectral distribution AM 1.5; Temperature 25 °C; wind speed 1 m/s.

Table 2. Semi-transparent photovoltaic electrical data

Details	Symbol	Value
Nominal power	P_{max}	190 Wp
Nominal voltage	V_{mp}	20.6 V
Nominal current	I_{np}	9.31 A
Open circuit voltage	V_{oc}	25.0 V
Short circuit	I_{sc}	9.76 A
Module efficiency		17.3 %

Details of the thermal features of semi-transparent photovoltaic is presented in Table 3.

Table 3. Thermal features for semi-transparent photovoltaic

Details	Value
Operating temperature range	-40 … +85 ℃
Ambient temperature range	-40 … +45 ℃
Temperature coefficient P_{max}	-0.38 %/K
Temperature coefficient V_{oc}	-0.31 %/K
Temperature coefficient I_{sc}	0.05 %/K
NMOT	44 ℃

Electrical data for nominal module operating temperature (NMOT) with irradiation 800 W/m^2, spectral distribution AM 1.5, temperature 20 ℃, the nominal temperature P_{max} is 141 W. Nominal power for weak conditions with irradiation intensity 200 w/m^2, temperature 25 ℃, wind speed 1 m/s, and load operation is 37.9 W.

Mathematical model

The global irradiation data in Table 4 is used to model the equation between global irradiation and energy production from semi-transparent photovoltaics; data was taken using PVsyst 6.7.0 in 2019. Global irradiation data can be used to

estimate equations showing the relationship between global irradiation and energy production from semi-transparent photovoltaics.

Table 4. Geographical site parameters for Gödöllő (PVsyst 6.7.0) (Kafui et al., 2019)

Period	**Global Irradiation ($kWh.m^{-2}.d^{-1}$)**	**Diffuse Irradiation ($kWh.m^{-2}.d^{-1}$)**	**Temperature (°C)**	**Wind speed ($m.s^{-1}$)**
January	0.97	0.69	-0.6	2.78
February	1.84	0.94	1.1	3.00
March	2.93	1.46	5.6	3.41
April	4.41	2.08	11.7	3.10
May	5.53	2.44	17.1	2.99
June	5.99	3.00	19.6	2.89
July	5.98	2.85	21.8	3.09
August	5.00	2.22	21.3	2.71
September	3.60	1.81	15.6	2.61
October	2.31	1.19	11.3	2.6
November	1.14	0.73	5.7	3.00
December	0.81	0.51	0.2	2.49
Year Average	**3.38**	**1.66**	**10.9**	**2.49**

Data on average global energy production is shown in Fig. 5, and global irradiation in Table 4 is used to determine the mathematical model. This mathematical model can estimate average energy production using global irradiation data obtained in Fig. 6. Monthly in-plane irradiation for fixed angle in Gödöllő is generated from Fig. 6 and used for estimating average energy production in 2023.

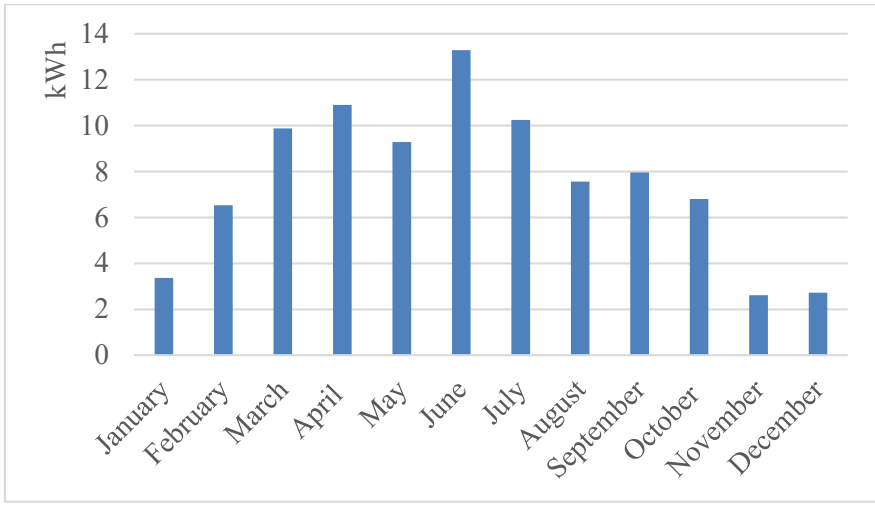

Figure 5. Average energy production for the year 2019

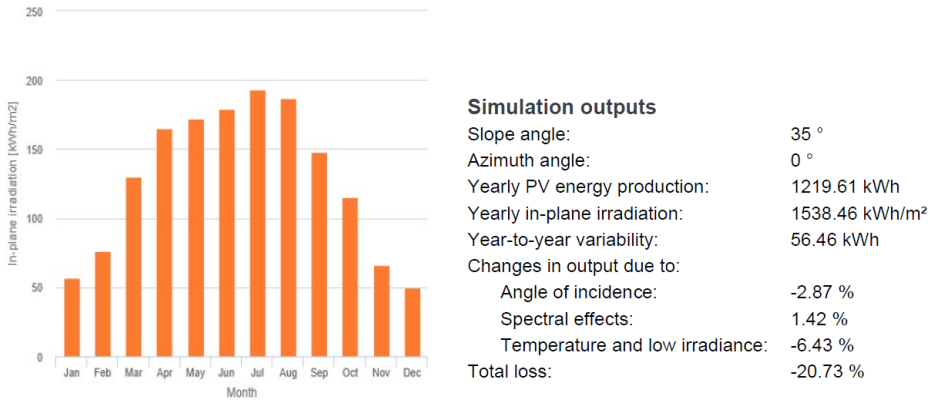

Figure 6. Monthly in-plane irradiation for fixed-angle **(European Commission, 2023)**

3. RESULTS AND DISCUSSION

Total energy production from semi-transparent photovoltaic

Total energy production recorded from the installed semi-transparent photovoltaic system for the period of 2017 – 2021 can be seen in Fig. 7, which shows that energy production in 2017 and 2021 is incomplete for 12 months. The first recorded data in 2017 started in June, and the last recorded data in 2021 was in October.

Generally, it can be concluded that solar panels perform better in colder climates. Even though there may be less sunlight throughout the winter, the

lower temperatures can increase solar panel efficiency, somewhat making up for the decreased sunlight. It is simply in connection with the classical characteristics of the Pv cells. Depending on the tilt of the Earth's axis and its orbit around the sun, the amount of sunlight that reaches the Earth's surface varies throughout the year.

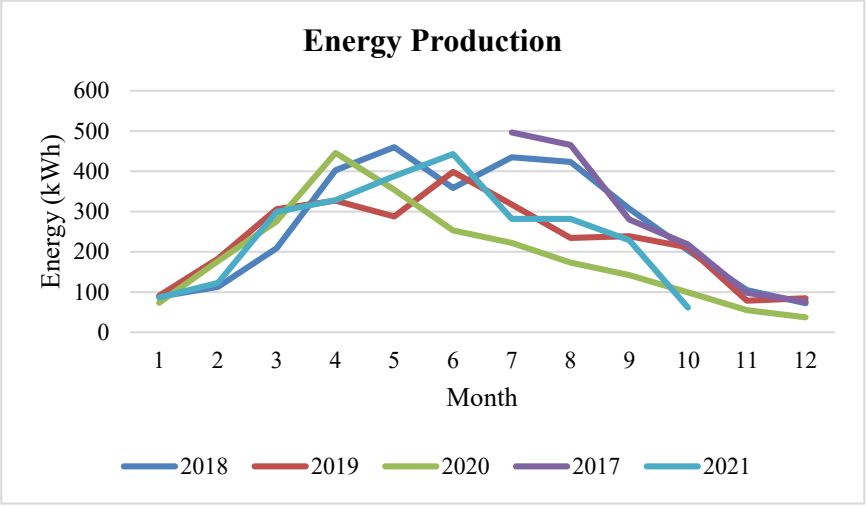

Figure 7. Monthly energy production from 2017 – 2021

The total energy data produced by STPV in 2017 and 2021 is incomplete. Energy production data produced in 2018 - 2020 is shown in Fig. 8. The average monthly energy data for 2019, shown in Fig. 5, is used to model the relationship between global irradiation and average energy production in semi-transparent photovoltaics.

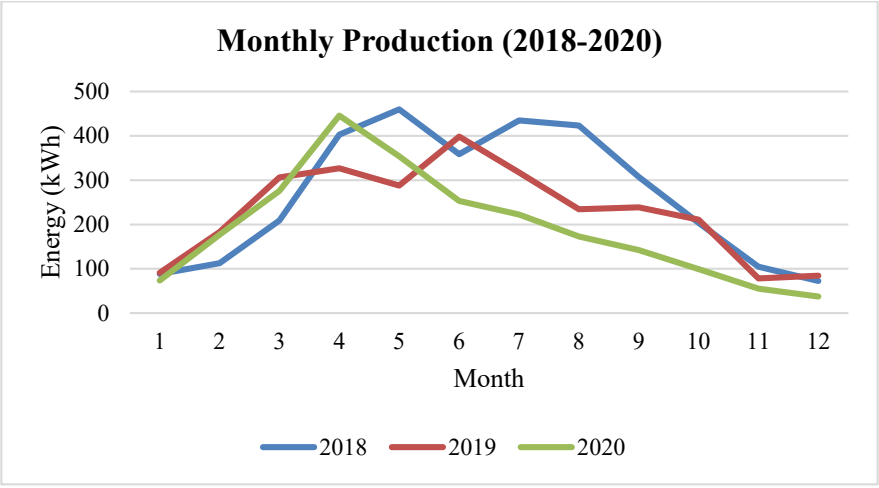

Figure 8. Energy production semi-transparent photovoltaic for the year 2018-2020

A similar pattern can be seen in the average energy production, which is higher in months with higher global irradiation and lower in months with lower global irradiation. June has the highest average energy production (13285.13 Wh), with July and April closely behind. Both the average energy production and global irradiation exhibit a distinct seasonal pattern. The highest energy production typically occurs in June and July, with longer daylight hours and stronger solar radiation. On the other hand, months like December and January, with fewer days and less solar intensity, produce less energy.

Fig. 9 was created using global irradiation data from 2019 (presented in Table 1). The average energy production value for semi-transparent photovoltaics was compared to global irradiation data in 2019. An equation was then modelled using these two data sets to predict the average energy production in semi-transparent photovoltaics using monthly global irradiation data based on the location used. With the mathematical model provided in Fig. 9, y = 1096.4x, the estimated energy production from semi-transparent photovoltaic is shown in Table 5.

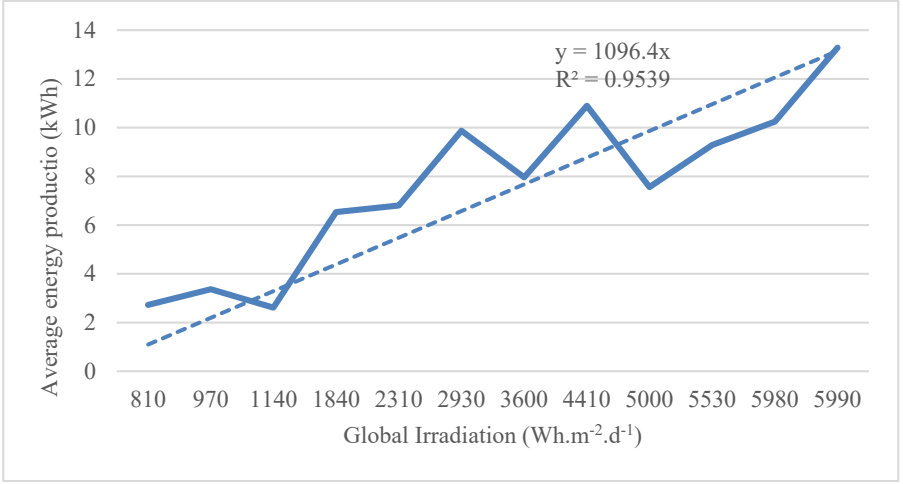

Figure 9. Model prediction for energy production

Table 5. Estimated monthly average energy production for the year 2023

Month	Global Irradiation (kWh/m^2)	Estimated average energy production (Wh)
January	56.9	62385.16
February	76.2	83545.68
March	130.2	142751.28
April	164.7	180577.08
May	171.7	188251.88
June	179.3	196584.52
July	193.4	212043.76
August	186.7	204697.88
September	148.2	162486.48
October	115.0	126086.00
November	66.3	72691.32
December	49.8	54600.72

The data shows a seasonal trend, with summer (June, July, and August) seeing higher global irradiation and estimated average energy production and winter seeing lower values (December, January, and February). Global irradiation and estimated energy production show a significant increase in March and April as spring approaches. December has the lowest values, suggesting less solar radiation and energy production during the winter solstice. Sunlight intensity usually increases in the summer and decreases in the winter in many places. This variation in sunlight intensity directly impacts the amount of energy solar panels produce. They are considering seasonal fluctuations in solar energy availability when developing the solar energy systems, which is crucial. It also draws attention to the possibility of increased energy output in the months with more sunlight.

Average energy production comparison

Average annual energy production for 2018 - 2020 is shown in Table 6.

Table 6. Average energy production for semi-transparent photovoltaic for the year 2018-2020.

Year	Average energy production (kWh)
2018	264,80
2019	229,83
2020	192,32

From Table 6, it can be seen that the declining trend in the mean energy output between 2018 and 2020 points to decreased energy production during these years. Energy production in 2019 decreased by 13.2% from energy production in 2018. In 2018, the average energy produced was 264.80 kWh; in 2019, it was 229.83 kWh, a decrease of 34.97 kWh. Meanwhile, the average energy produced in 192.32 kWh decreased by 72.48 kWh or around 27.4%. Several things, including variations in energy production efficiency, sources of energy, and demand changes, could cause this. The estimated average energy production per year for semi-transparent photovoltaic from Table 4 is 140558.48 Wh.

4. Conclusions

The average energy production and global irradiation follow a seasonal pattern, with June producing the most (13285.13 Wh), followed by July and April. With longer daylight hours, energy production is highest in June and July. The data show a seasonal trend, with summer having higher global irradiation and energy production and winter having lower values. Solar energy production is highest in March and April, with the lowest values in December. This seasonal variation is critical for the development of solar energy systems. Between 2018 and 2020, the average energy output decreased by 13.2 %, with an average of 229.83 kWh in 2019 and 192.32 kWh in 2020. This decrease can be attributed to factors such as energy production efficiency, energy sources, and changes in demand. Due to transparency trade-offs, material properties, design and technology limitations, orientation and positioning, environmental factors, maintenance and cleaning, and age and degradation, semi-transparent photovoltaic (PV) systems may experience a decrease in energy output. Transparent PV systems may receive less sunlight due to obstructions, and their efficiency may suffer from surface dirt, dust, or pollutants. Future design and material advancements may result in more efficient semi-transparent PV systems.

Acknowledgements

This work was supported by the Stipendium Hungaricum Programme and by the Mechanical Engineering Doctoral School, Hungarian University of Agriculture and Life Sciences, Gödöllő, Hungary.

References

[1] Ajitha, A., Kumar, N. M., Jiang, X. X., Reddy, G. R., Jayakumar, A., Praveen, K., & Anil Kumar, T. (2019). Underwater performance of thin-film

photovoltaic module immersed in shallow and deep waters along with possible applications. Results in Physics, 15. https://doi.org/10.1016/j.rinp.2019.102768

[2] Alghamdi, A. S., Bahaj, A. B. S., & Wu, Y. (2017). Assessment of large scale photovoltaic power generation from carport canopies. Energies, 10(5). https://doi.org/10.3390/en10050686

[3] Amber, K. P., Hussain, I., Kousar, A., Bashir, M. A., Aslam, M. W., & Akbar, B. (2019). A self-cleaning device for pole mounted solar PV installations. Thermal Science, 23. https://doi.org/10.2298/TSCI170401065A

[4] Anggraeni, N. D., Seres, I., & Farkas, I. (2022). Approaches to the performance evaluation of semi-transparent photovoltaic modules. Mechanical Engginering Letters, 22(1), 116–124.

[5] Anggraeni, N. D., Seres, I., & Farkas, I. (20223). Monthly average solar energy generated by semi-transparent solar modules. BioPhys Spring 2023, 22nd International Workshop for Young Scientists, 19.

[6] Araki, K., Ota, Y., & Yamaguchi, M. (2020). Measurement and modeling of 3D solar irradiance for vehicle-integrated photovoltaic. Applied Sciences (Switzerland), 10(3). https://doi.org/10.3390/app10030872

[7] Asanov, I. M., & Loktionov, E. Y. (2018). Possible benefits from PV modules integration in railroad linear structures. Renewable Energy Focus, 25, 1–3. https://doi.org/10.1016/j.ref.2018.02.003

[8] Attoye, D. E., Adekunle, T. O., Aoul, K. A. T., Hassan, A., & Attoye, S. O. (2018). A conceptual framework for a Building Integrated Photovoltaics (BIPV) Educative-communication approach. Sustainability (Switzerland), 10(10). https://doi.org/10.3390/su10103781

[9] Attoye, D. E., Aoul, K. A. T., & Hassan, A. (2017). A review on building integrated photovoltaic façade customisation potentials. In Sustainability (Switzerland) (Vol. 9, Issue 12). MDPI. https://doi.org/10.3390/su9122287

[10] Barron-Gafford, G. A., Pavao-Zuckerman, M. A., Minor, R. L., Sutter, L. F., Barnett-Moreno, I., Blackett, D. T., Thompson, M., Dimond, K., Gerlak, A. K., Nabhan, G. P., & Macknick, J. E. (2019). Agrivoltaics provide mutual benefits across the food–energy–water nexus in drylands. Nature Sustainability, 2(9), 848–855. https://doi.org/10.1038/s41893-019-0364-5

[11] Campos, J., Csontos, C., & Munkácsy, B. (2023). Electricity scenarios for Hungary: Possible role of wind and solar resources in the energy transition. Energy, 278. https://doi.org/10.1016/j.energy.2023.127971

[12] Costanzo, V., Yao, R., Essah, E., Shao, L., Shahrestani, M., Oliveira, A. C., Araz, M., Hepbasli, A., & Biyik, E. (2018). A method of strategic evaluation of energy performance of Building Integrated Photovoltaic in the urban context. Journal of Cleaner Production, 184, 82–91. https://doi.org/10.1016/j.jclepro.2018.02.139

[13] European Commission. (2023). https://joint-research-centre.ec.europa.eu/

[14] Fan, Z., Xiao, Z., & Liu, J. (2022). Energy performance assessment of semi-transparent photovoltaic integrated large-scale railway stations among various climates of China. Energy Conversion and Management, 269. https://doi.org/10.1016/j.enconman.2022.115984

[15] Fernández, E. F., Villar-Fernández, A., Montes-Romero, J., Ruiz-Torres, L., Rodrigo, P. M., Manzaneda, A. J., & Almonacid, F. (2022). Global energy assessment of the potential of photovoltaics for greenhouse farming. Applied Energy, 309. https://doi.org/10.1016/j.apenergy.2021.118474

[16] Gholami, H., Nils Røstvik, H., Manoj Kumar, N., & Chopra, S. S. (2020). Lifecycle cost analysis (LCCA) of tailor-made building integrated photovoltaics (BIPV) façade: Solsmaragden case study in Norway. Solar Energy, 211, 488–502. https://doi.org/10.1016/j.solener.2020.09.087

[17] Guerin, T. F. (2019). Impacts and opportunities from large-scale solar photovoltaic (PV) electricity generation on agricultural production. Environmental Quality Management. https://doi.org/10.1002/tqem.21629

[18] Kafui, A. D., Seres, I., & Farkas, I. (2019). Efficiency Comparison of Different Photovoltaic Modules. Acta Technologica Agriculturae, 22(1), 5–11. https://doi.org/10.2478/ata-2019-0002

[19] Kini, G. P., Jeon, S. J., & Moon, D. K. (2021). Latest Progress on Photoabsorbent Materials for Multifunctional Semitransparent Organic Solar Cells. Advanced Functional Materials, 31(15). https://doi.org/10.1002/adfm.202007931

[20] Kumar, N. M., Chopra, S. S., Malvoni, M., Elavarasan, R. M., & Das, N. (2020). Solar cell technology selection for a pv leaf based on energy and sustainability indicators-a case of a multilayered solar photovoltaic tree. Energies, 13(23), 6439–6462. https://doi.org/10.3390/en13236439

[21] Kumar, N. M., Subramaniam, U., Mathew, M., Ajitha, A., & Almakhles, D. J. (2020). Exergy analysis of thin-film solar PV module in ground-mount, floating and submerged installation methods. Case Studies in Thermal Engineering, 21. https://doi.org/10.1016/j.csite.2020.100686

[22] Kumar, N. M., Sudhakar, K., & Samykano, M. (2019). Performance comparison of BAPV and BIPV systems with c-Si, CIS and CdTe photovoltaic technologies under tropical weather conditions. Case Studies in Thermal Engineering, 13. https://doi.org/10.1016/j.csite.2018.100374

[23] Kumar, N. M., Yadav, S. K., Chopra, S. S., Bajpai, U., Gupta, R. P., Padmanaban, S., & Blaabjerg, F. (2020). Operational performance of on-grid solar photovoltaic system integrated into pre-fabricated portable cabin buildings in warm and temperate climates. Energy for Sustainable Development, 57, 109–118. https://doi.org/10.1016/j.esd.2020.05.008

[24] Mitali, J., Dhinakaran, S., Mohamad, A. A., Kumar, M. M. M., Haillot, D., Gibout, S., Junedi, M. M., Ludin, N. A., Hamid, N. H., Kathleen, P. R., Hasila, J., Affandi, N. A. A., Gorjian, S., Sharon, H., Ebadi, H., Kant, K., Scavo, F. B., Tina, G. M., Choab, N., … Senthil, R. (2022). Outdoor behaviour of organic photovoltaics on a greenhouse roof. Renewable and Sustainable

Energy Reviews, 52(4), 100641. https://doi.org/https://doi.org/10.1016/j.gsd.2020.100360

[25] Pintér, G., Zsiborács, H., Baranyai, N. H., Vincze, A., & Birkner, Z. (2020). The economic and geographical aspects of the status of small-scale photovoltaic systems in hungary-a case study. Energies, 13(13). https://doi.org/10.3390/en13133489

[26] Prasad, K. A., Chand, A. A., Kumar, N. M., Narayan, S., & Mamun, K. A. (2022). A Critical Review of Power Take-Off Wave Energy Technology Leading to the Conceptual Design of a Novel Wave-Plus-Photon Energy Harvester for Island/Coastal Communities' Energy Needs. In Sustainability (Switzerland) (Vol. 14, Issue 4). MDPI. https://doi.org/10.3390/su14042354

[27] Reddy, P., Surendra Gupta, M. V. N., Nundy, S., Karthick, A., & Ghosh, A. (2020). Status of BIPV and BAPV system for less energy-hungry building in India-a review. In Applied Sciences (Switzerland) (Vol. 10, Issue 7). MDPI AG. https://doi.org/10.3390/app10072337

[28] Santra, P., Pande, P., Kumar, S., Mishra, D., & Singh, R. (2017). Agri-voltaics or Solar farming: the Concept of Integrating Solar PV Based Electricity Generation and Crop Production in a Single Land use System (Vol. 7, Issue 2). http://pveducation.org/]:

[29] Suragtkhuu, S., Sunderiya, S., Myagmarsereejid, P., Purevdorj, S., Bati, A. S. R., Bold, B., Zhong, Y. L., Davaasambuu, S., & Batmunkh, M. (2023). Graphene-Like Monoelemental 2D Materials for Perovskite Solar Cells. In Advanced Energy Materials. John Wiley and Sons Inc. https://doi.org/10.1002/aenm.202204074

[30] Szabo, J., Weiner, C., & Deák, A. (2021). Energy Governance in Hungary. In Handbook of Energy Governance in Europe (pp. 1–32). Springer International Publishing. https://doi.org/10.1007/978-3-319-73526-9_13-2

[31] Torres, M., Burgos, C., Casagrande, D., Munoz, D., Pinto, M., Candia, G., Reyes, H., Acuna, B., & Section, A. C. de I. de C. A. G. ; I. C. C. S. I. C. S. (2022). The Photovoltaic Greenhouse as Energy Hub for a More Sustainable Agriculture. 2022 IEEE International Conference on Automation/25th Congress of the Chilean Association of Automatic Control, ICA-ACCA 2022. https://doi.org/10.1109/ICA-ACCA56767.2022.10006135

[32] Yang, R. J., & Zou, P. X. W. (2016). Building integrated photovoltaics (BIPV): Costs, benefits, risks, barriers and improvement strategy. International Journal of Construction Management, 16(1), 39–53. https://doi.org/10.1080/15623599.2015.1117709

[33] Zhu, Y., Shu, L., & Fan, Z. (2020). Recent Progress on Semi-transparent Perovskite Solar Cell for Building-integrated Photovoltaics. Chemical Research in Chinese Universities, 36(3), 366–376. https://doi.org/10.1007/s40242-020-0105-3

[34] Zsiborács, H., Vincze, A., Háber, I., Pintér, G., & Hegedűsné Baranyai, N. (2023). Challenges of Establishing Solar Power Stations in Hungary. Energies, 16(1). https://doi.org/10.3390/en16010530.

The effect of the functional components on the efficiency of a modular solar drying system

QuanKun ZHU[1], János BUZÁS[2], István FARKAS[2]
[1] *Doctoral School of Mechanical Engineering,*
Hungarian University of Agriculture and Life Sciences, MATE, Gödöllő
[2] *Department of Mechatronics, Institute of Technology* MATE, Gödöllő

Abstract

Introduce the purpose and significance of the study. The literature review outlines the influence of various functional components and system modes on the system. By analyzing the conclusions, suitable research directions are identified. The results are obtained through analysis using ANSYS FLUENT software. Subsequently, the experimental results are compared and validated against the simulation results to derive the final conclusion.

Keywords

functional components, efficiency, solar drying system

1. Introduction

Due to the economic development and rapidly growing energy demand in some countries, as well as the fluctuation of fossil fuel prices, environmental issues and the expected depletion of traditional fossil fuels, the search for alternative energy sources has become an important issue in today's society. Solar energy is an unlimited energy resource. As a renewable energy source, it has attracted much attention from researchers because of its smaller impact on the environment and its more sustainable characteristics. Currently, various types of solar drying systems are available for processing agricultural products (Fudholi et al., 2010). With the development and application of solar drying becoming more and more widespread, many studies have focused on the efficiency of solar drying system. Research on improving the efficiency of solar drying systems from various aspects, such as solar air collectors, drying chambers, chimneys, different drying systems, etc. In order to lay a solid theoretical foundation for promoting solar drying. Solar air collector (SAC) is a device that uses solar energy to collect heat energy. Its working principle is based on the process of absorbing and converting solar radiation into heat energy. The performance level of solar air collectors can be improved through a variety of technologies, such as the change of air flow pattern, absorber design, air flow pass and absorber materials (Vengadesan and Senthil., 2020). A drying chamber is an enclosed

space specifically designed to remove moisture or dry a variety of materials. The shape and number of drying chambers can affect the efficiency of the drying system. A chimney is a ventilation device used to achieve air circulation and natural ventilation. The performance level of solar drying system can be improved through changes of the size and internal structure of chimneys.

The main objective is to use the results of literature survey to design relevant experiments and analyze which functional components have the greatest impact on the efficiency of the drying process. According to the objective, design relevant experiments, control variables, and then change the necessary settings of functional components such as collectors, drying chambers, and chimneys for comparative experiments. Select appropriate predictive models and propose recommendations to maximize efficiency.

2. Literature review

The mode of the solar drying system is an important factor that affects the efficiency of the solar drying system. Solar drying systems are typically classified into two modes based on their system designs, as illustrated in Figure 1. The natural mode drying system represents a simple and cost-effective approach to harnessing solar energy for the drying of fruits, vegetables, grains, and various other products. In this model, the drying process relies on the heat generated by solar energy and the natural convection of air. Notably, it accomplishes the entire drying process without the necessity for supplementary electricity or mechanical equipment, making it an environmentally friendly and energy-efficient solution (Sansaniwal and Kumar., 2015). Forced mode involves expediting the drying process by employing forced airflow or alternative methods. In this mode, the system utilizes fans, ventilation, or other mechanical devices to enhance airflow, consequently elevating the evaporation rate from moist surfaces. This approach facilitates a more efficient completion of the drying process (El-Sebaii and Shalaby., 2013).

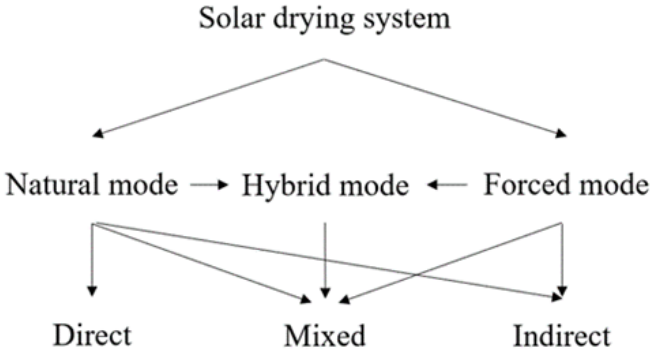

Figure 1. The classification of solar drying systems

Solar air collector is the major component of solar drying system which absorbs the incoming solar radiation, converts it into thermal energy and supplied to the drying chamber to dry the items. The efficiency of the solar collector can directly affect the overall efficiency of the solar drying system (Hu and Zhang., 2019). The efficiency of solar air collectors is influenced by many factors such as absorber design, absorber materials, air flow passes, air flow pattern and PV/T solar air collector. The specific classification of solar air collector is shown as Figure 2.

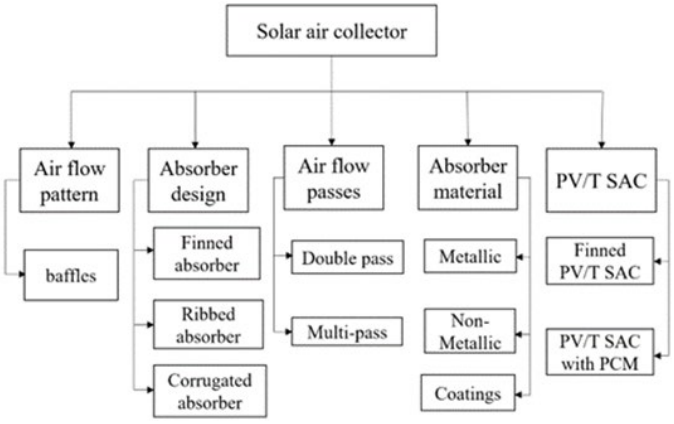

Figure 2. The classification of solar air collector.

Solar air collectors circulate air to absorb solar radiation and deliver it to the area that needs heating. Changes in airflow patterns may affect collector efficiency, heat transfer rates, and overall system thermal performance. The primary method of changing airflow patterns is to introduce baffles. The introduction of baffles can enhance the convection heat transfer process, extend the residence time of air in the collector, allow the air to flow through the collector evenly without generating eddy currents, avoid "heat flow", enhance internal disturbance, and reduce radiation heat loss, thus helping to improve efficiency (Hu et al., 2013). The absorber is the core component of a solar air collector and is used to absorb solar radiation energy. Different shapes of fins or ribs on the absorber, dimpled shaped roughness roughness, inclined discrete rib roughness, inclined transverse rib roughness, and the design of the absorber plate fins improve the convective heat transfer coefficient between air and the absorber, and reduce heat loss to the surrounding environment to enhance thermal efficiency (Singh et al., 2015). The airflow in solar collectors directly affects their performance and efficiency. Common airflow passages include single pass, double pass, and multi-pass. The function of airflow passages is to enhance heat transfer, increase temperature rise, promote uniform temperature distribution, improve efficiency, and reduce heat loss. A single-pass solar air collector (SPSAC) can be defined as a one-way flow from the inlet above or below the absorber plate to the outlet. A double-pass solar air collector (DPSAC)

has two air passages, and the airflow can pass in opposite directions or parallel directions. Compared to single-pass solar air collectors, DPSAC has advantages such as a larger heat exchange area, longer heat exchange time, and lower heat loss. Absorbing materials are responsible for trapping solar radiation and converting it into heat. Absorbing materials can also affect the efficiency of the collector, and its absorption, thermal conductivity, and radiation coefficient are important factors in determining the efficiency of a solar air collector. Common absorbing materials include metals such as aluminium and copper or selective coatings that enhance absorption and reduce emissivity (Jouybari and Lundström., 2020). PV/T solar air collectors are a type of hybrid solar technology that combines photovoltaic (PV) and thermal technologies, capable of generating electricity and heat simultaneously. It aims to effectively capture and utilize solar energy for electricity generation, space heating, agriculture products drying or other lower grade temperature applications (Pang et al., 2020).

The drying chamber is a component of the solar drying system. The drying chamber is a device for drying moist items using solar energy, and it contains the space for placing items. The working principle of the solar dryer is to heat the air using solar energy, and then introduce the heated air into the dryer to dry the items through natural convection. Drying chambers are used in various industries, including agriculture, food processing, pharmaceuticals, and manufacturing, to dry products ranging from fruits and vegetables to grains, herbs, textiles, and more. The chimney is a part of the solar drying system, using solar energy to help dry agricultural products, wood, clothes and other items. The role of the chimney in the drying system is to generate natural airflow to aid the drying process. As moisture is removed from the items being dried, a humid environment is created. The chimney helps to exhaust this moist air from the drying area and replace it with fresh, dry air. In summary, the function of the chimney in the drying system is to produce natural airflow, remove moisture, improve air quality, and help expedite the drying process.

3. Experimental

Experimental instruments

The experimental was carried out at Laboratory of the Hungarian University of Agriculture and Life Sciences, Gödöllő, Hungary (47.59^{o} N, 19.36^{o} E). The experiment involves measuring solar radiation values, system wind speed, humidity and temperature data values. To measure experimental data, we need to use instruments such as a thermocouple and a thermometer, a hygrometer, a pyranometer, and an anemometer. Thermocouples have the characteristics of low cost and easy replacement, and are a widely used temperature sensor. Thermometers instruments specifications is shown in Table 1.

Table 1. Thermometers instruments specifications

Parameter	Details
Temperature range	-200~1372°C
Power supply	9V Battery
Accuracy	>100 °C:±1°C <100 °C:±2°C
K-type thermocouple resolution	<1000°C: 0.1C/ ° F/K
Size	20×8.5×4cm

The anemometer is an instrument used to measure the airflow. Its basic principle involves generating a temperature difference between the heating wire and the fluid, with the fluid passing over the heating wire to transfer heat and carry away heat, allowing the fluid's speed to be determined through heat loss. The experimental instrument as shown in Figure 3. The relative humidity meter is an instrument for measuring humidity. These instruments have a humidity accuracy of 4%, with a measurement range of 10% to 99% relative humidity. The sensor line is 1.5 meters long and the probe is 6 centimeters long. The air humidity instrument is shown in Figure 4. During the experiment, solar radiation is important factor effect on solar drying system, the numerical solar power meters were used to test and record the solar radiation at different times. Its orientation is the same as the tilt angle of the collector. The specifications of solar power meter instrument as shown in Table 2.

Figure 3. Digital anemometer instrument

Figure 4. Air relative humidity

Table 2. Specifications of solar power meter instrument

Parameter	**Details**
Solar irrigation measuring range	1W/m^2 to 1300 W/m^2
Power supply	3LR3-AAA batteries
Operating temperature	-10 to 50 degrees
Frequency of measurement	2/s
Accuracy	5%
Size	20*8.5*4 cm

Solar air collector experiment

The function of the absorber is to absorb solar radiation and convert it into thermal energy for the drying system. Two different placement directions of the fin absorber, horizontal and Incline 45°, are designed in the experiment. The experimental data was collected every 10 minutes during the experiment period. Air speed was 2.3m/s in the solar system by using the inline air blower. The rest of the absorber surface area is the same, and the collector shell is made of wood with dimensions of 120*50*12 cm. Comparative analysis is conducted based on the experimental results (Zhu et al., 2022). The finned absorption surface structure is shown in Figure 5.

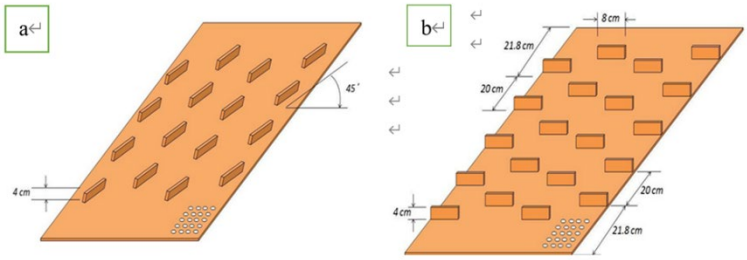

Figure 5. Incline 45° finned absorbing surfaces (a) and horizontal finned absorbing surfaces (b)

4. RESULTS AND DISCUSSION

Useful heat analysis of two collector

Figure 6. shows the variation of energy absorbed by horizontal fins collector and 45° inclined fins collector with time. The maximum solar radiation for inclined fins collector is 1015W/m^2, and for horizontal fins collector, it is 1080W/m^2. The solar radiation of inclined fins collector has always been higher than that of horizontal fins collector, but the useful heat values of the two collectors are not significantly different. This indicates that the horizontal fin collector has a stronger ability to absorb and convert solar radiation than the inclined fin collector.

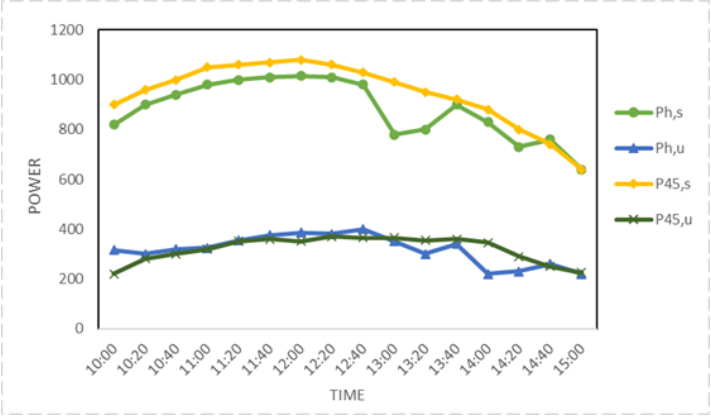

Figure 6. The collector useful heat

The average absorber plate and ambient temperature

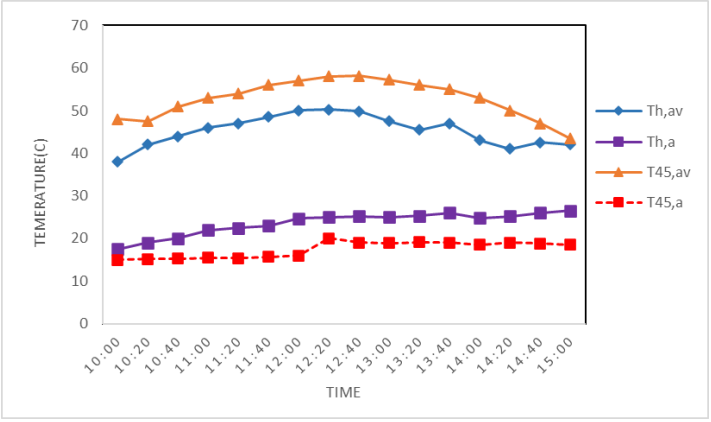

Figure 7. The average absorber surface and ambient temperature

The temperature changes of the two solar collectors over time are shown in Figure 7. For the horizontal fin collector, the average temperature of the absorber surface gradually increases with time, reaching a maximum temperature of 50°C. For the fin collector tilted at 45°, the maximum temperature of the absorber surface is 58°C. The graph shows that the ambient temperature for the horizontal fin collector is consistently higher than that for the inclined fin, but the absorber surface temperature of the inclined fin is consistently higher than that of the horizontal fin collector, indicating a larger amount of solar radiation absorbed.

The efficiency of two collectors

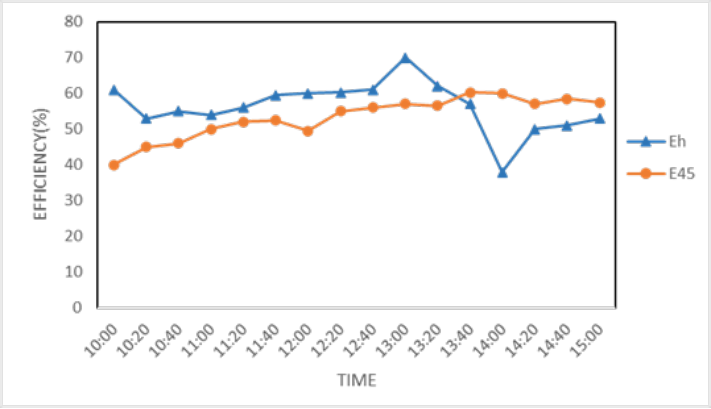

Figure 8. The efficiency of two collectors

Figure 8. shows the efficiency of horizontal and inclined fin collectors. The maximum efficiency of the horizontal fin collector is 70%, and the minimum

efficiency is 40%. The efficiency of the inclined fin collector is lowest at 40% and reaches a maximum of around 60%. Inclined-fin collector efficiency shows steady upward trend. The efficiency of the horizontal fin collector is higher than that of the inclined fin collector.

Future plans for experiments: On a sunny day in April or May, adjust the parameters of the solar air collector (different fin or rib absorbers), drying chamber (different size or shape) and the relevant parameters of the chimney (length, shape, air gap or the ratio of the drying chamber floor to the chimney cro-sectional area) to conduct several sets of experiments, comparing and analyzing their impact on the system's drying efficiency, and drawing relevant conclusions.

5. CONCLUSIONS

- From the above detailed investigations, the following conclusions can be drawn:
- In the same conditions, the forced mode of the solar energy drying system has higher drying efficiency than the natural mode and open-air drying. Some studies suggest that the efficiency of forced mode increases by about 10-20% compared to the natural mode.
- Compare to flat plate absorbers, by setting fins add to the heating plate to increase the heat transfer area, improve the convective heat transfer coefficient, and thus enhance the thermal efficiency.
- Double-pass/multi-pass SAC has the characteristics of more air passage times, larger heat exchange area, longer heat exchange time, and lower heat loss. Under the same operating conditions, DPSAC is about 10-15% more efficient than SPSAC arrangement.
- The temperature of the upper channel of the double pass air collector is higher than that of the lower channel in the experiment. The horizontal fin collector has a better ability to absorb and convert solar radiation energy. The average efficiency of horizontal fin collector is higher than inclined fin collector.

This work was supported by the Stipendium Hungaricum Programme and by the Doctoral School of Mechanical Engineering, Hungarian University of Agriculture and Life Sciences, Gödöllő, Hungary.

References

[1] Fudholi, A., Sopian, K., Ruslan, M. H., Alghoul, M. A., & Sulaiman, M. Y. (2010). Review of solar dryers for agricultural and marine products. Renewable and sustainable energy reviews, 14(1), 1-30.

[2] Vengadesan, E., & Senthil, R. (2020). A review on recent developments in thermal performance enhancement methods of flat plate solar air collector. Renewable and Sustainable Energy Reviews, 134, 110315.

[3] Sansaniwal, S. K., & Kumar, M. (2015). Analysis of ginger drying inside a natural convection indirect solar dryer: An experimental study. Journal of Mechanical Engineering and Sciences, 9, 1671-1685.

[4] El-Sebaii, A. A., & Shalaby, S. M. (2013). Experimental investigation of an indirect-mode forced convection solar dryer for drying thymus and mint. Energy conversion and management, 74, 109-116.

[5] Hu, J., & Zhang, G. (2019). Performance improvement of solar air collector based on airflow reorganization: A review. Applied Thermal Engineering, 155, 592-611.

[6] Hu, J., Sun, X., Xu, J., & Li, Z. (2013). Numerical analysis of mechanical ventilation solar air collector with internal baffles. Energy and Buildings, 62, 230-238.

[7] Singh, S., Chander, S., & Saini, J. S. (2015). Thermo-hydraulic performance due to relative roughness pitch in V-down rib with gap in solar air heater duct—comparison with similar rib roughness geometries. Renewable and Sustainable Energy Reviews, 43, 1159-1166

[8] Jouybari, N. F., & Lundström, T. S. (2020). Performance improvement of a solar air heater by covering the absorber plate with a thin porous material. Energy, 190, 116437.

[9] Pang, W., Cui, Y., Zhang, Q., Wilson, G. J., & Yan, H. (2020). A comparative analysis on performances of flat plate photovoltaic/thermal collectors in view of operating media, structural designs, and climate conditions. Renewable and Sustainable Energy Reviews, 119, 109599.

[10] Zhu QuanKun, Buzás János, Farkas István.: Effect of air collector structure on the efficiency of a solar dryer, Mechanical Engineering Letters, Gödöllő, Hungary, 2022, Vol. 23, pp. 59-67. HU ISSN 2060-3789

Application of plant growth chamber to evaluate agrotechnical potential of Mars and Lunar regolith

Jessica Ellen LIMA[1], György BARKÓ[2],
Réka OSZLANYI[2], Kate KRISTÓF[3]
[1] *Doctoral School of Mechanical Engineering,*
Hungarian University of Agriculture and Life Sciences, MATE, Gödöllő
[2] *Department of Chemistry, Institute of Mathematics and Basic Sciences,* MATE, Gödöllő
[3] *Institute of Horticultural Sciences,* MATE Budai Campus

Abstract

Future manned missions to the Moon and especially to Mars must address the challenge of having large food availability, presenting a significant logistical obstacle. In situ resource utilization involves leveraging local resources for food production and obtaining crucial raw materials like water and fuel for these missions. Therefore, this study conducted an experiment using two types of Moon regolith and two types of Mars regolith for planting selected plants based on specific criteria. These plants were cultivated in a chamber with controlled light, temperature, and humidity, without human intervention. It is worth noting that the experiment did not account for the lower atmospheric pressure and significantly lower temperatures present on Mars. However, the development of growing chambers and greenhouses for extraterrestrial exploration is an ongoing research endeavor. Nevertheless, valuable insights into plant survival were gleaned from the regolith experimentation. The experiment was carried out in two phases, during which the regoliths were combined with organic matter in varying ratios (50%, 75%, 90%, and 100%) to serve as substrates for the plants. It was observed that no plants could germinate or survive in 100% Moon and Mars regolith, while plants exhibited better survival rates in Moon regolith.

Keywords

Regolith; Mars; Moon; Chamber; Sensor; Plants

1. Introduction

In future manned missions to Mars, in situ resource utilization will be essential for survival and viability. In situ resource utilization (ISRU) is defined as the conversion of local resources at a space destination to provide valuable infrastructure and commodities (Starr & Muscatello, 2020). The concept is to use as many resources as available in situ, but the challenge lies in the implementation in space, partially because it has never been done before. Examples of practical assets on Mars include the carbon dioxide-rich

atmosphere that can be converted into breathable oxygen, and the Martian soil, or regolith, which can be processed to extract water. In this sense, regolith can also be used as a substrate to cultivate plants for oxygen and alimentation. Additionally, in 2021, NASA reported that the Perseverance rover used its MOXIE technology, Mars Oxygen In-Situ Resource Utilization Experiment, to successfully convert carbon dioxide to oxygen on Mars (NASA, n.d.).

Regolith is the layer of loose, fragmented material that covers the solid bedrock of a planet or Moon. It is found on celestial bodies such as the Moon, Mars, and asteroids. Regolith includes various materials, such as dust, small rocks, and larger boulders. The composition of regolith can vary depending on the location and geological history of the celestial body. Regolith is often compared to the soil as it shares some similarities. However, there are a few key differences between the two. Regolith is a broader term that encompasses any loose, fragmented material found on celestial bodies, including the Moon, Mars, and asteroids (Catling & Leovy, 2007). Conversely, soil refers to the upper layer of the Earth's surface, composed of organic matter, minerals, water, air, and living organisms. Unlike regolith, soil has a more complex structure and contains organic components that support plant growth and microbial activity (Hartemink, 2016).

On the Moon, regolith is primarily made of fine dust particles, referred as lunar soil. This soil results from billions of years of meteorite impacts and volcanic activity. On Mars, regolith contains a mix of dust, sand, and gravel, with different mineral compositions depending on the region.

The soil's relative proportions of sand, silt, and clay particles determine its texture. Dust particles are not considered part of the clay category. Clay particles are thin, smaller than 0.002 mm in diameter, and are a specific type of soil particle separate from dust. Dust is composed of various fine particles, including clay soil particles, organic matter, pollen, pollutants, and other debris. It is typically formed from the disintegration or abrasion of larger particles. Clay, on the other hand, refers to a specific type of soil particle with unique properties. It has a different mineral composition and behaves differently regarding water retention, plasticity, and other characteristics. So, while dust may contain some clay particles, it is not exclusively composed of clay. Therefore, soil particle classification does not encompass the Moon and Mars regolith particle classification, but based on soil particle sizes, Authors Fergason et al. (2006) have modeled the surface of Mars and divided the particle size distribution into dust, sand, and rock. Authors Delage et al. (2017) divide Martian regolith texture into drift, sand, crusty to cloddy sand, blocky indurated soil, dense float rock, clastic rock, sulfate rock, according to bulk density and grain size, and other mechanical properties.

Astronauts have walked on regolith during the missions to the Moon. During the Apollo missions, astronauts walked and conducted experiments on the regolith of the Moon. They described the regolith as fine-grained, powdery, and dusty, often comparing it to talcum powder or fine sand. Walking on the regolith

presented some challenges for astronauts, as it lacked the firmness and stability of solid ground on Earth. Their footprints on the Moon's regolith remained well-preserved due to the absence of wind, water, and significant erosion processes on the lunar surface (Agui & Nakagawa, 2005).

On Mars, the regolith results from impact gardening and various geological processes that have altered the surface layer. Unlike the lunar regolith, the Martian surface layer is also affected by aeolian processes, which sort grains by size and produce rounded grains (Goetz et al., 2010). Therefore, the regolith lacks a distinct structure, behaving like fine sand when dry. However, when wet, the very fine particles become plastic and moldable, eventually forming coherent structures that range from soft mud to solid rocks. The lack of structure and very fine texture of regolith is the first challenge for its use as substrate for growing plants in extraplanetary missions.

The challenges for life on Mars are vast and include extreme temperatures, a thin, unbreathable atmosphere with low pressure, high levels of radiation, and a lack of liquid water. These factors make it difficult for life as we know it to survive on the Martian surface. Mars has a much thinner atmosphere than Earth. Its atmospheric pressure is about 0.6% of Earth's, mainly composed of 95.3% carbon dioxide, 2.7% nitrogen, 1.6% argon, and 0.13% oxygen (Facts About Mars, n.d.). Therefore, a chamber that controls gases, temperature, humidity, and light is required to make cultivating plants, and life on Mars possible. The University of Arizona, in partnership with NASA, presented a prototype of a Lunar/Mars greenhouse. A completely closed, automatic sensor system that aims to mimic the entire Earth's biological system in a smaller scale. The scientists on this project are working on testing the Prototype Lunar Greenhouse to determine what plants, seeds, or other materials should be taken along to make the system work on the moon or Mars. Learning what to take and what to gather on site will be crucial for living in distant locations (NASA, 2023; Kaçıra et al., 2012). One of the primary challenges to address is the assurance of food availability and safety, a critical concern for prolonged space habitation (Cousins & Cockell, 2016). While transporting food is a viable option, the necessity for sustained, locally sourced food production on Mars or the Moon is emerging as a crucial consideration (Graham & Bamsey, 2016).

Various methods for growing crops on these extraterrestrial surfaces are under consideration to tackle this challenge. Hydroponics, the cultivation of plants on inert substances like rock wool using a nutrient solution, is a well-explored option with promising potential, especially given the presence of water, such as ice, on Mars (Hui et al., 2013). Another avenue is aeroponics (Maggi & Pallud, 2010), which requires only a nutrient solution and eliminates the need for additional soil-like material. A third approach involves utilizing the regolith present on Mars or the Moon for crop cultivation, requiring the transportation of only seeds. Regardless of the chosen agricultural method, each option necessitates fundamental equipment, including lamps, racks, solar panels, and habitable structures for sustained human presence.

2. Research significance

In recent decades, space exploration has witnessed a shift towards international cooperation. Organizations like NASA, ESA, Roscosmos, and others have joined forces to undertake collaborative missions, such as the International Space Station (ISS). This multinational endeavor has fostered scientific research and symbolized unity and peaceful cooperation among nations (International Space Station Cooperation - NASA, n.d.). Since the landing of the mission Mars Science Laboratory in 2011, carrying the Curiosity rover, equipped with a spectrometer for chemistry and mineralogy x-ray diffraction (NASA, n.d.), the understanding of Martian regolith chemical and physical properties has considerably improved. This mission goal included an investigation of the Martian climate and geology, an assessment of whether the selected field site, inside the Gale crater located on Mars, has ever offered environmental conditions favorable for microbial life, including a search for water and planetary habitability for human exploration.

However, missions to Mars still need to land and return to Earth. Therefore, there are no samples of Martian regolith physically available. For research purposes, engineers and scientists have relied on the Mars Regolith Simulants (MRS) designed in laboratories over the last 20 years (Cannon et al., 2019). The quality of the simulant is a determining characteristic of the success of experimental trials (Eichler et al., 2021). NASA has announced future missions planned for 2027 and 2028 to take samples from Mars to Earth. Therefore, studies continue to investigate the resources present on Mars and how they can be used in future missions. In current missions to Mars, NASA's Perseverance rover, which landed in February 2021, has its main objectives to collect samples of rock and regolith and prepare for a possible return to Earth (NASA Mars, 2020).

Researching with Moon and Mars regolith holds immense importance for future space missions. The Moon and Mars regolith contain valuable resources such as water, oxygen, and metals. By understanding their composition and properties, researchers develop techniques to extract and utilize these resources, for life support, plant growing, fuel production, and construction. This will enable sustainable, long-duration missions by reducing the need to transport resources from Earth.

In this study, as a partnership with the European Space Agency (ESA), Lunar and Mars regolith was used to investigate the potential of growing plants in regolith without human manipulation, considering its agrotechnical properties. Using a climatic chamber equipped with sensors for measuring the plant production of indicator plants. This research aims to grow indicator plants in Mars and Moon simulants. The plant growth chamber was designed to maintain constant humidity, temperature, standard soil composition, soil moisture, and light. Soil pH, conductivity, and nutrients were monitored.

3. Experimental

Regolith Selection

For testing the use of regolith to cultivate plants in an experiment, samples of Mars regolith simulant closely resembling the composition and properties of Martian soil should be selected. They should consider mineral composition, particle size distribution, and chemical properties.

Several types of Mars regolith simulants were developed based on the data collected by missions that landed on Mars. An updated list of these simulants is available in the Planetary Simulant Database of the Colorado School of Mines (Simulants at Mines - Space Resources Program, 2021). Authors Ramkissoon et al. (2019) state that simulants JSC, JMSS-1, MGS-1, and MMS were designed to be a global chemistry standard for Mars regolith, while simulants P- and S-MRS were the first simulants designed considering chemical variability. Authors Newson et al. (2021) characterized the geomechanical performance of different Lunar simulants. The results of the mechanical property tests showed that the simulants exhibit similar mechanical properties to angular and rough soils. The rough soils consist of shallow, somewhat excessively drained soils formed in residuum from shales, siltstones, and fine-grained sandstones on uplands (Official Series Description - Rough Series, n.d.).

The Mars Global Simulant MGS-1 was created by drawing upon quantitative mineralogy data from the CheMin instrument aboard Curiosity's Mars Science Laboratory. In contrast to predecessors like JSC and MMS, MGS-1 was meticulously synthesized from individual components to emulate the Martian regolith's mineral composition closely. This distinction sets MGS-1 apart as the most accurate basaltic Martian regolith simulant developed thus far, making it a crucial substrate for assessing plant growth and evaluating ISRU opportunities on Mars. MGS-1 is derived from the Gale Crater location Rocknest windblown soil, which is believed to mirror the basaltic soils found in various landing sites and remote sensing locations across Mars. As a result, MGS-1 stands as a representative simulant capturing the average characteristics of a considerably larger surface area of the Red Planet compared to earlier simulants, enhancing its suitability for diverse research applications (Cannon et al., 2019).

According to authors Barkó et al. (2023), MGS-1 represents Mars regolith, functioning as a mineralogical benchmark for basaltic soils discovered on the Red Planet. Constructed using quantitative mineralogy data gathered from the Curiosity rover, it is designed to mirror the soil's composition closely. This particular region data exhibits chemical similarities to other basaltic soils across diverse landing sites on Mars, positioning MGS-1 as a comprehensive and globally applicable representation of Martian basaltic soil. Also, authors Fackrell et al. (2020) concluded that the simulant MGS-1 is a viable option for agricultural studies when considering nutrient and bioavailability.

The Jezero Mars simulant is a recently developed simulant that closely mimics the mineralogical and geochemical properties of the Jezero Crater. The

Exolith Lab meticulously crafted the JEZ-1 simulant to replicate the anticipated materials found in the Jezero Crater deltas—a region of great interest for the NASA Mars 2020 Perseverance rover. As Perseverance explores the Martian surface, its primary mission is to search for signs of ancient life and collect samples of regolith that may eventually be returned to Earth. JEZ-1 is a blend of MGS-1 mineralogy, smectite clay, magnesium carbonate, and additional olivine, all detected through orbital remote sensing. While JEZ-1 represents unconsolidated material, it can be compacted under varying pressures to form a more cohesive solid. The bulk chemistry of simulants created from the JEZ-1 standard will differ depending on the source minerals' crystal chemistry. The latest analysis for the production version of JEZ-1 reports SiO_2 at 44.2%, Al_2O_3 at 11.3%, FeO at 9.5%, MgO at 25.9%, and CaO at 3.5%, among other minor components (Yin et al., 2021). This chemical composition is similar to the MGS-1, with main differences of FeO (MGS-1 has 10% more) and MgO (MSG-1 has 18% less).

The University of Central Florida has recently formulated two lunar regolith simulants, namely LHS-1 and LMS-1, to replicate the primary lunar soil varieties – the highland and the lunar mare correspondingly (Isachenkov et al., 2022). The Lunar Mare Simulant is a synthetic material developed to replicate the characteristics of the regolith found in the lunar maria, which are vast plains on the Moon's surface formed by ancient volcanic activity. LMS-1 is a low-titanium basaltic dark regolith with a high glass content. Authors Paul et al. (2022) germinated and grew plants for up to 8 days in 4 types of Lunar regolith, proving that terrestrial plants can grow in lunar regolith as the primary support matrix. However, the results showed that lunar regolith was not a benign substrate for plant growth, with plants failing to promptly establish and achieve growth phases.

At the same time, Lunar Highlands Simulants (LHS-1) are designed to replicate the regolith found in the lunar highlands, which are the bright, rugged, and heavily cratered regions of the Moon's surface. The highlands are composed of lighter-colored rocks, including anorthosite, rich in aluminum and calcium minerals such as plagioclase feldspar. These regions contrast with the darker, smoother plains known as lunar maria since it is a lighter colored regolith. Therefore, the regolith in these areas is typically composed of anorthosite, a type of rock rich in plagioclase feldspar, with lesser amounts of other minerals such as olivine and pyroxene (Sun et al., 2022).

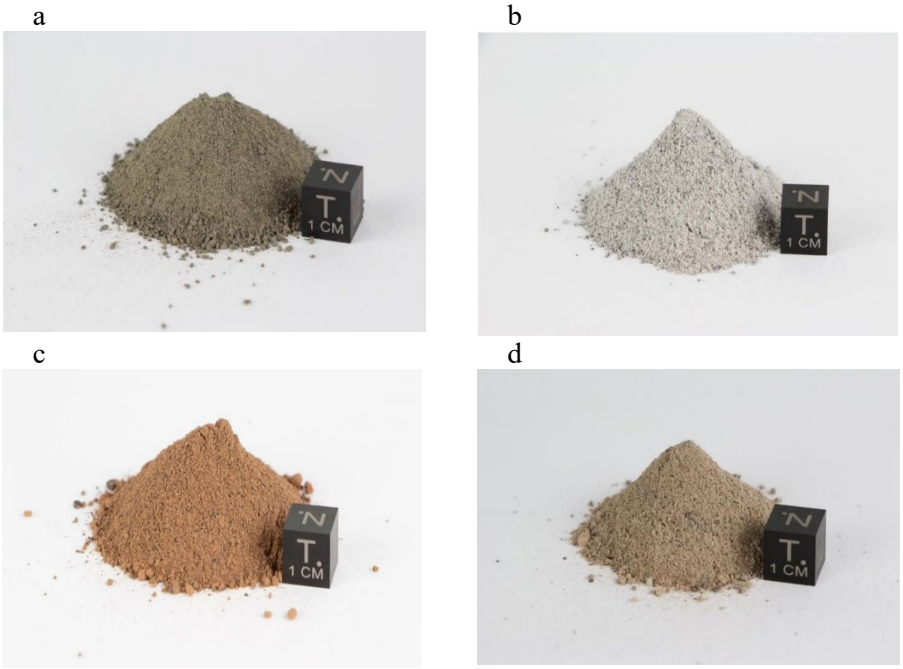

Figure 1: a) Lunar Mare Simulant LMS-1; b) Lunar Highlands Simulant LHS-1; c) Mars Global Regolith MGS-1; d) Jezero Delta Simulant JEZ-1. Source: Exolith Lab (Space Resource Technologies, 2024).

The regolith used in this research was selected for its suitability for monitoring tribological factors. Previous research conducted by Barkó et al. (2023) used the same regolith in testing moving shaft sealing pairs. The simulants used were two types for Mars: MGS-1 (Mars Global Simulant) and JEZ (Jezero Delta Simulant), and two types for Lunar soils: LMS-1 (Lunar Mare Simulant) and LHS-1 (Lunar Highlands Simulant). All the 4 regolith types sourced from Exolith Lab (Space Resource Technologies - All Simulants, n.d.).

Plant selection

Studies must carefully select plant varieties known for their nutritional value, growth characteristics, and adaptability to challenging conditions to indicate necessary adjustments to achieve food production in Mars regolith. Common food crops such as lettuce, tomatoes, radishes, and potatoes are among the species used in Lunar and Mars regolith experiments (Wamelink et al., 2014).

Indicator plants are indicator species that serve as a measure of the environmental conditions that exist in a given locale (Encyclopedia Britannica, 1998). The survival and growth of these plants can provide insights into the suitability of the environment for supporting other species. In this study, specific indicator plants were chosen to be cultivated in both the Lunar and Mars regolith to assess their potential for supporting plant life.

The indicator plants proposed by NASA and ESA for testing are chosen largely because they bind volatile organic compounds in the air. This is important for optimizing human presence in confined spaces (Mars or Moon facilities) and for confined plant cultivation (see Table 1).

In selecting indicator plants for the experiments, several criteria were considered to ensure their fitting to the intended purpose. Firstly, the plants needed to be edible to assess their potential as food sources. Additionally, preference was given to plants capable of producing oxygen and binding volatile compounds, ideally in more significant quantities than conventional Earth plants. Furthermore, the selected plants had to demonstrate resilience to extreme conditions, particularly cold environments nd adaptability to different soil types.

To qualify as indicator plants, it was required to meet at least two criteria. Practical considerations, such as the availability and ease of obtaining the plants, also factored into the selection process. Table 1 shows indicator plants recommended by NASA according to their ability to sequester volatile substances from the air.

	Benzol (C_6H_6)	**Formaldehyde (CH_2O)**	**Trichloroethylene (C_2HCl_3)**	**Xylene ($(CH_3)_2C_6H_4$ and Toluene ($C_6H_5CH_3$)**	**Ammonium (NH_3)**
Pygmy Date Palm ***(Phoenix roebelenii)***	x	✓	x	✓	x
Cane palm ***(Dypsis lutescens)***	x	✓	x	✓	x
Sword fern ***(Nephrolepis exaltata)***	x	✓	x	✓	x
Ivy ***(Hedera helix)***	✓	✓	✓	✓	x
Filodendro ***(Philodendron cordatum)***	x	✓	x	x	x
Weeping fig ***(Ficus benjamina)***	x	✓	x	✓	x
Rubber fig ***(Ficus elastica)***	x	✓	x	x	x
Daisy flower ***(Chrysanthemum morifolium)***	✓	✓	✓	✓	✓
Aloe ***(Aloe vera)***	✓	✓	x	x	x
Spider plant ***(Chlorophytum comosum)***	x	✓	x	✓	x

Table 1: Indicator plants by their ability to sequester volatile organic compounds. Source: Document provided by ESA: NASA report published as 'Interior Landscape Plants for Indoor Air Pollution (1989).

As indicated in Table 1, *Hedera helix* and *Chrysanthemum morifolium* are the two plants that best tolerate volatile organic compounds. As a result of these considerations, the following indicator plants were chosen for inclusion in the experiment: *Hedera helix, Sinapis alba, Salvia officinalis*, and *Vigna radiata*.

Hedera helix, commonly known as ivy, is a highly adaptable, low-maintenance and resilient plant species with widespread distribution in temperate forests. It flowers from August to September with inconspicuous yellowish-green flowers followed by black berries in autumn, which serve as winter food for birds. However, humans should not eat berries from *Hedera helix* as they are toxic.

Sinapsis alba or mustard, an annual plant belonging to the cabbage family. Well resistant plant, good for varied soils, and not sensitive to frost.

Salvia officinalis or sage is an essential oil-containing perennial shrub, native to the northern Mediterranean. It prefers average, dry to medium moist, well-drained soils. It dislikes overly compacted, clayey soils, which are sensitive to stagnant water. Grows planted in light shade, not direct sunlight.

Vigna radiata, the mung bean, is a legume crop, with nitrogen fixation capacity due to the symbiosis with the rhizobium bacteria present in the roots. It is a resistant plant, with fast biomass production. It is highly adaptable to various soil types, but not frost resistant.

1.1. Chamber design

The experiment was conducted in a controlled environment chamber in the Department of Mechanical Engineering at the Hungarian University of Agriculture and Life Sciences. The chamber was equipped with tungsten lights to simulate solar radiation, as well as soil humidity and temperature sensors to monitor environmental conditions. An automatic airflow system was employed to maintain optimal ventilation throughout the experiment.

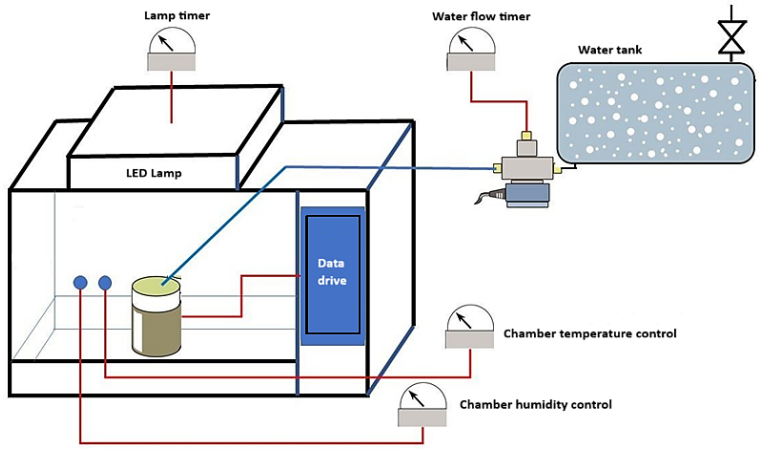

Figure 2: Schematic of the chamber.

The chamber incorporates a humidity control system, with humidity sensors positioned within the chamber to monitor moisture levels in the air. This system enables the regulation of humidity levels to create an ideal growing environment for the plants, preventing excessive dryness or moisture that may adversely affect plant health. To provide adequate illumination for photosynthesis and plant development, the chamber is fitted with specialized lighting. A Tungsram Agritech Toplight Series lamp as the primary light source for the experiment. This lamp is designed for closed system plant cultivation, offering customizable wavelengths and light intensities to optimize plant growth and metabolism. The lighting program was configured to provide 16 hours of light followed by 8 hours of darkness, with the cycle controlled by a programmable switch. The air temperature was kept around 21° to 22°C. Soil humidity around 30%.

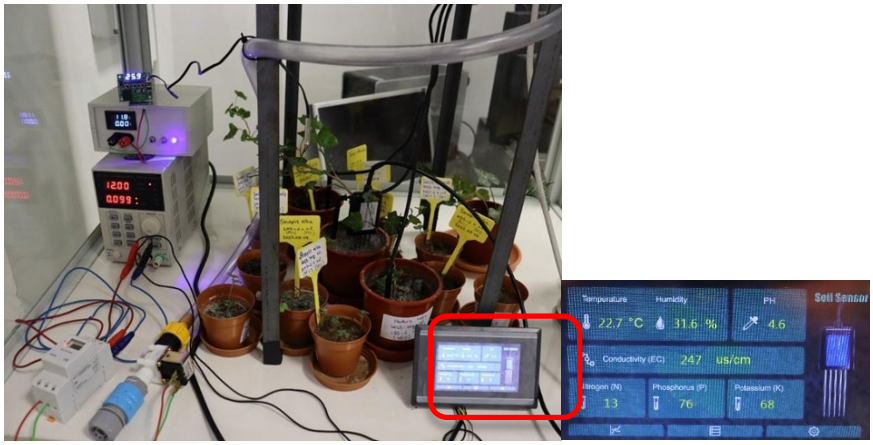

Figure 3: First experimental setup.

Experimental rounds

The four chosen plant species, namely *Hedera helix, Sinapis alba, Salvia officinalis*, and *Vigna radiata*, were planted in the substrate of regolith with organic matter soil. Before planting, each substrate was amended with varying proportions of organic matter soil, composing the treatments 50%, 75%, and 90%, while one treatment involved the substrate without added organic matter soil. Additionally, pure organic matter soil was included as a control group.

Two distinct setups were conducted using the four plants previously described. The temperature was kept around 21° to 22°C. Soil humidity around 30%. Conductivity and nutrients were measured but not controlled or added. Measurements were taken at regular intervals throughout the 30-day experimental period. Soil pH, as well as the nutrient status in terms of nitrogen (N), phosphorus (P), and potassium (K), were assessed using standard laboratory methods. Germination rates, plant survival rates, and root system development were monitored to evaluate plant growth and performance in different substrates and organic matter soil compositions. A qualitative comparison was performed

on the collected data to assess significant differences between treatments and controls. The results obtained from this experiment provided valuable insights into the feasibility of using different regolith as substrates with added organic matter compositions for plant cultivation in extraterrestrial environments.

The pH of the soil is important for nutrient uptake. Soils with weak acidity and neutral chemistry are considered the most ideal for plant production. The optimum pH of the soil is 6.5, as it is the most favorable value for nutrient uptake. The pH of the simulants was measured. The simulants MGS-1, LHS-1, and LMS-1 had pH 8, in the alkaline range, while JEZ-1 had pH 7, neutral.

Among other things, nitrogen, phosphorus, and potassium play a role in photosynthesis, development of leaves, and plant metabolic flux. The nutrient content of the regolith was measured using a photometer. The results of these measurements are in Table 2, the amount of nutrients available in the regolith is very low.

	Nutrients (mg/kg)			
Simulant	Nitrogen (N)	Phosphorus (P)	Potassium (K)	pH
MGS-1	18,0	131,7	372,0	8
JEZ-1	18,0	181,4	562,2	7
LHS-1	6,5	165,4	214,8	8
LMS-1	17,0	261,7	195,4	8
Organic peat soil	3000	1000	1000	6,5

Table 2: pH and nutrient content of studied simulants.

The pH of Martian soil simulants is typically adjusted to resemble the range observed in actual Martian regolith, which Mars rovers have measured. Mars soil simulants are often slightly alkaline, with pH values ranging from around 7 to 9. This alkalinity is influenced by the presence of minerals such as calcium and magnesium perchlorates, as well as other alkaline substances found in Martian soil. Adjusting pH in the simulants will influence the growing of plants, but in this study the pH was measured but not adjusted before using the regolith as substrate for the plants.

Figure 4: Second experimental setup.

The experiment was divided in two setups. In the first setup, *Hedera helix* branch was transplanted to individual pots with the treatments. Treatments were considered the substrate with proportions of regolith mixed to the organic matter (peat soil). Seeds of *Sinapis alba and Salvia officinalis* were planted in individual pots with the treatments. Small pots were filled with 100 g of substrate, in proportions of the determined treatments. The plants were regularly watered with 10 ml of normal tap water to keep soil humidity levels. A plate was placed on the bottom of each pot to prevent water and soil from leaking. Each plant was planted twice. In each pot 3 seeds were positioned. All seeds were tested for germination before planting in regolith. The germination test was made by randomly selecting 5 seeds from each lot, all lots germinated properly. In the second setup *Hedera helix* was not planted, and the *Vigna radiata* was planted from seeds. The full cycle of the plants was repeated, and the results were collected.

4. Results and discussion

Plant survival

Initially, the effect of the four pure simulants on the indicator plants was evaluated. It was anticipated, based on existing literature, that significant plant growth could not be expected due to the absence of nutrients or organic compounds in the simulants (Table 2). Instead, the comparative viability of the plants under similar conditions of irrigation, humidity, light, temperature was observed. Both JEZ-1 and LMS-1 simulants led to rapid deterioration of the *Hedera helix* ivy (See Figure 5). In contrast, the leaves of the plant in the JEZ-1 simulant soil on the left were observed to be incapable of photosynthesis, indicating plant death.

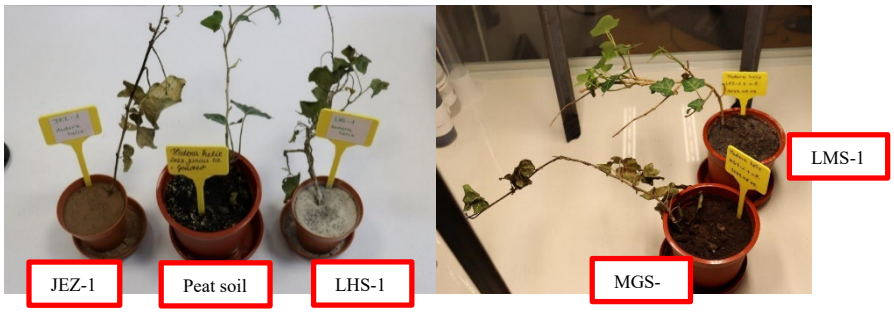

Figure 5: Hedera helix in the first experimental setup.

By increasing the ratio, the plants continued to develop in the lunar regolith. Based on practice, it can be established that the plant is functional in the lunar regolith, as it survives in the 90:10% mixture. For the mustard, which we sowed from seed, the plant germinated and survived up to a ratio of 75:25% and developed in both lunar and Mars regolith. Although slower development,

discoloration and deformations were observed on the leaves, the plants developed up to flowering, in surprisingly low organic matter ratios.

Figure 6: Mustard flowering but showing deformed leaves.

For the sage and mung beans they only managed half the proportions up to 50:50% ratio. It died in soil mixtures with a higher concentration. However, those plants that have sprouted in lower treatments did not show any disease, deformity, or discoloration, as in the case of mustard. Apart from a little elongation, they developed healthily. In summary, the plants are listed according to their survival in Table 3.

	Plants			
Treatment	*Hedera helix* Ivy	*Sinapsis alba* Mustard	*Salvia officinalis* Sage	*Vigna radiata* Mung beans
100% peat soil	☑	☑	☑	☑
50% MGS-1 + 50% peat soil	⊘	☑	☑	☑
75% MGS-1 + 25% peat soil	⊘	☑	☒	☒
90% MGS-1 + 10% peat soil	⊘	☒	⊘	☒
100% MGS-1	⊘	⊘	⊘	⊘
50% LHS-1 + 50% peat soil	☑	☑	☑	⊘
75% LHS-1 + 25% peat soil	☑	☑	☒	⊘
90% LHS-1 + 10% peat soil	☑	☑	⊘	⊘
100% LHS-1	⊘	⊘	⊘	⊘
50% LMS-1 + 50% peat soil	☑	☑	☑	⊘
75% LMS-1 + 25% peat soil	☑	☑	⊘	⊘
90% LMS-1 + 10% peat soil	⊘	⊘	⊘	⊘
100% LMS-1	⊘	⊘	⊘	⊘

☑ Planted, germinated, developed

☒ No survival after 7 days

⊘ No germination, no survival

Discussion

No plants could germinate or survive by simply planting them in the regolith. This corroborates with results found by authors Eichler et al. (2021). The authors (Eichler et al., 2021) conducted an experiment using three Mars regolith simulants, JSC-Mars-1, Mars Mojave Simulant MMS-1 from the Martian Garden, and the Mars Global Simulant-1 MGS- 1, Center for Lunar and Asteroid Surface Science. Their methodology consisted of verifying the characteristics of the selected regolith, plant selection, construction of a chamber for short-term plant growth, test of the seeds with germination test, and the plant growth on MRS. With two different treatments from just the regolith and regolith added to nutrients. The authors found that plants survived in JSC and MMS but not in the MSG-1. MGS-1 reveals two modifiable features of the regolith that could potentially enhance plant survival: particle size and pH. All three Martian Regolith Simulants, including MGS-1, exhibit hygroscopic properties, leading to aggregation upon watering. Particularly in the case of MGS-1, this aggregation effect was pronounced, prompting the hypothesis that it might impede root function, thus explaining the rapid demise of plants on this substrate.

MGS-1 could not support seed germination regardless of particle size after sieving and subsequent germination tests. Transferred seedlings faced mortality within seven days across all particle size categories. Considering the elevated pH of MGS-1 used in Eichler et al. test, which potentially reduces critical nutrients, such as iron, phosphorous, and zinc, inaccessible to plants. Lowering soil pH is achievable through various methods, and direct acid treatment was deemed practical for the experiment's relatively small volumes. Treatment with sulfuric acid adjusted the MGS-1 pH to approximately 7, enhancing seedling viability by an additional week, although plants on MGS-1 ultimately succumbed (Eichler et al., 2021).

Authors Rainwater and Mukherjee (2021) experimented with establishing the legume-rhizobia symbiosis using different Mars soil simulants, including various grades of the Mojave Mars Simulant MMS-1 in coarse, fine, unsorted, superfine, and the MMS-2 simulant. The indicator legume chosen, *Medicago truncatula*, along with its symbiotic bacteria partners, were employed in the experiments. Results indicated the successful development of root nodules on symbiotic bacteria in the roots when grown on Mars soil simulants, comparable to those formed in a sand medium. The study concluded that the Mars soil simulants investigated could indeed support the legume-rhizobia symbiosis. Although lateral roots and nodule numbers were consistent across different simulants, the total plant mass was higher in plants grown on MMS-2 soil compared to MMS-1 soil and its variants. This suggests that the chemical composition of the simulants is more influential than their grain size in determining plant mass. Based on these findings, the MMS-2 superfine soil simulant is recommended for future studies exploring beneficial plant-microbe associations for sustainable agriculture on Mars.

Authors Oze et al. (2021) conducted an experiment on MRS with two plant species *Amaranthus cruentus* (purple amaranth) and *Phaseous vulgaris* (French bean). In the case of beans, seeds inoculated with N-binding bacteria were also sown. However, this did not make a significant difference in the survival of the plants, because the experiment was too short to establish a symbiotic relationship between the Rhizobium and the plant root system. As a result, only the beans grew in regolith without perchlorate, which was treated by the authors. Compared to the control, no significant geochemical changes occurred after perchlorate addition in the normal Earth soil. Though, the Martian regolith simulant samples showed a relative increase in metal concentrations in the perchlorate containing samples. This suggests that perchlorate can modify the geochemistry of soils, especially in the absence of organic matter. These results highlight the need to develop effective methods to remove perchlorate before using Martian regolith as a planting substrate; however, perchlorate is not the only problem.

Direct phytotoxicity, salt stress, metal release or some combination of these variables stress or inhibit seed germination and plant growth. In addition, adding water to the Martian regolith simulant results in a compact structure that limits water infiltration of air and root growth. It is necessary to remove perchlorate by leaching or evaporation, and regolith amendment with organic matter to promote structure and nutrient cycling. Future research opportunities include the use of aqueous flushing, phytoremediation, evaporation, and perchlorate-reducing bacteria to remove or convert perchlorate from regolith and the use of plant tests to determine whether crops grown in restored Martian regolith are safe for consumption.

The quality of the simulant is a determining characteristic of the success of experimental trials (Eichler et al., 2021). Mars regolith simulants address the x-ray amorphous component through specialized treatments, acknowledging the presence of materials lacking a crystalline structure. This refinement adds a layer of complexity, enhancing the simulant's fidelity (Ramkissoon et al., 2019). Some Mars regolith simulants, such as the Johnson Space Center (JSC) and the Mojave Mars Simulant (MMS), have been shown to support plant growth with nutrients, when they are added to the substrate, while the Mars Global Simulant (MGS-1) has not.

The presence of Ca perchlorate ($Ca(ClO_4)_2$) in the simulant prevented plant growth. However, again, it resembles Martian soil chemically with high fidelity. Previously, Wamelink et al., 2019 also demonstrated germination and plant growth using a JSC simulant, including in nitrogen-fixing plants; however, perchlorate was not present in the simulants used. In addition, the authors Kasyap & Senetakis (2021) added organic residues to successfully increase the growth of *Lactuca sativa* (lettuce) in MMS-1 Mars regolith.

Nevertheless, due to the inability to grow plants solely in MGS-1, the effect of different levels of perchlorate in Martian regolith on plants needs further study. In this study, no plants grew from the Martian regolith in the presence of

perchlorate. In Earth's soil, as a control, perchlorate has shown to also inhibited healthy plant growth.

Future plans: The potential applications of Mars regolith in experiments is evidenced by the legume-rhizobia symbiosis on Mars soil simulants, opening avenues for sustainable food production in extraterrestrial environments. Challenges associated with the abrasive nature of Mars regolith and the limitations in accurately simulating Martian conditions necessitate ongoing research efforts to refine regolith simulants and experimental methodologies. The next experiment ongoing is considering the correction of not just the nutrient availability, but also the soil structure. Additionally, investigating reduced pressure effects on plant growth provides valuable insights for future space missions.

5. CONCLUSIONS

No plants could survive in pure regolith from either Mars or the Moon. Mustard exhibited the highest survival rate, particularly with the highest ratio of organic matter to regolith. Additionally, Ivy (*Hedera helix*) showed resilience even at high concentrations of regolith, although it is not an edible plant, but it offers environmental benefits. On the lunar simulant, many germinated plants exhibited slower growth or remained small but managed to survive. In essence, the results indicate the potential for plant growth in Martian and Lunar regolith simulants but requiring chemical and structural adjustments. Further research is necessary to assess the representativeness of the simulants, their water holding capacity, and other physical characteristics, as well as to explore the availability of nutrients, especially nitrogen, based on nutrient supplementation, as well as the impact of gravity, light, and other environmental conditions for extraplanetary plant growth.

ACKNOWLEDGEMENTS

This study was possible due to the support of ESA and the TDK program.
Thanks to the Stipendium Hungaricum Program for supporting the Mechanical Engineering PhD research, in the Institute of Technology of the MATE University.

References

[1] Adhikari, K., & Hartemink, A. E. (2016). Linking soils to ecosystem services — A global review. Geoderma (Amsterdam), 262, 101–111. https://doi.org/10.1016/j.geoderma.2015.08.009

[2] Agui, J. H., & Nakagawa, M. (2005). Dust on the moon and Mars. 43rd AIAA Aerospace Sciences Meeting and Exhibit. https://doi.org/10.2514/6.2005-539

[3] Barkó, G., Kalácska, G., Keresztes, R., Zsidai, L., Shegawu, H., & Kalácska, Á. (2023). Abrasion Evaluation of Moon and Mars simulants on Rotating Shaft/Sealing materials: Simulants and Structural Materials review and selection. Lubricants, 11(8), 334. https://doi.org/10.3390/lubricants11080334

[4] Cannon, K. M., Britt, D. T., Smith, T. M., Fritsche, R., & Batcheldor, D. (2019). Mars global simulant MGS-1: A Rocknest-based open standard for basaltic martian regolith simulants. Icarus, 317, 470–478. https://doi.org/10.1016/j.icarus.2018.08.019

[5] Catling, D. C., & Leovy, C. B. (2007). Mars Atmosphere: history and surface interactions. In Elsevier eBooks (pp. 301–314). https://doi.org/10.1016/b978-012088589-3/50019-0

[6] Curiosity Science Instruments - NASA Science. (n.d.). https://mars.nasa.gov/msl/spacecraft/instruments/chemin/

[7] Delage, P., Karakostas, F., Dhemaied, A., Belmokhtar, M., Lognonné, P., Golombek, M. P., De Laure, E., Hurst, K., Dupla, J., Kedar, S., Cui, Y., & Banerdt, B. (2017). An Investigation of the Mechanical Properties of Some Martian Regolith Simulants with Respect to the Surface Properties at the InSight Mission Landing Site. Space Science Reviews, 211(1–4), 191–213. https://doi.org/10.1007/s11214-017-0339-7

[8] Ehlmann, B. L., & Edwards, C. S. (2014). Mineralogy of the Martian surface. Annual Review of Earth and Planetary Sciences, 42(1), 291–315. https://doi.org/10.1146/annurev-earth-060313-055024

[9] Eichler, A., Hadland, N., Pickett, D. A., Masaitis, D., Handy, D., Perez, A. D., Batcheldor, D., Wheeler, B., & Palmer, A. G. (2021a). Challenging the agricultural viability of martian regolith simulants. Icarus, 354, 114022. https://doi.org/10.1016/j.icarus.2020.114022

[10] Fergason, R. L., Christensen, P. R., Bell, J. F., Golombek, M. P., Herkenhoff, K. E., & Kieffer, H. H. (2006). Physical properties of the Mars Exploration Rover landing sites as inferred from Mini-TES–derived thermal inertia. Journal of Geophysical Research, 111(E2). https://doi.org/10.1029/2005je002583

[11] Fox-Powell, M., Hallsworth, J. E., Cousins, C. R., & Cockell, C. S. (2016). Ionic strength is a barrier to the habitability of Mars. Astrobiology, 16(6), 427–442. https://doi.org/10.1089/ast.2015.1432

[12] Goetz, W., Pike, W. T., Hviid, S. F., Madsen, M. B., Morris, R. V., Hecht, M. H., Staufer, U., Leer, K., Sykulska, H., Hemmig, E., Marshall, J. R., Morookian, J. M., Parrat, D., Vijendran, S., Bos, B. J., El-Maarry, M. R., Keller, H. U., Kramm, R., Markiewicz, W. J., . . . Tanner, R. (2010). Microscopy analysis of soils at the Phoenix landing site, Mars: Classification of soil particles and description of their optical and magnetic properties. Journal of Geophysical Research, 115(E8). https://doi.org/10.1029/2009je003437

[13] Isachenkov, M., Chugunov, S., Landsman, Z., Akhatov, I., Metke, A., Тихонов, A. A., & Shishkovsky, I. (2022). Characterization of novel lunar highland and mare simulants for ISRU research applications. Icarus, 376, 114873. https://doi.org/10.1016/j.icarus.2021.114873

[14] Maggi, F., & Pallud, C. (2010). Space agriculture in micro- and hypo-gravity: A comparative study of soil hydraulics and biogeochemistry in a cropping unit on Earth, Mars, the Moon and the space station. Planetary and Space Science, 58(14–15), 1996–2007. https://doi.org/10.1016/j.pss.2010.09.025

[15] Mars: Facts - NASA Science. (n.d.). https://science.nasa.gov/mars/facts/ Official Series Description - ROUGH Series. (n.d.). https://soilseries.sc.egov.usda.gov/OSD_Docs/R/ROUGH.html

[16] Oze, C., Beisel, J., Dabsys, E., Dall, J., North, G. B., Scott, A., Lopez, A., Holmes, R. T., & Fendorf, S. (2021). Perchlorate and agriculture on Mars. Soil Systems, 5(3), 37. https://doi.org/10.3390/soilsystems5030037

[17] Pernet-Fisher, J. F., & Joy, K. H. (2016). The lunar highlands: old crust, new ideas. Astronomy & Geophysics/Astronomy and Geophysics, 57(1), 1.26-1.30. https://doi.org/10.1093/astrogeo/atw039

[18] Space Resource Technologies - all simulants. (n.d.). Space Resource Technologies. https://spaceresourcetech.com/collections/all-simulants

[19] Starr, S. O., & Muscatello, A. C. (2020). Mars in situ resource utilization: a review. Planetary and Space Science, 182, 104824. https://doi.org/10.1016/j.pss.2019.104824

[20] Sun, X., Zhang, R., Li, X., Zou, M., Wang, C., & Chen, L. (2022). JLU-H: A novel lunar highland regolith simulant for use in large-scale engineering experiments. Planetary and Space Science, 221, 105562. https://doi.org/10.1016/j.pss.2022.105562

[21] Wamelink, G., Frissel, J., Krijnen, W., Verwoert, & Goedhart, P. (2014a). Can plants grow on Mars and the Moon: A growth experiment on Mars and Moon soil simulants. PloS One, 9(8), e103138. https://doi.org/10.1371/journal.pone.0103138

[22] Wamelink, G., Frissel, J., Krijnen, W., Verwoert, & Goedhart, P. (2014b). Can plants grow on Mars and the Moon: A growth experiment on Mars and Moon soil simulants. PloS One, 9(8), e103138. https://doi.org/10.1371/journal.pone.0103138

High stability damping model for discrete element method

István OLDAL[1]
[1] *Institute of Technology,*
Hungarian University of Agriculture and Life Sciences, MATE, Gödöllő

Abstract

A proper contact model is essential for using the Discrete Element Method (DEM). The common damping used in DEM modeling is not ideal from the explicit dynamical modeling point of view. In this article we present the theory of a new contact model, where the evaluation of damping is based on the value of the coefficient of restitution and damping is proportional to contact force. Our new model is suitable for any type (linear and nonlinear) elastic models, and it is better than the existing ones from the point of view of numerical stability.

Keywords

particle, contact force, coefficient of restitution, DEM, numerical stability

1. Introduction

The Discrete Element Method (DEM) is a fairly new proceeding to model the mechanical properties of bulk materials. By the use of DEM, the model problem is solved by applying and solving the equation of motion on each singular particle of the bulk material assembly (Cundall, Strack, 1979). The goodness of the contact model is fundamentally determine the applicability of the DEM model.

The contact models describe the mechanical interactions between the grain particle pairs and the particle-wall interactions. The encounter between the two bodies is described as collision. In the course of our work, we have focused on modeling the normal forces, so the phenomenon and models will only be examined from this point of view.

Before contact with the bodies, the air between them acts as pressure on the surfaces. The next is the common viscoelastic deformation phase, which can be described with a simpler model than viscoelastic depending on the material. Depending on the boundary conditions and materials, there may be plastic deformation at the next stage. (Even material failure (breakage) can occure, but this case does not form the subject of DEM modeling.) After reaching maximum compression, the unloading can be viscoelastic (or simpler) and adhesion can also appear. Then after the contact has ceased again the air inflow can have mechanical effect. This phenomenon was described by Marshall (2018). The

phenomenon of impact can be further examined, the damping can be modelled by taking into account the size dependence, the surface quality of the conflicting bodies, even the microtopography can be considered. However, it is clear, that the description of all of these processes during the DEM modeling is not possible because of the enormous computation capacity needed. Because of this, there are simplified models used.

Throughout the entire process, part of the body's energy is absorbed, the kinetic energy of the bodies will be smaller after the collision than before it. The coefficient of restitution (e_n) is the specific scalar quantity describing this "lost" energy. In case of discrete element modeling, different methods can be used to describe the contact process, but the coefficient of restitution is usually a significant parameter. The coefficient of restitution is usually determined by measurement because of the complicated process of impact previously presented. Large number of researchers were involved in the measurement of the coefficient of restitution, so there are large number of measurement results for many different cases and materials. For the case of collision of spheres with walls, metals, ceramics, plastics (Dong,2006), (Weir, Tallon, 2005) and in case of spherical to spherical body collision there were large number of experiments for different materials (Stevens, Hrenya, 2005), (Lorenz et al., 1997). The value of the coefficient of restitution shall be determined based on measurements, but even for regular bodies of homogeneous material's coefficient of restitution has significantly high standard deviation (Tomar, Bose, 2018). In the case of natural substances where the homogeneity of the substance is also questionable and of irregular shape, the coefficient of restitution shows very high dispersion (Hlosta et al., 2018).

The coefficient of restitution can also be determined by using finite element method by modeling the collision process. Of course, some of the real boundary conditions have to be neglected or modelled in a simplified way (Wu, Li, Thornton, 2003, 2005). In the case of discrete element modeling, perfect geometry and homogeneous materials are generally not typical, so we apply more accurate models in vain, the collisions will show so high dispersion that there will be no more accurate model than a simpler description.

In the course of discrete element modeling, the energy absorbed during the impact is calculated using the contact model. In our work we concentrate on the energy absorption in normal direction. The interaction between two bodies is determined by the force-displacement values that are generated during modeling. The contact models have two types of energy absorption modes for normal force. In one case, the flexible member has a viscous damper, which ensures energy absorption, in the other case, the model shows different flexibility when compressed than when it is stretched.

In case of the "Hertz-Mindlin no slip" contact model the material and interaction parameters have their effect on the normal- and tangential forces. This forces and moments acting between the interacting particles can be written in the form of the following equations.

The normal force is

$$F_n = f(\delta) + kv_{nrel} \qquad (1)$$

where *f(δ)* is the force-overlap function, δ is the overlap (compression if the body is not rigid) between these two particles. This normal overlap represents the normal deformation of a particle. The normal overlap δ between two particles *i* and *j* at positions x_i and x_j (where *x* is the distance measured on the line connecting the centers of the two overlapping particles) with radii R_i and R_j is defined as $\delta = R_i + R_j - (x_j - x_i)$. v_{nrel}. v_{nrel} is the normal component of the relative velocity of the particles.
The tangential force is

$$F_t = f_t(\delta) + k_t v_{trel} \qquad (2)$$

where $f_t(\delta)$ is the force-overlap function, δ_t is the tangential overlap between the two particles and v_{trel} is the tangential component of the relative velocity of the particles. The tangential overlap is the tangential displacement of the contact point up to the point at which the contact ends or the particle begins to roll or slip. The tangential overlap represents the tangential deformation of a particle. The tangential force is limited by Coulomb friction $\mu_s F_n$, where μ_s is the coefficient of static friction.

The moment from rolling friction is $M_r = -\mu_r F_n R_i \omega_i$, where R_i is the distance of the contact point from the centre of the i-th particles and ω_i is the unit angular velocity vector, which is a dimensionless quantity representing only the direction of rotation of the particle. μ_r is the coefficient of rolling friction. The tangential force also has moment on the particle: $M_t = F_t R_i$.
As we see in the above equations, the normal and the tangential forces contain a velocity dependent damping part.

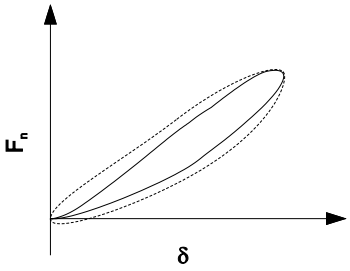

Figure 1. Different visco-elastic contact models (Horabik et al., 2017)

For viscous damping, a velocity-dependent damper is present in the model and one of the parameters describing the behaviour of this damper is the coefficient of restitution. In the original model of Cundall and Strack there was also this type of model applied. One common contact model is the Hertz-Mindlin model (Mindlin, Deresiewicz, 1953) and beside these various models of viscous and even non-Newtonian dampers are used. The viscous damping can be of different

characteristics, so the force-displacement functions and the simulated coefficient of restitution are different. Two types are presented in Fig. 1.
Due to the damping member, the force-displacement function describes a hysteresis loop over a load cycle, and the loop area characterizes the energy absorbed.
A completely different method to model the energy absorption uses different charge and discharge flexibility. Each model differs in the description mode of the charge and discharge section, and the path in which the function returns to its undeformed state. Some characteristic models are compared with Thornton et al (2013) which can be seen on Fig. 2.

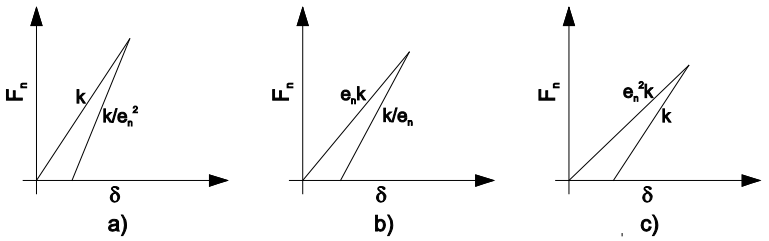

Figure 2. Different contact models (Thornton et al., 2013)

All three types are based on the different slope of load and unload branches. The slope ratio is equal, but they have different starting slopes.
First model, Fig. 2.a)

Loading: $F_n = k_1\delta = k\delta$

Unloading: $F_n = k_2(\delta - \delta_0) = \frac{k}{e_n^2}(\delta - \delta_0)$

Second model, Fig. 2.b),

Loading $F_n = k_1\delta = e_n k\delta$

Unloading: $F_n = k_2(\delta - \delta_0) = \frac{k}{e_n}(\delta - \delta_0)$

Third model, Fig. 2.c),

Loading $F_n = k_1\delta = e_n^2 k\delta$

Unloading: $F_n = k_2(\delta - \delta_0) = k(\delta - \delta_0)$

where:
F_n: normal force,
δ: compression (overlap in case of rigid model),
e_n: coefficient of restitution,
δ_0: compression where the loading function is 0,
k, k_1, k_2: constants.

The normal force function for these authors is the same, the tangential differs, but from our point of view, they are in the same group.
A flexible-ideally deformable material model can be the basis of model having different flexibilities, and adhesion can also be taken into account. Additional viscous damper member also can be applied.
The viscous member and the "different flexibility" models are also suitable for the use of DEM. In our comparison we found that in case of different types of materials, different models give better approximation results.
None of the methods are ideal from the point of view of numerical stability. In both cases, at the largest force will we have the smallest energy absorption. For viscous damping because of that the load "turns back" at the maximum compression point, and there the velocity is zero, and because of this there is no damping there. In case of the "two types of flexibility" models there is the change between the two curves is at the maximal compression point, and there is one vertex, and because of this the energy absorption is close to zero at that point.
If the collision of the bodies is in all cases happens until the full discharge (the particles do separate from each other), it is not significant from stability point of view which model is used, because in both cases energy absorption takes place. However, if the total extension (separation) does not occur, it is not indifferent, how much of energy is in the connection absorbed. In the case of the modelling of particulate material, it is very rare and in case of quasi-static cluster even may not occur the event of complete separation of particles because the assembly is loaded by force. During the filling phase, such high number of collisions appear, that after reaching the rest state, there is no total extension of the flexible members.
This means that the models are in the vicinity of full compression with minimal velocity and we are in the circled part of curves almost always. These models, however, provide very small energy absorption there, and this is detrimental from the stability point of view. In order to ensure the stability of the numerical calculation, global damping is used in many cases, but it corrupts the essence of DEM, which, like real granular materials, derives the behaviour of the particulate assembly only from the interactions between the particles.

2. Material and methods

The purpose of our work is to create a normal contact model, which is based on the coefficient of restitution, and is numerically more stable than the other models. The numerical stability can be achieved by the fact that in our case the energy absorption is proportional to the forces arising during the interaction, i.e. near the maximal compressing force we will have the maximal energy dissipation, in contrast with the previous models, which have been providing near to zero energy dissipation close to the maximal displacement.

The model is similar to the previous varying slope models, except that, at maximum compression, the recoil is based on another slope, which is not continuously connected to the load stage. DEM uses discrete time steps, so the continuous function is not required for calculations. Fig. 3. shows the new model, constant c must be chosen so that the e_n coefficient of restitution should be valid for the entire function.

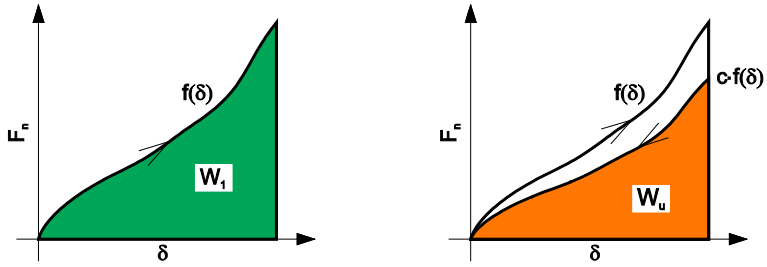

Figure 3. New model for normal load (loading, unloading)

3. RESULTS AND DISCUSSION

The coefficient of restitution can be calculated from the loading and unloading part of the force-displacement functions:

$$e_n = \sqrt{\frac{W_u}{W_l}} = \sqrt{\frac{\int cf(\delta)d\delta}{\int f(\delta)d\delta}} = \sqrt{\frac{c\int f(\delta)d\delta}{\int f(\delta)d\delta}} = \sqrt{c} \qquad (3)$$

i.e.:

$$c = {e_n}^2 \qquad (4)$$

for any types of linear or nonlinear force-deformation functions. The damped normal force function $F_n(\delta)$ can thus be derived from any $f_n(\delta)$ elastic function. Loading (normal relative speed is positive):

$$F_n(\delta) = f_n(\delta) \quad (5)$$

Unloading (normal realitve speed is negative):

$$F_n(\delta) = {e_n}^2 \cdot f_n(\delta) \qquad (6)$$

This method can be applied together with any type of elastic interaction model. The coefficient of restitution can be exactly derived from the force-deformation functions in the way shown above.

The application is greatly facilitated by the ability to write the function in a closed form. This is achieved by splitting the $F_n(\delta)$ function into two parts, a direction-dependent and one direction-independent part.

$$F_n(\delta) = (a + b) \cdot f_n(\delta) \qquad (7)$$

$$e_n{}^2 \cdot F_n(\delta) = (a - b) \cdot f_n(\delta) \quad (8)$$

For constants you can write:

$$a + b = 1 \quad (9)$$

$$a - b = e_n{}^2 \quad (10)$$

Then

$$a = \frac{1+e_n{}^2}{2} \quad (11)$$

$$b = \frac{1-e_n{}^2}{2} \quad (12)$$

Our model is:

$$F_n(\delta) = \left(\frac{1+e_n{}^2}{2} + sign(v_n)\frac{1-e_n{}^2}{2}\right) f_n(\delta) \quad (13)$$

Where:

- $f_n(\delta)$: arbitrary elastic force-displacement function,
- $F_n(\delta)$: the normal force-displacement function describing dissipation,
- δ: compression,
- e_n: coefficient of restitution,
- $sign$: sign function,
- v_n: normal relative speed of the two bodies.

Near to the maximal compression the type of energy dissipation and the type of numerical stability can be seen on Fig. 4. Three specific case is shown: the viscous damping, the "two slope model" and our new model.

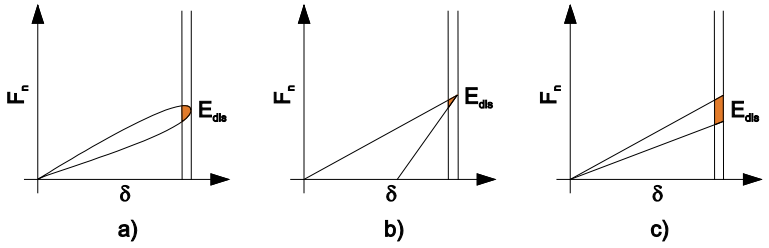

Figure 4. Dissipated energy (E_{dis}) of different model near the maximum force

With the right settings, the models absorb the same amount of coefficient of restitution dependent energy. The difference is in the distribution of energy absorption during deformation. In the case of the new model, the extent of energy absorption (unlike to other models) is proportional to the deformation (in the case of a flexible contact model, the energy absorption is also proportional to the force). In cases, when the full load-unload cycle takes place during the impact of particles, then there won't be much difference between the models. However, in the case of DEM, collisions can occur several times in succession

or simultaneously, and in the case of a compressed material, the particles are continuously loaded and no partial or complete expansion occurs. In these cases (in the vast majority of practical problems) the great advantage of the new model is that the energy absorption is proportional to the force, so that at the highest forces the energy absorption will be maximal, so greater stability is expected in the simulations.

4. Conlclusions

We presented here the theory of a new contact model, where the evaluation of damping is based on the value of the coefficient of restitution and damping is proportional to contact force. This model is not continuous what is not problem in case numerical applications like DEM. The benefits of the new model against the old ones:

- Damping is proportional to normal contact force,
- Simple, it may be written in a closed form using fewer member functions,
- The coefficient of restitution is presented exactly and derived analytically,
- Greater numerical stability,
- Easy to fit into any $f_n(\delta)$ elastic function of normal contact force (Fig. 5.). We can use the same form $F_n(\delta) = \left(\frac{1+{e_n}^2}{2} + sign(v_n)\frac{1-{e_n}^2}{2}\right) f_n(\delta)$ and valid coefficient of restitution for every case.

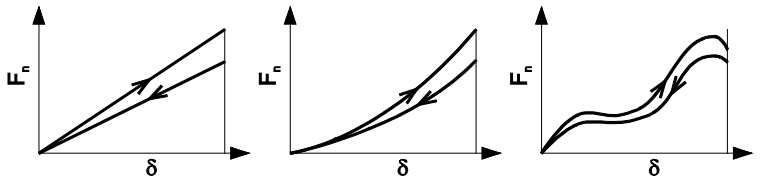

Figure 5. Application of new model for various type of elastic function

The advantage of the new model is that the energy absorption is proportional to the force, so that at the highest forces the energy absorption will be maximal, and because of this - in cases, when no full load-unload cycle occurs during the modelling of the particle interaction - greater stability is expected in the simulations.

References

[1] P.A. Cundall, O.D.L. Strack A discrete numerical model for granular assemblies GeoTechnique, 29 (1979), pp. 47-65

[2] Jeffrey S. Marshall: Modeling and sensitivity analysis of particle impact with a wall with integrated damping mechanisms Powder Technology, Volume 339, November 2018, Pages 17-24

[3] Yang Ye, Yawu Zeng the size-dependent viscoelastic normal contact model for particle collision International Journal of Impact Engineering 106 (2017) Pages 120-132

[4] Ali Ghanbarzadeh, Ali Hassanpour, Anne Neville: A numerical model for calculation of the restitution coefficient of elastic-perfectly plastic and adhesive bodies with rough surfaces Powder Technology, in press, accepted manuscript, Available online 21 December 2018

[5] Fabian Krull, Robert Hesse, Paul breuninger, Sergiy Antonyuk Impact behaviour of microparticles with microstructured surfaces: Experimentalstudy and DEM simulation Chemical Engineering Research and Design 135 (2018) pp. 175 – 184

[6] H. Dong, M.H. moys Experimental Study of oblique impacts with initial spin Powder Technol., 161 (2006), pp. 22-31

[7] G. Weir, S. Tallon The coefficient of restitution for normal incident, low velocity particle impacts Chem. Eng. Sci., 60 (13) (2005), pp. 3637-3647

[8] A.B. Stevens, C. Hrenya Comparison of soft-sphere models to measurements of collision properties during normal impacts Powder Technol., 154 (2-3) (2005), pp. 99-109

[9] Lorenz, C. Tuozzolo, M. Louge Measurements of impact properties of small, nearly spherical particles Exp. Mech., 37 (1997), pp. 292-298

[10] Vikul Tomar, Manaswita Bose: Anomalies in normal and oblique collision properties of spherical particles Powder Technology, Volume 325, 1 February 2018, Pages 669-677

[11] Jakub Hlosta, David Žurovec, Jiří Rozbroja, Álvaro Ramírez-Gómez, Jan Nečas, Jiří Zegzulka: Experimental Determination of particle – particle restitution coefficient via double pendulum method, Chemical Engineering Research and Design Volume 135, July 2018, Pages 222-233

[12] Chuan-Yu Wu, Long-Yuan Li, Colin Thornton Energy dissipation during normal impact of elastic and elastic – plastic spheres International Journal of Impact Engineering 32 (2005) pp. 593 – 604

[13] C.-Y. Wu, C. Thornton, L.-Y.Li: Coefficients of restitution for elastoplastic oblique impacts Advanced Powder technol., Vol. 14, No. 4, pp. 435 – 448 (2003)

[14] R.D. Mindlin, H. Deresiewicz, Elastic spheres in contact under varying oblique forces, J. Appl. Mech. 20 (1953) 327 – 344

[15] Ebrahim Alizadeh, François Bertrand, Jamal Chaouki: Development of a granular normal contact force model based on a non-Newtonian liquid filled dashpot Powder Technology, Volume 237, March 2013, Pages 202-212

[16] Józef Horabik, Michał Beczek, Rafał Mazur, Piotr Parafiniuk, Magdalena Ryżak, Marek Molenda: Determination of the restitution coefficient of seeds and coefficients of visco-elastic Hertz Contact models for DEM simulations Biosystems Engineering Volume 161, September 2017, Pages 106-119

[17] Colin Thornton, Sharen J. , Paul W. Cleary: An Investigation of the Comparative behaviour of alternative contact force models during inelastic collisions, Powder Technology Volume 233, January 2013, Pages 30-46

[18] Colin Thornton, Sharen J. Cummins, Paul W. Cleary: On elastic-Plastic normal contact force models, with and Without adhesion Powder Technology 315 (2017) 339 – 346

Breakage and shear testing of corn and wheat particles

Junhao HUANG[1], István KEPPLER[2], Adrienn BABLENA[2]
[1] *Doctoral School of Mechanical Engineering,*
Hungarian University of Agriculture and Life Sciences, MATE, Gödöllő
[2]*Department of Machine Constructions, Institute of Technology,* MATE, Gödöllő

Abstract

The discrete element method (DEM) simulation is one of the most effective ways to reproduce and visualize the dynamic behavior of agricultural particles. DEM simulation relies on the calibration process, which is contingent on accurate parameter measurements. The precision of DEM simulation result is intricately tied to the accuracy of the measured micromechanical parameters. Only accurate and reliable measurements of the properties and interactions of agricultural particles that inform the initial DEM simulation can speed up the DEM calibration process, shorten the DEM simulation cycle, reduce computational costs and give correct results. The agricultural particle measurements, therefore, play an important role in the DEM simulation. In this article, the breakage and shear tests of corn particles were conducted and the shear tests of wheat particles were also done.

Keywords

Agricultural granular material, wheat particle, corn particle, shear test, breakage test

1. Introduction

The so-called discrete element method (DEM) is a numerical technique applied in many particle fields to analyze the mechanical behavior of the particulate material assemblies micromechanical parameters [1]. The kinematic characteristics of wheat and corn particles can be obtained by calibrating their micromechanical parameters. In order to obtain accurate and reliable DEM simulation results, it is necessary to carry out adequate measurements of agricultural particles' mechanical properties. The standard shear test is extensively applied in the study of mechanical features and characteristics of the particle assemblies[2], [3], [4]. During harvesting, transportation, and post-processing, agricultural granular materials may be broken by interactions such as collision and compression between particles and between particles and equipment walls. The particle breakage also has received more and more attention from researchers [5], [6], [7], [8]. The purpose of this article is to

conduct standard shear and breakage tests on corn and wheat agricultural granular materials to know the maximum breakage force of corn particles and the tribological behavior of both particle assemblies.

2. Experimental

Granular materials preparation

In this article, wheat and corn particles (see Fig. 1 and Fig. 2) were used to conduct the measurement activities. These agricultural granular materials are from different regions of Hungary. Since the micromechanical parameters and macro behavior of these granular materials are affected by the moisture content [9], [10], these materials have been preserved in re-closable bag bags to maintain the moisture content of the agricultural particles since they were obtained. These agricultural granular materials were kept in closed bags.

Figure 1. Corn particles

Figure 2. Wheat particles

Measurements of moisture content

Moisture content, also known as water content, is a measure of the amount of water in a material. The proportion of the mass or volume of water in relation to the material's total mass or volume is used to indicate it. Moisture content has a very important connection with cohesion [9]. The initial moisture content has a small effect on the drying rate [11], which gives a clear way for future drying work. Moisture content is often determined through techniques such as drying oven analysis, using the change in weight before and after drying the material, or through instrumental methods like moisture meters. Here in this study, the Wile 55 Digital tool was utilized to quickly obtain moisture content data for those particles.

The Wile 55 Digital moisture meter (Fig. 3) was used in the moisture content measuring of agricultural seeds. This is a powerful tool that allows measurements to be taken on all agricultural particles, with direct readout of measurements for 16 common agricultural particles. In order to avoid the influence of temperature on the moisture content of the particles, the device has an automatic compensation of the temperature difference between the sample materials and the equipment. The accuracy of this meter is ± 0.5% moisture with normal agricultural particles if calibrated properly.

The Wile 55 Digital tool is easy to use. The simple way to conduct measurement is open the lid of this meter by rotating it upwards, add close to 4/5 of the agricultural granules to the meter's container, tighten the lid by rotating it upwards. This is to make sure the sample is compressed to unify, that is way to make to measurement very accurate. And then press the Function button to select the corresponding type of grain, and the display will show the moisture content of the grain directly. Each type of particle was measured 5 times to avoid measurement errors.

Figure 3. Wile 55 Digital moisture content meter

Table 7. Moisture content [%]

Corn 1	14.7	14.1	14.3	14.2	13.8
Corn 2	12.1	13.5	12.5	12.3	12.6
Wheat 1	11.6	11.5	11.8	11.6	11.8
Wheat 2	11.4	11.9	11.6	11.6	11.3

Measurement of bulk density

Bulk density is the mass of a material per volume when the particles are packed naturally. Pour a sufficient amount of granular material into a cup to ensure that the particles spill out of the mouth of the cup, and then use a scraper that is longer than the diameter of the cup to horizontally remove the particles that are above the level of the mouth of the cup in order to prevent them from being compacted.

The bulk density of the granular material is a very important physical quantity for input parameter setup before DEM simulation, which has a direct impact on the simulation results. Bulk density is closely related to particle density, which is a very important factor in the flow characteristic and heat transfer of grain particles [11]. The bulk density of each grain is shown in the Table 2. The bulk density was calculated based on the equation of

$$\rho = \frac{m_0 - m_1}{V}$$

where: ρ is the bulk density with unit of kg/m^3;

m_0 is the measured total mass of cup and particles with unit of kg;

m_1 is the mass of empty cup with unit of kg;

V is the volume of container with unit of m^3.

Table 8. Bulk density [kg/m^3]

Corn 1	793.16	782.7	781.52	766.92	772.74
Corn 2	737.96	754.5	754.14	749	747.3
Wheat 1	765.6	780.48	788.46	801.56	803.84
Wheat 2	786.78	798.3	795.68	794.22	798.78

Measurement of angle of repose

The angle of repose (AoR) of granular material is the angle between the steepest slope formed by the free fall of a given amount of particles from a funnel by gravity and the horizontal plane. The angle of repose is one of the parameters needed for DEM simulations [12]. Angle of repose measurement is one of the extremely easy ways to determine the micromechanical parameters [1] so the angle of repose can be a crucial indicator during the DEM calibration process. This result is corroborated by Hoshishima et al. [13], who reproduced and validated the DEM simulation by applying the angle of repose factor.

To conduct the AoR test, a funnel with filled agricultural particles was used to closely touch the surface of the lab table, then the funnel was lifted upwards at a

constant speed until all the particles have fallen to the table. The consequent step is taking a picture then calculating the repose angle (see Table 3).

Table 9. Measured angle of repose [degree]

Corn 1	15	13	15.5	17.7	14.7
Corn 2	11.9	12.2	14.5	13	13
Wheat 1	27.5	31.8	30.9	31	30.2
Wheat 2	28.9	27.9	25.1	28.5	29.1

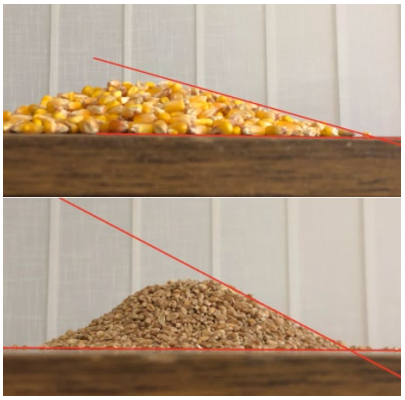

Figure 4. Angle of repose measurements of wheat and corn particles

Shear test measurement

Shear test is a type of mechanical test measuring the applied force of material causing deformation along parallel plane within the material. The primary purpose of the shear test is to determine the shear strength, which is the resistance force that act parallel tangential to the surface. The shear test helps to characterize the material's behavior under shear loading conditions, providing valuable information for applications such as material design, quality control, and DEM simulation.

The shear test is considered as a simple test that can be easily conducted [2], [14]. The shear anisotropy of rock particles is assessed by the maximum shear strength obtained in direct shear tests, and the predicted values of anisotropic rock shear coincide with the experimental values [15]. Then it is shown that the accurate measurement of the shear test is a key part of the later model development and validation. Keppler I. et al. [16] conducted many standard shear tests to determine the micromechanical parameters which related to the DEM simulations. This method is also used by J. Nečas et al. [17] to calibrate the input parameters for DEM simulations. They also investigated the displacement of the shear lid during shear testing due to volume changes caused by contraction of the granular material which in turn leads to displacement of the shear cap. The height of the shear box has a negligible effect on the results of the shear test reported by [2], [18]. On the contrary, they considered [19], [20] that

there is a relationship between the height of the shear box and the size of the particle. So, in subsequent DEM simulation the height of the shear box should be appropriately reduced to shorten the DEM simulation time. Liu et al. [5] found the phenomenon and investigated the particle breakage during shear test.

The used shear testing machine in this article is ELE 26-2112/01 digital soil shear equipment (see Fig. 5) with 0.1% accuracy for both displacement sensor and force sensor. The shear speed is 5 mm/min, and the measurement methods are: 1) open the software in the computer and turn on the displacement controller; 2) fill the granular materials into the shearing box with 4/5 height of the shear wall; 3) put the shear lid on the materials and slowly flatten the particles; 4) set up the shearing speed; 5) zero the displacement of the x-axis, 6) click the start button in the software and press the Run button on the displacement controller to start the shearing; 7) stop the software and stop the displacement. The schematic of the shear testing machine can be found in Fig. 6.

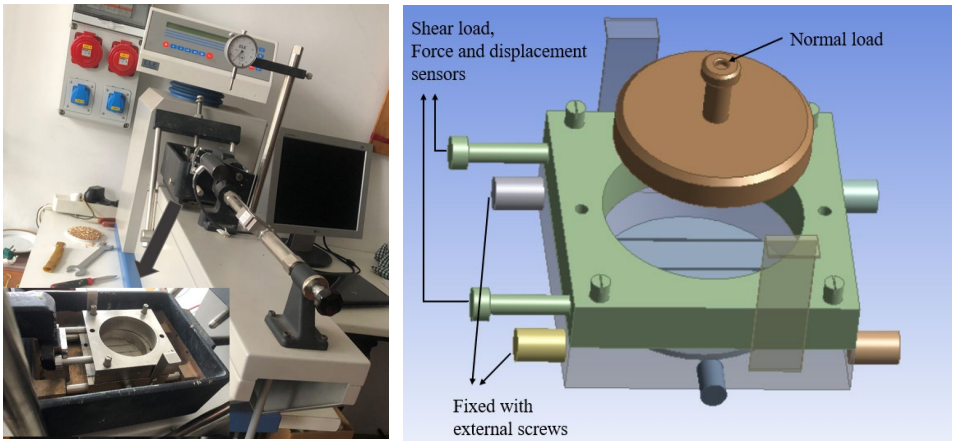

Figure 5. Shear testing machine (left), geometrical schematic of shear box (right)

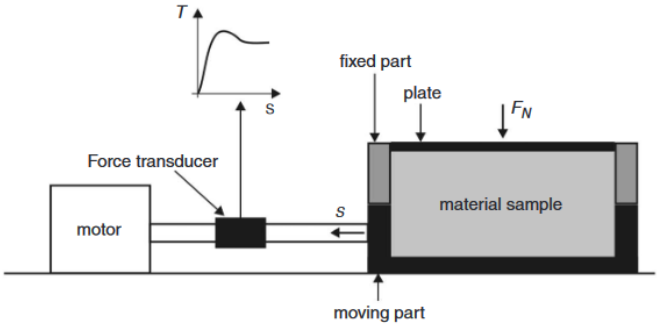

Figure 6. Schematic of the shearing system [16]

Measurement of particle breakage

Particle breakage refers to the process of which particles are broken or fractured into smaller fragments or particles due to mechanical forces or other external factors. The phenomenon is commonly observed in natural and engineering systems, such as in geotechnical engineering, settlement of buildings, pharmaceutical industrial and agricultural granular materials [6], [21], [22], [23]. During the storage and transportation of granular materials, crushing of granular materials is to be avoided as much as possible, but in the processing of granular materials, e.g., powdered pharmaceuticals, grain powders, etc., it is a goal to be achieved. It is, therefore, important to understand the breakage behavior of particles by analyzing their strength, shape and mechanical properties. And of course using the DEM simulation to be able to visualize and predict the breakage process.

Kong et al. [24] used a combination of CFD and DEM gas-solid two-phase flow simulation for the study of particle breakage of aquaculture particle feed during pneumatic conveying. The grain breakage in a vertical rice mill based on DEM simulation was studied to clarify the breakage mechanism during the rice milling process [25]. Similarly, Ghodki et al. [26] also used DEM simulations to study the breakage and flow patterns of pepper seed particles in the mill.

In this study, the INSTRON 5965 Universal Testing machine was utilized to conduct the breakage measurements. This machine has a high measurement accuracy of ±0.5%. The upper head movement speed is 3 mm/s, and the measurement steps are: 1) open the software in the computer which is connected with the INSTRON 5965Universal Testing machine and power on the machine; 2) put the corn particle on the lower part; 3) press the button to move the upper head downwards to close to the corn particle but not to touch the particle; 4) choose the proper measurement mode; 5) set the automatic stop at the force reduction by 20%; 6) start the measurements. Both the “flat” position and “side” position breakage measurements were conducted shown in Fig. 7.

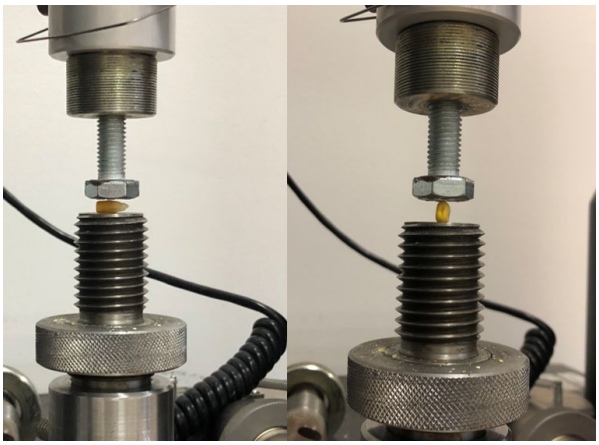

Figure 7. Corn breakage in “flat” position and “side” position

3. Results and discussion

Moisture contents

The moisture content is shown in Table 1, and the average moisture content of corn 1, corn 2, wheat 1 and wheat 2 are 14.22%, 12.6%, 11.66% and 11.56%, respectively, meanwhile the standard deviation of those are 0.33, 0.54, 0.13 and 0.23, respectively. The difference of the moisture content between the corn1 and corn2 is 11.39%. The moisture contents of wheat1 and wheat2 are almost the same, with just 0.86% difference. So, the moisture content could be somehow different even they are corns. The moisture content of agricultural granular materials has no relationship with the type of particles. However, the average moisture content of corn was in our case higher than that of wheat.

Bulk density

The average bulk density of corn 1, corn 2, wheat 1 and wheat 2 are 779.408 g/L, 748.58 g/L, 787.988 g/L and 794.752 g/L, respectively, meanwhile the standard deviation of those are 10.06, 6.72, 15.76 and 4.84, respectively. The relative difference between the corn particles is 3.96%, and the relative difference between wheat particles is 0.85%. Even the relative difference between the corn2 and wheat2 is less than 5.82%. Factors that have an effect on the bulk density of particles are the shape, size and density of the particles [27]. The shapes and sizes of corn and wheat particles are different, and the porosity rate of corn is higher than that of wheat. So the estimation is that the density of corn grains is high due to the high moisture content of corn grains and high porosity of corn as well, but the density of wheat grains is low due to low humidity of wheat grains, but the porosity of wheat grains is small, then the bulk densities of the grains of the two varieties tend to be the same.

Angle of repose

The average angle of repose of corn1, corn2, wheat1 and wheat2 are 15.18°, 12.92°, 30.28° and 27.9°, respectively, meanwhile the standard deviation of those are 1.69, 1.01, 1.65 and 1.63 respectively. The relative difference in the angle of repose for corn particles is 14.89%, and the relative difference in the angle of repose for wheat particles is 7.86%. However, the angle of repose between the corn and wheat is quite different. So, the different types of agricultural particles have different angles of repose based on the results.

Shear test

Fig. 8 and Fig. 9 below show the shear tests of two types of corn grains corn1 and corn2 under different normal loads and the shear forces obtained from the tests are different. At 30 kg normal load, the shear force of corn1 is around 200-250 N, and that of the corn2 is around 200-260 N. At 60 kg normal load, the shear force of corn1 is around 400-550 N, and that of corn2 is around 400-470 N. At 90 kg normal load, the shear force of corn1 is around 550-700 N, and that

of the corn2 is around 580-700 N. At 120 kg normal load, the shear force of corn1 is around 900-1000 N, and that of the corn2 is around 750-850 N. When the shear displacement reaches a certain value, the shear force reaches its maximum value, and then the shear force tends to dynamic equilibrium. The shear force increases with increase in normal load based on the curves below, which is consistent with their result in previous study [15]. In the first diagram of Fig. 8, there are two points of sudden drop, this could be caused by corn particle breakage by the shear force during the shearing process. They [5] also reported the particle breakage happened during shear test.

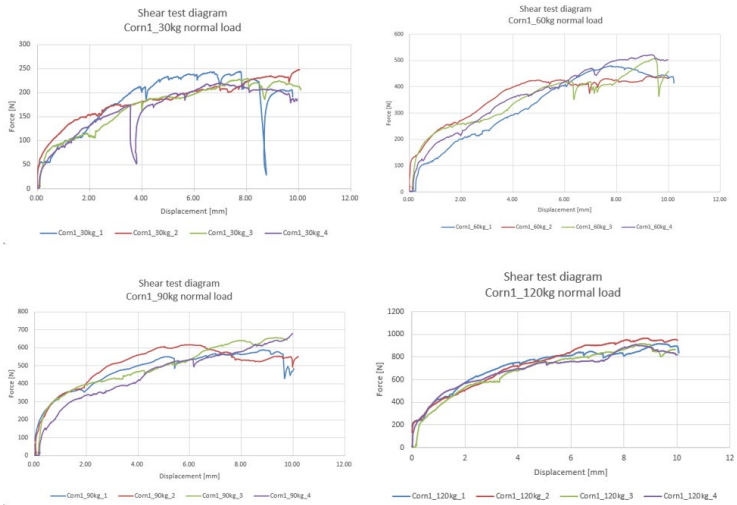

Figure 8. Shear test diagrams of corn1 particles with different normal loads

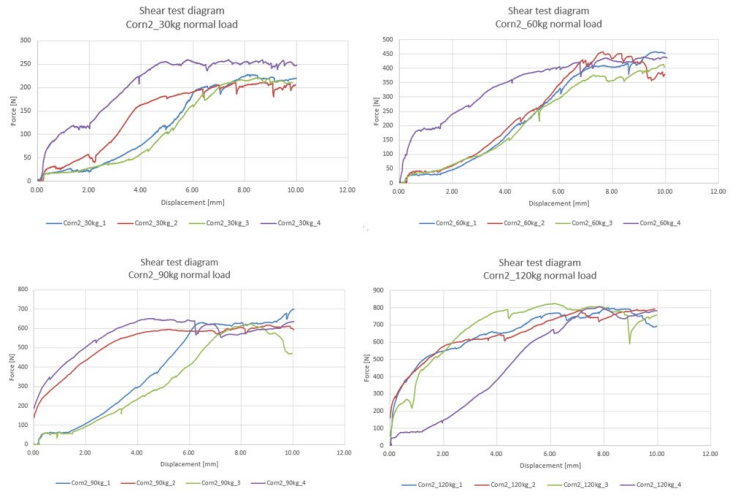

Figure 9. Shear test diagrams of corn2 particles with different normal loads

Fig. 10 and Fig. 11 show the shear test diagrams of wheat1 and wheat2 particles under 4 different normal loads. At 30 kg normal load, the shear force of wheat1 is around 200-250 N, and that of wheat2 is around 160-230 N. At 60 kg normal load, the shear force of wheat1 is around 380-480 N, and that of wheat2 is around 300-350 N. At 90 kg normal load, the shear force of wheat1 is around 500-600 N, and that of wheat2 is around 400-500 N. At 120 kg normal load, the shear force of wheat1 is around 700-800 N, and that of wheat2 is around 550-610 N. The particle breakage occurred in the process of shear test of wheat particles at 30kg normal load. The shear force of wheat particle has similar characteristics, which are higher normal causes higher shear force and the equilibrium status will be reached after the maximum shear with a certain shear displacement.

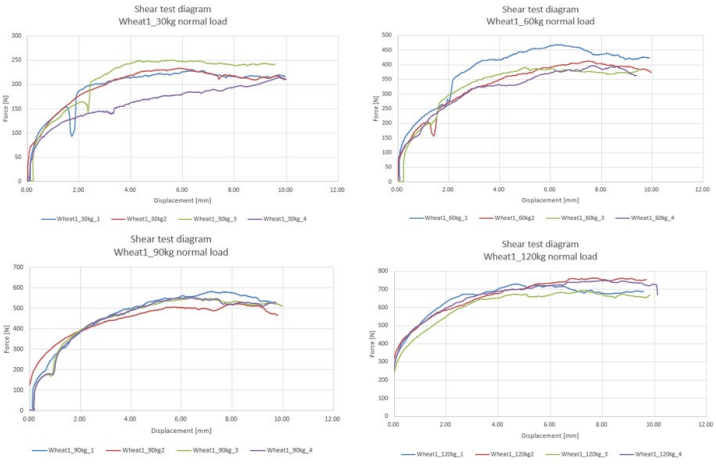

Figure 10. Shear test diagram of wheat1 particles with different normal loads

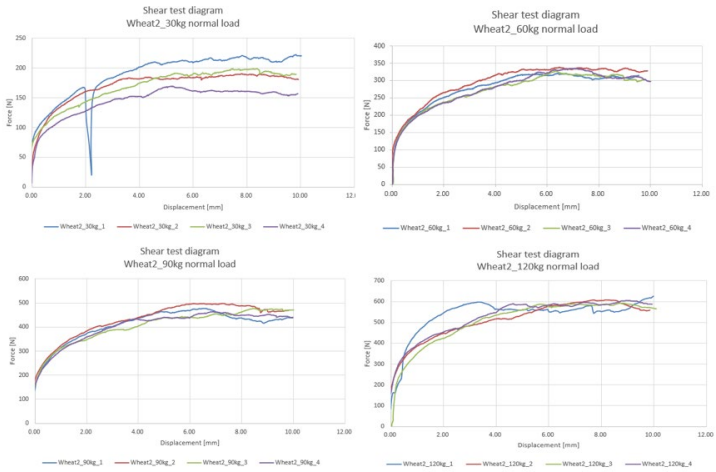

Figure 11. Shear test diagram of wheat2 particles with different normal loads

Particle breakage

Fig. 12 shows the different particles with different positions have different maximum breakage forces. For the same variety of particles, the maximum breakage force of particles placed in the "flat" position is much higher than that of particles placed in the "side" position. Fig. 13 shows the high value of the slope of the breakage curve, which can be translated to a higher value means steeper force-displacement curves for corn breakage can lead to. The slopes of breakage curves also show that "flat" position particles have bigger value than the "side" position. So, the breakage is related to the particle shape [28]. Particles of different shapes may have different stress concentration points when subjected to external forces, resulting in different breakage patterns.

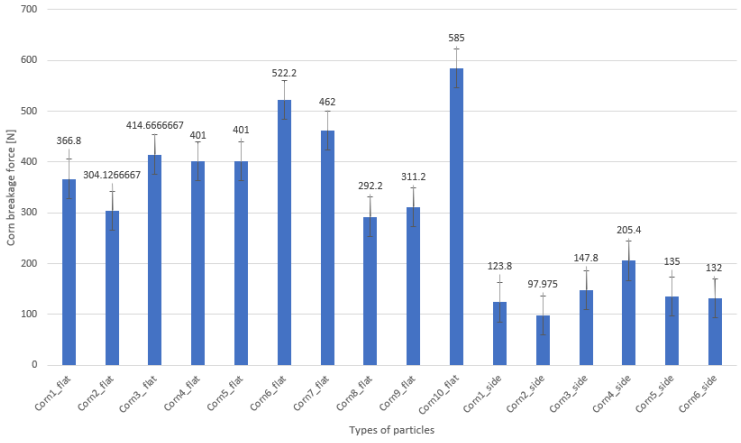

Figure 12. Diagram of corn breakage force

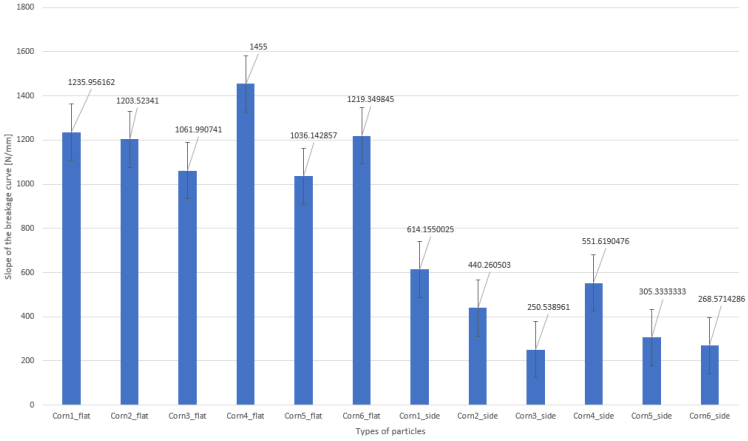

Figure 13. Slope of the breakage curves for all types

4. Conclusions

Regarding this data is needed for calibration modeling purposes, the following experiments will be conducted in future:

- Investigate the particle breakage phenomenon after having particle breakage model
- Analyze the breakage phenomenon
- Conduct DEM simulation of shear test using crushable particles without crushing the particles during shear testing
- Keep the ratio of the minimal shear lid size – particle size

Acknowledgement

This research was supported by China Scholarship Council (CSC), Stipendium Hungaricum Scholarship Programme of Hungary and Hungarian University of Agriculture and Life Sciences.

References

[1] A. Bablena, N. Schrempf, and I. Keppler, “The effect of particle shape on the angle of repose test based calibration of discrete element models,” Hung. Agric. Eng., no. 40, pp. 39–46, 2021, doi: 10.17676/HAE.2021.40.39.

[2] M. Nitka and A. Grabowski, “Shear band evolution phenomena in direct shear test modelled with DEM,” Powder Technol., vol. 391, pp. 369–384, Oct. 2021, doi: 10.1016/j.powtec.2021.06.025.

[3] Z. Wang, G. Jing, Q. Yu, and H. Yin, “Analysis of ballast direct shear tests by discrete element method under different normal stress,” Measurement, vol. 63, pp. 17–24, Mar. 2015, doi: 10.1016/j.measurement.2014.11.012.

[4] H. Huang and E. Tutumluer, “Discrete Element Modeling for fouled railroad ballast,” Constr. Build. Mater., vol. 25, no. 8, pp. 3306–3312, Aug. 2011, doi: 10.1016/j.conbuildmat.2011.03.019.

[5] S. Liu, H. Mao, Y. Wang, and L. Weng, “Experimental study on crushable coarse granular materials during monotonic simple shear tests,” Geomech. Eng., vol. 15, no. 1, pp. 687–694, May 2018, doi: 10.12989/GAE.2018.15.1.687.

[6] T. Afshar, M. M. Disfani, A. Arulrajah, G. A. Narsilio, and S. Emam, “Impact of particle shape on breakage of recycled construction and demolition aggregates,” Powder Technol., vol. 308, pp. 1–12, Feb. 2017, doi: 10.1016/j.powtec.2016.11.043.

[7] Y. Xiao, M. Meng, A. Daouadji, Q. Chen, Z. Wu, and X. Jiang, “Effects of particle size on crushing and deformation behaviors of rockfill materials,” Geosci. Front., vol. 11, no. 2, pp. 375–388, Mar. 2020, doi: 10.1016/j.gsf.2018.10.010.

[8] A. Bagherzadeh-Khalkhali, A. A. Mirghasemi, and S. Mohammadi, "Micromechanics of breakage in sharp-edge particles using combined DEM and FEM," Particuology, vol. 6, no. 5, pp. 347–361, Oct. 2008, doi: 10.1016/j.partic.2008.07.002.

[9] J. J. Fitzpatrick, T. Iqbal, C. Delaney, T. Twomey, and M. K. Keogh, "Effect of powder properties and storage conditions on the flowability of milk powders with different fat contents," J. Food Eng., vol. 64, no. 4, pp. 435–444, Oct. 2004, doi: 10.1016/j.jfoodeng.2003.11.011.

[10] Y. Han et al., "Breakage behaviour of single rice particles under compression and impact," Adv. Powder Technol., vol. 32, no. 12, pp. 4635–4650, Dec. 2021, doi: 10.1016/j.apt.2021.10.017.

[11] J. Azmir, Q. Hou, and A. Yu, "CFD-DEM study of the effects of food grain properties on drying and shrinkage in a fluidised bed," Powder Technol., vol. 360, pp. 33–42, Jan. 2020, doi: 10.1016/j.powtec.2019.10.021.

[12] M. Ucgul, J. M. Fielke, and C. Saunders, "Three-dimensional discrete element modelling of tillage: Determination of a suitable contact model and parameters for a cohesionless soil," Biosyst. Eng., vol. 121, pp. 105–117, May 2014, doi: 10.1016/j.biosystemseng.2014.02.005.

[13] C. Hoshishima, S. Ohsaki, H. Nakamura, and S. Watano, "Parameter calibration of discrete element method modelling for cohesive and non-spherical particles of powder," Powder Technol., vol. 386, pp. 199–208, Jul. 2021, doi: 10.1016/j.powtec.2021.03.044.

[14] A. El Hariri, A. Elawad Eltayeb Ahmed, and P. Kiss, "Review on soil shear strength with loam sand soil results using direct shear test," J. Terramechanics, vol. 107, pp. 47–59, Jun. 2023, doi: 10.1016/j.jterra.2023.03.003.

[15] N. Mashhadiali and F. Molaei, "Theoretical and experimental investigation of a shear failure model for anisotropic rocks using direct shear test," Int. J. Rock Mech. Min. Sci., vol. 170, p. 105561, Oct. 2023, doi: 10.1016/j.ijrmms.2023.105561.

[16] I. Keppler, F. Safranyik, and I. Oldal, "Shear test as calibration experiment for DEM simulations: a sensitivity study," Eng. Comput., vol. 33, no. 3, Jan. 2016, doi: 10.1108/EC-03-2015-0056.

[17] J. Nečas et al., "Shear lid motion in DEM shear calibration and the effect of particle rearrangement on the internal friction angle," Powder Technol., vol. 403, p. 117417, May 2022, doi: 10.1016/j.powtec.2022.117417.

[18] A. Grabowski and M. Nitka, "3D DEM simulations of basic geotechnical tests with early detection of shear localization," Stud. Geotech. Mech., vol. 43, no. 1, pp. 48–64, Dec. 2020, doi: 10.2478/sgem-2020-0010.

[19] X. Liu, A. Zhou, K. Sun, and S.-L. Shen, "Discrete element modelling of the macro/micro-mechanical behaviour of unsaturated soil in direct shear tests including wetting process," Powder Technol., vol. 415, p. 118125, Feb. 2023, doi: 10.1016/j.powtec.2022.118125.

[20] C. J. Coetzee and D. N. J. Els, "Calibration of discrete element parameters and the modelling of silo discharge and bucket filling," Comput. Electron. Agric., vol. 65, no. 2, pp. 198–212, Mar. 2009, doi: 10.1016/j.compag.2008.10.002.
[21] S. Wang et al., "Experimental investigation of rock breakage by a conical pick and its application to non-explosive mechanized mining in deep hard rock," Int. J. Rock Mech. Min. Sci., vol. 122, p. 104063, Oct. 2019, doi: 10.1016/j.ijrmms.2019.104063.
[22] B. Olaleye, C.-Y. Wu, and L. X. Liu, "Impact breakage of single pharmaceutical tablets in an air gun," Int. J. Pharm., vol. 597, p. 120273, Mar. 2021, doi: 10.1016/j.ijpharm.2021.120273.
[23] Y. Han et al., "Analysis of breakage behavior of rice under impact," Powder Technol., vol. 394, pp. 533–546, Dec. 2021, doi: 10.1016/j.powtec.2021.08.084.
[24] X. Kong, J. Liu, T. Yang, Y. Su, J. Geng, and Z. Niu, "Numerical simulation of feed pellet breakage in pneumatic conveying," Biosyst. Eng., vol. 218, pp. 31–42, Jun. 2022, doi: 10.1016/j.biosystemseng.2022.03.012.
[25] Y. Zeng, B. Mao, F. Jia, Y. Han, and G. Li, "Modelling of grain breakage of in a vertical rice mill based on DEM simulation combining particle replacement model," Biosyst. Eng., vol. 215, pp. 32–48, 2022, doi: https://doi.org/10.1016/j.biosystemseng.2021.12.022.
[26] B. M. Ghodki, K. Charith Kumar, and T. K. Goswami, "Modeling breakage and motion of black pepper seeds in cryogenic mill," Adv. Powder Technol., vol. 29, no. 5, pp. 1055–1071, May 2018, doi: 10.1016/j.apt.2018.01.023.
[27] Z. Chen, C. Wassgren, E. Veikle, and K. Ambrose, "Determination of material and interaction properties of maize and wheat kernels for DEM simulation," Biosyst. Eng., vol. 195, pp. 208–226, Jul. 2020, doi: 10.1016/j.biosystemseng.2020.05.007.
[28] T. Zhang, C. Zhang, J. Zou, B. Wang, F. Song, and W. Yang, "DEM exploration of the effect of particle shape on particle breakage in granular assemblies," Comput. Geotech., vol. 122, p. 103542, Jun. 2020, doi: 10.1016/j.compgeo.2020.103542.

Physical and mechanical properties of Mars global simulant MGS-1

Jessica Ellen LIMA DIAS[1], György BARKÓ[2]
[1] *Doctoral School of Mechanical Engineering,*
Hungarian University of Agriculture and Life Sciences, MATE, Gödöllő
[2]*Department of Machine Constructions, Institute of Technology,* MATE, Gödöllő

Abstract

This study provides a comprehensive overview of the physical and mechanical properties of Mars Regolith Simulants, with a particular focus on MGS-1, a widely used standard simulant in various research applications. Key mechanical properties such as density, particle size, porosity, friction angle, and thermal inertia are examined, drawing from the findings of previous studies to understand their impact on the interaction of Mars regolith simulant (MRS) with other materials. The characterization of Martian simulants in terms of particle size, color, and chemical and mineralogical variability is also discussed based on available literature. Additionally, the study proposes two methods of abrasivity testing to be conducted using MGS-1 to further explore its properties and potential applications.

Keywords

Regolith; Mars; Abrasion, Abrasivity

1. Introduction

In recent years, significant advances have been made in understanding the mechanical and physical properties of the Martian surface, geology, and soil. No physical samples of Martian regolith are available on Earth. Therefore, researchers rely on Mars Regolith Simulants (MRS) created in laboratories over the past two decades (Cannon et al., 2019). These simulants must accurately reflect the characteristics of the Martian regolith. The mechanical properties of regolith, including compressive and shear strength, are influenced by particle size and density. Therefore, accurate representation is crucial for testing materials and designing hardware for Martian conditions.

Unlike the Earth, Mars does not have widespread vegetation or plant life that helps anchor the soil and prevent erosion. The absence of vegetation means there are fewer mechanisms to stabilize the soil and reduce dust generation. The dusty atmosphere of Mars presents unique challenges for future human missions and robotic exploration. Materials need specific properties to function on the dusty

Mars surface; they should exhibit high abrasion resistance to withstand the abrasive nature of the Martian regolith. The fine-grained nature of Martian regolith can enter joints and extremely tiny cracks, causing significant abrasion and leading to wear and tear on exposed surfaces (Barkó et al., 2023). Additionally, Martian dust has electrostatic properties that can cause it to adhere to surfaces. Moreover, Mars experiences extreme temperature variations, ranging from frigid cold to relatively warmer temperatures. Materials must exhibit thermal stability to endure these fluctuations without degradation or loss of functionality.

Given the potential for dust entrance, materials used in equipment and habitats on Mars need to provide effective sealing and containment to protect internal components and maintain environmental control. On Apollo 16 and 17, the LRV batteries exceeded operational temperature limits because of dust accumulation and the inability to effectively brush off the dust (Gaier et al., 2019).

This review provides a comprehensive overview of the Martian regolith's physical and mechanical properties. It suggests abrasion test setups to evaluate the impact of Mars Global Simulant MGS-1 on material surfaces. It highlights the current understanding and emphasizes its implications for future exploration and research, underscoring the importance of this field of study.

2. Literature review

In this brief literature review about Mars regolith simulant, expect an examination of Martian regolith composition and properties, mechanisms of abrasion, and summaries of material testing against sand, soil, or simulants. The review will describe experimental setups, present key findings on material durability and abrasion resistance, and discuss Mars mission equipment design implications. Additionally, it will highlight gaps in current research and suggest directions for future studies to improve material performance under Martian conditions.

Types of Mars Regolith Simulants

Several types of Mars regolith simulants have been developed to aid in the study and testing of materials and equipment for Mars missions. Among the most notable are JSC Mars-1, derived from volcanic ash in Hawaii, and the Mojave Mars Simulant (MMS), created from Mojave Desert material to mimic Martian soil's physical and mineralogical properties. Additionally, Mars Global Simulant (MGS-1) has been designed to replicate the chemistry and the geochemical composition of regolith from the Gale crater closely.

JSC was developed by the Johnson Space Center, consisting mainly of X-ray amorphous palagonite, a gel-like hydrated and oxidized alteration product of volcanic glass, with crystallites of plagioclase and magnetite (Allen et al., 1998). It was based on enhancing the MMS to achieve a more realistic volatile release

pattern resembling the Rocknest sample. JSC Mars-1 and MMS have been used in a variety of laboratory studies as soil simulants, but these simulants are based on early studies of Martian regolith.

While the original MMS is exclusive to NASA, The Martian Garden company sells a product called Mojave Mars Simulant, renamed MMS-1. However, The Martian Garden company was not involved with the creators of MMS, and their substitutes do not completely resemble the original version as evaluated by the authors Peters et al. (2008). Quantitative mineralogical analysis is not accessible for JSC Mars-1, MMS, MMS-1, or MMS-2, the upgraded version of MMS-1.

Several significant distinctions exist between the earlier Mars substitutes and recent in-situ evaluations of Martian regolith. Regarding crystallinity, JSC Mars-1 is predominantly X-ray amorphous, while MMS, MMS-1, and MMS-2 are nearly 100% crystalline. In contrast, Martian soils consist of a roughly equal mixture of crystalline and amorphous phases, as the CheMin instrument on the Mars Science Laboratory Curiosity rover indicates. The presence of amorphous materials can influence the abrasion properties of the simulant. Due to their lack of a defined crystalline structure, they can alter the overall hardness and abrasiveness of the mixture. Specifically, they might increase the simulants' ability to wear down surfaces due to their irregular shapes and varied mechanical properties, potentially leading to higher rates of abrasion on materials that come into contact with it.

JSC Mars-1 exhibits high hygroscopic properties, holding over 20% of its weight in water under ambient conditions, and is known to contain substantial organic carbon, characteristics not realistic to Mars. Additionally, most of the older simulant types contain minimal sulfur, whereas Martian regolith contains up to 6% by weight of SO_3, assuming all sulfur is in the form of sulfate (Cannon et al., 2019). The exact composition of Martian regolith can vary depending on the location on Mars, but it is generally made up of a combination of minerals, including iron oxides, giving Mars its reddish color, basaltic rocks, volcanic ash, and other silicate minerals. This sulfur and iron content variation will give different simulants a different appearance, as shown in Figure 1.

Mars Global Simulants, represented by MGS-1, is a simulant designed to emulate the technical aspects of Martian regolith, including mineralogical, chemical, and physical characteristics. The mineral composition of these simulants strives to mirror Martian regolith, incorporating minerals such as olivine, pyroxenes, and feldspars in proportions that align with observations from Mars missions. Particle size distribution is a critical aspect, meticulously crafted to resemble the range found on Mars, influencing porosity and soil behavior.

P-MRS and S-MRS were simulants employed to evaluate the capabilities of the Raman Laser Spectrometer (RLS) on the ExoMars rover in identifying both organics and minerals. The ExoMars Program is a paired mission led by the European Space Agency (ESA) designed to understand if life ever existed on

Mars. The intention was to simulate the environmental transitions on Mars, ranging from early hydrothermal alteration to subsequent cold and dry oxidizing conditions (Böttger et al., 2012). The Jezero crater delta simulant (JEZ-1) was created by the Exolith Lab at the University of Central Florida to replicate the materials expected in the Jezero crater deltas location explored by NASA's Mars 2020 Perseverance Rover. It is based on the MGS-1 mineralogy, chemistry, and grain size distribution added to smectite clay, Mg-carbonate, and additional olivine, aiming to accurately reflect the anticipated composition of the Martian surface in this region. Other Mars simulants have been created using terrestrial basalts, natural weathering profiles, and commercial sand products. Various countries have formulated Mars simulants, such as a range of nepheline and quartz sands as geotechnical substitutes for the European Space Agency and terrestrial basalt combined with magnetite and hematite for China's Mars exploration program. However, these simulants have yet to be commercialized or adopted.

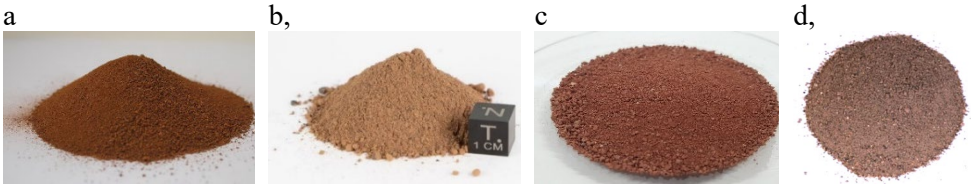

Figure 1: Different colors due to chemical variability in Mars simulants a) JSC-1 b) MGS-1 c) MMS-1 d) JEZ-1. Sources: JSC-1A Lunar and Martian Soil Simulants | Space Foundation, n.d.; Mojave Mars Simulant - the Martian Garden, n.d.; Exolith Lab (Space Resource Technologies, 2024).

Martian soils have been examined in situ at seven locations by landers and rovers, with additional insights from orbital remote sensing. The soil's major element chemistry and mineralogy show significant similarities at the Spirit, Opportunity, and Curiosity rovers in three landing sites, indicating the presence of a global basaltic soil that may have local to regional enrichment in rarer evolved volcanic compositions or alteration.

Nevertheless, the three landing sites compared are all from sulfur-rich terrains, and a genuine global average may have fewer sulfur-bearing minerals, aligning with MGS-1 bulk chemistry constraint. Nevertheless, the MGS-1 standard is based on the windblown soil at Gale crater, with additional data from measurements by other landed and orbital assets. MGS-1 stands out as the most thoroughly characterized Martian soil up to date, and its chemical resemblance to soils at different landing sites makes it a suitable reference material for developing a new simulant standard based on currently available data. Authors Cannon et al. (2019) suggested a standard design for MGS-1, concluding that the prototype simulants based on MGS-1 exhibit physical, chemical, spectral, and volatile properties that closely resemble those of the Rocknest crate and other Martian soils. They represent an advancement over previous simulants and are

well-suited for various applications, including ISRU development, agriculture, astrobiology studies, and testing flight hardware.

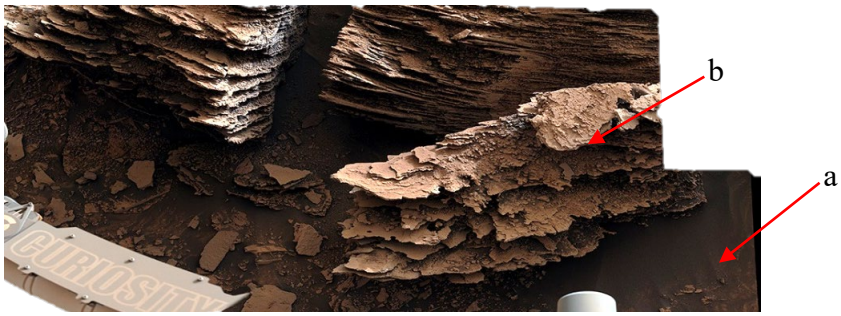

Figure 2: Mar's surface believed to have formed in a small ancient pond; a) Darker regolith b) Lighter bigger boulders. Source: Adapted from NASA (Greicius, 2023).

Figure 2 is from NASA's Curiosity rover, showing a transition zone between a clay-rich area and a sulfate-rich region. Both areas were explored to uncover evidence of water in the Martian past, but the transition zone is also proving scientifically intriguing. This zone might reveal a significant climate shift on Mars that occurred billions of years ago. Clay minerals formed from ancient lakes and streams are found at the base of Mount Sharp (a location on Mars).

Mechanical Properties

The mechanical properties of Martian soil have an impact on spacecraft landing and exploration on the planet's surface. These properties also influence various geomorphological processes, such as mass wasting, crater formation, and erosion, which are crucial for understanding the evolution of Mars' surface layers. Authors Fergason et al. (2006) stated that the surface layers of Mars soil differ from subsurface layers, using this information in a surface model.

Understanding Martian soil's mechanical properties will enhance future lander missions' success and provide more precise constraints for modeling geomorphological processes. High-resolution images from the Mars Global Surveyor, laser altimeter measurements, and photographs from the Mars Odyssey mission offer unique opportunities for conducting valuable soil mechanics analyses. An investigation was carried out to determine the soil's mechanical properties through computer reconstructions of natural slopes, mass wasting features, and landslides. This investigation focused on the 2003 Mars Exploration Rover (MER) landing sites. The findings of the investigation can be applied to estimate the soil's ultimate bearing capacity, dynamic penetration resistance, angle of critical slope stability, and rover trafficability.

While dynamic penetration in sands is a well-known phenomenon in terrestrial geotechnics, it is quite intricate as it involves the shearing properties of sand at significant strains. This includes the substantial influence of shear-induced plastic volume changes through contraction in loose sand or dilation in

dense sand. The primary factor influencing the mechanical properties of sand is its density, which is, in turn, dependent on characteristics such as grain size distribution and the shape and angularity of the grains.

On Mars, regolith forms from meteorite impacts and various uncovered geological processes that alter the surface layer. The Martian surface is also shaped by wind, which sorts grains by size and shapes them round (Goetz et al., 2010). Golombek et al. (2008, 2016) summarized the physical properties of Martian regolith using remote sensing data and previous in-situ observations, as detailed in Table 1.

On Mars, the regolith results from meteorite's impact and various geological processes that have altered the surface layer. Unlike the lunar regolith, the Martian surface layer is also affected by aeolian processes, which sort grains by size and produce rounded grains (Goetz et al., 2010). Golombek et al. (2020) have provided a summary of the physical properties of Martian regolith based on remote sensing data observations and comparisons to previous in-situ observations, summarized in Table 1.

Lai and Chen (2017) conducted a comprehensive study wherein the physical and mechanical properties of JSC-1 were systematically characterized through a series of laboratory tests. The properties under examination encompassed specific gravity, particle size, particle size distribution, particle shapes, and shear strength. The researchers employed X-ray computed tomography to acquire particle images, utilizing various imaging processing techniques to characterize particle shapes. Subsequently, these shape data were utilized to create irregularly shaped numerical particles through the domain overlapping filling method. The study on JSC-1 reveals that it can be classified as well-graded sand (SW) based on the Unified Soil Classification System, with a specific gravity of 1.94 ± 0.02. Notably, the particle shape plays a significant role, contributing to about 40% of the shear resistance in the JSC-1. Moreover, introducing irregular particles enhances both mobilized contact friction and the number of particle contacts within the assembly when compared to an assembly featuring an equivalent number of disc-shaped particles. Indicating the importance of shape size for mechanical testing using MRS.

A series of mechanical tests were carried out by authors Delage et al. (2017) on various Mars regolith simulants by authors to help estimate the mechanical properties of the regolith at the landing site of the InSight mission, in complement of previous estimations carried out from satellite observations and local observations during previous missions. These tests were conducted to complement previous estimations derived from satellite observations and local observations during previous missions. The investigation focused on the elastic interaction between the seismometer's feet and the regolith, contributing to the refinement of the seismometer's noise model, including noise caused by wind. The study also addressed the estimation of seismic wave velocity in the surface layer, a critical factor for understanding dynamic penetration. The mechanical characteristics of the first 5 meters of regolith, influencing dynamic penetration,

were explored, with a particular emphasis on density effects. The obtained densities ranged from 1.4 to 1.5 mg/m³, slightly higher than the 1.3 mg/m³ density estimated at the landing site's surface. Direct shear box tests suggested a friction angle of approximately 30°, with the possibility of increasing density variations in the first 5 meters of the regolith layer. Density gradients were estimated through oedometer compression tests, indicating potential stress release around the penetrating mole during penetration.

The abrasive characteristics of Mars regolith can be attributed to the unique geological processes and environmental conditions on the Martian surface. Mars is known for its dynamic and often harsh climate, characterized by frequent dust storms, high winds, and a thin atmosphere. Over time, the interaction of these environmental factors with the Martian surface has led to the creation of fine-grained dust particles that make up the regolith. The abrasive nature of the regolith arises from the constant mechanical weathering and erosion processes that occur as these dust particles are lifted, transported, and collide with each other and with the underlying rocks and surfaces (Göttler et al., 2019). In order to establish structures on Mars, the abrasive properties of the Martian regolith should be studied in medium to long-term trials to understand its potential impact on equipment, habitats, and exploration tools used in Mars missions.

In addition to the natural weathering processes, the presence of various minerals in the regolith contributes to its abrasive nature. For instance, basaltic minerals such as olivine and pyroxene, as well as amorphous materials, are common components of Martian regolith, as previously mentioned.

Particle Size Distribution

Soil particle size refers to the size of individual particles that comprise the soil structure. It plays a crucial role in determining soil properties and characteristics, such as water-holding capacity, drainage, fertility, and aeration. Soils can be classified as sandy, silty, clayey, or a combination of these, such as sandy loam, silty clay, or loamy soil. The soil texture influences its drainage capacity, water-holding capacity, nutrient retention, and workability. Sandy soils have good drainage but low water-holding capacity, while clayey soils have excellent water-holding capacity but poor drainage.

Authors Delage et al. (2017) divided Mars regolith according to bulk density and grain size, and other mechanical properties, as shown in Table 1.

	Bulk density (g/cm^3)	**Grain size (mm)**	**Cohesion (kPa)**	**Friction angle (°)**	**Thermal inertia (Jm^{-2} K^{-1} s$^{-1/2}$)**
Drift	1-1.3	0.001–0.01	0–3	15–21	40–125
Sand	1.1–1.3	0.06–0.2	0–1	30	60–200
Crusty to cloddy sand	1.1–1.6	0.005–0.5	0–4	30–40	200–326
Blocky, indurated soil	1.2–2	0.05–3	3–11	25–33	368–410
Dense float rock, volcanic	2.6–2.8	2–2000	1000–10000	40–60	> 1200–2500
Clastic rock	2				620–1100
Sulfate rock	> 2				> 400–1100

Table 1: Grain size distribution of Mars Regolith measured by in-situ observations. Adapted from Golombek et al. (2008) and Delage et al. (2017). Data derived from Moore et al. (1987, 1999), Moore and Jakosky (1989), Christensen and Moore (1992), Arvidson et al. (2004a, 2004b), Christensen et al. (2004a, 2004b), Herkenhoff et al. (2004a, 2004b), Fergason et al. (2006) from Delage et al. (2017).

Authors Cannon et al. (2019) considered the physical properties of the Mars Global Simulant MGS-1; their proposed prototype simulant has a bulk density of 1.29 g/cm^3. In comparison, soils at the Pathfinder landing site were estimated to have a bulk density ranging from 1.07 to 1.64 g/cm^3, while drift material at the Viking 1 landing site had an estimated bulk density of 1.15 ± 0.15 g/cm^3. It is worth noting that the lower gravity may impact the bulk density.

Sand deposits are characterized by a bulk density ranging from 1000 to 1300 kg/m³, with grain sizes falling from 0.06 to 0.2 mm. These deposits consist of low-cohesion particles, typically exhibiting cohesion values between 0 and 1 kPa, and possess an internal friction angle of approximately 30°. To assess the thermal inertia of these materials, one can employ the formula I = (kρc)1/2, where k denotes thermal conductivity, ρ represents bulk density, and c signifies specific heat. This thermal inertia parameter gauges the resistance to temperature changes within the surface's upper 2–30 cm. Thermal inertia is a property that describes how a material responds to changes in temperature. Specifically, it quantifies the resistance of a substance to temperature changes. In the context of planetary science and remote sensing, thermal inertia is often used to characterize the ability of a planetary surface to retain and release heat.

Fine particles, characterized by smaller sizes, exhibit lower thermal inertia values, typically ranging from 40 to 125 Jm^{-2} K^{-1} s$^{-1/2}$. In contrast, larger particles like sand display higher thermal inertia, with values falling between 60 and 200 Jm^{-2} K^{-1} s$^{-1/2}$, therefore higher heat holding capacity. Notably, the cementation of grains contributes to an increase in thermal inertia, signifying

potential cohesion. Cohesion levels in Mars regolith are typically weak, usually remaining below a few kPa. This comprehensive set of characteristics sheds light on the diverse properties of sand deposits and their thermal behavior, which is particularly crucial for understanding surface conditions on Mars (Cannon et al., 2019).

Authors Fergason et al. (2006) described the physical properties of the landing sites of the Curiosity and Spirit rovers, derived from thermal inertia data, with findings for particle size and mobile activity. Noteworthy findings include the thermal inertia values of 160 to 200 and 200, respectively, corresponding to particle diameters of 0.016 mm (fine sand). The similarity in thermal inertia suggests shared atmospheric conditions, indicating particle mobility in the current climate. Their study further explores Laguna Hollow at Gusev crater, revealing a modeled thermal inertia of 150, corresponding to particle diameters of 0.0045 mm (silt). This fine-grained material, observed in small craters, is filled with a combination of fine material and air-fall dust. In the Gusev crater, the rock target Beacon exhibits a thermal inertia of 1200, consistent with expectations for a basaltic rock of its size.

In their research, Gundlach and Blum (2013) introduced a methodology for determining particle size distribution within the regolith of diverse planetary bodies. Notably, smaller asteroids exhibit a regolith characterized by coarse particles within the millimeter to centimeter range. In instances of coarse regolith, radiative heat transport overwhelmingly dominates the total heat conductivity of the regolith. The reduction in grain size can be conceptually attributed to the collision history of asteroids.

Research indicates that hyper-velocity impacts are pivotal in size discrimination within regolith properties. These impacts result in the formation of fragments, where those with velocities below the escape speed of the parent body become integral components of the regolith. Naturally, smaller fragments propelled with the highest velocities during impacts predominate in this process. Gundlach and Blum (2013) analyzed planetary regolith grain sizes across various celestial bodies, including asteroids ranging from 0.3 km to 4,880 km in diameter, the Moon, the Martian moons, and Mercury. Their findings revealed an anti-correlation between regolith grain size and the gravitational acceleration of the planetary body. Importantly, this anti-correlation proved consistent across various spectral classes of asteroids. This correlation supports the hypothesis that planetary regolith originates from hyper-velocity impacts, progressively breaking down the initially rocky material into finer particle sizes. Their study enhances our understanding of regolith formation and underscores the universal impact of hyper-velocity events in shaping the surfaces of planetary bodies.

The challenges on planetary dust are primarily rooted in its intricate behavior, particularly in terms of transportation and adhesion to surfaces within poorly understood surface environments. Adhesion between solid particles involves five independent mechanisms (van der Waals forces, electrostatic forces, capillary forces, mechanical interlocking, and chemical bonding), with their combined

effect determining the total adhesion between two bodies. While diffusion, involving the intermixing of atoms or molecules on surfaces to create a mixed composition interface layer, is not expected to play a role when dust particles land on solid spacecraft surfaces, mechanical interlocking becomes more probable in airless bodies. This is due to impact agglutinates forming, leading to irregular surfaces that can interlock (Gaier et al., 2019).

Calle et al. (2011) discuss efforts to address the issue of dust accumulation on surfaces in lunar and Martian environments. The authors highlight that lunar dust is expected to be electrostatically charged due to factors like the solar wind, cosmic rays, and solar irradiation. Electrostatically charged lunar dust tends to adhere strongly to surfaces, as observed in the Apollo missions. The same is expected on Mars. The adhesion of lunar dust has been identified as a challenge for both manned and unmanned exploration activities. The authors describe their efforts to develop an electrodynamic dust shield to counter this issue. This technology utilizes electrostatic and dielectrophoretic forces to carry dust particles off surfaces and create a shield that prevents further dust accumulation. The concept of the electrodynamic dust shield was initially introduced by NASA in the late 1960s and later implemented in the 1970s for terrestrial applications. In 2003, Calle and collaborators applied this technology to space applications, specifically for removing dust from solar panels on Mars. Their technology is also demonstrated to be effective in lifting and removing uncharged dust from surfaces under simulated Martian environmental conditions. Furthermore, the authors have developed a version of the electrodynamic dust shield suitable for challenging vacuum conditions. These tests must be conducted on environments that closely mimic extraterrestrial conditions, including the use of regolith, low atmospheric pressures, and very low temperatures.

Chemical and Mineralogical Composition

The typical approach for designing asteroid and planetary simulants starts from mineralogy, as minerals form the fundamental constituents of planetary materials. By commencing with the accurate mineral components, many of the resulting properties (spectral, volatile, physical) should closely resemble the reference material, with necessary adjustments made after analyzing initial prototypes. Geomechanical properties play a crucial role in simulant behavior, and developers or end users can modify these through meticulous sieving (Cannon et al., 2019).

The mineralogical composition of Mars regolith contains various minerals, including silicates, olivine, pyroxene, oxides, and sulfates, indicating volcanic activity and igneous processes. Oxides, particularly iron oxides like hematite and magnetite, are abundant in Martian regolith and contribute to the planet's reddish appearance. These minerals are associated with water-related processes and can provide clues about the past presence of liquid water on Mars. Sulfates, such as gypsum and jarosite, are also present in Martian regolith and are linked to aqueous alteration, indicating the past interaction of water with the Martian

surface. Phyllosilicates, also known as clay minerals, are important indicators of water-rock interactions and are suggestive of environments conducive to microbial life. Furthermore, trace elements, including metals like magnesium, potassium, sodium, and others, are meticulously integrated into Mars simulants to capture the complexity of Martian soil composition.

MGS-1 functions as a mineralogical benchmark and the overall chemical composition of simulants derived from this standard will vary depending on the crystal chemistry of the utilized minerals. Table 2 illustrates the elemental chemistry of the bulk Rocknest Mars regolith, as proposed by Achilles et al. (2017). By employing the mineral recipe provided in Table 2, an estimated chemical composition for MGS-1 simulants is expected, as proposed by Authors Cannon et al. (2019).

Authors Cannon et al. (2019) state that discovering significant quantities of terrestrial minerals with suitable crystal chemistries for Mars, particularly olivine and pyroxene, can be challenging or even impossible. Consequently, actual MGS-1-based simulants may deviate from the calculated chemistry based on the silicates utilized. Enhancing efforts to source accurate mineral chemistries or combinations is imperative for achieving more precise elemental chemistry in the final product, which directly influences the quality of research conducted using the regolith simulant. Understanding the chemistry of Mars regolith is crucial for evaluating its suitability primarily for biological, ISRU, and plant experiments.

	Particle wt%	
	MGS-1 Prototype	Rocknest bulk
SiO_2	50.8	43.0
TiO_2	0.3	1.2
$Al2O_3$	8.9	9.4
FeOT	13.3	19.2
MnO	0.1	0.4
MgO	16.7	8.7
CaO	3.7	7.3
Na_2O	3.4	2.7
K_2O	0.3	0.5
P_2O_5	0.4	1.0
Cr_2O_3	0.1	0.5
Cl	0	0.7
SO_3	2.1	5.5
Total	100	100

Table 2: Major element composition in particles smaller than 0.15mm, showing the MGS-1 prototype proposed by Authors Cannon et al. (2019). Source: Adapted from Cannon et al. (2019) and Achilles et al. (2017).

Abrasion experiments

Abrasion tests are experimental procedures designed to evaluate the wear resistance of materials by simulating conditions of mechanical wear. These tests are essential for determining how materials and coatings perform when subjected to friction and abrasive forces. Common methods include the dry sand/rubber wheel test, which assesses the sliding abrasion resistance using dry sand; the Taber abrasion test, which involves a rotating platform with abrasive wheels; and block-on-ring tests, which examine metal-to-metal contact wear. These tests provide valuable data on material durability, aiding in material selection and engineering design for applications exposed to abrasive environments (Metallurgical Engineering Services, 2024).

Author Mucha (2023) describes abrasivity as the ability of mineral rocks to wear frictionally the surface of other solid materials, primarily metal, but not only. This process occurs in mechanical operations such as rock mining, drilling holes, load transport, and so on. Abrasivity is responsible for how much the element in contact with the mineral wears out. Under this perspective, it is expected that Martian regolith will present high abrasivity when in contact with materials.

The author presented common methods to test mineral abrasivity, and two are highlighted in this research due to their potential for application with MGS-1 samples, the LCPC and the SAT abrasivity tests.

The LCPC (Laboratoire Central des Ponts et Chaussées) test is schematic in Figure 3. The process begins with the preparation of a representative mineral sample, which is crushed to produce particles within a size range of 4 to 6.3 mm. Once the sample is prepared, it is weighed, typically around 500 grams. This precise measurement is crucial for calculating the abrasivity coefficient accurately. The metal sample is then placed in a rotating drum lined with a specific type of steel and equipped with steel balls or rods. The drum is rotated at a specified speed, often around 450 rpm, for a set duration of 5 minutes. This rotation causes the sample to interact abrasively with the steel lining and the steel balls or rods within the drum. The post-test analysis involves weighing the steel balls or rods before and after the test to determine the mass loss due to abrasion. This mass loss is then used to calculate the LCPC Abrasivity Coefficient (LAC), expressed in grams per ton (g/t). The LAC is obtained by dividing the mass loss of the steel elements by the initial mass of the sample. Higher LAC values indicate more abrasive materials.

The results of the LCPC abrasivity test are crucial for geotechnical engineering. They provide insights into the potential wear and tear on construction equipment and tools when dealing with different rock and soil materials.

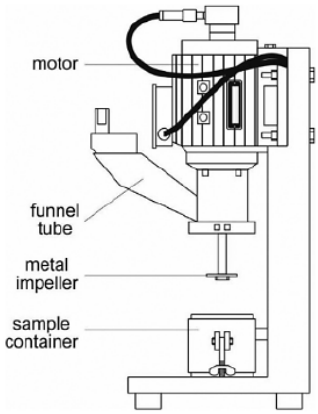

Figure 3: LCPC abrasivity test. Source: Adapted from Mucha (2023).

The SAT (Schmidt abrasivity test), developed at the Norwegian University of Science and Technology in Trondheim, is a standardized method used to evaluate the abrasivity of rock materials by measuring their potential to cause wear on a metal pin. The test begins with the selection and preparation of a representative rock sample, which is cut into a standard shape to fit the test apparatus. A standardized metal pin, typically made of steel, is then pressed against the rock sample using a consistent load. The test machine rotates the pin across the rock surface for a specified duration or number of cycles, simulating abrasive action. After the test, the wear on the metal pin is measured by assessing the mass loss or changes in its dimensions. These measurements are used to calculate the abrasivity index of the rock, providing a quantitative measure of its abrasiveness. The SAT is important in geotechnical engineering as it helps predict the wear on drilling, cutting, and excavating equipment. As research continues, Mars regolith should be tested on SAT.

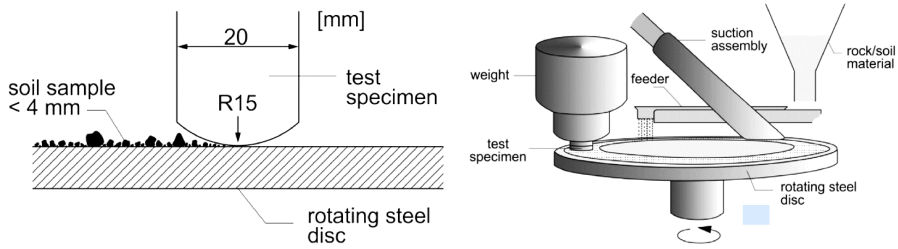

Figure 4: SAT abrasivity test. Source: Adapted from Mucha (2023).

3. Challenges and limitations

The scope of research involving Mars regolith is significantly constrained by the limited availability of Martian soil simulant. The high costs and technical challenges of transporting actual regolith samples from Mars to Earth raise questions about the quality and accuracy of Mars Regolith Simulants (MRS) (Cannon et al., 2019). This limitation impedes in-depth studies on the physical and chemical characteristics of Martian regolith, necessitating a reliance on simulated materials for experimental purposes. While these simulants are essential for making broader research accessible, their production and distribution are also expensive. Creating accurate simulants involves the careful selection and processing of terrestrial materials to mimic the chemical and mineralogical properties of Martian regolith. Ensuring the consistency and quality of these simulants requires continuous research and development efforts, adding to the overall cost of studies related to Mars regolith. Consequently, the mechanical parameters derived from these simulants may not fully represent the diverse conditions found on Mars (Cannon et al., 2019).

While valuable for understanding its physical properties, mechanical tests conducted on Mars regolith are subject to certain limitations that need careful consideration. One significant limitation is the difficulty in replicating the unique environmental conditions of Mars on Earth. Mars has lower gravity and different atmospheric conditions, added to extreme temperatures that heavily affect material properties. These factors can influence the mechanical behavior of regolith as well in ways that cannot be precisely simulated in laboratory settings on Earth (Delage et al., 2017). Mechanical tests conducted under Earth's gravity do not fully capture the response of regolith to stresses and strains under Martian conditions.

Additionally, the variability in the composition and properties of Mars regolith across different locations on the planet poses another challenge. Testing a limited set of samples may not reflect the full range of variability, affecting the generalizability of the results to broader Martian surface conditions. Despite these challenges, ongoing research is essential to evaluate and improve the properties of MRS, including its interaction with Earth materials, as suggested by the abrasivity tests.

4. Conclusions

In conclusion, the use of Mars Regolith Simulants, especially the MGS-1, which is the most accurate representation of Martian regolith nowadays, in abrasivity tests provides crucial insights into the mechanical and physical properties of Martian soil, aiding the preparation and optimization of equipment for future Mars missions. This field of research is rich in questions to be answered. Not only abrasivity tests, but impact tests, compressive, tensile, and penetration tests can be performed with MRS samples. These studies are essential for

understanding the wear resistance and durability of materials under simulated Martian conditions.

Acknowledgement

This study was possible due to the support of ESA and the TDK program.
Thanks to the Stipendium Hungaricum Program for supporting Mechanical Engineering PhD research at the Institute of Technology of MATE University.

References

[1] Abrasion Testing — Metallurgical Engineering Services. (n.d.). Metallurgical Engineering Services. https://www.metengr.com/testing-services/mechanical-testing/abrasion-testing

[2] Achilles, C. N., Downs, R. T., Ming, D. W., Rampe, E. B., Morris, R. V., Treiman, A. H., Morrison, S. M., Blake, D. F., Vaniman, D. T., Ewing, R. C., Chipera, S. J., Yen, A. S., Bristow, T. F., Ehlmann, B. L., Gellert, R., Hazen, R. M., Fendrich, K. V., Craig, P. I., Grotzinger, J. P., . . . Morookian, J. M. (2017). Mineralogy of an active eolian sediment from the Namib dune, Gale crater, Mars. Journal of Geophysical Research. Planets, 122(11), 2344–2361. https://doi.org/10.1002/2017je005262

[3] Allen, C., Morris, R.V., Jager, K.M., Golden, D.C., Lindstrom, D.J., Lindstrom, M.M., Lockwood, J.P., 1998. Martian regolith simulant JSC Mars-1. In: Proceedings of the Lunar and Planetary Science Conference, XXIX, 29 Abstract #1690.

[4] Białobrzeska, B., & Jasiński, R. (2023). Resistance to Abrasive Wear with Regards to Mechanical Properties Using Low-Alloy Cast Steels Examined with the Use of a Dry Sand/Rubber Wheel Tester. Materials, 16(8), 3052. https://doi.org/10.3390/ma16083052

[5] Böttger, U., De Vera, J., Fritz, J., Weber, I., Hübers, H., & Schulze-Makuch, D. (2012). Optimizing the detection of carotene in cyanobacteria in a martian regolith analogue with a Raman spectrometer for the ExoMars mission. Planetary and Space Science, 60(1), 356–362. https://doi.org/10.1016/j.pss.2011.10.017

[6] Calle, C., Buhler, C., Johansen, Hogue, M., & Snyder, S. (2011). Active dust control and mitigation technology for lunar and Martian exploration. Acta Astronautica, 69(11–12), 1082–1088. https://doi.org/10.1016/j.actaastro.2011.06.010

[7] Cannon, K. M., Britt, D. T., Smith, T. M., Fritsche, R. F., & Batcheldor, D. (2019). Mars global simulant MGS-1: A Rocknest-based open standard for basaltic martian regolith simulants. Icarus, 317, 470–478. https://doi.org/10.1016/j.icarus.2018.08.019

[8] Delage, P., Karakostas, F., Dhemaied, A., Belmokhtar, M., Lognonné, P., Golombek, M., De Laure, E., Hurst, K., Dupla, J. C., Kedar, S., Cui, Y., & Banerdt, B. (2017). An Investigation of the Mechanical Properties of Some Martian Regolith Simulants with Respect to the Surface Properties at the InSight Mission Landing Site. Space Science Reviews, 211(1–4), 191–213. https://doi.org/10.1007/s11214-017-0339-7

[9] Fergason, R. L., Christensen, P. R., Bell, J. F., Golombek, M. P., Herkenhoff, K. E., & Kieffer, H. H. (2006). Physical properties of the Mars Exploration Rover landing sites as inferred from Mini-TES–derived thermal inertia. Journal of Geophysical Research, 111(E2). https://doi.org/10.1029/2005je002583 Gaier, J. R.,

[10] Graps, A., & NASA Glenn Research Center, Cleveland, OH, USA. (2019). Managing planetary dust during surface operations. Planetary Science Institute; Baltics in Space; University of Latvia. https://ntrs.nasa.gov/api/citations/20190002304/downloads/20190002304.pdf

[11] Golombek, M., Warner, N. H., Grant, J. A., Hauber, E., Ansan, V., Weitz, C. M., Williams, N., Charalambous, C., Wilson, S. A., DeMott, A., Kopp, M., Lethcoe-Wilson, H., Berger, L., Hausmann, R., Marteau, E., Vrettos, C., Trussell, A., Folkner, W., Maistre, S. L., . . . Banerdt, W. B. (2020). Geology of the InSight landing site on Mars. Nature Communications, 11(1). https://doi.org/10.1038/s41467-020-14679-1

[12] Greicius, A. (2023, September 7). NASA's curiosity captures stunning views of a changing Mars landscape - NASA. NASA. https://www.nasa.gov/missions/mars-science-laboratory/curiosity-rover/nasas-curiosity-captures-stunning-views-of-a-changing-mars-landscape/

[13] Gundlach, B., & Blum, J. (2015). Regolith grain size and cohesive strength of near-Earth Asteroid (29075) 1950 DA. Icarus, 257, 126–129. https://doi.org/10.1016/j.icarus.2015.04.032

[14] Göttler, C., Hansen, O. L., Kinsey, J. C., Ball, A. J., & Burmeister, S. (2019). Abrasion and brush testing of spacecraft materials for the ExoMars 2020 mission. Planetary and Space Science, 174, 35-46.

[15] JSC-1A Lunar and Martian Soil Simulants | Space Foundation. (n.d.). https://web.archive.org/web/20140428054706/http://www.spacefoundation.org/programs/space-certification/certified-products/space-educational-product/jsc-1a-lunar-and-martian

[16] Mojave Mars Simulant — The Martian Garden. (n.d.). The Martian Garden. https://www.themartiangarden.com/mms1/mms1

[17] Mucha, K. (2023). Application of Rock Abrasiveness and Rock Abrasivity Test Methods—A Review. Sustainability, 15(14), 11243. https://doi.org/10.3390/su151411243

[18] Peters, G. H., Abbey, W., Bearman, G. H., Mungas, G. S., Smith, J. A., Anderson, R. C., Douglas, S., & Beegle, L. W. (2008). Mojave Mars simulant—Characterization of a new geologic Mars analog. Icarus, 197(2), 470–479. https://doi.org/10.1016/j.icarus.2008.05.004

[19] Ramkissoon, N. K., Pearson, V. K., Schwenzer, S. P., Schröder, C., Kirnbauer, T., Wood, D., Seidel, R. G., Miller, M. A., & Olsson-Francis, K. (2019). New simulants for martian regolith: Controlling iron variability. Planetary and Space Science, 179, 104722. https://doi.org/10.1016/j.pss.2019.104722

[20] .